SCUOLA DI DOTTORATO
UNIVERSITÀ DEGLI STUDI DI MILANO-BICOCCA

Department of Physics "Giuseppe Occhialini"

Ph.D. program in Physics and Astronomy, XVIII cycle
Curriculum of Theoretical Physics

Screening spectrum of QCD at high temperature

Pietro Rescigno
Registration number: 826333

Tutor: Dr. Marco Cè
Supervisor: Prof. Leonardo Giusti

Coordinator: Prof. Laura D'Alfonso

Academic Year 2024/2025

List of publications

An updated list of publications and bibliometric information can be found on my iNSPIRE page.

Articles

• M. Cè, L. Giusti, D. Laudicina, M. Pepe, P. Rescigno, "Non-static mesonic screening masses in high temperature QCD", *in preparation.*

[1] M. Cè, L. Giusti, D. Laudicina, M. Pepe, P. Rescigno, "The hyperfine splitting in QCD mesonic screening masses at asymptotically large temperatures", JHEP 05 (2025) 044

[2] L. Giusti, T. Harris, D. Laudicina, M. Pepe, P. Rescigno, "Baryonic screening masses in QCD at high temperature", Phys. Lett. B 855 (2024) 138799

[3] L. Giusti, M. Laine, D. Laudicina, M. Pepe, P. Rescigno, "Baryonic thermal screening mass at NLO", JHEP 06 (2024) 205

Contributions to conferences

As speaker

• P. Rescigno, M. Cè, L. Giusti, D. Laudicina, M. Pepe, "Non-perturbative behavior of thermal QCD up to the electroweak scale: computational strategy and screening masses", poster – XQCD 2025, Wroclaw, Poland

• P. Rescigno, L. Giusti, T. Harris, M. Laine, D. Laudicina, M. Pepe, "Nucleon screening masses in QCD at high temperature", plenary talk –
Strong and Electroweak Matter 2024, Frankfurt, Germany

[4] P. Rescigno, L. Giusti, T. Harris, D. Laudicina, M. Pepe, "Baryonic screening masses in high temperature QCD", parallel talk – The 40^{th} International Symposium on Lattice Field Theory, Fermilab, USA – PoS(LATTICE2023)

As author

• M. Cè, L. Giusti, M. Pepe, P. Rescigno, "Hadronic screening masses in thermal QCD up to the electroweak scale", parallel talk – The 42$^{\text{nd}}$ International Symposium on Lattice Field Theory (LATTICE26), TIFR Mumbai, India – Indico page

[5] D. Laudicina, L. Giusti, M. Bresciani, M. Dalla Brida, T. Harris, M. Pepe, P. Rescigno, "Non-perturbative thermal QCD at very high temperatures: computational strategy and hadronic screening masses", talk – The 41$^{\text{st}}$ International Symposium on Lattice Field Theory, University of Liverpool, UK – PoS(LATTICE24)

[6] L. Giusti, M. Bresciani, M. Dalla Brida, T. Harris, D. Laudicina, M. Pepe, P. Rescigno, "Non-perturbative thermal QCD at very high temperatures", parallel talk – 42$^{\text{nd}}$ International Conference on High Energy Physics, Prague, CZ – PoS(ICHEP24)

Contents

Summary

This thesis details the study of hadronic observables in thermal QCD in the regime of very high temperature. We have focused on screening masses of both baryonic and flavor non-singlet mesonic states, in sectors with both zero (static) and non-zero (non-static) Matsubara frequencies. They are important quantities as they characterize spatial correlation in the thermal medium and quantify how efficiently strong interactions are screened at high temperatures, and they serve as ideal probes of chiral symmetry restoration.

The first main original contribution of this thesis is the determination of screening masses at temperatures of about 1 GeV up to about 165 GeV from first-principles non-perturbative simulations of lattice QCD with 3 flavors of massless quarks, exploiting a recently proposed strategy that allows to define and efficiently simulate the theory in the aforementioned temperature range. Our findings represent the first results in the literature for baryonic screening masses, and the first results in the non-static mesonic sector at temperatures from 1 GeV up to 165 GeV. After observing a rather severe signal-to-noise-ratio problem in the non-static mesonic sector which prevented the determination of screening masses, we developed an algorithmic solution based on an efficient computation of volume-averaged correlators using random sources. This allowed us on one hand to obtain non-static mesonic screening masses with a precision of around 1% in the continuum, and on the other hand to determine static screening masses, previously computed at the permille level, with even higher accuracy.

The non-perturbative determinations have been complemented by perturbative computations of the same quantities, which represent the second main original contribution of this thesis. The perturbative calculations have been performed in the three-dimensional effective field theory that describes QCD at sufficiently high temperature. In particular, we have determined for the first time the next-to-leading-order correction to the free theory value of baryonic screening masses, of order g^2 in the strong coupling constant g, and the leading-order value of the difference between the screening masses of the vector and pseudoscalar mesons in

the static sector – the hyperfine splitting, which turns out to be of order g^4.

On the one hand, the perturbative results are instrumental to interpret the non-perturbative data and study their dependence on the temperature. On the other hand, we observe sizeable discrepancies between the available terms of the perturbative series and the non-perturbative data, in all channels and sectors considered and over the whole temperature range studied. In this context, the hyperfine splitting proved to be particularly interesting, as we find that the bulk of its value comes from terms of higher powers than the leading g^4, which receive contributions of non-perturbative nature.

The results collected in this thesis represent an extensive investigation of hadronic properties of thermal QCD and advance our understanding of the high-temperature phase of the theory, revealing that non-perturbative effects are relevant, and in some cases dominant, up to temperatures of the order of the electroweak scale.

Chapter 1

The theory of strong interactions

The strong interaction, together with the weak interaction, electromagnetism and gravity, is one of the four known fundamental interactions in Nature. It explains how particles such as the protons and neutrons, which constitute the vast majority of ordinary matter in the Universe, emerge from the fundamental quarks and gluons and interact to form atomic nuclei. Its experimentally observed properties are understood from a theoretical point of view as described by a quantum field theory with non-abelian gauge group SU(3), with quarks being fermionic fields in the fundamental representation and interacting with the gluons described by the non-abelian gauge bosons. This chapter provides a comprehensive summary of the formal continuum definition of the theory and a review of its most important features.

1.1 QCD action

Quantum Chromo-Dynamics (QCD) is the sector of the Standard Model which describes strong interactions. With just a few free parameters, it is able to account for the experimentally observed properties of hadrons from low to high energy scales (see [7] for a recent review celebrating 50 years of the theory). The first step to understand its formal definition consists in the identification of the QCD action; to this end it is instructive to consider the most general classical Euclidean[1] Lagrangian density that one can write requiring SO(4) invariance and renormalizability - in 4 dimensions - for a theory with a number N_f of spin $\frac{1}{2}$ fields transforming in the fundamental representation of a unitary gauge group SU(N_c)[2],

[1] Unless otherwise specified, throughout this thesis we adopt the Euclidean metric $\eta = (1, 1, 1, 1)$ implying the usual Wick rotation from real to imaginary time, see equation (1.2.4).

[2] For the notation and conventions used in this thesis, see Appendix A.

which reads[3]

$$\mathcal{L}_{\mathrm{QCD}}\left[A_\mu, \psi, \bar{\psi}\right] = \frac{1}{2g_0^2}\,\mathrm{Tr}\left\{F_{\mu\nu}(x)F_{\mu\nu}(x)\right\} + \sum_f \bar{\psi}_f(x)\left(\gamma_\mu D_\mu + m_f\right)\psi_f(x). \quad (1.1.1)$$

The first term in the above equation is the Yang-Mills action for the non-Abelian gauge fields A_μ (the gluons) with bare coupling constant g_0^2, while the second term is the gauge invariant Lagrangian for each of the N_f Dirac spinors ψ_f, $\bar{\psi}_f$ with bare masses m_f (the quarks). While it will be instrumental to keep N_c - the number of "colors" - and N_f - the number of quark "flavors" - general for parts of this chapter, QCD is defined by considering $N_c = 3$ and $N_f = 6$ with no degenerate quark masses. With a slight abuse of notation, I will refer to both this case and to the general case as QCD. Integrating the Lagrangian density over spacetime yields the QCD action

$$\mathcal{S}_{\mathrm{QCD}}\left[A_\mu, \psi, \bar{\psi}\right] = \int \mathrm{d}^4x\ \mathcal{L}_{\mathrm{QCD}}\left[x; A_\mu, \psi, \bar{\psi}\right]. \quad (1.1.2)$$

1.2 Path integral

The promotion of a classical theory with a given action to a Quantum Field Theory can be achieved within the Path Integral formalism; the central object in this formalism is the system's partition function which, inspired by its analogue in classical statistical mechanics, takes into account all the system's possible microstates - the values of the fields at each spacetime point, or *configurations* - each weighted with a Boltzmann factor given by the exponential of the action:

$$\mathcal{Z}_{\mathrm{QCD}} = \int DA_\mu D\bar{\psi} D\psi\ e^{-\mathcal{S}_{\mathrm{QCD}}}, \quad (1.2.1)$$

where the dependence of the action on the fields has been suppressed for clarity. Physical observables such as particle masses, decay widths and amplitudes are encoded in correlation functions of local fields, which take the form of statistical expectation values:

$$\langle O\left(x_1, \ldots, x_n\right)\rangle \equiv \frac{1}{\mathcal{Z}_{\mathrm{QCD}}}\int DA_\mu D\bar{\psi} D\psi\ O\left(x_1, \ldots, x_n\right) e^{-\mathcal{S}_{\mathrm{QCD}}}, \quad (1.2.2)$$

where $O\left(x_1, \ldots, x_n\right)$ denotes a general field constructed from the elementary fields appearing in the action of equation (1.2.1) with support at spacetime points $\{x_1, \ldots, x_n\}$. The above expressions are completely formal at this stage. On the

[3]The additional dimension 4, CP-violating operator that can be constructed from the gauge fields will be omitted throughout this thesis, due to the extremely small value of the QCD theta-term observed from experiment.

one hand, the path integral can be consistently defined in a perturbative setting *à la* Faddeev-Popov (see appendix B for a summary); on the other hand, it finds a natural and non-perturbative definition through the lattice regularization of the theory, which is the approach that will be adopted in this thesis and will be reviewd in detail in chapter 2. To conclude this section, it is important to remark that the definition of the path integral can equivalently be performed (and it historically has been) considering the usual real-time Minkowski metric, with fields being operators acting on the theory's Hilbert space. The key observation is that there exists a one-to-one correspondence between vacuum expectation values of time-ordered products of operators in Minkowski time and expectation values of fields in imaginary Euclidean time:

$$\left\langle O_1(x_1^{\mathrm{E}}) \dots O_n(x_n^{\mathrm{E}}) \right\rangle \longleftrightarrow \langle \Omega | \, \mathcal{T} \left\{ \hat{O}_1(x_1^{\mathrm{M}}) \dots \hat{O}_n(x_n^{\mathrm{M}}) \right\} | \Omega \rangle \,, \tag{1.2.3}$$

where $|\Omega\rangle$ is the theory's vacuum state, $\mathcal{T}$ denotes the time-ordering operation and hats indicate operators. Finally, the relation between Euclidean and Minkowski coordinates is expressed by the usual Wick rotation

$$x_0^{\mathrm{E}} \equiv i x^{\mathrm{M},0}, \quad x_j^{\mathrm{E}} \equiv x^{\mathrm{M},j}. \tag{1.2.4}$$

Equations (1.2.3) and (1.2.4) imply that all the information contained in a real-time Minkowskian correlation function can in principle be reconstructed from an Euclidean expectation value by performing an analytic continuation from imaginary to real time.[4] Among the convienient aspects of the Euclidean formulation of QFTs are the useful parallel with classical statistical mechanics and the fact that Euclidean path integrals are well suited for numerical solutions, as is discussed in section 2.5 and appendix D. Unless otherwise specified, all coordinates and fields are assumed to be Euclidean in this thesis.

1.3 Renormalization

Renormalization, together with the definition of the action and the path integral, is a fundamental and necessary step for the definition of a quantum field theory. Before entering into details, it is useful to have a general and intuitive picture in mind: very broadly speaking, renormalization is the process of fixing the free parameters in the action – such as couplings and masses, which in general do not have a direct physical interpretation – through the values of some physical observables (one for each parameter in the action). It can be shown that this can be done in a well-defined way for theories – in 4 dimensions – whose Lagrangian

[4] At the formal level, the equivalence between the two formulations follows from the Osterwalder-Schrader Axioms [8, 9].

contains only products of fields and derivatives of mass dimesion 4 or less. Such theories are said to be *renormalizable*. The process of renormalization can be split into three steps: first, the formally defined theory (1.2.1) is *regulated* through the introduction of a parameter (the regulator) that modifies the theory to make it finite and well defined. Next, at fixed value of the regulator, one imposes that a set of quantities assume their physical value at an arbitrary reference scale μ. To achieve this, the bare parameters acquire a dependence on the regulator and on the renormalization scale μ. For instance, regularizing the theory on a spacetime lattice with spacing a, i.e. defining the theory on a hypercubic grid of spacetime points of the form

$$x_\mu = a \cdot n_\mu, \;\; n_\mu \in \mathbb{Z}^4, \tag{1.3.1}$$

the bare coupling, mass and fields are renormalized by suitable factors which depend on the chosen scale μ and the regulator a:

$$\bar{g}^2(\mu) = Z_g\left(g_0^2, a\mu\right) g_0^2, \tag{1.3.2}$$

$$\bar{m}_i(\mu) = Z_{m,i}(g_0, a\mu) m_i, \tag{1.3.3}$$

$$A_\mu^R = \sqrt{Z_3} A_\mu, \tag{1.3.4}$$

$$\psi_i^R = \sqrt{Z_2}\psi_i. \tag{1.3.5}$$

The details of how this step is performed define the chosen *renormalization scheme*. Once the dependence of the parameters on the regulator is known, the latter can be removed while the chosen quantities remain fixed at the prescribed value: the *renormalized* theory now yields finite and well-defined predictions. Physical observables such as masses do not depend on the arbitrary scale μ or on the chosen scheme, but it is also possible to define and study scale and scheme-dependent quantities, see sections 1.3.3 and 1.3.2

While historically the renormalization procedure has been introduced in a perturbative setting, it must be remarked that the theory can be renormalized in a completely non-perturbative way, see e.g. [10]. Non-perturbative renormalization arises naturally when working with the lattice regularization, One of the main advantages of the lattice regularization are that, as we will see in chapter 2, this framework allows to retain exact gauge invariance of the theory without the need for gauge fixing and introducing ghost fields, as well as a remnant of the continuum Lorentz symmetry, and most importantly within the lattice formalism a rigorous definition of the path integral (1.2.1) can be given. At non-zero spacing any correlation function or observable in the regularized theory is a finite and well-defined function of the bare parameters and the lattice spacing. As noted above, naively removing the regulator takes us back to the divergent theory; in order to obtain finite predictions when the lattice spacing is sent to 0, one needs to impose

that some dimensionful physical observable computed on the lattice assumes its physical value,

$$\Theta_{\text{lat}}(g_0, a) = \Theta_{\text{phys}}, \tag{1.3.6}$$

and when removing the regulator $a \to 0$ the value of the bare coupling must be modified so that the condition (1.3.6) still holds. This implicitly defines the dependence of the lattice spacing on the bare coupling constant $a(g_0)$; a similar condition must be imposed for each bare coupling in the regularized lagrangian - for instance, the bare quark masses can be tuned to reproduce the physical mass of a chosen hadron. In this way, the continuum limit of the regularized theory can be approached while maintaining observable quantities finite and equal to their physical value; the variation of the bare parameters that ensures this conditions defines the so-called *lines of constant physics.* More details will be given in section 2.3.

It is worth mentioning at this point that *composite operators*, i.e. operators built from products of elementary fields, require their own renormalization factors in addition to those coming from the elementary fields. Moreover, in the renormalization procedure composite operators *mix* with all operators with the same quantum number (symmetries) and equal or smaller mass dimension:

$$\bar{O} = \sum_i Z_i O_i, \ \dim[O_i] \leq \dim[O]\,. \tag{1.3.7}$$

From a perturbative point of view, where correlation functions such as (1.2.2) are expanded in a power series around the non-interacting theory $g_0 = 0$, ultraviolet-divergent momentum integrals generally arise at the loop level, making the theory unpredictive. In a renormalizable theory it is possible to systematically reabsorb divergences in correlation functions to obtain finite results at any order in perturbation theory. Probably the most widely employed regularization for perturbative computations, which preserves Lorentz symmetry and gauge invariance, is given by *dimensional regularization.* The number of spacetime dimensions d is allowed to differ from 4, usually setting[5] $d = 4 - 2\epsilon$, so that integrals can be performed for values of d for which they are finite, and only afterwards the limit $\epsilon \to 0$ can be studied to obtain the renormalized theory. Popular renormalization schemes within dimensional regularization are the *minimal subtraction* (MS) and *modified minimal subtraction* ($\overline{\text{MS}}$) schemes.

[5]This procedure exploits the fact that loop integrals are analytic functions of the spacetime dimension d

1.3.1 Callan-Symanzik Equation

Additional insight about the structure of QCD can be obtained by carefully exhamining the implications of renormalization. Consider a bare correlation function $\Gamma_0^{n_G,n_F}$ containing n_G gluon fields and n_F quark fields. Given equations (1.3.4) and (1.3.5) the relation between the bare and renormalized correlator is

$$Z_3^{-n_G/2} Z_2^{-n_F/2} \bar{\Gamma}^{n_G,n_F}(\mu, \bar{g}, \bar{m}) = \Gamma_0^{n_G,n_F}(g_0, m_0). \tag{1.3.8}$$

Since the bare correlator does not depend on the renormalization scale μ, the total derivative of Γ_R with respect to μ (taking into account the implicit dependence in the renormalized coupling and masses) vanishes; this statement is encoded in the Callan-Symanzik equation, which is valid at the non-perturbative level:

$$\left[\mu\frac{\partial}{\partial\mu} + \beta(\bar{g})\frac{\partial}{\partial\bar{g}} + \bar{m}\tau(\bar{g})\frac{\partial}{\partial\bar{m}} - n_G\gamma_3(\bar{g}) - 2n_F\gamma_2(\bar{g})\right]\bar{\Gamma}^{n_G,n_F} = 0. \tag{1.3.9}$$

The variation of the coupling and the quark masses with the renormalization scale – their *running* – is determined by the theory's *beta* and *tau* functions

$$\beta(\bar{g}) \equiv \mu\frac{\partial}{\partial\mu}\bar{g}(\mu), \tag{1.3.10}$$

$$\tau(\bar{g}) \equiv \frac{\mu}{\bar{m}}\frac{\partial}{\partial\mu}\bar{m}(\mu), \tag{1.3.11}$$

while the scaling of the fields' renormalization is governed by the anomalous dimensions

$$\gamma_i(\bar{g}) \equiv \frac{1}{2}\mu\frac{\partial}{\partial\mu}\ln Z_i, \;\; i = 3, 2. \tag{1.3.12}$$

The beta function admits a series expansion in odd powers of the coupling constant

$$\beta(\bar{g}) = -\bar{g}^3\sum_{n=0}^{\infty} b_n\bar{g}^{2n}, \tag{1.3.13}$$

and the coefficients b_n can be computed in perturbation theory; while their values depend in general on the particular renormalization scheme chosen for the computation, it turns out that the first two coefficients are universal, i.e. they are scheme independent. Their expression, for general N_c and N_f, reads[11–13]:

$$b_0 = \frac{1}{(4\pi)^2}\left(\frac{11}{3}N_c - \frac{2}{3}N_f\right), \tag{1.3.14}$$

$$b_1 = \frac{1}{(4\pi)^4}\left(\frac{34}{3}N_c^2 - \frac{13N_c^2 - 3}{3N_c}N_f\right). \tag{1.3.15}$$

Relatedly, the tau function's expansion contains only even powers of $\bar{g}$:

$$\tau(\bar{g}) = -\bar{g}^2 \sum_{n=0}^{\infty} d_n \bar{g}^{2n}, \tag{1.3.16}$$

and the only universal coefficient is the leading one

$$d_0 = \frac{6}{(4\pi)^2} \frac{N_c^2 - 1}{2N_c}. \tag{1.3.17}$$

These three geometric coefficients, which only depend on the number of colors of the gauge group and the number of fermions in the theory, can reveal two of the most striking and important features of QCD: asymptotic freedom and the exhistence of a fundamental dimensionful scale in the theory.

1.3.2 The scale of strong interactions

Looking for explicit solutions to equation (1.3.10) highlights a central feature of QCD. It can be shown that integrating equation (1.3.10) between two arbitrary values of the scale μ_0 and μ yields

$$\frac{\mu}{\mu_0} = \exp \int_{\bar{g}(\mu_0)}^{\bar{g}(\mu)} \frac{\mathrm{d}g}{\beta(g)}, \tag{1.3.18}$$

which involves the integral of the reciprocal beta function. In a neighborhood of $g = 0$, this has non-integrable terms that involve the two universal coefficients b_0 and b_1:

$$\frac{1}{\beta(g)} \underset{g\to 0}{=} -\frac{1}{b_0 g^3} + \frac{b_1}{b_0^2 g} + \mathcal{O}(g). \tag{1.3.19}$$

To isolate the finite and divergent parts of the integral in equation (1.3.18) one can add and subtract the first two terms of equation (1.3.19)

$$\frac{\mu}{\mu_0} = \exp\left\{ \int_{\bar{g}(\mu_0)}^{\bar{g}(\mu)} \mathrm{d}g \left[\frac{1}{\beta(g)} + \frac{1}{b_0 g^3} - \frac{b_1}{b_0^2 g} \right] \right\} \exp\left\{ \int_{\bar{g}(\mu_0)}^{\bar{g}(\mu)} \mathrm{d}g \left[-\frac{1}{b_0 g^3} + \frac{b_1}{b_0^2 g} \right] \right\}, \tag{1.3.20}$$

making apparent that the first integral is finite even when $\bar{g} = 0$ while the second one diverges if the coupling at one of the scales vanishes. Nevertheless, the latter integral can be computed explicitly, and breaking up the former from $\bar{g}(\mu_0)$ to 0 and from 0 to $\bar{g}(\mu)$ allows to separate all the terms that depend on μ from those that depend on μ_0:

$$\mu \cdot \left(\bar{g}^2(\mu)\right)^{-b_1/(2b_0^2)} e^{-1/(2b_0 \bar{g}^2(\mu))} \cdot \exp\left\{ -\int_0^{\bar{g}(\mu)} \mathrm{d}g \left[\frac{1}{\beta(g)} + \frac{1}{b_0 g^3} - \frac{b_1}{b_0^2 g} \right] \right\} = \left\{ \mu \leftrightarrow \mu_0 \right\}. \tag{1.3.21}$$

The first thing to notice about the above equation is that both the left and right hand side are finite for any finite value of the renormalization scale. Secondly, since the left hand side only depends on μ and the right hand side only depends on μ_0, whose values are completely arbitrary, equation (1.3.21) tells us that this particular combination does not actually depend on the renormalization scale. These observations point to the existence of a quantity that carries the dimension of energy but that does not depend on the arbitrary scale at which the theory is renormalized; this is known as the Λ-parameter of QCD, or the QCD scale, and it is defined as[6]

$$\Lambda \equiv \mu \cdot \left[b_0 \bar{g}^2(\mu)\right]^{-b_1/(2b_0^2)} e^{-1/(2b_0 \bar{g}^2(\mu))} \cdot \exp\left\{ -\int_0^{\bar{g}(\mu)} \mathrm{d}g \left[\frac{1}{\beta(g)} + \frac{1}{b_0 g^3} - \frac{b_1}{b_0^2 g} \right] \right\}. \quad (1.3.22)$$

Through the beta-function, the Λ-parameter depends on the number of quark flavors present in the theory. Despite being renormalization scale-independent (RGI) quantity, its value depends on the chosen renormalization scheme; therefore, Λ is not strictly speaking a physically observable quantity. That being said, its existence means that the theory naturally produces a typical energy scale, even in the limit where all quark masses are set to zero.[7] The emergence of this dimensionful energy scale can be seen as a consequence of the fact that the scale μ introduced by the renormalization procedure, even though completely arbitrary and unphysical, breaks the scale invariance of the theory at the classical level. Indeed, one finds that upon quantization the trace of the energy-momentum tensor – which is zero in the classical theory, implying invariance under spacetime dilations – is proportional to the beta function. This is an example of an *anomaly* of the quantum theory (the trace anomaly), i.e. the breaking of a symmetry of the classical theory due to quantization, see section 1.5 for another example related to chiral symmetry. This observation has profound implications for the predictions of the theory: consider an hadron H, such as the proton or neutron; its mass M_H^{exp} is an experimentally measurable physical quantity, and therefore its value as predicted by QCD M_H^{QCD} must not depend neither on the renormalization scale μ nor on the chosen renormalization scheme. The previous discussion implies that in QCD the hadron mass must be proportional to the QCD-scale through an appropriate coefficient:

$$M_H^{\mathrm{QCD}} = y_X^H \cdot \Lambda_X, \quad (1.3.23)$$

[6]The inclusion of an additional b_0 factor that multiplies the squared coupling with respect to equation (1.3.21) is purely conventional and does not alter the properties of the Λ-parameter.

[7]In this limit, the dimensionless coupling g_0 is the only free parameter of QCD, and equation (1.3.22) relates it to the dimensionful Λ-parameter. This phenomenon is known as *dimensional transmutation*.

where the subscript X enphasizes the chosen renormalization scheme, This form ensures that the predicted mass is scale-independent; the coefficient y_X^H itself will depend on the chosen renormalization scheme in such a way that the product with Λ is also scheme-independent. Equation (1.3.23) also implies that the ratio of two hadron masses in QCD is scale and scheme-independent, i.e. it is a physical prediction of the theory. As said above, Λ is not a physical observable, therefore its value in physical units does not have direct phsyical meaning; it is however useful to point out that, depending on the chosen scheme, it generally lies in the range of a few hundred MeV: for 3 flavors of massless quarks in the $\overline{\text{MS}}$ scheme, for instance, one finds $\Lambda_{\overline{MS}} = 341$ MeV [14]. This number has been determined non-perturbatively in a renormalization scheme suitable for lattice simulations, and then matched to the $\overline{\text{MS}}$ scheme. Indeed it is interesting to notice that the values of Λ in two different schemes A and B are connected by an exact 1-loop relation. Indeed, if the perturbative relation between the renormalized couplings in the two schemes $\bar{g}_A^2$ and $\bar{g}_B^2$ is

$$\bar{g}_A^2 = \bar{g}_B^2 + b_{AB}\bar{g}_B^4 + \dots \tag{1.3.24}$$

the Λ parameters in the two schemes exactly satisfy

$$\Lambda_A/\Lambda_B = \exp\{b_{AB}/2b_0\}. \tag{1.3.25}$$

An analogous discussion can be applied to the running quark masses, and an RGI quark mass can be defined for each flavor by

$$m_{\text{RGI}} = \bar{m}(\mu)\left[2b_0\bar{g}(\mu)^2\right]^{-d_0/2b_0}\exp\left\{-\int_0^{\bar{g}(\mu)} \mathrm{d}g\left[\frac{\tau(g)}{\beta(g)} - \frac{d_0}{b_0 g}\right]\right\}, \tag{1.3.26}$$

which is not only scale independent, but it also does not depend on the choice of renormalization scheme.

1.3.3 Asymptotic freedom

In QCD with $N_c = 3$ and $N_f = 6$ the first and second coefficients of the perturbative expansion of the beta function (1.3.13) are negative; as an immediate consequence, the renormalized coupling *decreases* as the renormalization scale μ increases. The scale dependence of the running coupling can be expressed in terms of the QCD-scale: for instance, the two-loop renormalized coupling reads

$$\bar{g}^2(\mu) = \frac{1}{2b_0\ln(\mu/\Lambda) + \frac{b_1}{b_0}\ln(2\ln(\mu/\Lambda))}. \tag{1.3.27}$$

We thus see that Λ also sets the scale for the different regimes of QCD: the high-energy, UV regime is characterized by $\mu \gg \Lambda$, where the coupling becomes small and approaches 0 only at infinitely high energy; in the low energy IR regime $\mu \lesssim \Lambda$ the coupling instead becomes large. This equation implies that any computation in perturbation theory, which expands path integrals around the non-interacting theory $g_0 = 0$ and assumes the coupling constant to be "small", is well justified at high energy; instead at low energy, where the theory is strongly coupled, the expansion parameter becomes large and the perturbative series loses reliability, and non-perturbative methods become necessary to study the theory.

While not technically a physical observable – its value depends on both the renormalization scale and scheme – $\bar{g}(\mu)$ quantifies the intensity of interactions between quarks and gluons at a given energy scale. Indeed, if one chooses the renormalization scale equal to a physical momentum transfer in an experimentally accessible process (such as the decay of an hadron) it is possible to infer the value of $\bar{g}(\mu)$ in a given scheme from experimental data. On the other hand, being a fundamental property of the theory, it can be computed from first principles (see [15] for a review on the different determinations of the strong coupling constant). Perturbatively it is known up to 5-loop order [16, 17], i.e. the first 5 coefficients in equation (1.3.10) have been computed. At the time of writing, the most precise determination of the strong coupling constant and its runnning with the renormalization scale is obtained non-perturbatively from the lattice [18], see figure 1.1.

Historically, the discovery that non-abelian Yang-Mills theories such as QCD are renormalizable [19–21] and could display asymptotic freedom was probably the main point that consolidated QCD as the theory of strong interaction. Indeed it offered a natural and compelling explanation for the puzzling discoveries of deep inelastic scattering experiments: when high energy electrons collide with protons to probe their structure, it was found that as the energy of the incoming electron beam increased, and thus as the proton structure was investigated at shorter length scales, the proton progressively behaved as being composed of point-like non-interacting spin-1/2 objects at the time dubbed *partons*, reproducing the so-called Bjorken scaling and its violations. This behavior is now interpreted as the result of the interaction between quarks getting progressively weaker as the energy increases due to asymptotic freedom and, as we will see in the next section motivated the promotion of quarks from useful mathematical objects to interpret the observed symmetries of the hadron spectrum to quantum fields transforming in the fundamental representation of a color gauge group.

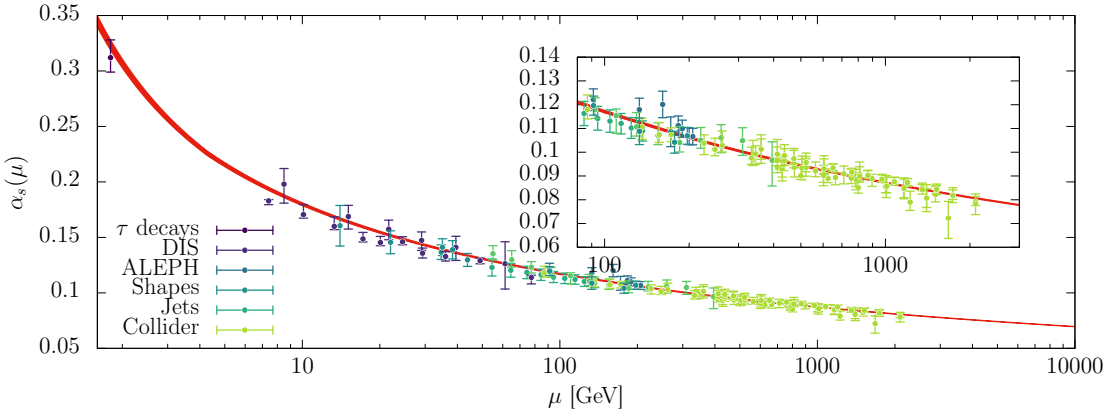

FIGURE 1.1: From [18]: Running of $\alpha_s(\mu) \equiv \bar{g}^2(\mu)/4\pi$ with the renormalization scale obtained non-perturbatively from the lattice (red band), compared to various determinations from experimental data from the Particle Data Group (errorbars) [22]

1.4 Hadrons

The QCD Lagrangian (1.1.1) is written in terms of elementary fields associated to quarks and gluons; however, in the plethora of subatomic particles that are produced at accelerator facilities or reach Earth as cosmic rays, neither quarks nor gluons are ever observed by the experiments' detectors[8]. Instead, aside from stable leptons and photons, what is observed is a numerous collection of *hadrons* with widely different values of mass, spin and electric charge. How hadrons emerge from quarks and gluons – and how the costituents' properties shape the properties of the observed composite states – is one of the most fascinating aspects of QCD, and this section summarizes some of the most important features of the hadron spectrum.

1.4.1 Color confinement

The idea that hadrons are not elementary particles, but rather bound states comprised of elementary spin-1/2 fermions named "quarks" was introduced by Gell-Mann [23] and Zweig [24] precisely as an attempt to make sense of the observed properties of the "particle zoo". Indeed, assuming that quarks of different flavors combine to form hadrons according to the representations of a flavor group $\mathrm{SU}(3)_\mathrm{f}$ furnishes a good explanation of the number of observed light hadrons, their spin and their electric charge, as well as the (approximate) mass degeneracy of the mul-

[8]This is at variance with what happens, for instance, in Quantum Electro-Dynamics (QED), where the quanta of the fields appearing in the Lagrangian are experimentally observable particles (electrons and photons).

tiplets, see figure 1.2. However, in order to correctly realize the symmetries of the total hadron wavefunction under the exchange of two quarks, it was conjectured that each quark carries an additional quantum number, a "color" degree of freedom, associated to the invariance of the theory under $\mathrm{SU}(3)_\mathrm{c}$ rotations of the quark fields. Postulating that the color wavefunction of an hadron must be completely antisymmetric under the exchange of any quark pair (i.e., the hadron belongs to the "colorless" singlet representation of $\mathrm{SU}(3)_\mathrm{c}$) yields the correct symmetry for the total wavefunction. Promoting $\mathrm{SU}(3)_\mathrm{c}$ to a group of local transformations that leave physics invariant requires the introduction of gluons, the carriers of the strong force, themselves charged under $\mathrm{SU}(3)_\mathrm{c}$ belonging to the adjoint representation; this results in the QCD Lagrangian (1.1.1). The founding hypothesis that the only physically observable states are those that have no net color charge is known as *confinement*. It immediately implies that quark and gluon fields, by construction gauge-variant objects, can not create physical states, and on the other hand dictates what types of composite states can be physical: only combinations that contain a singlet representation can compose observable hadrons. The simplest possibilities consist of a quark and antiquark, belonging to the fundamental and anti-fundamental representation of $\mathrm{SU}(3)_\mathrm{c}$,

$$q\bar{q} \ : \ 3_\mathrm{c} \otimes \bar{3}_\mathrm{c} = \mathbf{1_c} \oplus 8_\mathrm{c}, \tag{1.4.1}$$

or a bound state composed of 3 quarks

$$qqq \ : \ 3_\mathrm{c} \otimes 3_\mathrm{c} \otimes 3_\mathrm{c} = \mathbf{1_c} \oplus 8_\mathrm{c} \oplus 8_\mathrm{c} \oplus 10_\mathrm{c}, \tag{1.4.2}$$

where we highlighted the physical singlet representation, with all other representation being unphysical. Hadrons composed of a quark and an antiquark as in equation (1.4.1) are known as *mesons*, whereas particles containing three quarks are called *baryons*. *Exotic* states composed of four ($qq\bar{q}\bar{q}$) or five ($qqqq\bar{q}$) quarks can also form color-neutral combinations. Their exhistence has been conjectured since the 1980s, and conclusive experimental observations have been recently reported (see [25] for a recent review on the status and prospects of theoretical and experimental studies of exotic states). Gluons themselves can combine into color neutral objects called *glueballs*; the tensor product of two adjoint representations, for instance, contains a singlet:

$$gg \ : \ 8_\mathrm{c} \otimes 8_\mathrm{c} = \mathbf{1_c} \oplus 8_\mathrm{c} \oplus 8_\mathrm{c} \oplus 10_\mathrm{c} \oplus \bar{10}_\mathrm{c} \oplus 27_\mathrm{c}. \tag{1.4.3}$$

Because of their mixing with other flavor-singlet states (see next section) experimental searches of glueballs are notoriously hard, and unambiguous evidence for their production in is still debated, see [26–28] for recent reviews. They are also challenging objects to study from a theoretical point of view, see [29] for a review.

Light quarks				Heavy quarks			
Name	Symbol	Charge	$\bar{m}_{\overline{\text{MS}}}$	Name	Symbol	Charge	$\bar{m}_{\overline{\text{MS}}}$
Up	u	$+\frac{2}{3}$	2.16(7) MeV	Charm	c	$+\frac{2}{3}$	1.2730(46) GeV
Down	d	$-\frac{1}{3}$	4.70(7) MeV	Bottom	b	$-\frac{1}{3}$	4.183(7) GeV
Strange	s	$-\frac{1}{3}$	93.5(8) MeV	Top	t	$+\frac{2}{3}$	162.69(6) GeV

TABLE 1.1: List of quarks and their properties, including their electric charge and their mass. The reported masses are the renormalized quark masses in the $\overline{\text{MS}}$ scheme obtained as described in [22]. The renormalization scale at which the masses are specified is taken to be 2 GeV for the light quarks (u, d, s), while the heavy quarks (c, b, t) are renormalized at a scale equal to their mass.

1.4.2 Flavor structure

The QCD Lagrangian is obtained by requiring exact gauge invariance under $\text{SU}(3)_\text{c}$ and Lorentz invariance. Among other things, the non-abelian nature of $\text{SU}(3)_c$ dictates that gluons interact with different quark flavors in the exact same way, i.e. with the same coupling[9]. This simple observation suggests the exhistence of an additional "accidental" symmetry of QCD. Indeed, if some number $n_f \leq N_f$ of quarks had degenerate masses, they would be perfectly identical to the strong interaction, and the lagrangian (1.1.1) would be symmetric under the following global unitary transformations of the quark fields:

$$\begin{aligned} \psi &\to \psi' = V\psi \\ \bar{\psi} &\to \bar{\psi}' = \bar{\psi}V^\dagger \end{aligned} \quad \text{with } \psi = \begin{pmatrix} \psi_u \\ \psi_d \\ \vdots \\ \psi_t \end{pmatrix}, \; V \in \text{U}(n_f)_\text{f}, \tag{1.4.4}$$

The above equation defines a *flavor transformation*, and regimes in which QCD is invariant under such transformations are called *flavor symmetric*. In such scenarios, color singlet hadrons composed of multiple quarks and antiquarks can be classified according to their flavor quantum numbers, and in particular the spectrum of hadrons falls into irreducible representations of the unitary flavor group.

The values of the different quark masses in the $\overline{\text{MS}}$ scheme are reported in table 1.1, from which it is evident that no mass degeneracy is present in QCD - quite the opposite, the heaviest (top) and lightest (up) quark mass differ by 5 orders of magnitude. While this implies that flavor symmetry is not an exact property of

[9]The situation is quite different from the abelian case of QED, where each charged fermion can have its own electric charge.

QCD, the particular values of the quark masses allow for an approximately symmetric description in some cases. This statement is made quantitative owing to the exhistence of the QCD scale Λ: this is the typical energy scale to which other dimensionful quantities in the theory should be compared. Stressing once more that the exact values are scheme-dependent quantities, general conclusions can be drawn by keeping in mind the values for Λ and the quark masses in the $\overline{\text{MS}}$ scheme previously reported. Approximating the up and down quarks as mass degenerate is then well justified, as one finds

$$\frac{m_d \ - \ m_u}{\Lambda} \ \lesssim \ 1\%.$$

The relevant flavor group in this approximation is $\mathrm{U}(2)_\mathrm{f}$. Its unit-determinant component $\mathrm{SU}(2)_\mathrm{f}$, known as the " isospin group", can be used to classify hadrons composed of up and down quarks. Including the strange quark in the degenerate mass approximation is less justified, as it holds

$$\frac{m_s \ - \ (m_u + m_d)/2}{\Lambda} \sim 20\%;$$

nevertheless representations of the resulting $\mathrm{SU}(3)_\mathrm{f}$ group are still useful to classify the valence quark structure of hadrons composed of light quarks and some of their properties. The resulting organization of mesons in an octet and a singlet, and baryons in an octet with spin $1/2$ and a decuplet with spin $3/2$, was one of the early successes of Gell-Mann's "Eightfold Way", see figure 1.2.

In QCD with massive degenerate u, d and s quarks the masses of hadrons belonging to the same multiplets are identical. The approximate nature of flavor symmetry is reflected in the fact that in Nature hadrons in the same multiplet have different masses (and that the flavor symmetric states mix to yield the actual physical states, like in the case of the η and η' mesons). For instance, the mass hierarchy of the pseudoscalar meson octet and singlet is summarized in table 1.2.

The reason that pions are so much lighter than the rest of the octet and the fact that the singlet η' is so much heavier than the other mesons can be both traced to different aspects of a special type of flavor symmetry – or rather its remnant – which is of crucial importance both for the phenomenology of QCD and for the study of its formal properties, which is known as *chiral symmetry*. As we will see, the properties of the pions are largely determined by the spontaneous breaking of chiral symmetry, while the mass of the η' is related to the *anomalous* nature of a specific subset of chiral transformations.

[9]The reported flavor combinations mix to give the physical η and η' states.

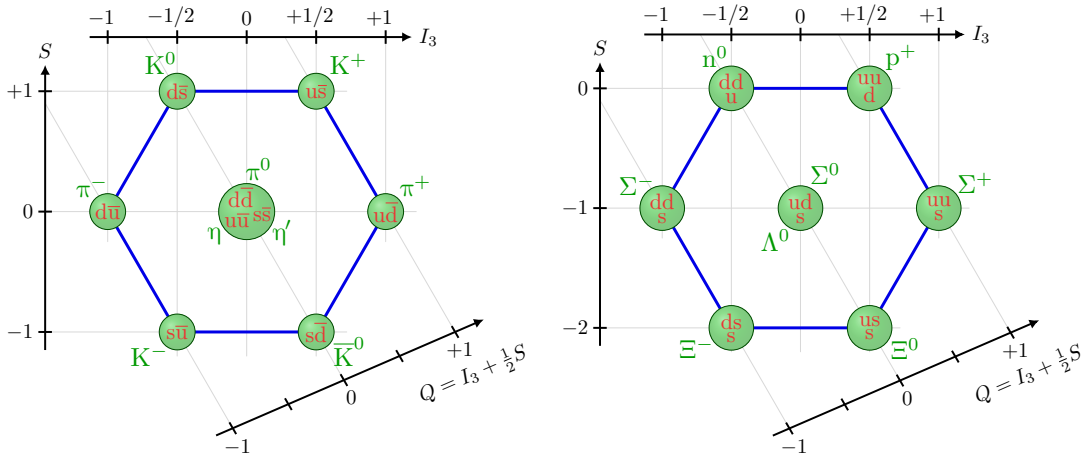

FIGURE 1.2: Pseudoscalar meson nonet (octet and singlet, left) and spin-1/2 baryon octet (right) in the $SU(3)_f$ limit, expressing the valence quark content, electric charge Q, strangeness S and third component of isospin I_3. Original pictures by Izaak Neutelings, modified and adapted here.

Particle	Mass [MeV]	$SU(3)_f$ content
π_0	134.9768(5)	$\frac{1}{\sqrt{2}}\left(u\bar{u} - d\bar{d}\right)$
$\pi^\pm$	139.57039(18)	$u\bar{d}$ / $d\bar{u}$
$K^\pm$	493.677(15)	$u\bar{s}$ / $s\bar{u}$
K_0 $\left(\bar{K}_0\right)$	497.611(13)	$d\bar{s}$ $\left(s\bar{d}\right)$
η	547.862(17)	$\frac{1}{\sqrt{6}}\left(u\bar{u} + d\bar{d} - 2s\bar{s}\right)$
η'	957.78(6)	$\frac{1}{\sqrt{3}}\left(u\bar{u} + d\bar{d} + s\bar{s}\right)$

TABLE 1.2: List of octet and singlet (last row) pseudoscalar mesons, their physical mass [22] and the corresponding quark content in the flavor symmetric limit.

1.5 Chiral symmetry

Let us consider in detail the quark sector of the QCD lagrangian,

$$\mathcal{L} = \bar{\psi}\left(\gamma_\mu D_\mu + M\right)\psi, \tag{1.5.1}$$

where the quark flavor vector ψ is defined in equation (1.4.4) and the mass matrix in flavor space is introduced as $M \equiv \mathrm{diag}\,(m_u, m_d, \ldots, m_t)$. As described in the previous section, the lagrangian admits $\mathrm{U}(N_f)_\mathrm{f}$ flavor symmetry if the mass matrix is proportional to the identity in flavor space: $M = m \cdot \mathbb{1}_\mathrm{f}$. It is also immediate to notice that the kinetic term in equation (1.5.1) is always invariant under flavor transformations, as it is also proportional to $\mathbb{1}_\mathrm{f}$. The different behavior of the kinetic and mass term can be further analysed by decomposing each spinor in its left and right-handed parts:

$$\psi = \psi_L + \psi_R \qquad \psi_{L/R} = P_{L/R}\psi \tag{1.5.2}$$

$$\bar{\psi} = \bar{\psi}_L + \bar{\psi}_R \qquad \bar{\psi}_{L/R} = \bar{\psi}P_{R/L}, \tag{1.5.3}$$

where the projectors on negative and positive chirality are defined as

$$P_{L/R} \equiv \frac{\mathbb{1} \mp \gamma_5}{2}. \tag{1.5.4}$$

In terms of these definite chirality fields, the quark lagrangian can be cast as

$$\mathcal{L} = \bar{\psi}_L \gamma_\mu D_\mu \psi_L + \bar{\psi}_R \gamma_\mu D_\mu \psi_R + \bar{\psi}_R M \psi_L + \bar{\psi}_L M \psi_R, \tag{1.5.5}$$

highlighting how the kinetic term (and thus the interaction with gluons) separates left and right-handed quarks, while the mass term mixes them. In the limit where quark masses vanish, $M = 0$, the original flavor symmetry is enlarged: it is now possible to redefine left and right handed fields independently, according to

$$\psi_L \to \psi'_L = V_L \psi_L, \quad \bar{\psi}_L \to \bar{\psi}'_L = \bar{\psi}_L V_L^\dagger, \qquad V_L \in \mathrm{U}(N_f)_L \tag{1.5.6}$$

$$\psi_R \to \psi'_R = V_R \psi_R, \quad \bar{\psi}_R \to \bar{\psi}'_R = \bar{\psi}_R V_R^\dagger, \qquad V_R \in \mathrm{U}(N_f)_R. \tag{1.5.7}$$

The limit where all quarks are massless is known as the *chiral limit*, and the invariance of the theory under $\mathrm{U}(N_f)_L \times \mathrm{U}(N_f)_R$ transformations is known as *chiral symmetry*. Once again, while no quark flavor is massless in Nature, the up and down quarks are not only almost mass degenerate, but also very light compared to Λ, therefore it makes physical sense to investigate chiral symmetry. To this end, it is instructive to separate the abelian and non-abelian subgroups of the unitary transformations via the isomorphism

$$\mathrm{U}(N_f)_L \times \mathrm{U}(N_f)_R \sim \mathrm{U}(1)_L \times \mathrm{U}(1)_R \times \mathrm{SU}(N_f)_L \times \mathrm{SU}(N_f)_R, \tag{1.5.8}$$

where the elements of each subgroup can be parameterized as

$$\mathrm{U}(1)_L: \quad \exp\{i\epsilon_L^0\} \tag{1.5.9}$$

$$\mathrm{U}(1)_R: \quad \exp\{i\epsilon_R^0\} \tag{1.5.10}$$

$$\mathrm{SU}(N_f)_L: \quad \exp\{i\epsilon_L^a T^a\} \tag{1.5.11}$$

$$\mathrm{SU}(N_f)_R: \quad \exp\{i\epsilon_R^a T^a\}, \tag{1.5.12}$$

and the $N_f^2 - 1$ traceless hermitean generators of $\mathrm{SU}(N_f)$ are denoted by $T^a \in \mathfrak{su}(N_f)$. An equivalent basis to express any element of the chiral group is given by the following *vector* and *axial* transformations:

$$\mathrm{U}(1)_V: \quad \psi \to \exp\{i\epsilon_V^0\}\psi, \qquad \bar{\psi} \to \bar{\psi}\exp\{-i\epsilon_V^0\} \tag{1.5.13}$$

$$\mathrm{U}(1)_A: \quad \psi \to \exp\{i\epsilon_A^0\gamma_5\}\psi, \qquad \bar{\psi} \to \bar{\psi}\exp\{i\epsilon_A^0\gamma_5\} \tag{1.5.14}$$

$$\mathrm{SU}(N_f)_V: \quad \psi \to \exp\{i\epsilon_V^a T^a\}\psi, \qquad \bar{\psi} \to \bar{\psi}\exp\{-i\epsilon_V^a T^a\} \tag{1.5.15}$$

$$\text{Axial non-singlet:} \quad \psi \to \exp\{i\epsilon_A^a T^a\gamma_5\}\psi, \qquad \bar{\psi} \to \bar{\psi}\exp\{i\epsilon_A^a T^a\gamma_5\} \tag{1.5.16}$$

provided that the parameters of equations (1.5.13 - 1.5.16) are related to those of equations (1.5.9 - 1.5.12) through

$$\epsilon_V^0 = \left(\epsilon_R^0 + \epsilon_L^0\right)/2, \qquad \epsilon_A^0 = \left(\epsilon_R^0 - \epsilon_L^0\right)/2 \tag{1.5.17}$$

$$\epsilon_V^a = \left(\epsilon_R^a + \epsilon_L^a\right)/2, \qquad \epsilon_A^a = \left(\epsilon_R^a - \epsilon_L^a\right)/2. \tag{1.5.18}$$

A few remarks are in order at this point. As we will see in the next sections, invariance of the theory under the vector singlet transformations (1.5.13) is associated to the conservation of baryon number in QCD. The axial singlet transformations (1.5.14) are an example of an *anomalously* broken symmetry. Non-singlet vector transformations (1.5.15) correspond to the unit-determinant part of the flavor transformations (1.3.20) described in the previous section. Finally, the different notation adopted for the the non-singlet axial transformations of equation (1.5.16) is due to the fact that they do not close under composition, but rather the composition of two different elements results in a non-singlet vector transformation; therefore they do not form a group, and one should only refer to the generators of these transformations. As we will see in section 1.5.2, the symmetry under non-singlet axial transformations is spontaneously broken in QCD, even in the chiral limit, a fact that has deep implications for the properties of the hadron spectrum.

Though chiral symmetry arises naturally when considering the massless limit of the theory, it reveals general features of QCD. The profound consequences of chiral symmetry are encapsuled in the set of Ward-Takahashi identities that involve the above defined transformations, which will be reviewed in the following sections.

1.5.1 Ward-Takahashi identities

Ward-Takahashi identities (WTI) are non-perturbative identities relating correlation functions in Quantum Field Theory that reflect the symmetry properties of a theory under arbitrary (infinitesimal) transformations of the fields. In the most general form, a WTI can be written as

$$\langle \delta O \rangle = \langle \delta S O \rangle + \langle \ln\{\mathrm{J}\} O \rangle, \tag{1.5.19}$$

where O is an arbitrary local operator (or product of operators), and the symbol δ denotes the variation of an object (the operator or the action) under the transformation that one wants to study. J is the jacobian factor of the transformation arising from the path-integral measure, which can thus only be present in the quantized theory. If this term is non-zero, the transformation is said to be *anomalous*. A symmetry of the classical theory, defined by $\delta S = 0$, can therefore cease to be a symmetry after quantization due to the presence of anomalies. In the following, the WTI's associated to chiral transformations of equations (1.5.13) through (1.5.16) will be analysed.

Singlet vector transformations

It is straightforward to see that the $\mathrm{U}(1)_V$ subgroup of chiral transformations is non-anomalous and leaves the QCD action invariant for arbitrary values of the quark masses. In a classical field theory, this would imply the exhistence of a conserved current (and a corresponding constant of motion) via Noether's theorem. The WTI derived from these transformations translates this statement in the quantum theory: we start the derivation by noticing that since chiral transformations involve the fermion fields only, we can focus solely on the non-interacting fermionic part of the action, namely

$$S = \int \mathrm{d}^4 z \; \bar{\psi}(z) \left\{ \gamma_\mu \partial_\mu^z + M \right\} \psi(z). \tag{1.5.20}$$

To derive WTIs, it is useful to first consider a *local* infinitesimal vector singlet transformationm, implying a variation of the fields (at first order) given by

$$\psi(z) \to \psi(z) + i\epsilon_V^0(z)\psi(z), \quad \bar{\psi}(z) \to \bar{\psi}(z) - i\bar{\psi}(z)\epsilon_V^0(z). \tag{1.5.21}$$

The corresponding variation of the action (1.5.20) is

$$\delta_{\epsilon_V^0(z)} S = i \int \mathrm{d}^4 z \; \partial_\mu^z \left[\epsilon_V^0(z) \right] \bar{\psi}(z) \gamma_\mu \psi(z) \overset{\text{IBP}}{=} -i \int \mathrm{d}^4 z \; \epsilon_V^0(z) \partial_\mu^z \left[\bar{\psi}(z) \gamma_\mu \psi(z) \right], \tag{1.5.22}$$

where for the last equality we made use of integration by parts. If we now consider vector singlet transformations localized at a single spacetime point $\epsilon_V^0(z) = \epsilon_V^0 \delta(x - z)$, the variation of the action can be cast as a total derivative

$$\delta_{\epsilon_V^0(z)} S = -i\epsilon_V^0 \partial_\mu^x V_\mu^0(x), \tag{1.5.23}$$

with the introduction of the flavor singlet vector current

$$V_\mu^0(x) \equiv \bar{\psi}(x) \gamma_\mu \psi(x). \tag{1.5.24}$$

The WTI related to vector singlet transformations in presence of a local field $O(y)$ therefore reads

$$-i\epsilon_V^0 \partial_\mu^x \left\langle V_\mu^0(x) O(y) \right\rangle = \left\langle \delta_{\epsilon_V^0(z)} O(y) \right\rangle, \tag{1.5.25}$$

where the right-hand side of the above equation involves the variation of the field $O(y)$ under the transformation defined by $\epsilon_V^0(z)$. Choosing the operator $O(y)$ with support at a point y different from the point x where the transformation is localized implies that its variation will be 0 and the left hand side of (1.5.25) vanishes. In this case, we can thus identify the conserved charge associated to this symmetry with

$$\bar{V}_0^0(x_0) \equiv \int \mathrm{d}^3x \; V_0^0(x) = \int \mathrm{d}^3x \; \psi^\dagger(x)\psi(x), \tag{1.5.26}$$

and equation (1.5.25) takes the form of a conservation law (for $x_0 \neq y_0$):

$$\partial_0^x \left\langle \bar{V}_0^0(x_0) O(y) \right\rangle = 0. \tag{1.5.27}$$

From the expression in equation (1.5.26), it is clear that the conserved charge is the number of quarks minus the number of antiquarks. For instance, mesons have $\bar{V}_0^0 = 0$ while baryons have $\bar{V}_0^0 = 3$; for this reason, it is customary to define *baryon number* as

$$B(x_0) \equiv \frac{1}{3} \bar{V}_0^0(x_0). \tag{1.5.28}$$

It is exactly conserved in QCD even with massive, non degenerate quarks, reflecting that $\mathrm{U}(1)_V$ is an exact, non-anomalous symmetry of the theory.

Non-singlet vector transformations

Next, let us consider $\mathrm{SU}(N_f)_V$ transformations. Proceeding in an anologous way by first considering a generic z-dependent vector non-singlet transformation with parameter $\epsilon_V^a(z)$ and then localizing it at a point x with $\epsilon_V^a(z) = \epsilon_V^a \delta(x - z)$, the WTI for these non-anomalous transformations reads

$$-i\epsilon_V^a \partial_\mu^x \left\langle V_\mu^a(x) O(y) \right\rangle = -i\epsilon_V^a \left\langle \bar{\psi}(x) \left[M, T^a\right] \psi(x) O(y) \right\rangle \; + \; \langle \delta_{\epsilon_V^a(z)} O(y) \rangle, \tag{1.5.29}$$

where the non-singlet vector current is defined as

$$V_\mu^a(x) \equiv \bar{\psi}(x) \gamma_\mu T^a \psi(x). \tag{1.5.30}$$

The first term of the right hand side of equation (1.5.29) stems from the variation of the action under infinitesimal transformations, and it involves the commutator of the mass matrix with the generators of $\mathrm{SU}(N_f)_V$; we thus see that, unlike $\mathrm{U}(1)_V$, the symmetry is broken at the classical level for generic values of the quark masses. It is preserved, however, in the case of degenerate mass quarks.

Non-singlet axial transformations

The last non-anomalous set of transformations is spanned by the axial non-singlet generators of equation (1.5.16). Repeating analogous steps, the corresponding WTI is

$$-i\epsilon_A^a \partial_\mu^x \left\langle A_\mu^a(x) O(y) \right\rangle = -i\epsilon_A^a \left\langle \bar{\psi}(x)\gamma_5 \{M, T^a\} \psi(x) O(y) \right\rangle + \langle \delta_{\epsilon_A^a(z)} O(y) \rangle, \quad (1.5.31)$$

with the non-singlet axial current, or *Partially Conserved Axial Current* (PCAC) given by

$$A_\mu^a(x) \equiv \bar{\psi}(x)\gamma_\mu\gamma_5 T^b \psi(x), \quad (1.5.32)$$

and where now the variation of the action is proportional to the anticommutator of the mass matrix and the flavor generators. This means that transformations in equation (1.5.16) are a symmetry of the classical theory only in the chiral limit, where $M = 0$. It is particularly useful to investigate this WTI with the insertion of a flavor non-singlet pseudoscalar density

$$O(y) = P^a(y) \equiv \bar{\psi}(y)\gamma_5 T^a \psi(y), \quad (1.5.33)$$

which, in the case of mass degenerate quarks, leads to

$$\partial_\mu^x \left\langle A_\mu^a(x) P^b(y) \right\rangle = 2m \left\langle P^a(x) P^b(y) \right\rangle - \frac{\delta^{ab}}{N_f} \delta(x-y) \left\langle S^0(y) \right\rangle, \quad (1.5.34)$$

where the flavor-singlet scalar density was introduced

$$S^0(y) \equiv \bar{\psi}(y)\psi(y). \quad (1.5.35)$$

The identity (1.5.34) holds also upon renormalization with the corresponding renormalized quantities, and it furnishes a non-perturbative definition of the renormalized quark mass:

$$\bar{m}_{\text{PCAC}} = \frac{\partial_\mu^x \left\langle A_\mu^a(x) P^b(y) \right\rangle}{2 \left\langle P^a(x) P^b(y) \right\rangle}, \quad x \neq y. \quad (1.5.36)$$

The above definition is particularly useful in lattice studies since it involves correlation functions straightforwardly computed in lattice simulations.

1.5.2 Spontaneous symmetry breaking and pions

Further investigating the WTI (1.5.34) in the physically justified limit of $N_f = 2$ mass-degenerate - or even massless - quarks (up, down) reveals the most salient features of the lightest mesons. Indeed, in the chiral limit $m = 0$, the PCAC relates

the presence of a conserved quantity to the expectation value of the singlet scalar density, or the chiral condensate. In particular, the non-singlet axial charge(s)

$$\bar{A}_0^0(x_0) = \int \mathrm{d}^3x \; A_0^a(x) \tag{1.5.37}$$

is conserved if the chiral condensate vanishes $\langle S^0 \rangle = 0$. Even in the theory with massless fermions, one observes that the chiral condensate assumes a non-zero value. Because the chiral condensate is not invariant under axial non-singlet transformation, a non-zero expectation value implies that also the vacuum of the theory is not symmetric under suhc transformations. This situation (the presence of a symmetry of the action which is not a symmetry of the vacuum) is referred to as *spontaneous symmetry breaking*, and the famous Goldstone theorem [30] predicts the presence of a massless spin 0 particle – a Nambu-Goldstone boson (NGB) – for each spontaneously broken generator of the symmetry. The relevant case for QCD is given by considering the up and down quark as massless $N_f = 2$; therefore we expect $N_f^2 - 1 = 3$ massless particles with the same quantum numbers of the non-conserved axial non-singlet charges in equation (1.5.37), i.e. pseudoscalars. Such states can be identified with the pions π^0, $\pi^\pm$, which carry the correct quantum numbers, but even though they are the lightest states in QCD, they are not massless. Generally speaking, this is due to the fact that chiral symmetry is broken not only spontaneously but also explicitly by the quark masses in equation (1.5.34), making pions pseudo-NGBs. This mechanism can be understood quantitatively through the Gell-Mann–Oakes–Renner (GMOR) relation [31], which describes how the pions approach the chiral limit, and that can be derived from the PCAC (1.5.34). We start from the correlator of the non-singlet axial current and pseudoscalar densitiy entering the PCAC. Setting $y = 0$, Lorentz invariance implies

$$\left\langle A_\mu(x) P^b(0) \right\rangle = C^{ab} \frac{x_\mu}{(x^2)^2}, \qquad x \neq 0 \tag{1.5.38}$$

for some constants C^{ab}. They can be computed from the integrated the PCAC in the chiral limit

$$\int \mathrm{d}^4x \; \partial_\mu \left\langle {}^x A_\mu^a(x) P^b(0) \right\rangle = -\frac{\delta^{ab}}{2N_f} \left\langle S^0 \right\rangle, \tag{1.5.39}$$

where we can suppress the dependence on the spacetime coordinate of the chiral condensate due to tralsational invariance of the theory. The integral over spacetime of the total derivative can be converted to an integral over the surface of an hypersphere odf radius R:

$$\int \mathrm{d}^4x \; \left\langle \partial_\mu^x A_\mu^a(x) P^b(0) \right\rangle \overset{(1.5.38)}{=} C^{ab} \int\limits_{|x|=R} \mathrm{d}n_\mu(x) \frac{x_\mu}{(x^2)^2} = C^{ab} 2\pi^2 \tag{1.5.40}$$

where $n_\mu(x)$ represents the normal vector to the hypersphere's surface, and in the last equality we have recognized the volume of the 4-dimensional sphere. Comparing with equation (1.5.39) allows to relate C^{ab} to $\langle S^0 \rangle$, taking us to the final expression for the correlator (1.5.38)

$$\left\langle A_\mu(x) P^b(0) \right\rangle = -\delta^{ab} \frac{1}{2\pi^2} \frac{\langle S^0 \rangle}{2N_f} \frac{x_\mu}{(x^2)^2}, \qquad x \neq 0 \tag{1.5.41}$$

and furhter integrating over spatial directions leads to the appearance of axial charge

$$\left\langle \bar{A}_0^a(x_0) P^b(0) \right\rangle = -\frac{\delta^{ab}}{2N_f} \left\langle S^0 \right\rangle, \quad x \neq 0; \tag{1.5.42}$$

crucially, the r.h.s. of this equation is independent of the coordinate x_0 explicitly appearing on the left. The lightest states from which the expectation value on the left receives contributions are the pions π^a, since they carry the same quantum numbers of P^b. At this point, it is useful to define the relevant matrix elements between the vacuum and pion states

$$\langle 0 | A_\mu^a(x) \left| \pi^b(p) \right\rangle = i\delta^{ab} F_\pi p_\mu \exp\{-E_\pi(\boldsymbol{p}) x_0 + i\boldsymbol{p}\boldsymbol{x}\} \tag{1.5.43}$$

$$\left\langle \pi^b(p) \right| P^a(x) | 0 \rangle = -i\delta^{ab} G_\pi \exp\{-E_\pi(\boldsymbol{p}) x_0 - i\boldsymbol{p}\boldsymbol{x}\}, \tag{1.5.44}$$

where the energy satisfies the Euclidean dispersion relation $E_\pi(\boldsymbol{p}) = \sqrt{M_\pi^2 + \boldsymbol{p}^2}$ and M_π is the pion mass. After a few lines of algebra the leading contribution to the correlator in equation (1.5.42) arising from pion states can be expressed as

$$\left\langle \bar{A}_0^a(x_0) P^b(0) \right\rangle = \delta^{ab} \frac{G_\pi F_\pi}{2} \exp\{-M_\pi x_0\} + \ldots, \tag{1.5.45}$$

where the dots indicate subleading contribution from other states. We thus see that for the r.h.s. of the above equation to be independent of x_0 it is necessary that pions are massless in the chiral limit: this is nothing else than the statement of the Goldstone theorem. Moreover, one finds that in the chiral limit

$$G_\pi F_\pi = -\frac{S^0}{N_f}, \quad m = 0. \tag{1.5.46}$$

Away from the chiral limit, the pion mass ceases to be zero, and following similar considerations the contribution from pion states to (1.5.34) leads to

$$\left(M_\pi^{(m)} \right)^2 F_\pi^{(m)} = 2m G_\pi^{(m)} \tag{1.5.47}$$

where the superscripts stress that the quantities are evaluated at nonzero quark mass, and it holds $F_\pi = \lim_{m \to 0} F_\pi^{(m)}$ and similarly for M_π and G_π. Combining

the above equation with equation (1.5.46) finally leads to the GMOR relation, expressed in terms of a renormalized quark mass $\bar{m}$:

$$\lim_{\bar{m}\to 0} \frac{\left(M_\pi^{(m)}\right)^2 \left(F_\pi^{(m)}\right)^2}{2\bar{m}} = -\frac{\langle S^0\rangle}{N_f}\bigg|_{\bar{m}=0}, \tag{1.5.48}$$

The above expression can be recast as an expansion in $\bar{m}$ for the pion mass, which to leading order reads

$$\left(M_\pi^{(m)}\right)^2 = -\bar{m}\frac{2}{F_\pi^2}\frac{\langle S^0\rangle}{N_f} + \mathcal{O}\left(\bar{m}^2\right), \tag{1.5.49}$$

and where the coefficient of $\bar{m}$ is defined in the chiral limit. This relation then explains why pions are much lighter than the other hadrons: their pseudo-NGB nature, related to the spontaneous breaking of the approximate chiral symmtery, implies that their mass scales as the square root of the QCD scale

$$M_\pi \propto \sqrt{\Lambda\bar{m}}, \tag{1.5.50}$$

at variance with hadron masses not related to chiral symmetry breaking (1.3.23). The validity of the GMOR relation was proved from first principles lattice calculations [32], see figure 1.3. There, all the terms entering equation (1.5.49) - M_π, F_π and $\langle S\rangle$ - have been computed non-perturbatively in QCD with $N_f = 2$. In particular, the chiral condensate has been computed from the density of zero-modes of the Dirac operator in the chiral limit via the Banks-Casher relation [33]

$$\rho(0) = -\frac{1}{\pi}\frac{\langle S^0\rangle}{N_f}\bigg|_{\bar{m}=0}, \tag{1.5.51}$$

where the spectral density $\rho(\lambda)$ counts the average number of eigenvalues of the Dirac operator λ_i in a neighborhood of λ; it can be defined starting from a theory in a finite volume

$$\rho_V(\lambda) = \frac{1}{V}\sum_i \langle\delta(\lambda-\lambda_i)\rangle, \tag{1.5.52}$$

and taking the infinite volume and chiral limit:

$$\rho(0) = \lim_{\lambda\to 0}\lim_{\bar{m}\to 0}\lim_{V\to\infty}\rho_V(\lambda). \tag{1.5.53}$$

Overall, it is by now well established that QCD with light quark flavors exhibits spontaneous chiral symmetry breaking, which is related to the condensation of zero modes of the Dirac operator and in turn to a non-zero chiral condensate. Since chiral symmetry is softly broken by the quark masses, the would-be Nambu-Goldstone bosons acquire a mass parametrically smaller than that of other hadrons

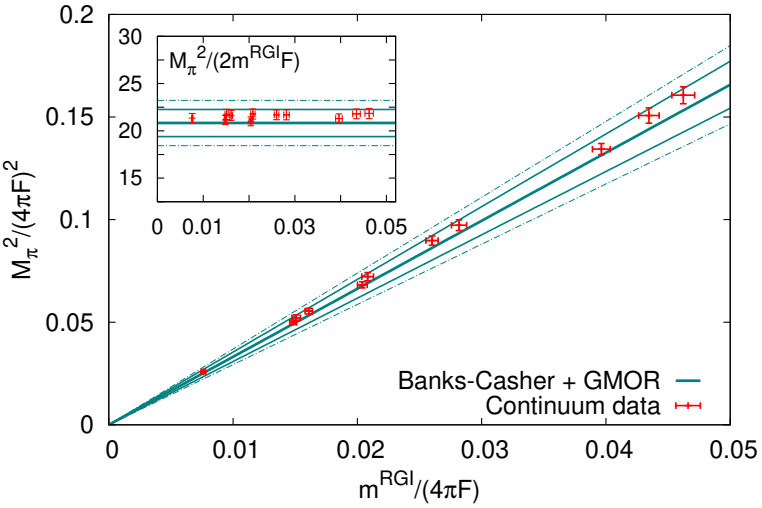

FIGURE 1.3: From [32]: Pion mass squared as a function of the RGI quark mass, as predicted by the GMOR (cyan lines) and as obtained from lattice calculations (red crosses).

in the theory, which is again tied to the value of the chiral condenstate. The properties of the pions observed in Nature accurately match the predictions based on this picture. We remark that the same derivation can be applied considering chiral symmetry including the strange quark, i.e. for $N_f = 3$: while as argued before the explicit breaking of chiral symmetry is worse in this case, one still finds that the strange flavored mesons (kaons and the η meson) are sensibly lighter than other hadrons. In the next section, we will exhamine more closely the mechanism that explains the much larger mass of the singlet η' meson.

1.5.3 Axial anomaly

To conclude this chapter, let us examine the WTI related to the $\mathrm{U}(1)_A$ transformations in equation (1.5.14). Differently from the other chiral transformations, these are anomalous, as they are a symmetry of the classical action in the chiral limit, but they do not leave the path integral measure invariant:

$$D\bar{\psi}D\psi \underset{\mathrm{U}(1)_A}{\longrightarrow} D\bar{\psi}D\psi \exp\{-2i\epsilon_A Q\}. \tag{1.5.54}$$

The anomaly involves a central object in QCD, the *topological charge* Q. As the name suggests, it is related to the topology of gauge fields, and it assumes integer values. It can be defined as the integral of the topological charge density $q(x)$ via

$$Q = \int \mathrm{d}^4x\; q(x), \quad q(x) = \frac{1}{32\pi^2}\varepsilon_{\mu\nu\rho\sigma}\,\mathrm{Tr}\{F_{\mu\nu}(x)F_{\rho\sigma}(x)\}. \tag{1.5.55}$$

The anomalous WTI then assumes the form

$$-i\epsilon_A\partial_\mu\left\langle A^0_\mu(x)O(y)\right\rangle = -2i\epsilon_A N_f\left\langle q(x)O(y)\right\rangle - 2i\epsilon_A\left\langle\bar\psi(x)\gamma_5 M\psi(x)O(y)\right\rangle + \left\langle\delta O(y)\right\rangle, \tag{1.5.56}$$

with the singlet axial current defined by

$$A^0_\mu(x) \equiv \psi(x)\gamma_\mu\gamma_5\psi(x). \tag{1.5.57}$$

In section 1.4.2 it was noted that the η' flavor-singlet pseudoscalar meson has a much higher mass than the rest of meson octet. The mechanism that gives rise to its mass is related to the $\mathrm{U}(1)_A$ anomaly, and it can be understood starting from the WTI (1.5.56) in the chiral limit inserting a topological charge density operator $O(y) = q(y)$ at $y = 0$,

$$\partial_\mu\left\langle A^0_\mu(x)q(0)\right\rangle = 2N_f\left\langle q(x)q(0)\right\rangle, \tag{1.5.58}$$

and considering the *topological susceptibility*

$$\chi \equiv \int \mathrm{d}^4x\ \left\langle q(x)q(0)\right\rangle. \tag{1.5.59}$$

This quantity measures the fluctuations between different integer values of the topological charge, which are induced by non-perturbative objects called instantons. The Witten-Veneziano formula [34, 35] relates the value of the η' mass in the chiral limit to the value of the topological susceptibility in the theory without fermions and in the $N_c \to \infty$ limit, denoted by χ^{YM}:

$$\lim_{N_f/N_c\to 0}\ \lim_{m\to 0}\ \frac{F^2_{\eta'}m^2_{\eta'}}{2N_f} = \chi^{\mathrm{YM}}_\infty, \tag{1.5.60}$$

with the η' mass and decay constant defined through the matrix elements

$$\left\langle 0\right|q(0)\left|\eta'\right\rangle = \frac{F_{\eta'}m^2_{\eta'}}{\sqrt{2N_f}}, \quad \left\langle 0\right|\bar A^0_0(x_0)\left|\eta'\right\rangle = i\sqrt{2N_f}F_{\eta'}m_{\eta'}e^{-m_{\eta'}x_0}. \tag{1.5.61}$$

The relation (1.5.60) states that the η' meson acquires its mass, even in the chiral limit, from a non-vanishing topological susceptibility in the pure pure gauge theory. The latter quantity was computed non-perturbatively from lattice simulations of $\mathrm{SU}(N)$ Yang-Mills theory for various values of N and extrapolated to the $N \to \infty$ limit [36–39]; a recent and precise determination expressed in units of the theory's string tension, reads [40]

$$\chi^{\mathrm{YM}}_\infty/\sigma^2 = 0.02088(39), \tag{1.5.62}$$

accurately reproduces the Witten-Veneziano mechanism involving the mass of the η' meson when inserted in equation (1.5.60).

To conclude this chapter, I remark that many of QCD's most crucial features – asymptotic freedom, the formation of hadrons from partons, chiral symmetry, its spontaneous breaking and its impact on the light meson spectrum – all require a non-perturbative treatment, both for their formal definition and for practical computations of observable quantities. In the next chapter, I will introduce and describe the lattice regularization of QCD, which allows to define and solve the theory non-perturbatively, and which provides the methodological framework for most of the work that will be presented in this thesis.

Chapter 2

Lattice QCD

In this chapter we provide a general overview of lattice QCD, from its formal definition to practical methods to obtain its predictions. Several complete introductions to the subject can be found in the literature, see e.g. [41, 42]. As mentioned in section 1.3, the central purpose of regulating a quantum field theory on a discrete regular lattice of points with spacing a

$$x_\mu = a \cdot n_\mu, \;\; n_\mu \in \mathbb{Z}^4 \tag{2.0.1}$$

is to provide a non-perturbative definition of the theory by rigorously defining the path integral. The lattice explicitly breaks SO(4) Lorentz invariance to a discrete group of 4-dimensional rotations (the *octahedral group*), but in the following it will be shown how it is possible to preserve exact gauge invariance at the level of the discretized action. Moreover, a minimal spacetime distance corresponds to an ultraviolet cutoff in momentum integrals, which as anticipated regulates the theory. Unless otherwise specified, the case of an infinite collection of equally spaced points, i.e. an infinite volume lattice, will be considered. In practical numerical computations – and also for some formal arguments – the lattice volume must be made finite. Some more technical details on the lattice construction are collected in appendix C to keep the main text contained.

2.1 Yang-Mills theory

Let us start by considering the Yang-Mills sector of the QCD lagrangian (1.1.1) with generic N_c. In lattice gauge theory the dynamics of the gauge vector bosons is not directily described by the fields in the Lie algebra $A_\mu(x) \in \mathfrak{su}(N_c)$ as in the continuum, but rather through *link* variables, which can be thought of as parallel transporters between neighboring lattice sites. To make explicit from the start the relation between the continuum and lattice fields, we introduce the parallel gauge

transporter between positions x and y in the continuum as

$$G(x,y) \equiv \mathcal{P}\exp\left\{ i \int_x^y \mathrm{d}z_\mu \; A_\mu(z) \right\} \tag{2.1.1}$$

where $\mathcal{P}$ denotes the path-ordered exponential integral along a path connecting points x and y. $G(x,y)$ is an element of $\mathrm{SU}(N_\mathrm{c})$, and crucially it transforms under a local gauge transformation $\Omega(x)$ as

$$G(x,y) \xrightarrow{\Omega(x)} \Omega(x) G(x,y) \Omega^\dagger(y). \tag{2.1.2}$$

In the lattice construction, we define the basic link variables $U_\mu(x) \in \mathrm{SU}(N_\mathrm{c})$ as the parallel transporters between the lattice site x and $x + a\hat{\mu}$, and following the result of equation (2.1.2), we impose that they transform under an element of the gauge group $\Omega(x)$ as

$$U_\mu(x) \xrightarrow{\Omega(x)} U'_\mu(x) = \Omega(x) U_\mu(x) \Omega^\dagger(x + a\hat{\mu}). \tag{2.1.3}$$

Requiring that the link U_μ reproduces the continuum parallel transporter for small lattice spacing, i.e. that

$$U_\mu(x) = G(x, x + a\hat{\mu}) + \mathcal{O}(a), \tag{2.1.4}$$

allows us to relate the link field with the gauge field $A_\mu(x)$ evaluated at lattice site x:

$$U_\mu(x) = \exp\{ i a A_\mu(x) \} + \mathcal{O}(a). \tag{2.1.5}$$

The last equation is obtained with the approximation – valid at $\mathcal{O}(a)$ – of the line integral from x to $x + a\hat{\mu}$ in the left-hand-side of equation (2.1.4) with the length of the integration interval times the value of the field at the starting point, i.e. $aA_\mu(x)$. It is now easy to see that any product of link variables along a closed oriented lattice path transforms locally; the simplest closed path that can be built starting from point x in the $\mu - \nu$ plane is called a *plaquette* (see figure 2.1). It is defined by

$$U_{\mu\nu}(x) \equiv U_\mu(x) U_\nu(x + a\hat{\mu}) U_\mu^\dagger(x + a\hat{\nu}) U_\nu^\dagger(x) \tag{2.1.6}$$

and transforms according to

$$U_{\mu\nu}(x) \xrightarrow[\Omega]{} U'_{\mu\nu}(x) = \Omega(x) U_{\mu\nu}(x) \Omega^\dagger(x). \tag{2.1.7}$$

From the above equation it is clear that the trace of a plaquette is a gauge invariant object. At this stage it is useful to define the *naïve* or *classical* continuum limit, which consists in sending the lattice spacing to zero while keeping the bare

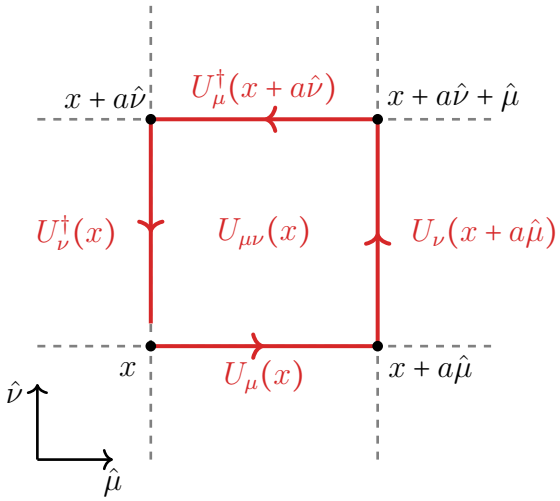

FIGURE 2.1: Two-dimensional section of a lattice, with link variables (red arrows) forming a plaquette. The gap indicates that, before taking the trace over color indices, the plaquette is not gauge invariant.

parameters in the action fixed. As we have argued in section 1.3, removing the regulator without renormalization takes us back to the divergent theory, but making sure that the action and operators reduce to their formal continuum expression when the lattice spacing is sent to zero is a necessary condition to ensure that the correct continuum theory is reproduced. With these considerations in mind, and considering equation (2.1.5), one can show that close to the classical continuum limit $a \to 0$ the plaquette behaves as

$$U_{\mu\nu}(x) = \exp\left\{ia^2 F_{\mu\nu}(x) + \mathcal{O}\left(a^3\right)\right\}, \tag{2.1.8}$$

and with these elements it is now straightforward to build an exactly gauge invariant action that reduces to the continuum Yang-Mills action in the limit $a \to 0$. This is the famous Wilson plaquette action [43], and it reads

$$S_G[U] = \frac{\beta}{2N_c} \sum_x \sum_{\mu,\nu} \mathrm{Re}\,\mathrm{Tr}\left[\mathbb{1} - U_{\mu\nu}(x)\right]. \tag{2.1.9}$$

The sums run over all lattice points and all plaquettes, and it is customary to introduce the inverse bare coupling as $\beta = 2N_c/g_0^2$. Expanding (2.1.9) for $a \to 0$ reveals that the deviations from the continuum action due to the finite lattice spacing (discretization effects) are of order a^2:

$$\begin{aligned} S_G[U] &= \frac{1}{2g_0^2} a^4 \sum_x \mathrm{Tr}\{F_{\mu\nu}(x) F_{\mu\nu}(x)\} + \mathcal{O}\left(a^2\right), \\ \lim_{a\to 0} S_G[U] &= \frac{1}{2g_0^2} \int \mathrm{d}^4x \;\; \mathrm{Tr}\{F_{\mu\nu}(x) F_{\mu\nu}(x)\}. \end{aligned} \tag{2.1.10}$$

2.1.1 Pure gauge path integral

Having defined a gauge invariant discretized action, it is now possible to rigorously define a path integral for the quantum field theory. As it was noted in section 1.2, the integration over field configurations introduced in equation (1.2.1) is at this stage formal, as no notion of integration over a continuum of variables has been defined. To overcome these shortcomings, we begin by now considering a finite volume lattice with N points in each direction, and a finite physical extent in each direction given by $L = aN$,

$$\mathrm{L} = \left\{ x_\mu \in \mathbb{R}^4 \;\middle|\; x_\mu = a \cdot n_\mu, \quad n_\mu = 0, \ldots, N-1 \;\; \forall \mu \right\}. \tag{2.1.11}$$

This lattice, with total physical volume $V = L^4$, will then contain a finite number of link variables $U_\mu(x)$, and thus a path integral over the value of these fields at all space-time points will be a very large but finite-dimensional integral:

$$\mathcal{Z}(a, V) = \int DU \;\; \exp\{-S_G[U]\}, \tag{2.1.12}$$

where the integration over all link fields is denoted by

$$DU \equiv \prod_{x \in \mathrm{L}} \prod_{\mu=0}^{3} \mathrm{d}U_\mu(x). \tag{2.1.13}$$

At this point, the only thing missing to have a consistent definition of (2.1.12) is the notion of integration over an element of $\mathrm{SU}(N_c)$. This is provided by the *Haar measure*, which allows integration over a compact continuous group, and whose properties are summarized in appendix C.1. With these notions, the path integral (2.1.12) for the finite-volume discretized theory is unambiguously and rigorously defined. In the same way we can define expectation values of gauge-invariant operators and correlation functions by

$$\langle O \rangle (a, V) = \frac{1}{\mathcal{Z}(a, V)} \int DU \;\; O[U] \exp\{-S_G[U]\}. \tag{2.1.14}$$

We have now defined in a rigorous way a path integral for Yang-Mills theory which preserves gauge-invariance exactly. Another convenient feature comes from the fact that since we are now integrating over elements of the compact group $\mathrm{SU}(N_c)$, and not over elements of the unbounded Lie algebra $\mathfrak{su}(N_c)$, the volume of the integration measure is finite. To conclude this section, we remark that from a formal point of view the path integral representation of continuum expectation values such as (1.2.2) is *defined* as the infinite volume and vanishing spacing limit of the regularized path integral in (2.1.12)

$$\langle O \rangle_{\text{continuum}} = \lim_{a \to 0} \left\{ \lim_{V \to \infty} \langle O \rangle (a, V) \right\}. \tag{2.1.15}$$

In this sense, the lattice is not only a convenient regulator of the theory which preserves many of its symmetries, but it is most importantly a natural formalism to define quantum field theories at the fundamental level.

2.2 Fermions on the lattice

The discretization of the fermionic action is at face value more straightforward than that of Yang-Mills theory, as it directly involves the discrete version of the continuum quark fields, but it actually requires a careful treatment even in the non-interacting case, and it is thus instructive to start from the continuum Dirac action for a massless free quark

$$\mathcal{S}_D = \int d^4x \ \bar{\psi}(x)\gamma_\mu\partial_\mu\psi(x). \tag{2.2.1}$$

The simplest way to discretize the first derivative is given by the forward and backward nearest-neighbors finite differences

$$\partial_\mu\psi(x) \equiv \frac{\psi(x+a\hat{\mu}) - \psi(x)}{a} \tag{2.2.2}$$

$$\partial^*_\mu\psi(x) \equiv \frac{\psi(x) - \psi(x-a\hat{\mu})}{a}, \tag{2.2.3}$$

which can be combined to give a Hermitean discretization. The naïve discretized Dirac action is then given by[1]

$$S_F^{\text{naïve}} = a^4 \sum_x \sum_\mu \bar{\psi}(x)\gamma_\mu \frac{1}{2}\left(\partial_\mu + \partial^*_\mu\right)\psi(x) \tag{2.2.4}$$

$$= a^4 \sum_x \sum_\mu \bar{\psi}(x)\left(\gamma_\mu \frac{\psi(x+a\hat{\mu}) - \psi(x-a\hat{\mu})}{2a}\right) \tag{2.2.5}$$

$$= a^4 \sum_{x,y} \bar{\psi}(x) D_{\text{naïve}}(x,y)\psi(y), \tag{2.2.6}$$

with the naïve discrete Dirac operator defined as

$$D_{\text{naïve}}(x,y) \equiv \frac{1}{2a}\sum_\mu \gamma_\mu \left(\delta_{x+a\hat{\mu},y} - \delta_{x-a\hat{\mu},y}\right). \tag{2.2.7}$$

In momentum space, afer applying a Fourier transform, the naïve Dirac operator takes the form

$$D_{\text{naïve}}(p) = \ a^{-1} \ \sum_\mu \gamma_\mu \sin(ap_\mu), \tag{2.2.8}$$

[1]For sums over Dirac indices on the lattice we adopt the shorthand notation $\sum_\mu \equiv \sum_{\mu=0}^{3}$.

and its inverse gives the free massless quark propagator on the lattice

$$D^{-1}_{\text{naïve}}(p) = a \frac{\sum_\mu -i\gamma_\mu \sin(ap_\mu)}{\sum_\mu \sin^2(ap_\mu)}, \tag{2.2.9}$$

which correctly reproduces the free quark propagator in the classical continuum limit

$$\lim_{a\to 0} D^{-1}_{\text{naïve}}(p) = -i\frac{\gamma_\mu p_\mu}{p^2}. \tag{2.2.10}$$

The lattice geometry in spacetime has also implication on the value of the momentum. Specifically, each component of the lattice momenta is continuous and periodic, with period given by $2\pi/a$. For this reason, it is sufficient to focus on the interval $(-\pi/a, \pi/a]$, which is denoted as the first Brillouin zone (IBZ).

2.2.1 Fermion doubling

The analytic structure of the propagator informs about the states in the theory: in particular, a pole in the momentum space propagators signals the presence of a particle whose mass is given by the pole position. For instance, the continuum propagator coming from equation (2.2.1) has a single pole at $p^2 = 0$, which corresponds to the single massless fermion described by the action. While the discrete propagator (2.2.9) exhibits a pole at $p^2 = 0$, each sine factor in the denominator vanishes when the corresponding momentum component assumes the value $p_\mu = \pm\pi/a$ at the edge of the IBZ. This implies that the naïvely discretized propagator has a total of 16 poles, since each of the 4 momentum components can be either 0 or π/a and make the denominator vanish. This situation is sketched in figure 2.2. The presence of 15 additional massless fermions in the spectrum of the naïve discrete Dirac operator is known as *fermion doubling*, and it represents a problem as one aims to describe a single massless fermion in the continuum. The appearance of doublers can be understood in the context of the Nielsen-Ninomiya theorem, which constrains the properties of a general discretization of the continuum Dirac operator.

2.2.2 Nielsen-Ninomiya theorem

Nielsen and Ninomiya's *no-go* theorem [44–46] is a statement about what properties can simultaneously be satisfied by a discretization[2] of the Dirac action. Before enunciating the satement of the theorem, it is useful to list a minimal set of properties that a discretized Dirac operator should satisfy in order to describe the correct

[2] As a matter of fact, the theorem is not only restricted to the lattice regularization, but it provides constraints for a general regularization of the fermion action.

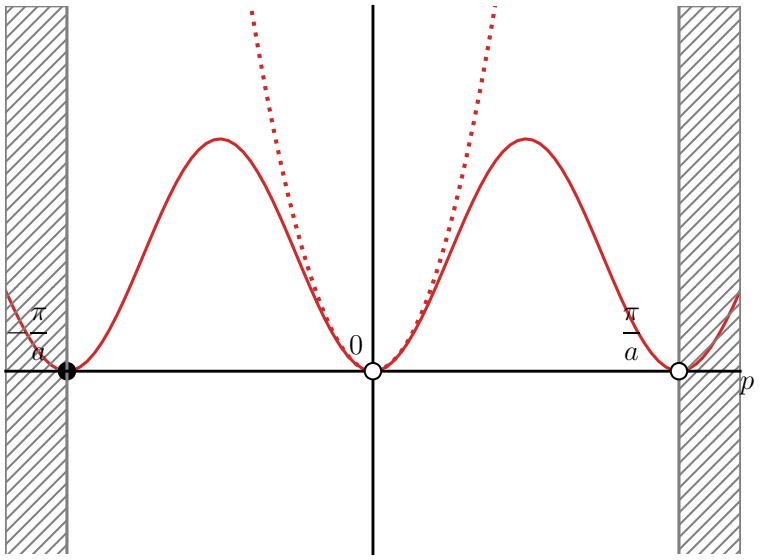

FIGURE 2.2: The denominator of the propagator as a function of momentum (for a single component) for the continuum case (red dotted curve) and for the naïve discrete Dirac operator (red curve). The white points correspond to the poles of the discrete propagator contained in the Brillouin zone; the pole at $p = -\pi/a$ is excluded.

continuuum physics. The Fourier transform of the discrete Dirac operator $D_{\text{lat}}(p)$ should satisfy the following:

1. It has the correct classical continuum limit $\lim_{a\to 0} D_{\text{lat}}(p) = D_{\text{cont}}(p)$;
2. $D_{\text{lat}}(p)$ is a continuous and periodic function of p with period $2\pi/a$;
3. $D_{\text{lat}}(p)$ is invertible for all momenta except $p = (0,0,0,0)$;

Clearly, condition 1 is necessary for any sensible discretization. Condition 2 guarantees that the discrete Dirac operator is local in position space, i.e. it is zero for spacetime points sufficiently far apart[3] , while condition 3 must be met to avoid the presence of doublers in the spectrum. As we have seen, the naïve discretization (2.2.7) satisfies conditions 1 and 2 but violates condition 3 due to the extra poles in the free propagator. The emergence of doublers in a discretizaion of the Dirac operator is elucidated by the Nielsen-Ninomiya theorem, which states that it is

[3] A less stringent constraint, known as *exponential locality*, can be accomodated. It states that the norm of the Dirac operator should decay exponentially fast with distance:

$$\|D(x,y)\| \leq c \ \exp\{-\gamma|x-y|\}$$

for some constants $c,\ \gamma$.

not possible to satisfy the three conditions listed above *and also* preserve chiral symmetry at fixed lattice spacing, i.e. satisfy the following fourth condition:

4. $D_{\text{lat}}(p)$ is *chiral*: $\{\gamma_5, D_{\text{lat}}(p)\} = 0$.

Because the naïve discretization satisfies conditions 1, 2 and 4, it has to violate condition 3 and produce doublers in the spectrum. Several formulations have been proposed over time to circumvent the presence of doublers in the continuum, each one coming with its perks and disadvantages. The discretization of fermions *à la* Wilson, which is the relevant discretization for the work described in this thesis, will be reviewed in detail in the following section.

2.2.3 Wilson fermions

Wilson's proposal for the removal of doublers involves a rather simple modification of the naïve discrete action (2.2.5) by the inclusion of a dimension 5 operator in the Lagrangian. Since the action must be dimensionless, this extra operator must be multiplied by a single power of the lattice spacing a: specifically, the Wilson fermion action involves the discretization of the second derivative,

$$S_F^{\text{wil}} = S_F^{\text{naïve}} - a^4 \sum_x a\bar{\psi}(x)\Delta\psi(x), \tag{2.2.11}$$

where the lattice Laplacian operator is defined by

$$\bar{\psi}(x)\Delta\psi(x) \equiv \frac{1}{2}\sum_\mu \bar{\psi}(x)\partial_\mu^*\partial_\mu\psi(x) \tag{2.2.12}$$

$$= \sum_\mu \frac{1}{2a^2}\bar{\psi}(x)\left(\delta_{x+a\hat{\mu},y} + \delta_{x-a\hat{\mu},y} - 2\delta_{x,y}\right)\psi(y). \tag{2.2.13}$$

This corresponds to a local operator in position space given by

$$D_W(x,y) = \frac{4}{a}\delta_{x,y} - \frac{1}{2a}\sum_\mu (1-\gamma_\mu)\,\delta_{x+a\hat{\mu},y} + (1+\gamma_\mu)\,\delta_{x-a\hat{\mu},y}, \tag{2.2.14}$$

and it is interesting to notice that the effect of the Wilson term is to generate a term in the action proportional to the cutoff scale $1/a$ and to the identity in flavor space, thus explicitly breaking chiral symmetry even if one starts with a massless fermion. This affects the corresponding momentum space propagator as

$$D_W^{-1}(p) = a\frac{\sum_\mu -i\gamma_\mu \sin(ap_\mu) + M(ap)}{\sum_\mu \sin^2(ap_\mu) + M^2(ap)}, \tag{2.2.15}$$

which formally can be seen as the naïve discrete propagator (2.2.9) in the presence of a momentum-dependent "mass term" given by

$$M(p) = \frac{4}{a}\sum_{\mu}\sin^2(ap_\mu/2). \tag{2.2.16}$$

The net effect is that the pole at $p = (0,0,0,0)$ remains massless as expected, but the 15 doublers associated to non-zero momentum components π/a now acquire a large mass proportional to $4/a$, and crucially they become infinitely massive in the limit $a \to 0$, i.e. they completely decouple from the continuum theory. Wilson fermions bypass the Nielsen-Ninomiya theorem because the additional operator in the action explicitly breaks chiral symmetry, even if the bare quark mass is set to zero. Chiral symmetry is only recovered in the contitnuum limit, as it holds

$$\{\gamma_5, D_W\} = \mathcal{O}(a). \tag{2.2.17}$$

The promotion of the Wilson action to the case of non-zero mass is straighforward by adding a mass diagonal mass term:

$$D_W(x,y) + m = \left(\frac{4}{a} + m\right)\delta_{x,y} - \frac{1}{2a}\sum_{\mu}(1-\gamma_\mu)\,\delta_{x+a\hat{\mu},y} + (1+\gamma_\mu)\,\delta_{x-a\hat{\mu},y}, \tag{2.2.18}$$

and it is customary to define the hopping parameter κ as $\kappa \equiv (8+2am)^{-1}$. The inclusion of quark interactions with the gauge fields, just like in the continuum case, is completely specified by the requirement of gauge invariance. The discretized kinetic term (2.2.5) involves the product of fields at neighboring lattice sites, which is not invariant under local $\mathrm{SU}(N_c)$ transformations. To make it gauge invariant, the forward and backward discrete derivatives are promoted to covariant lattice derivatives by including link variables that connect the neighboring points:

$$a\partial_\mu\psi(x) \longrightarrow a\nabla_\mu\psi(x) \equiv U_\mu(x)\psi\left(x+a\hat{\mu}\right) - \psi(x), \tag{2.2.19}$$

$$a\partial^*_\mu\psi(x) \longrightarrow a\nabla^*_\mu\psi(x) \equiv \psi(x) - U^\dagger_\mu(x-a\hat{\mu})\psi\left(x-a\hat{\mu}\right). \tag{2.2.20}$$

Performing the above substitutions and including the mass term yields the interacting Wilson fermion action for N_f flavors

$$S_F\left[U,\psi,\bar{\psi}\right] = a^4\sum_x\sum_f \bar{\psi}_f\left(D_W[U] + m_f\right)\psi_f, \tag{2.2.21}$$

with the interacting Wilson operator given by

$$D_W[U] = \frac{1}{2}\left\{\gamma_\mu\left(\nabla_\mu + \nabla^*_\mu\right) - a\nabla^*_\mu\nabla_\mu\right\}. \tag{2.2.22}$$

Although Wilson fermions are arguably the simplest way to describe a single quark flavor on the lattice, the additional chiral symmetry breaking operator in the action complicates the mass renormalization of the theory. Specifically, this operator transforms in the same way as the quark mass term in the action under chiral transformations: by equation (1.3.7), it means that the quark mass mixes with the Wilson term in the renormalization process, and in particular that it is no longer enough to renormalize the mass with a multiplicative factor according to equation (1.3.3), but that also an additive renormalization is necessary. Moreover, from dimensional analysis, the additive renormalization constant must have dimension 1 in mass, and thus be proportional to $1/a$, which is a much worse divergence with the regulator than the logarithmic one typically arising in multiplicative renormalization factors.
For a single flavor, or even in the case of several flavors with degenerate masses, the renormalized mass can be written as

$$\bar{m} \;=\; Z_m\left(g_0^2, a\mu\right)\left[m_0 - m_{\mathrm{cr}}\left(g_0^2\right)\right]. \tag{2.2.23}$$

The chiral limit of Wilson fermions is obtained by imposing that a given definition of renormalized mass – for instance the PCAC mass (1.5.36) – vanishes at fixed lattice spacing (fixed g_0^2). To achieve this non-perturbatively, as equation (2.2.23) suggests, a parameter scan over the values of the bare mass m_0 is required to empirically find the critical mass $m_{\mathrm{cr}}(g_0^2)$, which is a very computationally demanding task.

2.2.4 Lattice QCD path integral

Having discretized both the gauge and fermionic actions, one arrives at an expression for the discretized QCD action:

$$S\left[U, \psi, \bar{\psi}\right] = S_G\left[U\right] + S_F\left[U, \psi, \bar{\psi}\right], \tag{2.2.24}$$

and following the steps outlined in section 2.1.1 the partition function of lattice QCD can be defined by the functional integral

$$\mathcal{Z} = \int DUD\bar{\psi}D\psi \;\; \exp\left\{-S\left[U, \psi, \bar{\psi}\right]\right\}, \tag{2.2.25}$$

where the definition of the integral over anticommunting Grassmann variables and its properties are summarized in appendix C.2. In particular, for actions that are bilinear in the quark fields, the integral over Grassmann variables describing the

quark fields can always be computed analytically according to equation (C.2.7), resulting in the determinat of the Dirac operator (considering one flavor for the moment), which in turn can be interpreted as a purely gluonic effective action:

$$\mathcal{Z} = \int DU \det\left(D[U] + m\right) \exp\{-S_G[U]\} \tag{2.2.26}$$

$$= \int DU \exp\{-S_G\left[U\right] - S_{\text{eff}}\left[U\right]\}, \tag{2.2.27}$$

$$S_{\text{eff}}\left[U\right] = -\ln\det\left(D\left[U\right] + m\right). \tag{2.2.28}$$

Being the product of all eigenvalues of $D\left[U\right]$, the determinant requires knowledge about all elements of the Dirac matrix; it is therefore not a local object in the gauge fields when interpreted as an action, which makes lattice simulations with dynamical fermions significantly more involved.[4]

2.3 Renormalization and continuum limit

As remarked in the previous sections, the fact that a lattice action reduces to the continuum action in the classical continuum limit is a necessary condition to describe the correct physical theory. However, as argued in section 1.3, to remove the regulator a the theory has to be renormalized, and it is necessary to vary the bare parameters of the theory while requiring that some quantity assumes a prescribed value. In this section we briefly summarize hadronic schemes to non-perturbatively renormalize lattice field theories and perform the continuum limit.

2.3.1 Hadronic schemes

Perhaps the most widely employed approach to this procedure imposes that an hadronic quantity Θ which is taken to have dimensions of energy (possible choices include hadron masses or combination of hadron masses, decay constants...) computed at a given value of the bare parameters on the lattice assumes its physical value Θ_{phys}. In actual numerical computations both the inputs (the bare parameters of the action) and the outputs (energy levels, matrix elements...) of the simulations are dimensionless numbers. In particular, the measured dimensionful quantities are extracted in lattice units, i.e. multiplied by a suitable power of the lattice spacing. Therefore one has access to the dimensionless number $a\Theta_{\text{lat}}(g_0, a)$,

[4]Not performing the fermionic integral analytically but trying to solve it numerically like the integral over gauge fields would be even more costly by classical means. Indeed, it would be necessary to represent a large number of anticommuting variables, which on a classical computer require at best a 2×2 matrix for each integration variable, leading to an exponential growth of necessary resources.

and imposing the condition $\Theta_{\text{lat}}(g_0, a) = \Theta_{\text{phys}}$ yields a way to "set the scale" of the lattice theory and determine the lattice spacing of the simulation at the given value of g_0 in physical units:

$$a(g_0) = \frac{a\Theta_{\text{lat}}(g_0, a)}{\Theta_{\text{phys}}}. \tag{2.3.1}$$

This relation fixes the dependence of the lattice spacing a on the bare coupling g_0^2; vice-versa, the scaling of the coupling with the cutoff a^{-1} is governed by the renormalization group flow. Rearranging equation (1.3.27) and keeping only the leading term one has that near the continuum

$$g_0^2(a) \underset{a\sim 0}{\sim} -\frac{1}{2b_0 \ln(a\Lambda)}. \tag{2.3.2}$$

We thus see that the continuum limit $a \to 0$ corresponds to the theory with $g_0 = 0$, and knowing how the lattice spacing a depends on the bare coupling g_0 as expressed by equation (2.3.1) is crucial to obtain the continuum limit from multiple simulations at different lattice spacing by extrapolating to $a \to 0$. Because at zero coupling the theory's beta function also vanishes, the continuum limit is a fixed point of the RG flow. In the language of statistical mechanics, this signals the presence of a critical point of the system: the statement that different lattice actions reduce to the same theory in the continuum can thus be understood as the different lattice theories all belonging to the same universality class.
The renormalization of quark masses proceeds in a similar way. For each bare quark mass in the action, one imposes that the ratio of two aptly chosen hadron masses computed on the lattice assumes its physical value

$$\left.\frac{M_A}{M_B}\right|_{a,g_0,am_i} = \left.\frac{M_A}{M_B}\right|_{\text{phys}}. \tag{2.3.3}$$

It is convenient to study mass ratios because, being dimensionless, they can be directly compared to the raio of experimentally determined masses. Ideally, one would choose ratios which are more sensitive to some quark masses than others in order to disentangle as much as possible the dependence on the different flavors' masses. Simulations at several different values of the bare quark masses are performed until the above conditions are met; more frequently, the target value of the bare masses can be determined by interpolating the measured values of the mass ratios and inferring the bare quark mass that satisfies the constraint.

2.3.2 Window problem in hadronic schemes

As anticipated in section 2.1.1, practical lattice lattice computations are carried in a box with finite volume. Denoting with L the extension of the box in each

direction, the exhistence of a maximum length scale provides an infrared cutoff L^{-1} for the theory. Combined with the UV cutoff given by the lattice spacing a^{-1}, it holds that if one aims to accurately describe physics at a given energy scale Θ_A on a lattice with spacing a and extent L the following inequalities must be respected

$$L^{-1} \ll \Theta_A \ll a^{-1}. \tag{2.3.4}$$

In the approach described in the previous section, the lattice is calibrated to accomodate a hadronic scale, which is typically of a few hundred MeV. If, on the same lattice, one wants to study a process which takes place at an energy scale Θ_B much larger than Θ_A, the UV cutoff must be enlarged accordingly, requiring the following condition to be valid

$$L^{-1} \ll \Theta_A \ll \Theta_B \ll a^{-1}. \tag{2.3.5}$$

With modern algorithms it is possible - with considerable computational cost - to simulate lattices with $L/a = \mathcal{O}(100)$ points in each direction. As soon as the scales Θ_B and Θ_A become significantly separated, the number of lattice points required to satisfy (2.3.5) grows far beyond what is feasible with reasonable resources. This type of situation, known as a "window problem", makes it prohibitively hard to employ an hadronic scheme in systems where two highly separated scales need to be accomodated, as it would be necessary to simulate lattices that are simultaneously very fine and very large. This type of problem was encountered when studying the non-perturbative renormalization of gauge theories from the lattice at scales μ spanning $1 - 100$ GeV. The solution, first proposed for SU(3) gauge theory [47] and then extended to QCD with several flavors [48–53], combines a finite-volume scheme for the definition of the renormalized coupling and step-scaling techniques to efficiently track its non-perturbative running. The same strategy served as the basis for the first exploration of thermal QCD up to electroweak-scale temperatures [54]. More general details on the construction can be found in appendix C.3, and in section 3.5 its application to high-temperature QCD will be briefly reviewed.

2.4 Symanzik improvement program

The lattice version of the QCD action and correlation functions computed on the lattice differ from their continuum counterparts by terms proportional to the lattice spacing; for instance, while in the Wilson gauge action discretization effects start at $\mathcal{O}(a^2)$, for the Wilson-Dirac action they are expected to start at $\mathcal{O}(a)$, essentially due to the order of the differential operator entering the kinetic term. The approach to the continuum limit of a lattice field theory can be accelerated, i.e. it is possible to achieve a higher-power scaling with a of the lattice artifacts,

following the so-called Symanzik improvement program [55, 56]. An instructive way of formulating this procedure is provided by the lenses of effective field theory. Indeed, close to the continuum, the lattice theory with discrete action S_{lat} can be described by an effective continuum theory whose action can be expanded in the lattice spacing as

$$S_{\text{latt}} \to \mathcal{S}_{\text{eff}} = \int d^4x \ \left\{\mathcal{L}_0(x) + a\mathcal{L}_1(x) + a^2\mathcal{L}_2(x) + \ldots\right\} \tag{2.4.1}$$

where $\mathcal{L}_n$ denotes a lagrangian containing operators of dimension $4+n$ that can be built from elementary fields and respecting the symmetries of the lattice theory S_{lat}. In particular, the lagrangian $\mathcal{L}_0$ is that of continuum QCD. This defines the so-called *Symanzik effective theory*. In an effective field theory picture one would interpret the lattice cutoff $1/a$ as the scale associated to "new physics", i.e. unkown degrees of freedom not contained in S_{lat}, whose effects can be described by an infinite tower of higher dimensional operators. For instance, the 5-dimensional continuum operators that satisfy the symmetries of the Wilson-Dirac action, and thus enter $\mathcal{L}_1$, are

$$O_{5,1} = \bar{\psi}\sigma_{\mu\nu}F_{\mu\nu}\psi, \tag{2.4.2}$$
$$O_{5,2} = \bar{\psi}\left\{D_\mu D_\mu + D^\dagger_\mu D^\dagger_\mu\right\}\psi \tag{2.4.3}$$
$$O_{5,3} = m\left\{\bar{\psi}\gamma_\mu D_\mu - \bar{\psi}D^\dagger_\mu\gamma_\mu\right\}\psi \tag{2.4.4}$$
$$O_{5,4} = m\,\mathrm{Tr}\{F_{\mu\nu}F_{\mu\nu}\} \tag{2.4.5}$$
$$O_{5,5} = m^2\bar{\psi}\psi \tag{2.4.6}$$

where $\sigma_{\mu\nu} = \frac{i}{2}\left[\gamma_\mu, \gamma_\nu\right]$. Any local operator that enters lattice correlation functions also has a similar representation in the continuum effective theory

$$O_{\text{lat}} \to O_{\text{eff}} = O_0 + aO_1 + \ldots \tag{2.4.7}$$

Expectation values in the lattice theory are then represented by continuum expectation values in the effective theory; to order a for instance one finds

$$\langle O_{\text{latt}}\rangle_{\text{latt}} \to \langle O_{\text{eff}}\rangle_{\text{eff}} = \langle O_0\rangle - a\left[\langle O_1\rangle + \langle O_0\mathcal{S}_1\rangle - \langle\mathcal{S}_1\rangle\right] + \mathcal{O}\big(a^2\big), \tag{2.4.8}$$

where $\mathcal{S}_1 = \int d^4x\ \mathcal{L}_1(x)$ and the subscripts in the expectation values signal whether they are computed with respect to the lattice action, the effective action (2.4.1) or the continuum action $\mathcal{S}_0$ (no subscript). The Symanzik effective theory then allows to identify discretization effects in lattice correlation functions. Exploiting the liberty to add terms to the lattice action which vanish in the classical continuum limit, it is possible to cancel the leading discretization effects of a given order from (2.4.8), and thus obtain correlation functions which approach the continuum limit

at a faster rate. This procedure is known as *improvement*, and as two concrete examples, which will be relevant for the simulations that have been performed for this thesis, the tree-level improvement of the Wilson gauge action and the $\mathcal{O}(a)$-improvement of the Wilson fermion action will be described.

2.4.1 Lüscher-Weisz gauge action

The full improvement procedure involves the non-perturbative removal of discretization effects from observables as described above. Alternatively, the theory can be improved at a given order in perturbation theory. It can be shown that to improve the theory at tree-level it is enough to remove lattice artifacts from the action by the addition of higher dimensional operators. For instance, the tree-level improvement of the Wilson gauge action, leading to the Lüscher-Weisz [57] action, involves the addition of a sum over all 2×1 rectangular plaquettes defined by

$$\tilde{U}_{\mu\nu}(x) \equiv U_\mu(x) U_\mu(x + a\hat{\mu}) U_\nu(x + 2a\hat{\mu}) U_\mu^\dagger(x + a\hat{\mu} + a\hat{\nu}) U_\mu^\dagger(x + a\hat{\nu}) U_\nu^\dagger(x). \quad (2.4.9)$$

The crucial observation is that this object and the elementary plaquette $U_{\mu\nu}$ share the same asymptotic behavior in the vanishing spacing limit given by (2.1.8), i.e. they both reproduce the exponential of the field strength $F_{\mu\nu}$, but with different discretization effects. It is therefore possible to find a linear combination that still yields the continuum action for $a \to 0$ but also cancels the leading $\mathcal{O}(a^2)$ artifacts, resulting in discretization effects that start at $\mathcal{O}(a^4)$. The combination is found to be

$$S_G^{\mathrm{LW}} = \frac{\beta}{2N_c} \sum_x \sum_{\mu,\nu} \mathrm{Re} \left\{ \frac{5}{3} \mathrm{Tr} \left[\mathbb{1} - U_{\mu\nu}(x) \right] - \frac{1}{12} \mathrm{Tr} \left[\mathbb{1} - \tilde{U}_{\mu\nu}(x) \right] \right\}. \quad (2.4.10)$$

2.4.2 $\mathcal{O}(a)$-improved Wilson fermions

As anticipated, the improvement of the Wilson fermion action requires the addition of the lattice versions of the dimension 5 operators eqs. (2.4.2) to (2.4.6). Using the equation of motion, it is possible to discard terms proportional to O_2 and O_3. The contributions of O_4 and O_5 can be absorbed in the definition of the coupling and mass respectively, specifically with the introduction of an improved bare coupling and mass which depend on the subtracted quark mass $m_q \equiv m_0 - m_{\mathrm{cr}}$ appearing in equation (2.2.23):

$$g_{0,\mathrm{impr}}^2 = g_0^2 \left(1 + b_g a m_q\right), \quad m_{q,\mathrm{impr}} = m_q \left(1 + b_m a m_q\right). \quad (2.4.11)$$

It is thus enough to add a single term proportional to the discretization of O_1 to the Wilson-Dirac operator to remove $\mathcal{O}(a)$ discretization effects, leading to the

$\mathcal{O}(a)$-improved Wilson fermion [58]

$$D = D_W + aD_{\mathrm{SW}}, \tag{2.4.12}$$

where the Sheikholeslami-Wohlert term takes the form

$$D_{\mathrm{SW}} = c_{\mathrm{SW}}(g_0)\frac{1}{4}\sigma_{\mu\nu}\hat{F}_{\mu\nu}(x). \tag{2.4.13}$$

The lattice discretization of the field strength can be expressed as

$$\hat{F}_{\mu\nu}(x) = \frac{i}{8a^2}\{Q_{\mu\nu}(x) - Q_{\nu\mu}\} \tag{2.4.14}$$

where $Q_{\mu\nu}$ is the four-plaquette clover operator

$$\begin{aligned} Q_{\mu\nu}(x) = {} & U_\mu(x)U_\nu(x+a\hat{\mu})U_\mu^\dagger(x+a\hat{\nu})U_\nu^\dagger(x) \\ & + U_\nu(x)U_\mu^\dagger(x-a\hat{\mu}+a\hat{\nu})U_\nu^\dagger(x-a\hat{\mu})U_\mu(x-a\hat{\mu}) \\ & + U_\mu^\dagger(x-a\hat{\mu})U_\nu^\dagger(x-a\hat{\mu}-a\hat{\nu})U_\mu(x-a\hat{\mu}-a\hat{\nu})U_\nu(x-a\hat{\nu}) \\ & + U_\nu^\dagger(x-a\hat{\nu})U_\nu(x-a\hat{\nu})U_\nu(x+a\hat{\mu}-a\hat{\nu})U_\mu^\dagger(x). \end{aligned} \tag{2.4.15}$$

The value Sheikholeslami-Wohlert coefficient $c_{\mathrm{SW}}(g_0)$ has to be varied with g_0 to remove $\mathcal{O}(a)$ discretization effects form an observable such as (2.4.8). The dependence of c_{SW} on g_0 has been computed to one-loop in perturbation theory and also non-perturbatively from lattice simulations for both the Wilson [59–61] and Lüscher-Weisz gauge action [62], by requiring that the PCAC relation (1.5.34) holds up to discretization effects of order $\mathcal{O}(a^2)$.

2.4.3 Field improvement and renormalization

Using the improved lattice action guarantees that discretization effects in spectral quantities, such as hadron masses, are reduced as described, since they do not depend on the choice of interpolating operator used to build the correlation functions (provided they have overlap with the desired state). However if one aims to extract matrix elements or impose Ward identities, which depend on the explicit form of the interpolating field, the improvement procedure must be applied to the relevant fields as well to remove discretization effects of a given order from individual correlation functions. For instance, the improvement of the non-singlet axial current (1.5.32) requires the addition of an operator with the same quantum numbers, which can be built from the non-singlet pseudoscalar density (1.5.33):

$$A^a_{\mu,\mathrm{impr}} = A^a_\mu + a\ c_A(g_0)\frac{\partial_\mu + \partial^*_\mu}{2}P^a. \tag{2.4.16}$$

Adopting an improved action also impacts the renormalization of the theory's bare parameters. In particular, the renormalization constants will now depend on the improved coupling defined in equation (2.4.11):

$$\bar{g}^2 = Z_g\left(g^2_{0,\mathrm{impr}}, a\mu\right) g^2_{0,\mathrm{impr}} \tag{2.4.17}$$

$$\bar{m}_q = Z_m\left(g^2_{0,\mathrm{impr}}, a\mu\right) m_{q,\mathrm{impr}} \tag{2.4.18}$$

2.5 Measurement of expectation values

With the definition of the lattice action and path integral, expectation values of operators constructed from elementary fields take the form

$$\langle O\rangle = \frac{1}{\mathcal{Z}}\int DU \prod_{i=1}^{N_f}\left(\det D_i[U]\right)\; O[U]\, e^{-S_G[U]}., \tag{2.5.1}$$

where for definiteness we consider Wilson fermions and we introduce the shorthand notation $D_i[U] \equiv D_W[U] + m_i$ for the massive Wilson-Dirac operator of the i^{th} quark flavor with mass m_i. The goal of lattice computations is to numerically evaluate this type of path integrals. On a typical lattice, where each spacetime direction is discretized in $\mathcal{O}(100)$ points, one easily reaches $\mathcal{O}(10^9)$-dimensional integrals, which can not be computed through deterministic numerical integrators. Instead, path integrals are evaluated by Monte Carlo methods making use of an important analogy with statistical mechanics ensemble averages. Indeed, the above equation can be interpreted as the expectation value of an observable which depends on statistical variables U that follow a Boltzmann-type[5] probability distribution with density

$$P[U] = \frac{1}{\mathcal{Z}}\prod_{i=1}^{N_f}\det\left(D_i[U]\right) e^{-S[U]}. \tag{2.5.2}$$

Of course, for this picture to be valid it is crucial that the above expression is positive definite; when fermions are included the determinant factors may spoil this property, depending both on the number of flavors considered and on the particular discretization employed. For instance, since the Wilson-Dirac operator satisfies γ_5-hermiticity

$$\gamma_5 D \gamma_5 = D^\dagger, \tag{2.5.3}$$

its determinant is real

$$\det(D) = \det\left(\gamma_5 D^\dagger \gamma_5\right) = \det\left(D^\dagger\right) = \left(\det(D)\right)^*. \tag{2.5.4}$$

[5]The formulation of the theory in Euclidean spacetime plays a crucial role in allowing this interpretation and making it possible to sample from a positive definite distribution.

This fact implies that (2.5.2) is positive for any even number of degenerate flavors. A particularly relevant case is given by the theory with $N_f = 2$ flavors with equal mass – the u and d quarks – for which the Boltzmann distribution reads (the inclusion of a third, non-degenerate quark – the strange quark– will be discussed in section D.3)

$$P[U] = \frac{1}{\mathcal{Z}} \exp\left\{-S_G[U] + \ln|\det D[U]|^2\right\}, \tag{2.5.5}$$

and which will be assumed in the following for definiteness. In this case, the costly estimation of the fermionic determinant can be ameliorated by interpreting it as the result of a functional integration over a set of auxiliary complex scalar fields $\phi, \phi^\dagger$

$$|\det D[U]|^2 = \exp\{-S_{\text{eff}}[U]\} \propto \int D\phi^\dagger D\phi \ \exp\left\{-S_{\text{pf}}\left[U, \phi, \phi^\dagger\right]\right\} \tag{2.5.6}$$

described by the following action

$$S_{\text{pf}}\left[U, \phi, \phi^\dagger\right] \equiv a^8 \sum_x \phi^\dagger(x) Q^{-2}[U](x, y)\phi(y), \quad Q[U] = \gamma_5 D[U]. \tag{2.5.7}$$

Like quark fields, $\phi, \phi^\dagger$ carry Dirac and color indices, but they are not described by Grassmann variables; for this reason, they are known as pseudofermion fields. Since the pseudofermion action is quadratic in the fields, representative configurations can be sampled directly starting from a sample of normally distributed numbers and applying a set of transformations.

2.5.1 Monte-carlo estimation

If one is able to sample an ensemble of N representative configurations of gauge fields $\{U_i\}_{i=1,\dots,N}$ distributed according to (2.5.2), the expectation value (2.5.1) (i.e. the multidimensional integral) can be estimated up to a statistical error through the ensemble average:

$$\bar{O} \equiv \frac{1}{N} \sum_{i=1}^{N} O[U_i] = \langle O \rangle + \mathcal{O}\left(\frac{1}{\sqrt{N}}\right). \tag{2.5.8}$$

The ensemble average comes with an error $\sigma^2_{\bar{O}}$ proportional to the ensemble variance σ^2_O, which has a path integral representation itself:

$$\sigma^2_O \equiv \left\langle (O - \langle O \rangle)^2 \right\rangle. \tag{2.5.9}$$

Assuming that the N configurations are statistically independent, the error on the ensemble average (2.5.8) can be estimated as

$$\sigma^2_{\bar{O}} = \frac{1}{N}\sigma^2_O \approx \frac{1}{N}\frac{1}{(N-1)} \sum_{i=1}^{N} \left(O[U_i] - \bar{O}\right)^2. \tag{2.5.10}$$

Both the generation of gauge field ensembles distributed according to the desired Boltzmann distribution and, more often than not, the evaluation of the observable on the generated configurations are highly non-trivial tasks, and they require vast computational resources and state-of-the-art algorithms to be efficiently implemented. Appendix D describes how ensembles of gauge field configurations can be extracted through the Hybrid Monte-Carlo algorithm.

2.5.2 Correlators and the exponential problem

The primary expectation values that one aims to compute in lattice field theory are correlation functions of fields. The prototypical example involves correlators of the form

$$C(x_0) \equiv \left\langle O(x_0)O^\dagger(0)\right\rangle = \frac{1}{\mathcal{Z}}\int DUD\psi D\bar{\psi}\; O(x_0)O^\dagger(0)\; e^{-S}, \tag{2.5.11}$$

where $O(x_0)$ is a gauge-invariant composite field defined on a fixed timeslice of the lattice. Exploiting the connection between path integral expectation values and expectation values of operators on the theory's vacuum state (see equation (1.2.3)), one can write

$$C(x_0) = \langle 0|\, \hat{O}(x_0)\hat{O}^\dagger(0)\, |0\rangle\,. \tag{2.5.12}$$

The Euclidean time dependence of the operator can be expressend in the Heisenberg picture

$$\hat{O}(x_0) = e^{x_0\hat{H}}\hat{O}e^{-x_0\hat{H}}, \tag{2.5.13}$$

where the Hamiltonian of the theory $\hat{H}$ generates translation in time. Inserting an identity in equation (2.5.12) in the form of a sum over a complete set of energy eigenstates

$$\mathbb{1} = \sum_n |n\rangle\langle n|\,, \qquad \hat{H}\,|n\rangle = E_n\,|n\rangle \tag{2.5.14}$$

leads to the following spectral decomposition for the correlator,

$$C(x_0) = \sum_n |\,\langle 0|\,\hat{O}\,|n\rangle\,|^2\; e^{-E_n x_0}, \tag{2.5.15}$$

provided that $\hat{O}$ has overlap with one-particle states carrying its quantum numbers. This central equation furnishes a way to extract energy levels (masses) of particles and matrix elements from a correlator that can be computed on the lattice. The choice of the "interpolating operator" O selects the quantum numbers of the states in the theory that one wants to study, i.e. those for which $\langle 0|\,\hat{O}\,|n\rangle \neq 0$. Equation (2.5.15) implies that at large enough Euclidean times the contribution of states

with energies higger than the lowest energy E_0 are exponentially suppressed, so that the correlator will be dominated by the ground state

$$C(x_0) \underset{x_0 \gg a}{=} A e^{-E_0 x_0} \left(1 + \mathcal{O}\left(e^{-(E_1 - E_0)x_0}\right)\right). \tag{2.5.16}$$

It is therefore possible to obtain the mass of a particle and the matrix element of a relevant operator by inspecting the large Euclidean time behavior of correlation functions (more details on how to practically implement this procedure will be given in section 5.1.3). As mentioned in the previous section, all expectation values in a lattice computation are estimated stochastically, and come with a stastisical error given by equation (2.5.10); the variance of O has its own spectral decomposition, which in general receives contributions from different states with respect to O. A clear and relevant example involves the correlator of an interpolating field carrying the quantum number of a nucleon[6]

$$N(x) = \varepsilon^{abc} \left(\psi_u^a(x)^T \; C\gamma_5 \psi_d^b(x)\right) \psi_d^c(x), \tag{2.5.17}$$

whose correlation function, projected to zero spatial momentum, will be domninated by the mass of nucleon state m_N at large Euclidean times

$$C(x_0) \underset{x_0 \gg a}{\propto} e^{-m_N x_0}. \tag{2.5.18}$$

Its variance, on the other hand, involves the two point function of an operator containing six quarks; the lightest state in the theory that has non-zero overlap with this operator is not a state containing two nucleons, but rather a state containing three pions. Therefore at large Euclidean times the variance will decay as

$$\sigma_C^2(x_0) \underset{x_0 \gg a}{\propto} e^{-3 m_\pi x_0}. \tag{2.5.19}$$

If one computes the correlator and its error as an average over N gauge field configurations as described in the previous section, the statistical precision with which the correlator can be estimated is given by the signal-to-noise ratio (StNR, which at large times behaves as

$$\frac{\bar{C}(x_0)}{\sigma_{\bar{C}}(x_0)} \underset{x_0 \gg a}{\propto} \sqrt{N} \exp\left\{-\left(m_N - \frac{3}{2} m_\pi\right) x_0\right\}. \tag{2.5.20}$$

Since in Nature $m_N - \frac{3}{2} m_\pi \sim 730$ MeV ~ 3.7 fm^{-1}, the StN decays exponentially with Euclidean time, preventing a precise determination of the correlator in the

[6] In QCD with degenerate up and down quarks the proton and neutron states become degenerate as well.

large time region of interest for the determination of the mass. Of course increasing the number of measurements N will increase the StN, but it is clear that an exponential increase in statistics would be necessary to maintain a constant StN while going to larger Euclidean times. This is a rahter general feature of correlators computed by lattice simulations known as the exponential problem [63, 64], and it remains the primary obstacle for the precise determination of hadronic quantities. The only real exception is given by correlators which couple to the lightest flavor non-singlet mesonic states (the pions), which are the lightest hadrons in QCD.

Popular strategies to ameliorate the StN problem involve the construction of interpolating operators with optimal overlap on the ground state through "smearing" of the link fields [65–67], or the analysis of an $N \times N$ correlation matrix $C_{ij}(x_0) \equiv \left\langle O_i(x_0) O_j^\dagger(0) \right\rangle$ built from a set of operators O_i which all overlap on the states of interest [68]. In the latter case, solving a generalized eigenvalue problem associated to the correlator matrix can lead to the precise determination of the $n < N$ lightest states in the spectrum, as contaminations depend on $(E_{N+1} - E_i)\, x_0$ for the i^{th} state. While the combination of these methods is by now an established tool in precision studies of the hadronic spectrum to mitigate the exponential problem, they do not represent a true solution as the exponential increase of necessary resources with the desired precision still persists. A solution to the exponential problem, i.e. an algorithm that achieves polynomial rather than exponential scaling with the euclidean time extent of the lattice, is given by the multilevel update scheme [69]: in bosonic theories such as SU(3) Yang-Mills the locality of the action allows to factorize the lattice in independent domains that are influenced by other regions of the lattice only through the value of the link fields at their boundary. To estimate the expectation value of an observable, which has to be factorized itself, the links in the different domains of the lattice can effectively be updated independently, and the local factors of the observable can be evaluated as an average over these "nested" samples. Repeating this procedure multiple times yields an estimate of the original global observable as the average over a set of measurements which have drastically reduced fluctuations, achieving in practice an exponential error reduction with respect to a standard update. The theory in the presence of fermions loses manifest locality of due to the appearance of the quark determinant[7]; the generalization of the multilevel algorithm to this case is an active area of research [70–73] with promising exploratory results [74].

[7] Taking as an example the case of Wilson fermions, we have that the Dirac operator is ultralocal, but its inverse is not.

Chapter 3

Thermal QCD

This chapter summarizes the properties of QCD at non-zero temperature, its relevance from an experimental, observational and conceptual point of view and its formulation in the path-integral formalism. The perturbative expansion of high-temperature QCD and its infrared problem are discussed, together with the dimensionally reduced effective field theory that describes QCD at asymptotically high temperature. Screening masses, the primary object of study of this thesis, are defined and their relevance is discussed, and an overview of the state of the art for their determination, both in a perturbative setting and from the lattice, is provided.

3.1 Matter in extreme conditions

Up to now, all the properties of strong interactions that were discussed referred to systems composed of a few isolated hadrons in the vacuum, i.e. zero temperature and density. These conditions are relevant for the description of phenomena that take place at everyday temperature and density scales, as well as proton-proton collisions at particle accelerators such as the LHC.[1] Many physically relevant and fascinating cases, on the other hand, involve matter in states characterized by non-zero, and possibly very high, temperature and density. Relevant properties of galaxies are inferred by the electromagnetic radiation emitted by matter contained in stars, which exhists in a plasma phase with temperatures in the range 3000 – 50 000 K (0.26 – 4.3 eV). Compact objects such as white dwarves and neutron stars can reach extreme densities, up to hundreds of trillions times higher than that of ordinary matter. Moreover, decades of observational data have consolidated the

[1] Even though they can involve a large number of hadrons at technically non-zero temperature, the relevant energy scale for QCD is of a few hundred MeV per hadron, orders of magnitude higher than what is reached for matter in ordinary conditions.

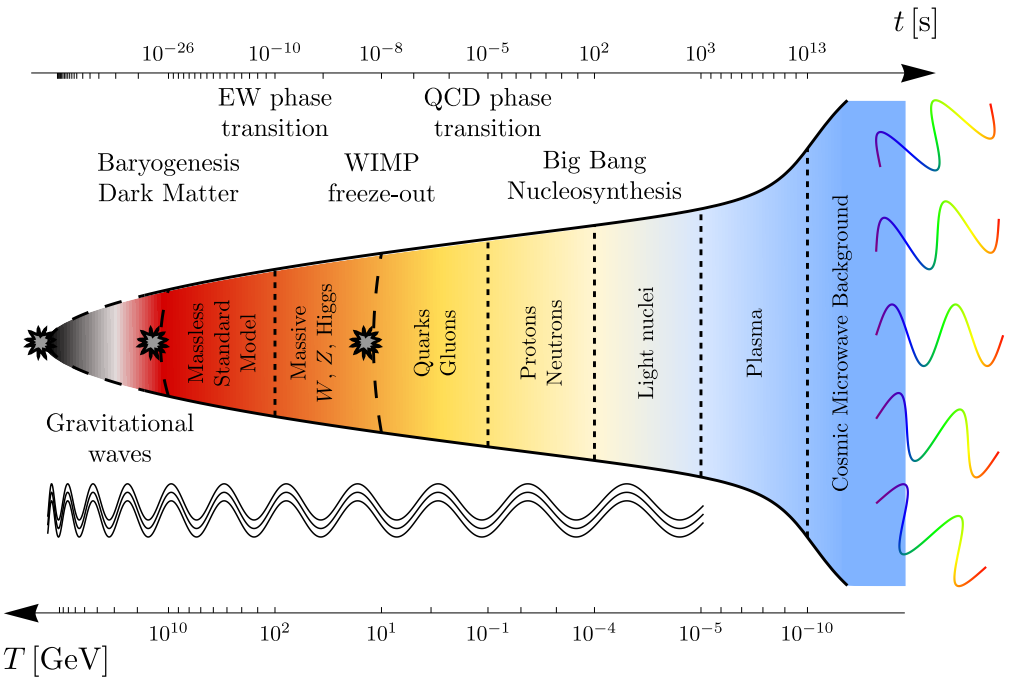

FIGURE 3.1: From [75]: sketch of the evolution of the early Universe from the Big Bang to the Cosmic Microwave Background. The relevant time and temperature scales are reported, together with key physical processes. Notice that, for both the electroweak and strong sectors, it is more correct to speak of an analytic crossover rather than a phase transition.

Big-Bang picture as the most compelling model to describe the dynamics of the early Universe during its first instants. Starting from a pointlike - singular - extremely hot and dense configuration, the Universe underwent rapid expansion, progressively cooling down. Having a solid grasp on what the Standard Model predicts immediately after the Big Bang is thus of central importance to interpret cosmological observations and understand the origin of matter as is seen today.

3.1.1 The phases of QCD

Much like the properties of water can change with temperature, and its constituent molecules can transition from a solid to a liquid or gaseous phase, or even with the ionization of neutral molecules into a plasma of unbound ions and electrons, it was soon conjectured that the properties of ordinary hadronic matter may exhibit a phase transition at high enough temperatures [76–79] or densities. Due to asymptotic freedom, it was conjectured that at high enough temperatures the quarks and gluons that make up hadrons should deconfine, effectively behaving like a gas of

weakly interacting particles. Understanding the details of how – and if – hadronic matter transitions to the "Quark-Gluon Plasma" (QGP) state described above has been one of the focal points in a vast body of both experimental and theoretical research during the last decades, and it continues to be an actively investigated topic. In the aforementioned context of early Universe cosmology, if the change from the QGP phase to the ordinarty hadronic phase happens with a strong first-order phase transition, the associated release of energy in the form of latent heat can produce gravitational waves [80–82], which travel virtually unaffected at the speed of light and could be detected by present and future experiments [83–86], enabling a direct study of the properties of the Universe at times prior to the formation of the Cosmic Microwave Background.

The nature of phase transitions is intimately related to the symmetries of the theory. For this reason, it is often instructive to consider deformations of QCD such as the chiral limit or, in the opposite case, the theory with infinitely massive - static - quarks, where it enjoys enlarged exact symmetries. In the latter limit of infinite mass, the quarks effectively decouple from the dynamics, and QCD is described by SU(3) Yang-Mills theory in the presence of static fermions. In this case, the theory exhibits a first order phase transition associated to the spontaneous breaking of the symmetry under transformations in the center of SU(3), given by the abelian subgroup $\mathbb{Z}_3$ [87–89]. The order parameter for this phase transition is the Polyakov loop, which has a vanishing expectation value in the unbroken, zero-temperature phase and instead develops three non-center symmetric vacua with non-zero expectation value at high temperatures. The expectation value of the Polyakov loop is directly related to the free energy of a static quark placed in the vacuum: a zero expectation value corresponds to infinite free energy, while a non-zero value corresponds to a finite free energy. Hence, this is known as the *deconfinement* phase transition of SU(3) Yang-Mills theory (or QCD with static quarks). The critical temperature for the deconfinement phase transition is now known at the permille level [90]; although the theory with no quarks is unphysical, and there is thus no unambiguous way to express dimensionful quantities in physical units, employing the Wilson-flow reference scale t_0 [91] yields

$$T_{\mathrm{c}}^{\mathrm{SU(3)}}\sqrt{t_0} = 0.24915(29) \;\longrightarrow\; T_{\mathrm{c}}^{\mathrm{SU(3)}} = 292.7(3)\ \mathrm{MeV}. \tag{3.1.1}$$

As soon as dynamical quarks are inserted in the theory, $\mathbb{Z}_3$ symmetry is explicitly broken. Nevertheless, for finite but very high values of the quark mass the deconfinement transition remains first-order; as the quark masses are lowered, the transition weakens until it becomes second order at a "critical line" in the $m_{u,d}-m_s$ plane, beyond which it disappears into an analytic crossover.

As we have seen in section 1.5, chiral symmetry plays a central role in vacuum QCD: though explicitly broken by the quark masses, it is also spontaneously broken in the chiral limit by the non-zero value of the chiral condensate. At sufficiently high temperatures, the chiral condensate vanishes and chiral symmetry gets effectively restored. The transition between these two phases, relevant for the case of massless (or possibly even light) quarks is known as the *chiral transition* of QCD. About 15 years ago it was established through lattice simulations that QCD with $N_{\mathrm{f}} = 2 + 1$ quarks at the physical point does not feature a phase transition between the chirally broken and restored phases, but rather a smooth crossover [92–97]. It is important to stress that, at variance with what happens in a true phase transition, there is a degree of ambiguity in the definition of the crossover temperature, as the analysis of different observables will in general yield slightly different values of the transition temperature. With this *caveat* in mind, the typical value of the pseudocritical temperature of QCD, as extracted from the analysis of the chiral condensate, is

$$T_{\mathrm{pc}} \approx 156 \text{ MeV}. \tag{3.1.2}$$

This discovery excluded the possibility of detecting the signatures of early universe phase transitions within the strong sector of the SM.[2] Although also the electroweak transition, related to the activation of the Higgs mechanism, was shown to be a crossover with a pseudocritical temperature of ~ 160 GeV [102–104], it is interesting to point out that the presence of BSM fields at higher energies can turn this crossover back into a first order phase transition, see e.g. [105].

The fate of the QCD transition in the chiral limit is an interesting and relevant matter, which is still subject of active discussion and that has recently gained a lot of attention. Original arguments based on models of QCD [106] predicted that the chiral transition should be either first or second order depending on the number of quark flavors and on whether $\mathrm{U}(1)_A$ gets effectively restored. Lattice simulations at fixed lattice spacing and non-zero quark masses do indeed see a first order transition for sufficiently small masses, but it has been recently argued that the first order region may significantly shrink in the continuum or even disappear, making the transition a crossover for all finite quark masses and only second order in the chiral limit [107–109]. The conjectured nature of the QCD transition as a function of the light quark masses is usually summarized in the so-called "Columbia plot" [110], see figure 3.2.

[2]Recently, evidence at the $2\sigma - 4\sigma$ level for a stochastic gravitational wave background [98–100] has been reported. Analysis of the data seems to favor the inspiral of supermassive black holes as the source of the detected signal over potential transitions in the early universe [101].

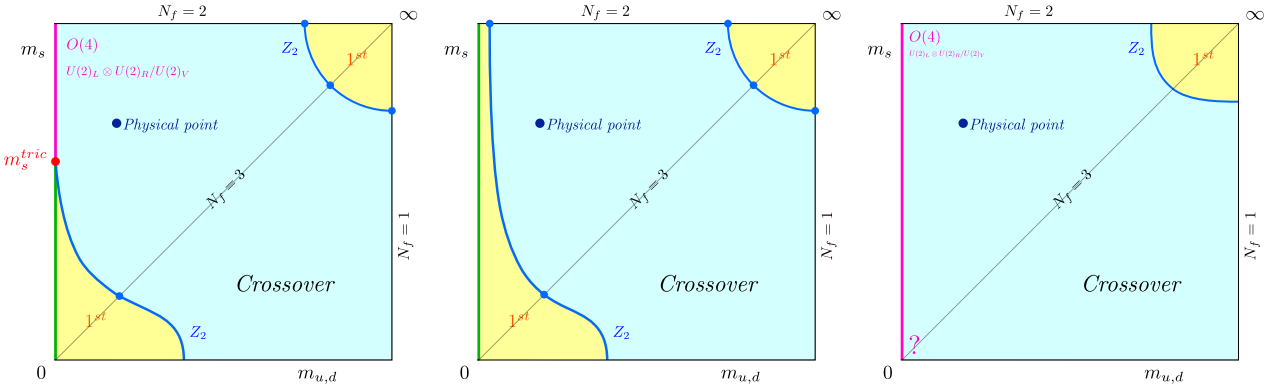

FIGURE 3.2: From [107]: The Columbia plot in its original version (left) and with recently proposed possible modifications regarding the shape or presence of the first order region for the chiral transition (center, right). Each point in this diagram corresponds to a different theory, namely SU(3) Yang-Mills in the presence of 2 mass-degenerate quarks with mass $m_{u,d}$ and a third quark with mass m_s. Different regions are colored according to the order (or presence) of a thermal phase transition as marked on the diagrams; second-order critical lines and their universality class are denoted by thick lines. The axes range from the massless to the static (infinitely massive) limits, where quarks decouple (therefore the top and right edges of the diagram correspond to the theory with 2 dynamical degenerate quarks and 1 quark respectively, and the top-right corner represents pure Yang-Mills theory).

3.1.2 Heavy ion collisions

During the last few decades a wealth of information about the properties of QCD at high temperature and density has been accumulated thanks to experimental efforts, such as the ALICE experiment at CERN's LHC or the STAR and PHENIX experiments at the Relativistic Heavy Ion Collider (RHIC) in Brookhaven. In these experiments, the nuclei of heavy atoms, typically lead or gold, are accelerated to relativistic velocities and collided: the large number of colliding nucleons and the high energies provide the environment for the formation of a dense thermal medium. Inferring the properties of the state produced right after the collision from the miriad of particles detected in the final state of these events is a highly non-trivial task, which requires the use of several different approaches to model the complicated dynamics involved, see figure 3.3 for a schematic representation. Nevertheless, consensus has developed that in the initial stages of the collision a different state of matter is produced [114, 115] at temperatures that reach up to ~ 350 MeV. The observed properties of the final-state particles are compatible with the production of a fluid composed of strongly interacting particles, which is thus interpreted as the Quark-Gluon Plasma.

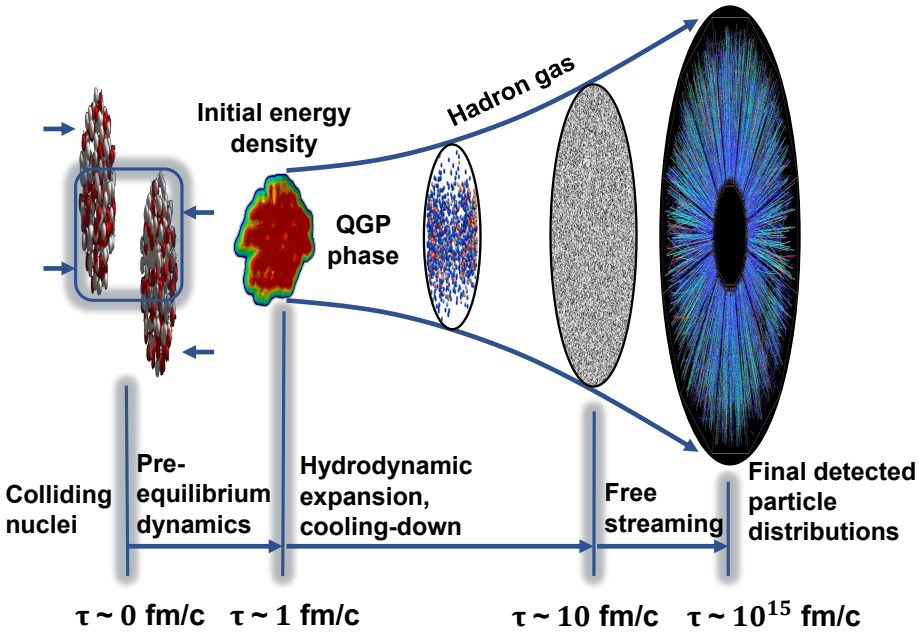

FIGURE 3.3: From [111], adapted from [112, 113]: sketch of the dynamical phases of a relativistic heavy ion collision event.

Aside from high temperatures, collisions of heavy atomic nuclei probe matter at high densities, usually expressed in terms of the baryon chemical potential μ_B. The behavior of matter at high densities is crucial, among other things, to understand the nature of neutron stars, since the equation of state in such conditions directly impacts the structure of the compact objects. With regards to phase transition, an early success of heavy ion colliders was the discovery of a first order liquid-gas phase transition of nuclear matter around $\mu_B \sim 930$ MeV [116]; at even higher densities, several possible states of QCD have been conjectured to exhist, such as color-superconductivity [117] or the color glass condensate [118]. Another central goal of the experimental heavy ion collision program, specifically at RHIC and the future FAIR, NICA and J-PARC facilities, is to map out the QCD phase diagram in the temperature - baryon chemical potential plane, see figure 3.4. One of the pressing open questions in this field is whether the properties of the chiral crossover change when the density is increased, specifically whether it turns into a 1st order phase transition culminating at a critical end point (CEP) at high enough densities. Studies based on the truncation of momentum modes in the path-integral such as the functional renormalization group [119–124] and Dyson-

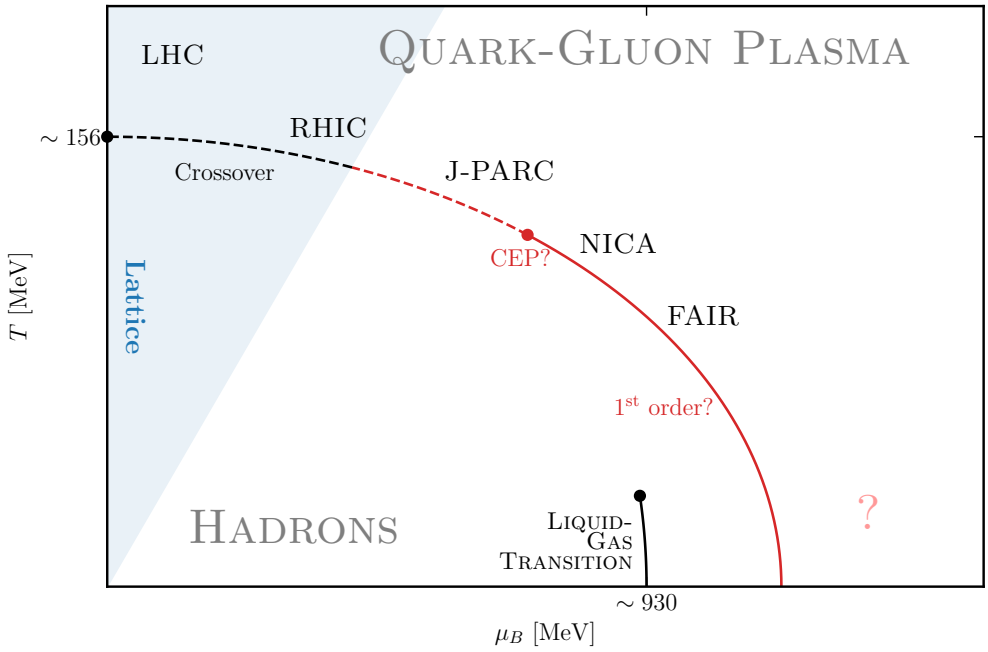

FIGURE 3.4: Sketch of a possible QCD phase diagram in the $\mu_B - T$ plane. Red parts are conjectured features under current theoretical and experimental investigation. Lattice computations are directly applicable on the $\mu_B = 0$ line, while extrapolations to finite chemical potential are currently limited to the blue region. The expected range in parameter space of current and future heavy-ion collision programs is also reported.

Schwinger equations [125–128] seem to hint at the presence of a crititcal endpoint around $(T_{\text{CEP}},\ \mu_{\text{CEP}}) \approx (110\ \text{MeV},\ 620\ \text{MeV})$ [125, 129] First-principles lattice simulations cannot be straightforwardly extended to the case of non-zero μ_B due to the infamous *sign problem*: the inclusion of the baryon chemical potential makes the quark determinant complex, and thus the possibility to evaluate path integrals via Monte Carlo importance sampling is completely spoiled. Several methods have been proposed over the years to ameliorate - see [130, 131] for reviews - or possibly solve the problem [132, 133]; in particular, methods based on controlled extrapolations have been able to explore the region $\mu_B/T \lesssim 3,\ \mu_B \lesssim 300$ MeV [134–141].

In conclusion, studying the properties of matter in extreme conditions is of prime interest to understand the behaviour of the Universe at its earliest stages and to interpret present and future experimental results coming from heavy ion collisions. For this reason, it is essential to have reliable first-principles predictions in this regime. In the following sections the formulation of quantum field theories in thermal equilibrium will thus be summarized.

3.2 QFT at non-zero temperature

The properties of a QFT in thermal equilibrium at temperature T are encoded in the canonical partition function of quantum statistical mechanics. In the real-time operator formalism it can be expressed as[3]

$$\mathcal{Z} = \mathrm{Tr}\left[e^{-\hat{H}/T}\right], \tag{3.2.1}$$

where the trace is over the theory's Hilbert space and $\hat{H}$ is the system's Hamiltonian. This trace can be obtained by integrating over all possible field configurations; denoting all fields by the collective label Φ, one can write

$$\mathcal{Z} = \int D\Phi \ \langle\Phi| e^{-\hat{H}/T} |\Phi\rangle . \tag{3.2.2}$$

Formally, the expectation value in the integrand is the quantum-mechanical amplitude of the system starting from the state $|\Phi\rangle$ and returning to it after evolving in time by an *imaginary* aumount $\delta t = -i/T$. We thus see that the canonical partition function admits a natural formulation in the Euclidean theory after performing the Wick rotation (1.2.4); furthermore, the trace over the theory's Hilbert space leads to the following path integral representation of the canonical partition function of QCD at temperature T:

$$\mathcal{Z}[T] = \int DAD\psi D\bar{\psi} \ \exp\left\{ - \int_0^{1/T} dx_0 \int d^3\boldsymbol{x} \ \mathcal{L}_{\mathrm{QCD}} \right\}, \tag{3.2.3}$$

where bosonic (fermionic) fields are taken to satisfy (anti-)periodic boundary conditions in the now compact imaginary time direction with period $L_0 = 1/T$:

$$A_\mu(x_0 + L_0, \boldsymbol{x}) = A_\mu(x_0, \boldsymbol{x}), \tag{3.2.4}$$
$$\psi(x_0 + L_0, \boldsymbol{x}) = -\psi(x_0, \boldsymbol{x}), \tag{3.2.5}$$
$$\bar{\psi}(x_0 + L_0, \boldsymbol{x}) = -\bar{\psi}(x_0, \boldsymbol{x}). \tag{3.2.6}$$

From the formal point of view, introducing temperature in the system simply amounts to a finite volume effect; in particular, since it does not involve the short-distance UV sector of the theory, the renormalization procedure is unaffected, meaning that the thermal theory does not require any additional renormalization. We see that the imaginary-time formulation of QCD, which as seen in the previous chapter enables the numerical solution of the lattice theory by allowing to sample from a positive-definite distribution through Markov-Chain Monte Carlo

[3] We will assume throghuout vanishing chemical potential.

simulations, also offers a natural framework to extract equilibrium properties of the thermal theory.
The (anti)periodicity in Euclidean time implies that in Fourier space the frequencies assume discrete values, known as the Matsubara frequencies [142], as opposed to the continuous spatial momenta. Employing a mixed momentum-coordinate representation with a conventional normalization, the gluon and quark fields can be decomposed in their Matsubara modes as

$$A_\mu(x_0, \boldsymbol{x}) = \sqrt{T} \sum_n \exp\{i\omega_n x_0\} A_\mu(\omega_n, \boldsymbol{x}), \tag{3.2.7}$$

$$\psi(x_0, \boldsymbol{x}) = \sqrt{T} \sum_n \exp\{i\omega_n x_0\} \psi(\omega_n, \boldsymbol{x}), \tag{3.2.8}$$

with the Matsubara frequencies defined as

$$\omega_n = \begin{cases} 2\pi n T & \text{for bosons,} \\ (2n+1)\pi T & \text{for fermions.} \end{cases} \tag{3.2.9}$$

Equations (3.2.7) and (3.2.8) imply that in the non-interacting limit the QCD action factorizes in a sum of terms with definite Matsubara frequency; moreover, equation (3.2.9) immediatly implies that only bosonic degrees of freedom contain static modes, i.e. time-independent configurations with $\omega = 0$, whereas fermionic degrees of freedom are inherently non-static. Notice also that with the chosen normalization the Matsubara modes have mass dimension $[A_\mu(\omega_n, \boldsymbol{x})] = 1/2$ and $[\psi(\omega_n, \boldsymbol{x})] = 1$. Field-theoretic expectation values are defined as per equation (1.2.2) with respect to the thermal partition function (3.2.3); thermodynamical observables can be derived from the partition function, such as for instance the free energy density, pressure and entropy

$$f = -\frac{T \ln(\mathcal{Z})}{V}, \quad p = -f, \quad s = \frac{\partial}{\partial T} T \ln(\mathcal{Z}). \tag{3.2.10}$$

As was pointed out in the previous sections, QCD exhibits a change in behaviour above a characteristic temperature $T_{\text{pc}} \sim 156$ MeV. At temperatures much higher than T_{pc}, and thus much higher than Λ, the temperature T becomes the relevant dimensionful scale of the theory, and in particular due to asymptotic freedom one expects a pertubative treatment of thermal QCD to be a viable method to extract the theory's predictions. Even though the theory becomes weakly coupled at high temperatures, the pertubative expansion is severely hampered by the so-called *infrared problem*, which will be discussed below.

3.3 Dimensionally reduced effective theory

In this section we describe a useful framework to study thermal QCD and organize the weak coupling expansion of observables, which is based on the construction

of an effective field theory (EFT) that describes QCD at high temperatures and is exact in the infinite temperature limit. This construction also allows to study in detail the presence and relevance of non-perturbative contributions to the weak coupling series. The aim of the effective theory is to describe thermal QCD at length scales much larger than the Euclidean time extent $1/T$, and the first step in the construction of the EFT is to identify the relevant degrees of freedom in such conditions. As we have seen in equations (3.2.7) and (3.2.8), in the free theory at high temperatures non-static Matsubara modes are characterized by a large frequency $\sim \pi T$, while the static modes of bosonic fields have zero Matsubara frequency. If we want to study physics involving distances much larger than $1/T$, the former can be regarded as *heavy* fields and be integrated out from the dynamics, whereas the latter are the *soft* degrees of freedom that are included in the effective theory. The static modes of the gauge fields, which we denote as

$$A_\mu(\omega = 0, \boldsymbol{x}) \equiv A_\mu(\boldsymbol{x}) \tag{3.3.1}$$

will be the degrees of freedom of the EFT, with the assumption that they remain the relevant dynamic fields also when interactions are included. As noted earlier, being modes with fixed Matsubara frequency all dependence on Euclidean time is removed, and they can bee seen as three-dimensional gauge fields: the theory at high temperatures is said to undergo *dimensional reduction* [143–145]. In the next section, we will describe the three-dimensional EFT that can be constructed by incorporating the dynamics of static gauge fields only.

3.3.1 Electrostatic QCD

Due to the fact that we identified the relevant degrees of freedom as three-dimensional gauge fields, it is crucial to notice that the temporal and spatial components of A_μ transform differently under a gauge transformation $\Omega(\boldsymbol{x})$, which will now also be time-independent:

$$A_k(\boldsymbol{x}) \longrightarrow \Omega(\boldsymbol{x}) A_k(\boldsymbol{x}) \Omega^\dagger(\boldsymbol{x}) + \frac{i}{g} \Omega(\boldsymbol{x}) \partial_k \Omega^\dagger(\boldsymbol{x}), \tag{3.3.2}$$

$$A_0(\boldsymbol{x}) \longrightarrow \Omega(\boldsymbol{x}) A_0(\boldsymbol{x}) \Omega^\dagger(\boldsymbol{x}), \tag{3.3.3}$$

which tell us that while the spatial component of the gauge field still transforms as a vector field, A_0 now behaves as a scalar field in the adjoint representation of SU(3). This implies for instance that a mass term for A_0 is not forbidden by gauge invariance and can be included in the EFT action. The resulting dimensionally reduced theory is defined by the most general action that can be built from the identified degrees of freedom respecting the symmetries of QCD, yielding the

Electrostatic QCD (EQCD) action:[4]

$$\mathcal{S}_{\text{EQCD}} = \int d^3\boldsymbol{x} \left\{ \frac{1}{2} \operatorname{Tr}\left[F_{ij}F_{ij}\right] + \operatorname{Tr}\left[(D_jA_0)(D_jA_0)\right] + m_{\text{E}}^2 \operatorname{Tr}\left[A_0^2\right] \right\} + \dots, \tag{3.3.4}$$

where the dots represent the inclusion of higher-dimensional operators, and the three dimensional field strength is defined as usual in terms of the covariant derivative D_i:

$$F_{ij}(\boldsymbol{x}) \equiv \frac{i}{g_{\text{E}}}\left[D_i, D_j\right], \qquad D_i = \partial_i - ig_{\text{E}}A_i(\boldsymbol{x}). \tag{3.3.5}$$

The constants g_{E} and m_{E} are low-energy constants of the EFT that have to be matched to QCD, requiring that the two theories yield the same predicitions in the domain where the EQCD can be applied. The matching procedure determines the relation between the low energy constants and the parameters of QCD (the coupling g, the temperature T, the number of color N_c and of quark flavors N_f). The matching of g_{E} has been carried in perturbation theory to 2-loop order [146], and to leading order it reads

$$g_{\text{E}}^2 = g^2T + \mathcal{O}\left(g^4T\right), \tag{3.3.6}$$

whereas the matching of m_{E} is known to three-loops [147] and to leading order it holds

$$m_{\text{E}}^2 = g^2T^2\left(\frac{N_c}{3} + \frac{N_f}{6}\right) + \mathcal{O}\left(g^4T^2\right). \tag{3.3.7}$$

It is worth noticing that the matching of the effective theory to full QCD can in principle be performed non-perturbatively way throguh lattice simulations of both theories. From the EQCD action, we see that the A_0 field is characterized by a typical scale $m_E \sim gT$, whereas the dynamics of the spatial gauge field A_k involves a dimensionful scale $g_{\text{E}} \sim g^2T$. The effective description obtained by integrating out non-static modes is justified if they are actually much heavier than the dynamical static ones. Therefore, the following hierarchy between the relevant scales must hold in order for the EFT to be valid:

$$\frac{g^2T}{\pi} \ll gT \ll \pi T, \tag{3.3.8}$$

which holds at asymptotically high temperatures since QCD becomes weakly coupled. Aside from the *hard* scale πT which has been integrated out, it is useful to

[4]The fields appearing the EFT action are *not* the same fields of full QCD; with a slight abuse of notation, we will denote them with the same symbol, and the ambiguity can be resolved from the context. Moreover, we will adopt a convention more suitable for perturbative calculations, absorbing the gauge coupling in front of the Yang-Mills action through the rescaling of the fields $A_\mu \to gA_\mu$.

further separate the *soft* scale gT characterizing A_0 and the *ultrasoft* scale g^2T of spatial gauge fields. Observables computed in EQCD can be expanded in a weak coupling series that, due to the soft scale being of order gT, can now contain terms with odd powers of the QCD coupling constant; crucially, the contributions from EQCD can be computed in perturbation theory.

3.3.2 Magnetostatic QCD

EQCD is valid at distances much larger than $1/(gT)$, or equivalently at energies much lower than gT. If one is interested in dynamics at even larger distances (lower energies), also the A_0 field can be regarded as heavy with respect to the spatial gauge fields A_k, and can be integrated out from the EQCD action. The remaining theory involves the dynamics of static chromomagnetic gluons only, and for this reason is denoted as *Magnetostatic QCD* (MQCD), whose action reads

$$\mathcal{S}_{\text{MQCD}} = \int \mathrm{d}^3\boldsymbol{x} \, \left\{ \frac{1}{2} \operatorname{Tr}\left[F_{ij}F_{ij}\right] \right\} \, + \, \ldots , \tag{3.3.9}$$

where again the dots represent the inclusion of higher-dimensional operators. As noted earlier, the theory inherently contains a single dimensionful scale g^2T, which implies that all other dimensionful quantities, such as the string tension or the mass gap, must be proportional to it. Since MQCD is a three dimensional confining non-abelian gauge theory with a mass gap of order g^2T, it has to be solved non-perturbatively. Observables computed in this theory admit a small coupling expansion in g^2, but the coefficients of this series can not be computed in perturbation theory. This fact implies that, for any given observable, the perturbative expansion cannot be performed to arbitrarily high order in g, because contributions coming purely from ultrasoft gluons will generate terms of finite order in the expansion that must be computed non-perturbatively. This is the statement of the infamous *infrared problem* of thermal non-abelian plasmas [148], which fundamentally limits the applicability of perturbation theory in high temperature QCD. A relevant example is given by the pressure of QCD, which can be computed in perturbation theory only up to order g^6, after which non-perturbative terms begin contributing [149]. To conclude this section, two remarks are in order:

(a) the infrared problem concerns chromo-magnetic gauge fields specifically. Indeed, also the chromo-electric field A_0 develops a typical scale, which is however of order gT and thus does not spoil the applicability of pertubration theory (although it leads to the appearance of odd powers of g in the perturbative series, which is another typical feature of thermal QFT). This is the QCD analogue of Debye screening of electric fields in QED [150];

(b) the infrared problem is a feature of non-abelian gauge theories: indeed, in QED magnetic fields are not screened and continue to be massless giving rise to long distance forces.

3.3.3 Non-relativistic quark action

As anticipated, at high temperature quarks behave as heavy fields due to their non-zero Matsubara frequency. The lightest quark modes correspond to the $n = 0$ and $n = -1$ sectors, with frequency $\omega = \pm\pi T$ respectively. Due to their large mass, if one is interested in fermionic quantities such as hadron correlators, the dynamics of these fermionic three-dimensional modes can be included in the effective theory in a non-relativistic treatment [151–153]. The Non-Relativistic QCD (NRQCD) action for the $n = 0$ and $n = -1$ modes of a single quark flavor reads[5] (see appendix E.1 for notation and the derivation)

$$\begin{aligned}\mathcal{S}_{\text{NRQCD}} = i\int \mathrm{d}^3\boldsymbol{x} \sum_{n=0,-1} \Bigg\{ &\bar{\psi}_n^{\uparrow}\left[M_n - g_{\text{E}}A_0 + D_3 - \frac{1}{2\omega_n}\left(D_\perp^2 + \frac{g_{\text{E}}}{4i}\left[\sigma_j,\sigma_k\right]F_{jk}\right)\right]\psi_n^{\uparrow} \\ &+\bar{\psi}_n^{\downarrow}\left[M_n - g_{\text{E}}A_0 - D_3 - \frac{1}{2\omega_n}\left(D_\perp^2 + \frac{g_{\text{E}}}{4i}\left[\sigma_j,\sigma_k\right]F_{jk}\right)\right]\psi_n^{\downarrow}\Bigg\} + \ldots,\end{aligned} \tag{3.3.10}$$

where M_n is a low energy constant which is equal to the fermionic Matsubara frequency ω_n tree level, while at one loop the matching to QCD yields [154]

$$M_0 = -M_{-1} = \pi T\left(1 + \frac{g^2\left(N_c^2-1\right)}{16\pi^2 N_c} + \mathcal{O}\left(g^4\right)\right). \tag{3.3.11}$$

The fields $\psi^{\uparrow}$ and $\psi^{\downarrow}$ are Weyl spinors defined in equation (E.1.2) which, due to the relative sign between the mass and kinetic term, propagate forwards and backwards respectively in the x_3 direction for the $n = 0$ sector, and vice-versa for the $n = -1$ sector. The shorthand notation $\perp$ was introduced to indicate coordinates transverse to the third direction, i.e. $\boldsymbol{x}_\perp = (x_1, x_2)$. Correlation functions in NRQCD admit a series expansion in powers of g, starting at order g^2, with coefficients that can be computed in perturbation theory.

The resulting three-dimensional effective field theory incorporating the relevant static bosonic and degrees of freedom and the lightest fermionic modes for the computation of hadron correlators, often referred to as QCD_3, is defined by the action $\mathcal{S}_{\text{QCD}_3} = \mathcal{S}_{\text{EQCD}} + \mathcal{S}_{\text{NRQCD}}$. We thus see how the dimensionally reduced effective field theory construction allows to isolate the contributions to a given observable coming from the different relevant scales in the theory, and separate those that

[5] Throughout this thesis, the third spatial direction will be selected as the screening direction.

field / operator	power counting
$\psi^{\uparrow}$, $\psi^{\downarrow}$	m_{E}
∂_3	g_{E}^2
$D_{\perp}^2$	m_{E}^2
d^2x	$g_{\mathrm{E}}^{-2}m_{\mathrm{E}}^{-2}$

TABLE 3.1: Power counting for various terms in the fermionic action 3.3.10.

can be computed perturbatively (the hard and soft ones) from those that have to be computed non-perturbatively (the ultra-soft ones). Although the dynamics at the ultra-soft scale has to be solved through lattice simulations, the purely bosonic three dimensional theory is significantly less expensive than the full four dimensional theory with fermions, and very precise results can thus be obtained. In table 3.1 we establish the power-counting rules forf relevant fields and operators in the action.

Flavor symmetry of high temperature QCD

The matching coefficient M in the NRQCD action (3.3.10) highlights the fact that at high temperatures the quark masses are effectively replaced by the Matsubara frequencies; this means that the heavy quarks are essentially mass degenerate and the fermion action is invariant under separate $\mathrm{SU}(N_f)$ transformations of the χ and ϕ fields. Moreover, up to the spin-dependent term proportional to $[\sigma_i, \sigma_j]\, F_{ij}$ - which has mass dimension 2 and is of order $g_{\mathrm{E}}^4 \sim g^4T^2$ - the action is also invariant under $\mathrm{SU}(2)_{\mathrm{spin}}$ transformations for each of the two dimensional spinors. In regimes where the aformentioned spin-dependent term is negligible, the resulting symmetry group is thus enlarged to $\mathrm{SU}(2N_f)$.

3.4 Screening masses

Spatial correlations in a medium at thermal equilibrium encode important information about the structure and dynamics of the underlying degrees of freedom, and they can be studied from the behaviour of correlation functions of fields measured along spatial rather than temporal direction. It is useful to project the two point function of a given interpolating field O to definite Matsubara frequency ω_n

$$C_O^{(n)}(x_3) = \int_0^{L_0} \mathrm{d}x_0 \exp\{i\omega_n x_0\} \int \mathrm{d}^3\boldsymbol{x}\ \left\langle O(x)O^{\dagger}(0)\right\rangle \tag{3.4.1}$$

obtaining a so-called *screening* correlator. While the behavior of the correlator at large Euclidean times is determined by the mass of the lightest state with O's

quantum numbers, the exponential decay of a screening correlator at large spatial distances is governed by the correlation length $\xi_O^{(n)}$ related to O's quantum numbers and the Matsubara frequency ω_n:

$$C_O^{(n)}(x_3) \propto \exp\left\{-x_3/\xi_O^{(n)}\right\}(1+\mathcal{O}(-\Delta x_3)) \tag{3.4.2}$$

where the factor Δ contains the contributions from the next shorter correlation length ξ' in the same channel: $\Delta = (\xi')^{-1} - \left(\xi_O^{(n)}\right)^{-1}$. The correlation length measures the typical length scale over which strong interactions related to the presence of a particle carrying O's quantum numbers are screened in the thermal medium. It is customary to define the *screening mass* as the inverse correlation length,

$$m_O^{(n)} \equiv 1/\xi_O^{(n)}, . \tag{3.4.3}$$

which, from equation (3.4.2), can be extracted from the large distance behavior of the correlator as

$$m_O^{(n)} = -\lim_{x_3\to\infty}\frac{\mathrm{d}}{\mathrm{d}x_3}\ln C_O^{(n)}(x_3). \tag{3.4.4}$$

Screening masses depend in a non-trivial way on the temperature of the system: at zero temperature, which corresponds to sending $L_0 \to \infty$, SO(4) symmetry is restored, and there is no difference between measuring a correlator along a spatial rather than the Euclidean temporal direction, meaning that the screening mass equals the lightest pole (physical) mass of a particle with O's quantum numbers – that is, if O couples to a QCD-stable one-particle state. In the opposite limit of infinte temperature, due to asymptotic freedom screening masses approach the value they assume in a non-interacting theory: specifically, since the lightest quark modes have frequency πT, at asymptotically high temperatures the lowest screening mass of a meson will be equal to $2\pi T$, while that of a baryon to $3\pi T$. Studying how screening masses evolve with temperature is then an ideal way to probe how thermal effects modify hadronic excitations and, as will be discussed in sections 3.4.1 and 3.4.3, to study the relevant symmetries of the thermal medium. Moreover, as we will see, since they can be computed both on the lattice and in the weak coupling expansion of QCD_3, they are ideal probes to investigate the relevance of non-perturbative contributions in high-temperature QCD.

Aside from their significance as inverse correlation lengths, screening masses can be interpreted as actual masses in two ways. On one hand, one can regard the spatial screening direction as the imaginary Euclidean time, and x_0 as a compact spatial direction; in this sense, screening masses in thermal QCD correspond to physical pole masses in a zero-temperature theory with one temporal and two spatial directions plus an additional compact spatial direction[6]. On the other hand,

[6]The situation is similar to the appearance of a tower of massive Kaluza-Klein modes due to the compactification of extra dimensions, for instance in some realizations of string theory.

screening masses in QCD correspond to pole masses in the three-dimensional effective theory described in section 3.3, where once again the screening direction plays the role of time in addition to two spatial directions.

3.4.1 Chiral symmetry of screening correlators

In section 1.5 a collection of Ward identites related to different sectors of the chiral symmetry group have been derived, and their impact on the properties of the hadron spectrum was discussed. The role played by the chiral condensate $\langle\bar{\psi}\psi\rangle$ in the spontaneous breaking of chiral symmetry was emphasized, particularly in the non-singlet axial transfromations. It is straightforward to show that the WTIs hold also at finite temperature, i.e. when a compact Euclidean time extent is considered: while the values of individual correlators may differ from those at zero-temeprature, the identities between correlators continue to be valid. As was argued in the previous sections, the non-zero value of the chiral condensate in the vacuum decreases steeply with temperature around the crossover point T_{pc}, and it effectively vanishes above said temperature signaling the restoration of chiral symmetry. Under these conditions, the WTI's described in section 1.5.1 and lead to non-trivial equalities between correlators (in the following the chiral limit $M = 0$ will be assumed).

Non-singlet axial WTI

We start by considering the non-singlet axial WTI (1.5.31) with the insertion of the following interpolating operator ($y \neq z$)

$$O = A^b_\mu(y)V^c_\nu(z), \tag{3.4.5}$$

whose variation under an infinitesimal axial non-singlet rotation is

$$\delta O = \epsilon^d_A \left[f^{dba} V^a_\mu(y)V^c_\nu(z) + f^{dca} A^b_\mu(y)A^a_\nu(z) \right]. \tag{3.4.6}$$

When the expectation value is taken in the WTI, the only non-zero contributions come from the two point functions of V and A with the same flavor index ($a = c$ and $a = b$ respectively). Specifying $\mu = \nu$, this leads to ($x \neq y \neq z$)

$$-i\epsilon^a_A \partial^x_\mu \left\langle A^a_\mu(x)A^b_\nu(y)V^c_\nu(z) \right\rangle \;=\; \epsilon^d_A f^{dbc} \left[\langle V^c_\nu(y)V^c_\nu(z)\rangle - \left\langle A^b_\nu(y)A^b_\nu(z) \right\rangle \right], \tag{3.4.7}$$

where no summation on b, c or ν is intended. In section 1.5.2 the conservation of the non-singlet axial current was shown to be related to the spontaneous breaking of chiral symmetry via the chiral condensate. In the vacuum, this implies that the l.h.s. of equation (3.4.7) is not zero, even in the chiral limit, while it vanishes

above the pseudocritical temperautre since chiral symmetry is restored and the chiral condensate goes to zero. Therefore the following equality holds in high temperature QCD:

$$\langle V_\nu^c(y)V_\nu^c(z)\rangle \;=\; \left\langle A_\nu^b(y)A_\nu^b(z)\right\rangle, \tag{3.4.8}$$

which is valid for all c and b, and again no summation is assumed. Since the two correlators become equal, one of the consequences of this identity is that if chiral symmetry is restored the screening masses in these two channels become degenerate.
Investigating the same WTI with interpolating field

$$O = P^b(y)S^0(y) \tag{3.4.9}$$

reveals the degeneracy of the flavor singlet scalar screening mass with the flavor non-singlet pseudoscalar. The l.h.s. of the WTI vanishes by the same token as above, while now the variation of the operator reads

$$\delta O = i\epsilon_A^a\bar{\psi}(y)\left\{d^{abc}T^c + \frac{\delta^{ab}}{N_f}\right\}\psi(y)S^0(z) + 2i\epsilon_A^a P^b(y)P^a(z); \tag{3.4.10}$$

the expectation value of the first term vanishes since it is proportional to $\mathrm{Tr}[T^c]$, while in the third term the only contribution arises from $a = b$. The resulting identity relates the non-singlet pseudoscalar correlator to the singlet scalar one,

$$2\left\langle P^a(y)P^a(z)\right\rangle \;=\; -\frac{1}{N_f}\left\langle S^0(y)S^0(z)\right\rangle, \tag{3.4.11}$$

which again implies the degeneracy of the related screening masses. Starting from the field

$$O = S^a(y)P^0(z)$$

and following nearly identical steps leads to

$$2\left\langle S^a(y)S^a(z)\right\rangle = -\frac{1}{N_f}\left\langle P^0(y)P^0(z)\right\rangle \tag{3.4.12}$$

signaling that non-singlet scalar and singlet pseudoscalar screening masses are equal.
Flavor non-singlet axial transformation are also relevant for the baryonic sector of the theory. While equation (2.5.17) provides the simplest expression for an inteprolating operator with nucleon quantum numbers, it has no definite parity eigenvalue. A parity sector can be selected in the operator and the two point function (2.5.18) through parity projectors; at zero temperature the correlator is measured along the time direction, and thus the relevant projectors are

$P_{0,\pm} \equiv (\mathbb{1} \pm \gamma_0)/2$, while when measuring a screening correlator the relevant sectors are identified by "x_3-parity", with projectors defined through the natural modification $P_{3,\pm} \equiv (\mathbb{1} \pm \gamma_3)/2$. A valid baryonic screening correlator with definite parity is therefore given by

$$C_{N^\pm}(x_3) \;=\; \int_0^{L_0} \mathrm{d}x_0 e^{i\omega_n x_0} \int \mathrm{d}^3\boldsymbol{x}\;\; \mathrm{Tr}\left[P_{3,\pm} N(x)\bar{N}(0)\right],$$

where ω_n is a fermionic Matsubara frequency. Consider the specific axial non-singlet transformation $\Omega = \exp\{i\epsilon_A^3 \sigma_3\gamma_5\}$ involving only u and d fields:

$$\begin{aligned} &\delta u = i\epsilon_A^3\gamma_5 u, && \delta d = -i\epsilon_A^3\gamma_5 d \\ &\qquad\qquad \Downarrow \\ &\delta N = -i\epsilon_A^3\gamma_5 N, && \delta\bar{N} = -i\epsilon_A^3\bar{N}\gamma_5. \end{aligned} \tag{3.4.13}$$

The corresponding variation of the interpolating field

$$O = i\,\mathrm{Tr}\left[\gamma_5 P_{3,\pm} N(y)\bar{N}(z)\right] \tag{3.4.14}$$

reads

$$\delta O = \epsilon_A^3 \left\{\mathrm{Tr}\left[P_{3,\pm} N(y)\bar{N}(z)\right] + \mathrm{Tr}\left[P_{3,\mp} N(y)\bar{N}(z)\right]\right\}; \tag{3.4.15}$$

once again, if chiral symmetry is not spontaneously broken the expectation value of the above field vanishes, which in turn implies that the correlators of opposite parity nucleons are equal up to an overall sign, and their screening masses are thus degenerate.

Singlet axial WTI

Additional and useful relations can be derived by considering the anomalous WTI (1.5.56). Considering the field

$$O = P^a(y)S^a(z) \tag{3.4.16}$$

and its variation under an anomalous singlet transformation (1.5.14)

$$\delta O = 2i\epsilon_A S^a(y)S^a(z) + 2i\epsilon_A P^a(y)P^a(z), \tag{3.4.17}$$

the integrated version of (1.5.56) becomes

$$\langle P^a(y)P^a(z)\rangle + \langle S^a(y)S^a(z)\rangle = N_f \langle Q P^a(y)S^a(z)\rangle \tag{3.4.18}$$

where the topological charge Q appears due to the spacetime integration. We thus see that in this case the degeneracy of scalar and pseudoscalar non-singlet screening

masses is related to the topology of QCD. At zero temperature, as was shown in section 1.5.3, transitions between different topological sectors are relevant and can not be ignored. In contrast, at temperatures above the pseudocritical one, thermal fluctuations highly suppress the presence of non-trivial topological sectors $Q \neq 0$, with the dilute instanton gas approximation (DIGA) predicting a suppression of the topological susceptibility χ with a high power of temperature ($\chi \sim T^{-b} m^3$ with $b \sim 8$ for three flavors of light quarks with mass m) and non perturbative lattice simulations confirming this both in the pure gauge theory [155] and in the theory with fermions [156, 157]. With this considerations, at high temperature the r.h.s of equation (3.4.18) becomes negligible, leading to the degeneracy of screening masses also in the pseudoscalar and scalar flavor non-signlet channels.

The degeneracy pattern of screening correlators at high temperature is contained

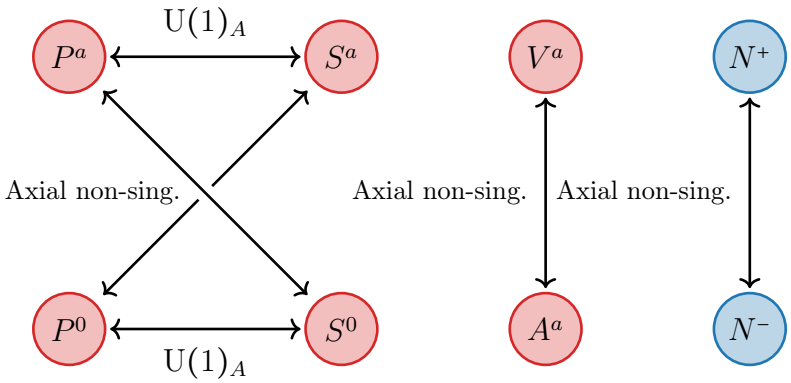

FIGURE 3.5: Degeneracy pattern of mesonic (red) and nucleon (blue) states under singlet and non-singlet axial transformations, both expected to be restored symmetries of QCD at high temperature.

in the diagram 3.5. Notice that partners in the high temperature chiral multiplets have widely different masses at zero temperature: for instance, the N^+ operator overlaps with the nucleon state with a mass of $\sim$ 940 MeV, while the negative parity N^- couples to an excited with a significantly larger mass of $\sim$ 1500 MeV. For this reason, studying how the screening masses of states belonging to the same chiral multiplet evolve with the temperature is an ideal way to test the restoration of chiral symmetry in thermal QCD – with regards to both the spontaneously broken axial non-singlet generators and the anomalous U(1)$_A$.

Hadronic screening masses have been extensively studied in the literature over the last three decades, both analytically through perturbation theory in QCD$_3$ and from non-perturbative lattice simulations[7]. In the following sections we provide an

[7]For completeness, we point out that determinations from Dyson-Schwinger based approaches

Sector	Channel	Screening mass
$n = 0$	$P^a,\ V_T^a$	$2\pi T\left(1 + g^2\, 0.032739\ldots\right)$
	V_0^a	$2\pi T\left(1 + g^2\, 0.071877\ldots\right)$
$n = 1$	$P^a,\ V_T^a$	$2\pi T\left(1 + g^2\, 0.074840\ldots\right)$
	V_0^a	$2\pi T\left(1 + g^2\, 0.053347\ldots\right)$
$n = 2$	$P^a,\ V_T^a$	$4\pi T\left(1 + g^2\, 0.028770\ldots\right)$
	V_0^a	$4\pi T\left(1 + g^2\, 0.018821\ldots\right)$

TABLE 3.2: NLO screening masses of flavor non-singlet mesonic channels in different Matsubara sectors, computed in [154, 160]. All expressions are valid up to $\mathcal{O}\big(g^3T\big)$ corrections.

overview of the state of the art – at the time this project started – in pertubative and lattice determinations of mesonic and baryonic screening masses. Emphasis will be given to the sectors and aspects most relevant for the original work that I will present in this thesis.

3.4.2 Perturbative results

At sufficiently high temperatures, the scale hierarchy (3.3.8) is valid and QCD can be described by the dimensionally reduced QCD_3. Screening masses can be expanded in a weak coupling series in g_{E}, where contributions from hard and soft degrees of freedom are computable perturbatively following the construction described in section 3.3. The matching of the EFT low-energy constants to QCD allows to then express screnning masses as a series in the QCD coupling g. Screening masses of flavor non-singlet mesonic states have been computed at next-to-leading order (NLO) [154, 160], and the $\mathcal{O}(g^2T)$ correction to the free theory value turns out to be perturbative. Table 3.2 summarizes the NLO screening masses in the flavor non-singlet pseudoscalar, transverse ($V_T \equiv V_k, \quad k = 1, 2$) and temporal ($V_0$) vector channels, for Matsubara sectors $n = 0, 1, 2$ in the theory with $N_f = 3$ massless quarks. Notice that the free theory limit of screening masses in the static and

are also present in the literature [158, 159].

$n = 1$ sectors is $2\pi T$, while for $n > 1$ it is given by $2\pi nT$. Another key observation is that at this order in the weak coupling expansion the spin-1 and pseudoscalar states (V_T^a and P^a) have the same screening mass, and spin-dependent corrections start at higher orders. The leading order expression for the difference between the V_T^a and P^a screening mass - the *hyperfine splitting* - had not been computed in perturbation theory prior to the start of this project. Its calculation in [1] is one of the main achievements of this thesis, and it will be described in detail in section 4.2. Similarly, the NLO correction to baryonic screening masses beyond the tree level value $3\pi T$ was only estimated qualitatively with variational methods [161], and the full computation carried in [3] is another achievement of this thesis presented in section 4.1.

3.4.3 Lattice results

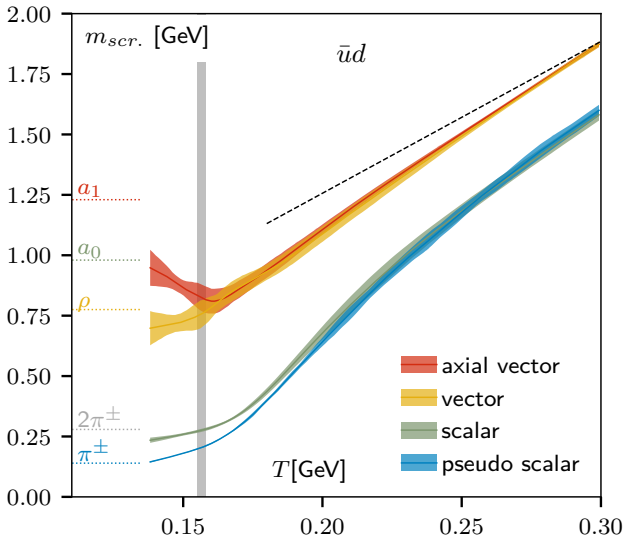

FIGURE 3.6: From [162]: continuum limit of mesonic screening masses in different channels across the chiral crossover (gray band). The zero-temperature pole masses are reported on the left side of the plot, and the dashed line represents the free theory limit $2\pi T$. Results come from lattice simulations with $N_f = 2 + 1$ flavors of quarks at the physical point.

Mesonic screening masses have been extensively studied on the lattice [160, 163–165]. Continuum-extrapolated results for the static sector in several channels for temperatures around and above the crossover [162] have detailed how screening masses start from the pole mass value at low temperature, fall into chiral multiplets

above $T_{\rm pc}$ (with multiplets related to the restoration of $\mathrm{U}(1)_A$ also appearing at higher temperatures) and begin to approach the free theory limit $2\pi T$, up to temperatures of about ~ 300 MeV, see figure 3.6. Non-static mesonic screening masses have also been investigated since the correlators from which they are extracted can be related to the photon or dilepton emission rates of the quark gluon plasma, see [160, 166–168]. On the other hand, significantly less was known about the baryonic sector, with no continuum extrapolated results neither for the quenched case [169, 170] nor for the theory with dynamical quarks [171]; nevertheless, parity doubling of nucleon states as expected from equation (3.4.15) due to chiral symmetry restoration was observed.
Until recently, lattice simulations at finite temperature were restricted to temperatures below ~ 1 GeV, essentially due to the difficulties of accomodating an hadronic scale typically used to calibrate the lattice and a much higher temperature, as described in section 2.3.2. Building on the knowledge developed to non-perturbatively renormalize QCD over a wide range of energies, in [54] a strategy to study thermal QCD at temperatures ranging from ~ 1 GeV up to ~ 165 GeV was developed, and first applied to the computation of static mesonic screening masses. The studies carried during this Ph.D. are a direct continuation of this exploration of high-temperature QCD; the most relevant findings of [54] will be summarized in the next section.

3.5 Thermal QCD up to the Electroweak scale

As was argued in the previous sections, the study of thermal QCD for temperatures up to about 300 MeV is relevant to understand the chiral crossover and for the physics of heavy ion collision. However, investigating the theory at higher temperatures is motivated by the interest in probing the state of matter that was present at earlier times in the primordial Universe; moreover, the further temperature is increased the better the EFT described in section 3.3 is expected to reproduce QCD. A detailed study of thermal QCD at very high temperatures is therefore also of great formal interest from a theoretical point of view. Given the eventual appearance of the infrared problem, the validity of the effective theory can only be assessed by a comparison with non-perturbative lattice results, and reaching very high temperatures $T \gg T_{\rm pc}$ on the lattice is thus crucial. Having access to lattice data at high temperature then allows to investigate in detail the convergence of the weak coupling series, and to assess the presence and relevance of non-perturbative contributions. The key elements of the strategy that allowed to reach Electroweak scale-temperatures non-perturbatively will be reviewed; for a full discussion see section 4 of [54].

3.5.1 Shifted boundary conditions

In section 3.2 it was shown how equilibrium properties of thermal QCD can be formally obtiained by considering the theory defined with a compact Euclidean time direction, in which periodic boundary conditions eqs. (3.2.4) to (3.2.6) are imposed and the temperature is given by the inverse temporal extend $T = 1/L_0$. An equivalent description of thermal field theories can be achieved by requiring that fields statisfy *shifted* boundary conditions [172–174],

$$U_\mu(x_0 + L_0, \boldsymbol{x}) = U_\mu(x_0, \boldsymbol{x} - L_0\boldsymbol{\xi}) \tag{3.5.1}$$
$$\psi(x_0 + L_0, \boldsymbol{x}) = -\psi(x_0, \boldsymbol{x} - L_0\boldsymbol{\xi}) \tag{3.5.2}$$
$$\bar{\psi}(x_0 + L_0, \boldsymbol{x}) = -\bar{\psi}(x_0, \boldsymbol{x} - L_0\boldsymbol{\xi}), \tag{3.5.3}$$

with the introduction of the three-dimensional shift vector $\boldsymbol{\xi}$. The above conditions can be seen as the description of a system with usual periodic boundary conditions from a relativistic moving frame. In this picture, the shift vector is the imaginary velocity of the moving frame. In this thesis we will always choose the shift in the x_1-direction $\boldsymbol{\xi} = (\xi, 0, 0)$; with this choice, shifted boundary conditions only mix the x_0 and x_1 components, and the relation between the primed coordinates in the moving frame and the unprimed ones is given by a usual Euclidean Lorentz boost

$$\begin{cases} x_0' = (x_0 + \xi x_1)\,\gamma \\ x_1' = (x_1 - \xi x_0)\,\gamma \\ x_2' = x_2 \\ x_3' = x_3 \end{cases} \tag{3.5.4}$$

with the Euclidean Lorentz γ factor given by $\gamma = 1/\sqrt{1+\xi^2}$. The system is thus periodic in the x_0' coordinate with a dilated temporal extent $L_0' = L_0/\gamma$, which in turn means that the relation between the temperature of the system T and the extend L_0 of Euclidean time is modified to

$$T = \frac{1}{L_0'} = \frac{\gamma}{L_0}; \tag{3.5.5}$$

for the particular value $\boldsymbol{\xi} = (1, 0, 0)$, which will be the one considered in this thesis, the relation between T and L_0 is thus $T = 1/\sqrt{2}L_0$. Matsubara frequencies are therefore rescaled by a factor of γ when expressed in terms of L_0:

$$\omega_n = \begin{cases} 2\pi n T = \dfrac{2\pi\gamma}{L_0} n & \text{for Bosons,} \\ \pi T\,(2n+1) = \dfrac{\pi\gamma}{L_0}\,(2n+1) & \text{for Fermions,} \end{cases} \tag{3.5.6}$$

and momentum projection phases in correlation functions are modified accordingly:

$$\frac{\pi}{L_0}\bar{n}x_0 \to \frac{\pi}{L_0'}\bar{n}x_0' = \frac{\pi}{L_0}\bar{n}\gamma^2\left(x_0 + \xi x_1\right) \tag{3.5.7}$$

where $\bar{n}$ is either $2n$ or $2n+1$ for bosons or fermions respectively.
Shifted boundary conditions are not strictly necessary for the computation of screening masses[8]; they have however proved instrumental in the computation of thermodynamic quantities relevant for the equation of state without the need for zero-temperature subtractions both in pure Yang-Mills theory [90, 175] and very recently also in $N_f = 3$ QCD [176, 177], and they offer a convenient and powerful framework to carry out the non-perturbative renormalization of composite operators [178, 179]. We have employed shifted boundary conditions because the aforementioned studies and this project have utilized the very same gauge field configurations in order to share the computational cost of generating them.

3.5.2 Lines of constant physics

Temperature values much higher than typical hadronic scales have been reached thanks to the strategy outlined in section 2.3.2 and in appendix C.3. In particular, the theory is renormalized by imposing that a non-perturbative definition of the renormalized coupling assumes its continuum value at fixed lattice spacing. The relevant schemes for this thesis' work are the Schrödinger Functional (SF) coupling $\bar{g}^2_{\mathrm{SF}}$ [180] and the Gradient Flow (GF) coupling $\bar{g}^2_{\mathrm{GF}}$ [181, 182]. The renormalization conditions thus read

$$\bar{g}^2_{\mathrm{X}}\left(g_0^2, a\mu\right) = \bar{g}^2_{\mathrm{X}}\left(\mu\right) \quad \text{for} \quad a\mu \ll 1 \tag{3.5.8}$$

where X indicates either scheme. In these schemes the renormalization scale μ is related to the finite extent of the lattice L^4, in particular

$$\mu = \begin{cases} 1/L & \text{Schrödinger Functional,} \\ 2/L & \text{Gradient Flow.} \end{cases} \tag{3.5.9}$$

Equation (3.5.8) fixes the lines of constant physics, i.e. the dependence of the lattice spacing a on the bare coupling g_0 (or viceversa). The non-perturbative running of the renormalized couplings defined above has been determined over a wide range of energies up to ~ 100 GeV [52, 53, 182, 183] and the overall physical scale has been set by matching the Gradient Flow coupling to an hadronic scale at low temperatures [14]. In a lattice simulation the temperature is provided by

[8] Although, milder discretization effects have been empirically observed in the presence of shifted rather than periodic boundary conditions

the finite extent of the temporal direction compared to the larger spatial ones, i.e. considering a lattice geometry $L_0 \times L^3$ with $L/L_0 \gg 1$. Our choice is then to renormalize the theory at a scale μ proportional to the temperature of the system, which given the previous considerations opens the way to study thermal QCD on the lattice up to the Electroweak scale. Taking into account the modification due to shifted boundary conditions for $\boldsymbol{\xi} = (1, 0, 0)$, the relation between the temperature of the system and the renormalization scale is

$$T = \frac{1}{\sqrt{2}L_0} = \begin{cases} \dfrac{\mu}{\sqrt{2}} & \text{SF} \\ \sqrt{2}\mu & \text{GF} \end{cases} \tag{3.5.10}$$

Table 3.3 summarizes the values of the renormalized coupling in the continuum used to set the lines of constant physics and the corresponding temperature values considered in this thesis.
Once the lattice scale has been set through the renormalized coupling, the value of the bare quark mass for the three degenerate flavors is determined by imposing that the PCAC mass of equation (1.5.36) measured on the lattice in a finite volume vanishes. This strategy, which builds on the knowledge developed for the renormalization of QCD over a wide energy range [52, 53, 182, 183], allows to simulate lattice QCD with $N_f = 3$ $\mathcal{O}(a)$–improved Wilson fermions in the chiral limit with a moderate computational cost for temperatures spanning two orders of magnitude from 1 GeV up to 165 GeV.

3.5.3 Mesonic screening masses

Employing the strategy outlined above, in [54] it was possible for the first time to study thermal QCD with dynamical fermions up to temperatures of 165 GeV from non-perturbative lattice simulations. The study focused on the screening masses of static mesons in the flavor non singlet pseudoscalar (P) and transverse vector (V) channels, together with their scalar (S) and axial vector (A) partners under chiral symmetry. They were determined with a precision of the permille over the whole temperature range. Aside from confirming the restoration of chiral symmetry through the observation of the degeneracy pattern reported in figure 3.5, figure 3.7 highlights two of the most interesting features found in the spectrum. For one, at such high temperatures a comparison with the NLO perturbative prediction is justified: to this end, the lattice data is analysed as a function of the 2-loop coupling in the $\overline{\text{MS}}$ scheme renormalized at a scale $\mu = 2\pi T$

$$\hat{g}^2(T) \equiv \left[\frac{9}{8\pi^2} \ln \frac{2\pi T}{\Lambda_{\overline{\text{MS}}}} + \frac{4}{9\pi^2} \ln \left(2 \ln \frac{2\pi T}{\Lambda_{\overline{\text{MS}}}} \right) \right]^{-1}, \tag{3.5.11}$$

label	T[GeV]	$\overline{g}^2_{\rm SF}(\mu)$
T_0	165(6)	1.01636
T_1	82.3(2.8)	1.11000
T_2	51.4(1.7)	1.18446
T_3	32.8(1.0)	1.26569
T_4	20.6(6)	1.3627
T_5	12.8(4)	1.4808
T_6	8.03(22)	1.6173
T_7	4.91(13)	1.7943
T_8	3.04(8)	2.0120
		$\overline{g}^2_{\rm GF}(\mu)$
T_9	2.83(7)	2.7359
T_{10}	1.82(4)	3.2029
T_{11}	1.167(23)	3.8643

TABLE 3.3: Name, value in physical units and corresponding renormalized coupling of the 12 temperatures considered in this thesis.

where for N_f = 3, $\Lambda_{\overline{\rm MS}}$ = 341MeV has been determined non-perturbatively [14]. It is important to stress that this is just a convenient choice to study the temperature dependence of the non-perturbative lattice data, which is suggested by the effective theory analysis, and that allows for a comparison bewteen the lattice determination and the known perturbative terms of the weak coupling series. The non-perturbative data is compatible with the NLO behaviour only at asymptotically high temperatures, and displays a clear non-monotonic temperature dependence in the explored range which requires the inclusion of higher powers of g in the weak coupling series to be quantitatively explained. Perhaps even more striking is the fact that the screening masses in the two channels are non-degenerate up to the highest temperature explored, contrary to what was expected from the perturbative analysis at order g^2 reported in table 3.2. When investigated as a function of g^4 the data shows a distinct linear behavior, so much so that it can be explained by a single parameter fit - a linear function in g^4 passing through the origin - over the whole temperature range, within the reported statistical precision. This suggested that the hyperfine splitting is of order $g^4_{\rm E}$ in the weak coupling series, and in turn motivated the effort to compute this quantity in $\rm QCD_3$, since no prediction from the effective theory analysis was available when the lattice data were published.

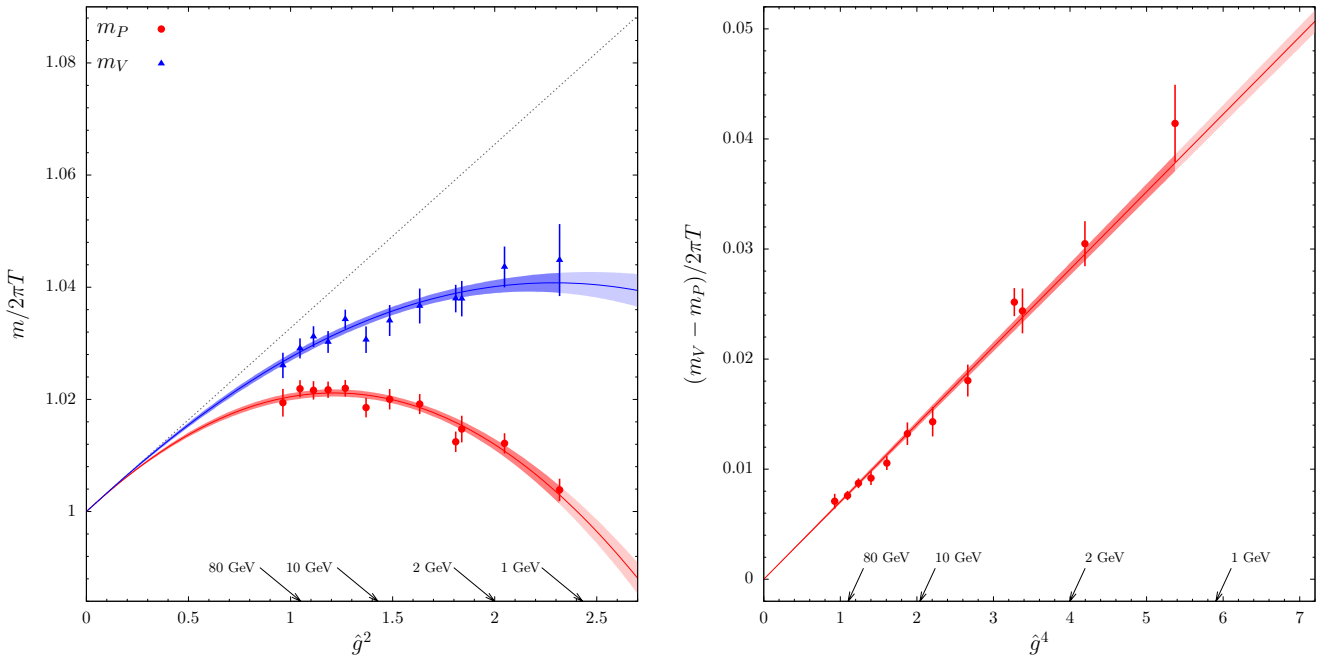

FIGURE 3.7: From [54]: **Left** Static pseudoscalar (red) and transverse vector (blue) screening masses normalized by the free theory (infinite temperature) value $2\pi T$. The dotted line is the NLO perturbative prediction, and the colored bands are fits to the lattice data. **Right** Splitting between the transverse vector and pseudoscalar screening mass. The red band is a linear fit in $\hat{g}^4$ passing through 0. All data are extrapolated to the continuum.

In the remaining chapters, which contain the original results obtained during my Ph.D., I will present a direct continuation of the work summarized in the previous sections on screening masses in thermal QCD for temperatures ranging from ~ 1 GeV up to ~ 165 GeV, employing both perturbative methods in the effective field theory setting and non-perturbative lattice simulations. More specifically, I will summarize the first non-perturbative determination of baryonic screening masses in the aforementioned temperature range from contiuum-extrapolated lattice results [2], complemented by the first complete NLO computation in the effective theory [3]. I will then focus on the non-static mesonic screening masses presenting soon-to-be-published results for the $n = 1$ sector, which required the use of variance reduction techniques to surpass a signal-to-noise-ratio problem [184]. In turn, this allowed to re-compute static mesonic screening masses with increased precision and in more channels compared to the original work [54], and in particular resulted in a determination of the hyperfine splitting about one order

of magnitude more precise than the one reported in [54]. At this level of precision, a single g^4 term is not enough to explain the non-perturbative data, further motivating the first perturbative computation of the leading spin-dependent term in static mesonic screening masses [1], which combined with the new data allowed a stringent test of the validity of the pertubative expansion and the presence of non-perturbative contributions in the high temperature regime of QCD.

Chapter 4

Perturbative computations in QCD_3

This chapter collects two of the main original contributions of this thesis, involving perturbative studies of screening masses in the three-dimensional effective field theory that describes QCD at high temperatures. In section 4.1 we describe the first computation of the $\mathcal{O}(g_{\mathrm{E}}^2) = \mathcal{O}(g^2T)$ correction to the free-theory value $3\pi T$ for baryonic screening masses, which is based on results published in [3]. Next, section 4.2 reports the computation of the leading spin-dependent correction to static mesonic screening masses, which results in an $\mathcal{O}(g^4T)$ difference between the screening masses extracted from correlators of flavor non-singlet transverse vector and pseudoscalar densities, published in [1]. The determination of these previously unknown quantities will be instrumental to interpret the non-perturbative lattice results collected in chapter 5.

4.1 Baryonic screening mass at NLO

In this section we focus on the baryonic sector of the theory by considering an interpolating operator that carries the nucleon quantum numbers. We stress once again that we work in a theory with mass degenerate – massless – quarks, and therefore there is no distiction between proton and neutron as far as QCD is concerned. For definiteness, we select a neutron state, i.e. with two d and one u valence quarks. Maybe the simplest interpolating field is (we consider $N_{\mathrm{c}} = 3$ colours throughout)

$$N_\alpha = \epsilon^{abc}\big(u^{a\mathrm{T}} C\gamma_5 d^b\big) d^c_\alpha\,, \qquad \overline{N}_\alpha = \epsilon^{feg}\big(\bar{d}^f C\gamma_5 \bar{u}^{g\mathrm{T}}\big)\bar{d}^e_\alpha\,, \tag{4.1.1}$$

where a, b, c are colour indices and C is the charge-conjugation matrix, defined in equation (A.2.8). The contraction with the totally anti-symmetric symbol ϵ^{abc} guarantees that the field is in the singlet representation of SU(3), i.e. gauge in-

variant. The two-point correlation functions we set to study are

$$\mathcal{C}_{\pm}(x_3) \equiv \int_0^{1/T} \mathrm{d}x_0\, e^{-i\omega_0 x_0} \int_{\mathbf{r}} \mathrm{Tr}\left\langle N(x_0,x)\overline{N}(0)P_{\pm}\right\rangle, \quad x \equiv (\mathbf{r},x_3), \tag{4.1.2}$$

where $\omega_0 = \pi T$ is the lowest positive fermionic Matsubara frequency, arising due to anti-periodic boundary conditions in the temporal direction, $P_{\pm} = (1 \pm \gamma_3)/2$ is the x_3-parity projector, the trace is over Dirac space, and $\int_{\mathbf{r}} \equiv \int \mathrm{d}^2\mathbf{r}$ denotes an integration over the transverse spatial directions.

The corresponding screening masses, characterizing the long-distance exponential fall-off of the correlators, are defined according to eq. (3.4.4) as

$$m_{\pm} \equiv -\lim_{x_3\to\infty} \frac{\mathrm{d}}{\mathrm{d}x_3} \ln\left[\mathcal{C}_{\pm}(x_3)\right]. \tag{4.1.3}$$

As pointed out in section 3.4.1, due to the spontaneous breaking of chiral symmetry, the positive (N, $\mathcal{C}_+$) and the negative (N^*, $\mathcal{C}_-$) parity partners have masses which differ by several hundreds of MeV in the vacuum. On the contrary, at high temperatures, owing to chiral symmetry restoration, the screening masses associated with the parity partners are expected to become degenerate (for numerical evidence, see refs. [185, 186]).

4.1.1 Relevant Matsubara sectors

Our aim is to compute the correlator (4.1.2) at next-to-leading order in the effective field theory QCD$_3$. As it was noted is section 3.3.3, in this construction only the $n = 0, -1$ Matsubara modes of quarks contribute the dynamics; moreover, as we will now show, depending on the interpolating field in consideration only a subset of the Weyl spinors $\psi_n^{\uparrow}$, $\psi_n^{\downarrow}$ will contribute to the forward-propagating two-point function. Projected to the lowest fermionc Matsubara frequency, the nucleon field can be expressend in terms of the Weyl spinors as

$$\begin{aligned}\int \mathrm{d}x_0\; e^{-i\pi T x_0} N(x) = \sum_{n,m,l} \delta\left(k_n + k_m + k_l - \pi T\right) \times \\ \left[u_n^{\uparrow \mathrm{T}}(x)\sigma_2 d_m^{\downarrow}(x) + u_n^{\downarrow \mathrm{T}}(x)\sigma_2 d_m^{\uparrow}(x)\right] \begin{pmatrix} d_l^{\uparrow}(x) \\ d_l^{\downarrow}(x) \end{pmatrix},\end{aligned} \tag{4.1.4}$$

where the integers n, m, l identify the quarks' Matsubara frequencies ω_n, ω_m and ω_l, which sum to the overall nucleon frequency πT as imposed by the Dirac delta. By recalling that the fields which propagate forwards in the third spatial direction are $\psi_0^{\uparrow}$ and $\psi_{-1}^{\downarrow}$, only two combinations in (4.1.4) wil contribute to the forward-propagating correlator in (4.1.2), namely

$$\begin{aligned}\left[u_{-1}^{\downarrow \mathrm{T}}(x)\; \sigma_2\; d_0^{\uparrow}(x)\right]\; d_0^{\uparrow}(x), \\ \left[u_0^{\uparrow \mathrm{T}}(x)\; \sigma_2\; d_{-1}^{\downarrow}(x)\right]\; d_0^{\uparrow}(x).\end{aligned} \tag{4.1.5}$$

For this reason, in the rest of this section we will only consider these forward propagating fields in the NRQCD dynamics; dubbing for compactness $\psi_0^{\uparrow} \equiv \chi$ and $\psi_{-1}^{\downarrow} \equiv \phi$ for each flavor, the NRQCD action can be written as

$$\begin{aligned} S_{\mathrm{NRQCD}} = i \sum_{f=u,d,s} \int \mathrm{d}^3x \Bigg\{ & \bar{\chi}_f(x) \left[M - g_{\mathrm{E}} A_0 + D_3 - \frac{\nabla_\perp^2}{2\pi T} \right] \chi_f(x) \\ & - \bar{\phi}_f(x) \left[M + g_{\mathrm{E}} A_0 + D_3 - \frac{\nabla_\perp^2}{2\pi T} \right] \phi_f(x) \Bigg\} + O\left(\frac{g_{\mathrm{E}}^2}{\pi T} \right), \end{aligned} \tag{4.1.6}$$

where f is a flavour index, and according to the power-counting rules, we neglect higher-dimensional operators such as the spin dependent term since we are interested in corrections up to order g_{E}^2. In section 4.2 we will also include this term in the action, since the quantity that we will compute – the hyperfine spin splitting in static mesonic screening masses – is of order $\mathcal{O}(g^4)$.

4.1.2 Equations of motion

From the effective action in eq. (4.1.6) and an infinitesimal transformation of path-integration variables, it is straightforward to see that the three-dimensional fields χ and ϕ for each flavour[1] satisfy for a generic interpolating operator $O(y)$ the equations of motion

$$i \left\langle \left[M - g_{\mathrm{E}} A_0 + D_3 - \frac{\nabla_\perp^2}{2\pi T} \right] \chi(x)\, O(y) \right\rangle = \left\langle \frac{\delta O(y)}{\delta \bar{\chi}(x)} \right\rangle , \tag{4.1.7}$$

$$i \left\langle \left[M + g_{\mathrm{E}} A_0 + D_3 - \frac{\nabla_\perp^2}{2\pi T} \right] \phi(x)\, O(y) \right\rangle = - \left\langle \frac{\delta O(y)}{\delta \bar{\phi}(x)} \right\rangle , \tag{4.1.8}$$

where the derivatives act on the x coordinates. Analogous equations hold for $\bar{\chi}$ and $\bar{\phi}$. The propagators of χ and ϕ are defined as

$$S_\chi(x) \equiv \langle \chi(x)\, \bar{\chi}(0) \rangle_f , \qquad S_\phi(x) \equiv \left\langle \phi(x)\, \bar{\phi}(0) \right\rangle_f , \tag{4.1.9}$$

where in eq. (4.1.9) the expectation value $\langle \cdot \rangle_f$ indicates the path integral over fermions only. Then by choosing $O = \bar{\chi}$, $\bar{\phi}$ at $y = 0$ in eqs. (4.1.7) and (4.1.8), respectively, the fermion propagators satisfy the equations

$$\left\langle \left[M + \partial_3 - \frac{\nabla_\perp^2}{2\pi T} \right] S_\chi(x) \right\rangle = g_{\mathrm{E}} \left\langle \Big[i A_3(x) + A_0(x) \Big] S_\chi(x) \right\rangle - i \mathbb{1} \delta^{(3)}(x) , \tag{4.1.10}$$

$$\left\langle \left[M + \partial_3 - \frac{\nabla_\perp^2}{2\pi T} \right] S_\phi(x) \right\rangle = g_{\mathrm{E}} \left\langle \Big[i A_3(x) - A_0(x) \Big] S_\phi(x) \right\rangle + i \mathbb{1} \delta^{(3)}(x) , \tag{4.1.11}$$

[1] The flavour index is omitted unless it is necessary for the clarity of presentation.

where $\mathbb{1}$ stands for the identity in spinor and colour indices. Since the fermions had been integrated out, the expectation values in eqs. (4.1.10) and (4.1.11) indicate the path integral over the gauge fields. Note that these equations are valid also without integrating over the gauge fields, i.e. for a fixed gauge field background, and that at this order the fermion propagators are diagonal in flavour and spin.

4.1.3 Perturbation theory

The free fermion action is obtained by setting $g_{\rm E} = 0$ in eq. (4.1.6). The corresponding equations of motion are readily worked out from eqs. (4.1.10) and (4.1.11). The free propagators can be written as (the coordinate-space expression is given in eq. (E.2.1))

$$S_\chi^{(0)}(\mathbf{r}, x_3) = -i\theta(x_3)\mathbb{1}\int_{\mathbf{p}} e^{i\mathbf{p}\cdot\mathbf{r}}\, e^{-x_3\left(M+\frac{\mathbf{p}^2}{2\pi T}\right)}\,, \tag{4.1.12}$$

$$S_\phi^{(0)}(\mathbf{r}, x_3) = -\,S_\chi^{(0)}(\mathbf{r}, x_3)\,, \tag{4.1.13}$$

where $\int_{\mathbf{p}} \equiv \int \mathrm{d}^2\mathbf{p}/(2\pi)^2$. At next-to-leading order in $g_{\rm E}$, we can define

$$S_\chi(\mathbf{r}, x_3) = S_\chi^{(0)}(\mathbf{r}, x_3) + g_{\rm E}\, S_\chi^{(1)}(\mathbf{r}, x_3) + O(g_{\rm E}^2)\,, \tag{4.1.14}$$

and analogously for $S_\phi(\mathbf{r}, x_3)$. By solving eqs. (4.1.10) and (4.1.11) and approximating the transverse movement (cf. appendix E.2), we obtain

$$S_\chi^{(1)}(\mathbf{r}, x_3) \simeq \int_0^{x_3} \mathrm{d}z_3 \big[iA_3 + A_0\big]\Big(\frac{z_3}{x_3}\mathbf{r}, z_3\Big)\, S_\chi^{(0)}(\mathbf{r}, x_3)\,, \tag{4.1.15}$$

$$S_\phi^{(1)}(\mathbf{r}, x_3) \simeq \int_0^{x_3} \mathrm{d}z_3 \big[iA_3 - A_0\big]\Big(\frac{z_3}{x_3}\mathbf{r}, z_3\Big)\, S_\phi^{(0)}(\mathbf{r}, x_3)\,. \tag{4.1.16}$$

4.1.4 Baryonic correlators in the effective theory

The effective-theory expression for the baryonic interpolating operator from eq. (4.1.1) is readily obtained by using the definitions in appendix E.1. After taking the Fourier transform in the time direction, we may restrict to the contributions that involve the lowest Matsubara modes propagating in the positive x_3-direction. This implies that N is represented by two χ fields and one ϕ field. Furthermore, by displacing the fundamental fields in the transverse direction, i.e. by introducing a point-splitting, the Fourier transform in the compact direction of the baryonic interpolating operator leads to

$$\begin{aligned} N(\mathbf{r}_1, \mathbf{r}_2, \mathbf{r}_3; x_3) &\to \epsilon^{abc}\big[\,\chi_u^{aT}(\mathbf{r}_1, x_3)\,\sigma_2\,\phi_d^b(\mathbf{r}_2, x_3) + \phi_u^{aT}(\mathbf{r}_1, x_3)\,\sigma_2\,\chi_d^b(\mathbf{r}_2, x_3)\,\big]\,\chi_{d,\alpha}^c(\mathbf{r}_3, x_3)\,, \\ \overline{N}(0) &\to \epsilon^{feg}\big[\,\bar\phi_d^f(0)\,\sigma_2\,\bar\chi_u^{gT}(0) + \bar\chi_d^f(0)\,\sigma_2\,\bar\phi_u^{gT}(0)\,\big]\,\bar\chi_{d,\alpha}^e(0)\,, \end{aligned} \tag{4.1.17}$$

where α is a two-component spinor index. To avoid clutter, we have omitted overall factors $T^{3/2}$ from both operators, originating from the normalization of fermionic Matsubara modes, however they are restored in eq. (4.1.20). The two-point correlators from eq. (4.1.2) are defined in the effective theory as

$$\mathcal{C}_{\pm}(x_3) \;=\; \int_{\mathbf{r}} \mathcal{C}_{\pm}(\mathbf{r},\mathbf{r},\mathbf{r};x_3)\,, \tag{4.1.18}$$

$$\mathcal{C}_{\pm}(\mathbf{r}_1,\mathbf{r}_2,\mathbf{r}_3;x_3) \;\equiv\; \frac{1}{T}\,\mathrm{Tr}\left\langle N(\mathbf{r}_1,\mathbf{r}_2,\mathbf{r}_3;x_3)\overline{N}(0)P_{\pm}\right\rangle\,, \tag{4.1.19}$$

where $1/T$ comes from $\int_0^{1/T}\mathrm{d}x_0$, and $P_{\pm} = (\mathbb{1}\pm\gamma_3)/2$. We have used the same symbols as in QCD, given that the ambiguity can be resolved from the context.

We remark that, as long as $\mathbf{r}_i \neq \mathbf{r}_j$, neither the interpolating operator above eq. (4.1.17) nor the correlation function in eq. (4.1.19) is gauge invariant under gauge transformations involving the transverse coordinates. Gauge invariance could be restored by contracting the point-split operator with transverse Wilson lines. However, such transverse Wilson lines play no rôle in the calculation of the screening masses. Indeed, the final result will be gauge independent even without them, as gauge dependence vanishes in the large-separation limit in the longitudinal direction.[2] In order to streamline the presentation, we omit the transverse Wilson lines, and display results only for the Feynman gauge.

By exploiting the antisymmetry of the Levi-Civita symbol, and noting that the propagators are flavour independent, integration over the fermionic fields yields (see equation (C.2.9))

$$\mathcal{C}_{\pm}(\mathbf{r}_1,\mathbf{r}_2,\mathbf{r}_3;x_3) = \mp T^2\left\langle\, 2W(\mathbf{r}_1,\mathbf{r}_2,\mathbf{r}_3;x_3) + 3W(\mathbf{r}_2,\mathbf{r}_1,\mathbf{r}_3;x_3)\,\right\rangle, \tag{4.1.20}$$

where the Wick contraction is defined as

$$W(\mathbf{r}_1,\mathbf{r}_2,\mathbf{r}_3;x_3) \;\equiv\; -i\,\epsilon^{abc}\epsilon^{gfe}\,S_{\chi}^{ag}(\mathbf{r}_1,x_3)\,S_{\phi}^{bf}(\mathbf{r}_2,x_3)S_{\chi}^{ce}(\mathbf{r}_3,x_3)\,. \tag{4.1.21}$$

Equation (4.1.20) implies that our $\mathcal{C}_{\pm}$ is a sum of two independent correlation functions. This is a consequence of the fact that the action in (4.1.6) displays "emergent" global symmetries, with the numbers of χ and ϕ-particles separately conserved. Given that the two correlators in (4.1.20) differ just by a permutation of coordinates, and that in the end all coordinates are set equal (cf. eq. (4.1.18)), the two correlators yield the same baryonic screening mass. This degeneracy could be broken by higher-dimensional operators in the effective theory [151], leading to a "fine structure" of the screening spectrum, but this is an effect of higher order than our $O(g^2T)$.

[2]The technical reason is that we need the component Δ_{33} of the gauge propagator, cf. eq. (E.3.4), but the third component of the momentum is zero, cf. eq. (E.3.6), so only the transverse part plays a rôle.

Free limit

By inserting the free propagators from eqs. (4.1.12) and (4.1.13) into eq. (4.1.21), we see that

$$W^{(0)}(\mathbf{r}_1,\mathbf{r}_2,\mathbf{r}_3;x_3) = -6\,\theta(x_3)\int_{\mathbf{p}_1,\mathbf{p}_2,\mathbf{p}_3} e^{i(\mathbf{p}_1\cdot\mathbf{r}_1+\mathbf{p}_2\cdot\mathbf{r}_2+\mathbf{p}_3\cdot\mathbf{r}_3)}e^{-x_3\left(3M+\frac{\mathbf{p}_1^2}{2\pi T}+\frac{\mathbf{p}_2^2}{2\pi T}+\frac{\mathbf{p}_3^2}{2\pi T}\right)}\,. \tag{4.1.22}$$

From here it follows that $W^{(0)}$ satisfies a (2+1)-dimensional Schrödinger equation,

$$\left[3M+\partial_3-\sum_{i=1}^{3}\frac{\nabla^2_{\mathbf{r_i}}}{2\pi T}\right]W^{(0)}(\mathbf{r}_1,\mathbf{r}_2,\mathbf{r}_3;x_3)\overset{x_3>0}{=}0\,. \tag{4.1.23}$$

Thus, if quarks have small transverse momentum (indeed we will see that parametrically $\nabla^2_{\mathbf{r_i}}\sim m_{\rm E}^2\sim g^2T^2$), the exponential falloff is dominated by $3M=3\pi T+O(g^2)$, which then represents the leading contribution to the baryonic screening masses $m_\pm$.

Next-to-leading order

To date, the only estimate of $O(g^2)$ corrections to a baryonic screening mass in the high temperature regime of QCD is qualitative [161], with no IR resummation performed. Here the full $O(g^2)$ correction is derived in the same way as for the mesonic case [154], demonstrating in particular its IR finiteness up to this order in the weak-coupling expansion.

The equation of motion for W in the interacting case is readily worked out from eqs. (4.1.10) and (4.1.11), and it reads

$$\begin{aligned}\left[3M+\partial_3-\sum_{i=1}^{3}\frac{\nabla^2_{\mathbf{r_i}}}{2\pi T}\right]\big\langle W(r_1,r_2,r_3)\big\rangle &\overset{x_3>0}{=} -ig_{\rm E}\epsilon^{abc}\epsilon^{gfe}\Big\langle\Big[(iA_3+A_0)S_\chi\Big]^{ag}(r_1)S_\phi^{bf}(r_2)S_\chi^{ce}(r_3)\\ &+S_\chi^{ag}(r_1)\Big[(iA_3-A_0)S_\phi\Big]^{bf}(r_2)S_\chi^{ce}(r_3)+S_\chi^{ag}(r_1)S_\phi^{bf}(r_2)\Big[(iA_3+A_0)S_\chi\Big]^{ce}(r_3)\Big\rangle,\end{aligned} \tag{4.1.24}$$

where we have introduced $r_i\equiv(\mathbf{r}_i,x_3)$ to simplify the notation. Inserting S_χ and S_ϕ from eqs. (4.1.15) and (4.1.16), respectively, and performing the gluon contractions (cf. appendix E.3 for the gluon propagator and further details on intermediate steps), we get

$$\left[3M+\partial_3-\sum_{i=1}^{3}\frac{\nabla^2_{\mathbf{r_i}}}{2\pi T}\right]\big\langle W(r_1,r_2,r_3)\big\rangle\overset{x_3>0}{=}-\mathcal{U}(r_1,r_2,r_3)\,W^{(0)}(r_1,r_2,r_3)+O(g_{\rm E}^3)\,. \tag{4.1.25}$$

Here, with the notation from eq. (E.3.4),

$$\mathcal{U}(r_1,r_2,r_3) = \frac{4g_{\rm E}^2}{3}\Bigg\{ \frac{\mathcal{V}^-(\mathbf{r}_1,\mathbf{r}_2,x_3)+\mathcal{V}^-(\mathbf{r}_2,\mathbf{r}_1,x_3)}{2} + \frac{\mathcal{V}^+(\mathbf{r}_1,\mathbf{r}_3,x_3)+\mathcal{V}^+(\mathbf{r}_3,\mathbf{r}_1,x_3)}{2} + \frac{\mathcal{V}^-(\mathbf{r}_2,\mathbf{r}_3,x_3)+\mathcal{V}^-(\mathbf{r}_3,\mathbf{r}_2,x_3)}{2} - \mathcal{V}^+(\mathbf{r}_1,\mathbf{r}_1,x_3) - \mathcal{V}^+(\mathbf{r}_2,\mathbf{r}_2,x_3) - \mathcal{V}^+(\mathbf{r}_3,\mathbf{r}_3,x_3) \Bigg\}. \tag{4.1.26}$$

To extract the screening masses, we take the limit $x_3 \to \infty$, which leads to

$$U(\mathbf{r}_1,\mathbf{r}_2,\mathbf{r}_3) \;\equiv\; \lim_{x_3\to\infty} \mathcal{U}(r_1,r_2,r_3) = \frac{1}{2}\Big[\, V^-(r_{12}) + V^+(r_{13}) + V^-(r_{23}) \,\Big], \tag{4.1.27}$$

where $r_{ij} \equiv |\mathbf{r}_i - \mathbf{r}_j|$, and $V^\pm$ are the static potentials defined in ref. [160],

$$V^\pm(r) \;\equiv\; \frac{4}{3}\frac{g_{\rm E}^2}{2\pi}\left[\ln\Big(\frac{m_{\rm E} r}{2}\Big) + \gamma_{\rm E} \pm K_0(m_{\rm E} r)\right], \tag{4.1.28}$$

where $\gamma_{\rm E}$ is the Euler-Mascheroni constant and K_0 is a modified Bessel function of the second kind. It is appropriate to stress that according to eq. (4.1.27), the three-body potential receives contributions from two-body interactions only.

Finally, by replacing $W^{(0)} \to \langle W \rangle$ on the right-hand side of eq. (4.1.25), which is justified at $O(g_{\rm E}^2)$ and implements a resummation of potential-like interactions, and taking the already-mentioned limit $x_3 \to \infty$, the equation of motion for the correlator reads

$$\left[\partial_3 - \sum_{i=1}^{3} \frac{\nabla^2_{\mathbf{r_i}}}{2\pi T} + V(\mathbf{r}_1,\mathbf{r}_2,\mathbf{r}_3)\right] \Big\langle\, W(\mathbf{r}_1,\mathbf{r}_2,\mathbf{r}_3;x_3) \,\Big\rangle \;=\; 0 + O(g_{\rm E}^3)\,, \tag{4.1.29}$$

where

$$V(\mathbf{r}_1,\mathbf{r}_2,\mathbf{r}_3) \;\equiv\; 3M + U(\mathbf{r}_1,\mathbf{r}_2,\mathbf{r}_3)\,. \tag{4.1.30}$$

The two contributions in eq. (4.1.20) satisfy the same equation, just with a permutation of coordinates (which in the end are set the same, cf. eq. (4.1.18)). Therefore, the solutions of both equations yield the same screening mass, which is then also the screening mass extracted from $\mathcal{C}_\pm(x_3)$ at $O(g_{\rm E}^2)$.

We end this section by remarking that the potential $U(\mathbf{r}_1,\mathbf{r}_2,\mathbf{r}_3)$ from eq. (4.1.27) is symmetric in the exchange of its first and last coordinate. For the first contribution from eq. (4.1.20), this corresponds to $\mathbf{r}_1 \leftrightarrow \mathbf{r}_3$, which in terms of eq. (4.1.17) is due to an accidental symmetry in the action from the exchange $\chi_u \leftrightarrow \chi_d$. In contrast, for the second contribution from eq. (4.1.20), this corresponds to $\mathbf{r}_2 \leftrightarrow \mathbf{r}_3$, the exchange of two identical χ_d particles.

4.1.5 Schrödinger equation for baryonic correlators

From the discussion in sec. 4.1.4, for large separations in the longitudinal direction, the equation of motion for a generic two-point correlation function related to baryonic interpolating operators (in both parity channels) implies the Schrödinger equation

$$\left[-\frac{\nabla^2_{\mathbf{r}_1} + \nabla^2_{\mathbf{r}_2} + \nabla^2_{\mathbf{r}_3}}{2\pi T} + V(\mathbf{r}_1, \mathbf{r}_2, \mathbf{r}_3) \right] \psi(\mathbf{r}_1, \mathbf{r}_2, \mathbf{r}_3) = E\, \psi(\mathbf{r}_1, \mathbf{r}_2, \mathbf{r}_3) \,, \tag{4.1.31}$$

where the potential is given by eq. (4.1.30). The energy eigenvalue of the ground state yields our screening masses, i.e. $m_{\pm} = \min\{E\} + O(g^3 T)$.

In order to solve the three-body Schrödinger equation, we employ the Jacobi coordinates

$$\begin{aligned} \mathbf{R} &\equiv \frac{\mathbf{r}_1 + \mathbf{r}_2 + \mathbf{r}_3}{3} \,, \\ \boldsymbol{\xi}_1 &\equiv \mathbf{r}_3 - \mathbf{r}_1 \,, \\ \boldsymbol{\xi}_2 &\equiv \frac{2}{\sqrt{3}} \left(\mathbf{r}_2 - \frac{\mathbf{r}_1 + \mathbf{r}_3}{2} \right) = \sqrt{3} \, (\mathbf{r}_2 - \mathbf{R}) \,, \end{aligned} \tag{4.1.32}$$

where $\mathbf{R}$ is the position of the center-of-mass in the transverse plane, $\boldsymbol{\xi}_1$ is the relative separation between two quarks located at $\mathbf{r}_1$ and $\mathbf{r}_3$, while $\boldsymbol{\xi}_2$ describes, up to some numerical factor, the relative separation between the quark in $\mathbf{r}_2$ and the center-of-mass of the other pair. In this sense the set of coordinates $(\boldsymbol{\xi}_1, \boldsymbol{\xi}_2)$ describes the relative separations of the underlying two-body problems. With this change of variables the potential only depends on $\boldsymbol{\xi}_1$ and $\boldsymbol{\xi}_2$, given that

$$\begin{aligned} \mathbf{r}_2 - \mathbf{r}_1 &= \frac{\boldsymbol{\xi}_1 + \sqrt{3}\boldsymbol{\xi}_2}{2} \,, \\ \mathbf{r}_3 - \mathbf{r}_2 &= \frac{\boldsymbol{\xi}_1 - \sqrt{3}\boldsymbol{\xi}_2}{2} \,. \end{aligned} \tag{4.1.33}$$

In this way, the Laplace operator can be separated into the center-of-mass and relative motions. The Schrödinger equation for the relative motion can be written as

$$\left[-\frac{1}{\pi T} \left(\nabla^2_{\boldsymbol{\xi}_1} + \nabla^2_{\boldsymbol{\xi}_2} \right) + V(\boldsymbol{\xi}_1, \boldsymbol{\xi}_2) \right] \psi(\boldsymbol{\xi}_1, \boldsymbol{\xi}_2) = E\, \psi(\boldsymbol{\xi}_1, \boldsymbol{\xi}_2) \,, \tag{4.1.34}$$

where it is understood that the static potential and the wave function are expressed in terms of the new coordinates $\boldsymbol{\xi}_1$ and $\boldsymbol{\xi}_2$.

4.1.6 Numerical solution

In order to find a numerical solution to eq. (4.1.34), it is convenient to define the dimensionless transverse coordinates

$$\hat{\boldsymbol{\xi}}_1 \equiv m_{\mathrm{E}}\boldsymbol{\xi}_1\,, \quad \hat{\boldsymbol{\xi}}_2 \equiv m_{\mathrm{E}}\boldsymbol{\xi}_2\,. \tag{4.1.35}$$

Moreover, we express E in terms of a dimensionless eigenvalue $\hat{E}$, by writing

$$E = 3M + \frac{4}{3}\frac{g^2T}{2\pi}\hat{E} + O(g^3T) \overset{(3.3.11)}{=} 3\pi T + \frac{g^2T}{2\pi}\left(1 + \frac{4\hat{E}}{3}\right) + O(g^3T)\,. \tag{4.1.36}$$

This leads to a Schrödinger equation in terms of dimensionless variables,

$$\left[-\frac{1}{\rho}\left(\nabla^2_{\hat{\boldsymbol{\xi}}_1} + \nabla^2_{\hat{\boldsymbol{\xi}}_2}\right) + \hat{V}(\hat{\boldsymbol{\xi}}_1, \hat{\boldsymbol{\xi}}_2) - \hat{E}\right]\psi(\hat{\boldsymbol{\xi}}_1, \hat{\boldsymbol{\xi}}_2) = 0\,, \tag{4.1.37}$$

where $\hat{V}$ is a rescaled static potential from eqs. (4.1.27) and (4.1.28),

$$\hat{V} \equiv \frac{\hat{V}^-(\hat{r}_{12}) + \hat{V}^+(\hat{r}_{13}) + \hat{V}^-(\hat{r}_{23})}{2}\,, \quad \hat{V}^\pm(\hat{r}) \equiv \ln\frac{\hat{r}}{2} + \gamma_{\mathrm{E}} \pm K_0(\hat{r})\,, \tag{4.1.38}$$

and ρ is a re-parametrization of the dimensionful quantities of the problem [154],

$$\rho \equiv \frac{4}{3}\frac{g^2T}{2\pi}\frac{\pi T}{m_{\mathrm{E}}^2} \overset{N_f=3}{=} \frac{4}{9} + O(g^2)\,. \tag{4.1.39}$$

Equation (4.1.37) can be solved numerically by exploiting a two-dimensional generalization of the so-called hyperspherical harmonics method. It is usually employed for three-dimensional quantum many-body problems, see ref. [187] for an introduction and appendix D of [3] for the application to the case of interest. Here, we instead describe in detail an alternative method – which yields the same final result for $\hat{E}$ and thus the screening mass – based on the direct discretization of the system's Hamiltonian

$$\hat{H} = -\frac{1}{\rho}\left(\nabla^2_{\hat{\boldsymbol{\xi}}_1} + \nabla^2_{\hat{\boldsymbol{\xi}}_2}\right) + \hat{V}\left(\hat{\boldsymbol{\xi}}_1, \hat{\boldsymbol{\xi}}_2\right) \tag{4.1.40}$$

which is diagonalized to obtain its lowest eigenvalue $\hat{E}$. Concretely, we consider the system in a finite volume with characteristic size L (in units of m_{E}) where both relative positions $\hat{\boldsymbol{\xi}}_1$, $\hat{\boldsymbol{\xi}}_2$ assume values in $[-L/2, L/2]$. Following the procedure described in appendix E.7, each component of the position vectors is discretized, taking N evenly spaced values between $-L/2(1-1/N)$ and $L/2(1-1/N)$. The states in the system are described by N^4 vectors in position space, and the Hamiltonian operator is then represented by a $N^4 \times N^4$ matrix, which can be constructed

$am_{\rm E}$	N	$Lm_{\rm E}$	$\hat{E}(N,L)$
0.75	20	15	1.314396
	30	22.5	1.317246
	40	30	1.317253
	50	37.5	1.317253
0.60	20	12	1.290292
	30	18	1.313900
	40	24	1.314176
	50	30	1.314178
0.50	30	15	1.309743
	40	20	1.312495
	50	25	1.312548
	60	30	1.312554
0.45	30	13.5	1.303481
	40	18	1.311575
	50	22.5	1.311844
	60	27.0	1.311850

TABLE 4.1: Results for the lowest eigenvalue keeping the lattice spacing fixed and increasing the volume.

and diagonalized to determine the lowest eigenvalue. The potential term is diagonal in our choice of basis, while an order 5 representation of the second derivative was used to build the Laplacian. Both N and L can be varied to control discretization and finite size effects (due to memory constraints and the fast scaling of the algorithm with the number of points in each direction, in this analysis we consider $20 \leq N \leq 64$). Table 4.1 collects the results for the lowest eigenvalue $\hat{E}(N,L)$ for different values of N and L keeping the lattice spacing $a = L/N$ fixed. In particular, we note that for $Lm_{\rm E} \gtrsim 25$ the results at fixed lattice spacing are compatible up to the fith decimal place; for each value of a, we thus consider the value of $\hat{E}(a,L)$ at the largest volume considered as an estimate of the ground state energy in inifnite volume

$$\hat{E}(a) \equiv \hat{E}(a, L_{\rm max}), \tag{4.1.41}$$

To obtain $\hat{E}$ in the continuum, we have fitted the values $\hat{E}(a)$ with several functional forms to model the dependence on a, considering combinations of discretization effects up to order a^3 or a power-like *ansatz* of the form

$$\hat{E}(a) = \hat{E} + b \cdot a^p. \tag{4.1.42}$$

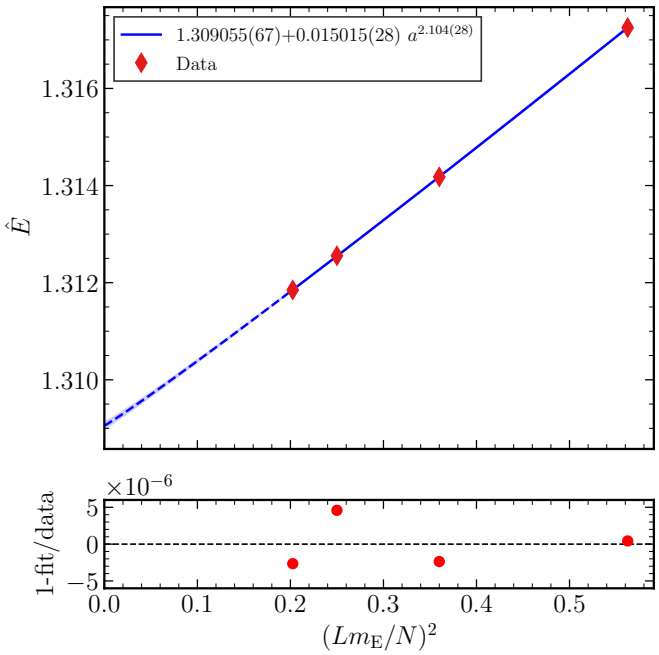

FIGURE 4.1: Top panel: extrapolation of the baryonic ground state energy computed at the largest considered volume at each lattice spacing (red diamonds) to the continuum limit according to the power-law functional form of equation (4.1.42) (blue line). Bottom panel: relative deviation of the fit function from the data.

It turns out that the above functional form with parameters $\hat{E} = 1.30906(7)$, $b = 0.01502(3)$ and $p = 2.10(3)$, yields the smallest squared sum of residuals out of all models considered – with the fit function deviating from the data by a few parts per million, as depicted in the bottom panel of figure 4.1– and reveals an approximately quadratic scaling of the eigenvalue with a. The continuum values of $\hat{E}$ obtained from extrapolations based on a quadratic and/or cubic *ansatz* for discretization effects are nevertheless compatible with the one reported above, as well as with the estimate coming from the hyperspherical harmonics method. Solving the discretized Schrödinger equation on a cartesian mesh grid allows us to visualize the ground state wave-function in position space, as exemplified by figure 4.2. We find that the ground state favors configurations in which the three quarks are aligned and close-by, in line with what one would expect from an s-state.

The final estimate for the ground-state eigenvalue for $N_f = 3$, is therefore

$$\hat{E} = 1.309\ldots . \tag{4.1.43}$$

Inserting eq. (4.1.43) into eq. (4.1.36), leads to our NLO estimate of the baryonic

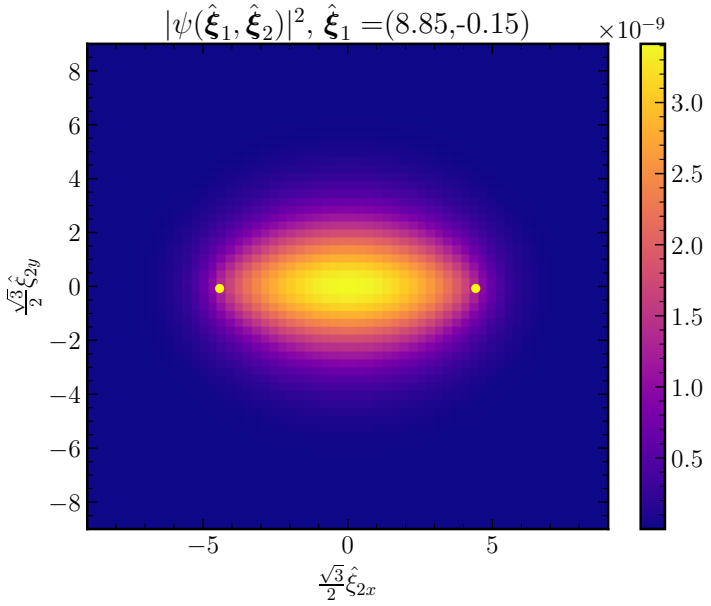

FIGURE 4.2: Ground state probability density for fixed relative position of two quarks in the baryon (yellow dots) as a function of the third quark's position, as obtained by the diagonalization of the discretized Hamiltonian ($Lm_{\mathrm{E}} = 18,\ N = 60$).

screening masses with $N_f = 3$ massless flavors,

$$\min\{E\} \;=\; 3\pi T\left[\,1+\left(\frac{1}{6\pi^2}+\frac{2\hat{E}}{9\pi^2}\right)g^2+O(g^3)\,\right] \;\approx\; 3\pi T\left[\,1+0.046\,g^2+O(g^3)\,\right]. \tag{4.1.44}$$

The NLO term represents a $\sim 4.6\%$ positive correction to the free-theory result $3\pi T$ at the electroweak scale, i.e. $g^2 \approx 1$ [146].

4.2 Hyperfine splitting at LO

In this section we turn our attention on the flavour non-singlet pseudoscalar and vector screening masses at zero Matsubara frequency related to the interpolating fields

$$\mathcal{O}^a(x_0, x) = \overline{\psi}(x_0, x)\Gamma_{\mathcal{O}} T^a \psi(x_0, x)\,, \tag{4.2.1}$$

where $\mathcal{O} = \{P, V\}$, $\Gamma_{\mathcal{O}} = \{\gamma_5, \gamma_2\}$, and we make the definite choice of selecting the component for the vector current in direction 2. The T^a are the $a = 1, \ldots, N_f^2 - 1$ generators of the SU(N_f) algebra, normalized so that $\mathrm{Tr}\left[T^a T^b\right] = \delta^{ab}/2$, which dictate the flavour structure of the interpolating fields. This section collects the results published in [1] on the computation of the leading-order value of the difference between the trasnverse vector screening mass m_V and the pseudoscalar screening mass m_P, i.e. the hyperfine splitting

$$\Delta m_{\mathrm{VP}} = m_{\mathrm{V}} - m_{\mathrm{P}}\,. \tag{4.2.2}$$

The two-point screening correlation functions we consider are

$$\mathcal{C}_{\mathcal{O}}(x_3) = \int_0^{1/T} \mathrm{d}x_0 \int_{\mathbf{R}} \langle \mathcal{O}^a(x_0, x)\mathcal{O}^a(0)\rangle\,, \qquad x = (\mathbf{R}, x_3)\,, \tag{4.2.3}$$

where no summation over the flavour index a is understood. Here $\int_{\mathbf{R}} = \int \mathrm{d}^2\mathbf{R}$ denotes the integration over the transverse spatial directions. Since we are assuming mass-degenerate quarks, the two-point correlation functions above are independent on the flavour structure of the interpolating fields, and therefore we drop the flavour index a on the l.h.s. of eq. (4.2.3). The corresponding screening masses probe the exponential fall-off of the screening correlators at asymptotically large distances, and are defined as

$$m_{\mathcal{O}} = -\lim_{x_3\to\infty} \frac{\mathrm{d}}{\mathrm{d}x_3} \ln\left[\mathcal{C}_{\mathcal{O}}(x_3)\right]\,. \tag{4.2.4}$$

The $O(g^2)$ next-to-leading correction to $m_{\mathcal{O}}$ was computed in the three-dimensional effective theory in Refs. [154, 188], see table 3.2. For three massless quarks, its expression reads

$$m_{\mathcal{O}}^{\mathrm{nlo}} = 2\pi T\left(1 + 0.032740 \cdot g^2\right)\,, \tag{4.2.5}$$

where the first term on the r.h.s. is the free-field theory value, while the second one is due to interactions. Notice that, at $O(g^2)$ the value of the screening mass is independent of the field $\mathcal{O}^a$ defined in eq. (4.2.1), i.e. it is spin-independent. This is because the hyperfine splitting of equation (4.2.2) starts at $O(g^4)$, see below.

4.2.1 Non-relativistic fermionic action

In the following we will consider the NRQCD action including the spin-dependent term (3.3.10); recalling that in the $n = 0$ sector $\psi_0^\uparrow$ and $\psi_0^\downarrow$ propagate forwards and backwards in x_3 respectively, and vice-versa for the $n = -1$ sector, in this computation we adopt a slightly different notation than the one used for the baryonic sector. Motivated *a posteriori* by the fact that both sectors contribute in the same way to the correlators we set to compute, to keep the notation more compact in this section we will focus only on the action of the $n = 0$ fermionic sector. Denoting $\chi \equiv \psi_0^\uparrow$ and, at variance with the previous section, $\phi \equiv \psi_0^\downarrow$, the action for a single quark flavor reads

$$S_{\mathrm{NRQCD}} = i \int \mathrm{d}^3x \left\{ \bar{\chi} \left[M - g_{\mathrm{E}} A_0 + D_3 - \frac{1}{2\pi T} \left(D_\perp^2 + \frac{g_{\mathrm{E}}}{4i} [\sigma_j, \sigma_k] F_{jk} \right) \right] \chi \right. \\ \left. + \bar{\phi} \left[M - g_{\mathrm{E}} A_0 - D_3 - \frac{1}{2\pi T} \left(D_\perp^2 + \frac{g_{\mathrm{E}}}{4i} [\sigma_j, \sigma_k] F_{jk} \right) \right] \phi \right\} + \dots , \tag{4.2.6}$$

where $j, k = 1, 2$. The leading contribution to the hyperfine splitting in the mesonic screening masses is due to the non-diagonal (in spinor indices) term in eq. (4.2.6), and it is due to the exchange of ultrasoft gluons between two quark propagators, whose dynamics is described by the Yang–Mills part of the action in eq. (3.3.4). We stress once again that, according to the power counting rules established in table 3.1 and taking into account that the relevant dimensionful scale is g_{E}^2, it follows that $F_{jk} = O(g_{\mathrm{E}}^3)$. As a consequence, the non-diagonal term (in spinor indices) in eq. (4.2.6) satisfies the power counting rule

$$g_{\mathrm{E}} \left[\sigma_j, \sigma_k \right] F_{jk} = O(g_{\mathrm{E}}^4) , \tag{4.2.7}$$

which translates, by using eq. (3.3.6), into a term of $O(g^4)$. By taking into account the discussion reported in Appendix E.4, the non-relativistic effective action in eq. (4.2.6) can be written in a compact way as

$$S_{\mathrm{NRQCD}} = i \int \mathrm{d}^3x \left[\bar{\chi} \left(\mathcal{D}^+ - g_{\mathrm{E}} \mathcal{K}^+ \right) \chi + \bar{\phi} \left(\mathcal{D}^- - g_{\mathrm{E}} \mathcal{K}^- \right) \phi \right] , \tag{4.2.8}$$

where the differential operators $\mathcal{D}^\pm$ and the interaction vertices $\mathcal{K}^\pm$ are defined in eqs. (E.4.5) and (E.4.6) respectively.

4.2.2 Fermionic equations of motion

Starting from the action in eq. (4.2.8), under infinitesimal transformations of the quark fields, we see that, for each flavour, the χ and ϕ fields satisfy the equations

of motion

$$i\left\langle \left[\mathcal{D}^{+} - g_{\mathrm{E}}\,\mathcal{K}^{+}\right]\chi(y)\,O(z)\right\rangle = \left\langle \frac{\delta O(z)}{\delta\bar{\chi}(y)}\right\rangle \tag{4.2.9}$$

$$i\left\langle \left[\mathcal{D}^{-} - g_{\mathrm{E}}\,\mathcal{K}^{-}\right]\phi(y)\,O(z)\right\rangle = \left\langle \frac{\delta O(z)}{\delta\bar{\phi}(y)}\right\rangle , \tag{4.2.10}$$

for a generic interpolating field $O(z)$, where the differential operators $\mathcal{D}^{\pm}$ act on the y coordinates. Analogous equations hold for $\bar{\chi}$ and $\bar{\phi}$. We are interested in the field propagators of χ and ϕ defined as

$$\mathcal{S}_{+}(x) = S_{\chi}(x,0) = \left\langle \chi(x)\bar{\chi}(0)\right\rangle_{f} , \qquad \mathcal{S}_{-}(x) = S_{\phi}(0,x) = \left\langle \phi(0)\bar{\phi}(x)\right\rangle_{f} , \tag{4.2.11}$$

where $\langle\cdot\rangle_{f}$ refers to the expectation value performed by integrating over the fermionic variables only. By choosing $O(z) = \bar{\chi}(z)$, $y = x$ and $z = 0$ and $O(z) = \bar{\phi}(z)$, $y = 0$ and $z = y$ in eqs. (4.2.9) and (4.2.10) respectively, the propagators satisfy the equations of motion

$$\left\langle \left[\mathcal{D}^{+} - g_{\mathrm{E}}\,\mathcal{K}^{+}\right]\mathcal{S}_{+}(x)\right\rangle = -i\mathbb{1}\delta^{(3)}(x) , \quad \left\langle \left[\mathcal{D}^{+} - g_{\mathrm{E}}\,\mathcal{K}^{-}\right]^{\mathrm{T}}\mathcal{S}_{-}^{\mathrm{T}}(x)\right\rangle = -i\mathbb{1}\delta^{(3)}(x) , \tag{4.2.12}$$

where $\mathbb{1}$ is the identity in spinor and colour indices, and the transpose acts on the same indices. The expectation values in eq. (4.2.12) are meant to be taken over the gauge field only, however such equations are also valid at fixed gauge field background.

Perturbative expansion

By setting $g_{\mathrm{E}} = 0$ in the equations of motion, it straightforward to derive their solutions for the quark propagators at tree-level, which are of course identical to (4.1.12) and (4.1.13) except for a minus sign in front of the ϕ-propagator

$$\mathcal{S}_{\pm}^{(0)}(\mathbf{r},x_3) = -i\theta(x_3)\mathbb{1}\int_{\mathbf{p}} e^{i\mathbf{p}\cdot\mathbf{r}} e^{-x_3\left(M+\frac{\mathbf{p}^2}{2\pi T}\right)} , \tag{4.2.13}$$

where we have shown separately the dependence on the transverse and longitudinal coordinates. At the next-to-leading order, by expanding at $O(g_{\mathrm{E}})$, the quark propagators read

$$\mathcal{S}_{\pm}(\mathbf{r},x_3) = \mathcal{S}_{\pm}^{(0)}(\mathbf{r},x_3) + g_{\mathrm{E}}\mathcal{S}_{\pm}^{(1)}(\mathbf{r},x_3) + \dots , \tag{4.2.14}$$

where

$$\mathcal{S}_{\pm}^{(1)}(\mathbf{r},x_3) = \int_0^{x_3} \mathrm{d}z_3\,\mathcal{K}^{\pm}\Big(\frac{z_3}{x_3}\mathbf{r},z_3\Big)\,\mathcal{S}_{\pm}^{(0)}(\mathbf{r},x_3) , \tag{4.2.15}$$

and, as in the previous section, in eq. (4.2.15) we have safely taken that, since quark fields are very heavy, they propagate along the classical trajectory between $(\mathbf{0},0)$ and $(\mathbf{r},x_3)$. Notice that, at variance with the propagators relevant for the baryonic sector eqs. (4.1.15) and (4.1.16), here the quark propagators at the next-to-leading order are no longer diagonal in Dirac space due to the presence of the non-diagonal term in $\mathcal{K}^{\pm}$.

4.2.3 Mesonic correlators

The expression for the mesonic interpolating fields in the dimensionally reduced effective theory can be promptly derived from eq. (4.2.1) by using the conventions defined in the previous section. Coherently with the choice made for the action, we consider the contributions from the $n = 0$ fermionic Matsubara sector only, and we displace the quark fields in the transverse directions, so that

$$\int_0^{1/T} \mathrm{d}x_0\, \mathcal{O}^a(x_0,x) \to \mathcal{O}^a(\mathbf{r}_1,\mathbf{r}_2;x_3)\,, \tag{4.2.16}$$

and the point-split fields read[3]

$$\mathcal{O}^a(\mathbf{r}_1,\mathbf{r}_2;x_3) = \Big[\bar{\chi}(\mathbf{r}_1,x_3)\,\Sigma_{\mathcal{O}}\,T^a\phi(\mathbf{r}_2,x_3) - \bar{\phi}(\mathbf{r}_1,x_3)\,\Sigma_{\mathcal{O}}\,T^a\chi(\mathbf{r}_2,x_3)\Big]\,, \tag{4.2.17}$$

where from passing from QCD to the effective theory $\Gamma_{\mathcal{O}} = \{\gamma_5,\gamma_2\} \to \Sigma_{\mathcal{O}} = \{\sigma_3,\sigma_1\}$ for pseudoscalar and vector fields respectively. These fields are not gauge invariant for $\mathbf{r}_1 \neq \mathbf{r}_2$. However, as we will see in the following, the results for the screening masses will be gauge independent, as one can easily prove that gauge dependent contributions in their correlation functions vanish in the large x_3 limit. In the effective field theory, the two-point screening correlation functions introduced in eq. (4.2.3) map to

$$\mathcal{C}_{\mathcal{O}}(x_3) = \int_{\mathbf{R}} \mathcal{C}_{\mathcal{O}}(\mathbf{r}_1,\mathbf{r}_2;x_3)\Big|_{\mathbf{r}_1=\mathbf{r}_2=\mathbf{R}} = T\int_{\mathbf{R}} \langle \mathcal{O}^a(\mathbf{r}_1,\mathbf{r}_2;x_3)\mathcal{O}^a(0)\rangle\Big|_{\mathbf{r}_1=\mathbf{r}_2=\mathbf{R}}\,. \tag{4.2.18}$$

When performing the integration over the fermionic variables and taking the Wick contractions, the quark propagators are diagonal in flavour space. As a consequence, by making explicit the flavour indices, the flavour structure simplifies to $\mathrm{Tr}[T^aT^b] = \delta^{ab}/2$. By considering the latter, and the factor 2 which takes into account the contribution from the $n = -1$ Matsubara sector not explicitly indicated in the previous formulas, the general expression for the correlation functions is

$$\mathcal{C}_{\mathcal{O}}(\mathbf{r}_1,\mathbf{r}_2;x_3) = T\left\langle \mathrm{Tr}\left[\Sigma_{\mathcal{O}}\,\mathcal{S}_+(\mathbf{r}_1,x_3)\,\Sigma_{\mathcal{O}}\,\mathcal{S}_-(\mathbf{r}_2,x_3)\right]\right\rangle = T\left\langle W_{\mathcal{O}}(\mathbf{r}_1,\mathbf{r}_2;x_3)\right\rangle \tag{4.2.19}$$

where the trace is over colour and spinor indices.

[3]We use the same symbol for the fields and correlation functions in QCD and in the effective theory since the ambiguity is easily resolved from the context.

Free-theory limit

The expression of the Wick contraction in the free theory is derived by inserting the propagators in eq. (4.2.13) into eq. (4.2.19). By contracting colour and spinor indices, the Wick contraction, independently of the matrix $\Sigma_{\mathcal{O}}$, can be written as

$$\begin{aligned} W_{\mathcal{O}}^{(0)}(\mathbf{r}_1,\mathbf{r}_2;x_3) &= \mathrm{Tr}\left[\mathcal{S}_+^{(0)}(\mathbf{r}_1,x_3)\mathcal{S}_-^{(0)}(\mathbf{r}_2,x_3)\right] \\ &= -2N_c\,\theta(x_3)\int_{\mathbf{p}_1,\mathbf{p}_2} e^{i(\mathbf{p}_1\cdot\mathbf{r}_1+\mathbf{p}_2\cdot\mathbf{r}_2)} e^{-x_3\left(2M+\frac{\mathbf{p}_1^2}{2\pi T}+\frac{\mathbf{p}_2^2}{2\pi T}\right)}, \end{aligned} \tag{4.2.20}$$

and it satisfies the (2+1)-dimensional Schrödinger equation

$$\left[2M+\partial_3-\sum_{i=1,2}\frac{\nabla_{\mathbf{r}_i}^2}{2\pi T}\right] W_{\mathcal{O}}^{(0)}(\mathbf{r}_1,\mathbf{r}_2;x_3) \overset{x_3>0}{=} 0\,. \tag{4.2.21}$$

It follows that, by assuming heavy quarks with small transverse momentum, i.e. longitudinal propagation, the exponential fall-off of $W_{\mathcal{O}}^{(0)}(\mathbf{r}_1,\mathbf{r}_2;x_3)$ is dominated by $2M = 2\pi T + O(g^2)$ which is therefore the leading contribution to both the pseudoscalar and the vector screening masses.

Next-to-leading order

The next-to-leading order spin-independent correction to the flavour non-singlet mesonic screening masses has been computed, in the framework of the dimensionally-reduced effective theory, in Ref. [154], see eq. (4.2.5). Here such calculation is extended in order to obtain the leading spin-dependent correction to the screening masses. Starting from the equations of motion for the quark propagators in eq. (4.2.12), the equation of motion for $\langle W_{\mathcal{O}}\rangle$ in the interacting case reads

$$\begin{aligned} &\left[2M+\partial_3-\sum_{i=1,2}\frac{\nabla_{\mathbf{r}_i}^2}{2\pi T}\right]\Big\langle W_{\mathcal{O}}(\mathbf{r}_1,\mathbf{r}_2;x_3)\Big\rangle \overset{x_3>0}{=} \\ &\qquad \overset{x_3>0}{=} g_{\mathrm{E}}\Bigg\langle \mathrm{Tr}\left\{\Big[\mathcal{A}^+(\mathbf{r}_1,x_3)+\mathcal{A}^-(\mathbf{r}_2,x_3)\Big]\Sigma_{\mathcal{O}}\mathcal{S}_+(\mathbf{r}_1,x_3)\Sigma_{\mathcal{O}}\mathcal{S}_-(\mathbf{r}_2,x_3)\right\} \\ &\qquad\quad -\frac{1}{2\pi T}\,\mathrm{Tr}\left\{\Big[s_{\mathcal{O}}B_3(\mathbf{r}_1,x_3)+B_3(\mathbf{r}_2,x_3)\Big]\sigma_3\,\Sigma_{\mathcal{O}}\mathcal{S}_+(\mathbf{r}_1,x_3)\,\Sigma_{\mathcal{O}}\,\mathcal{S}_-(\mathbf{r}_2,x_3)\right\}\Bigg\rangle. \end{aligned} \tag{4.2.22}$$

where $\mathcal{A}^{\pm}$ is defined in eq. (E.4.2), and we have introduced the notation $s_{\mathcal{O}} = (+1,-1)$ for pseudoscalar and vector respectively, see Appendix E.5. By using

the quark propagators at $O(g_{\rm E})$ in eq. (4.2.14), and by performing the gluon contractions (see Appendix E.5 for further details) we obtain

$$\left[2M+\partial_3-\sum_{i=1,2}\frac{\nabla^2_{\mathbf{r}_i}}{2\pi T}\right]\Big\langle W_{\mathcal{O}}(\mathbf{r}_1,\mathbf{r}_2;x_3)\Big\rangle \overset{x_3>0}{=} -\mathcal{U}(\mathbf{r}_1,\mathbf{r}_2;x_3)\,W^{(0)}_{\mathcal{O}}(\mathbf{r}_1,\mathbf{r}_2;x_3)+O(g_{\rm E}^3)\,, \tag{4.2.23}$$

where the potential is

$$\mathcal{U}(\mathbf{r}_1,\mathbf{r}_2;x_3)=\mathcal{U}_{\rm SI_1}(\mathbf{r}_1,\mathbf{r}_2;x_3)+\mathcal{U}_{\rm SI_2}(\mathbf{r}_1,\mathbf{r}_2;x_3)+\mathcal{U}_{\mathcal{O}}(\mathbf{r}_1,\mathbf{r}_2;x_3)\,, \tag{4.2.24}$$

with

$$\begin{aligned}\mathcal{U}_{\rm SI_1}(\mathbf{r}_1,\mathbf{r}_2;x_3) &= -\frac{g_{\rm E}^2}{N_c}\Big\langle \mathrm{Tr}\Big\{\Big[\mathcal{A}^+(\mathbf{r}_1,x_3)+\mathcal{A}^-(\mathbf{r}_2,x_3)\Big]\times \\ &\qquad \int_0^{x_3}\mathrm{d}z_3\Big[\mathcal{A}^+\Big(\frac{z_3}{x_3}\mathbf{r}_1,z_3\Big)+\mathcal{A}^-\Big(\frac{z_3}{x_3}\mathbf{r}_2,z_3\Big)\Big]\Big\}\Big\rangle\,,\end{aligned} \tag{4.2.25}$$

$$\begin{aligned}\mathcal{U}_{\rm SI_2}(\mathbf{r}_1,\mathbf{r}_2;x_3) &= -\frac{g_{\rm E}^2}{(2\pi T)^2N_c}\times \\ &\qquad \int_0^{x_3}\mathrm{d}z_3\Big\langle \mathrm{Tr}\Big\{B_3(\mathbf{r}_1,x_3)B_3\Big(\frac{z_3}{x_3}\mathbf{r}_1,z_3\Big)+B_3(\mathbf{r}_2,x_3)B_3\Big(\frac{z_3}{x_3}\mathbf{r}_2,z_3\Big)\Big\}\Big\rangle,\end{aligned} \tag{4.2.26}$$

and the chromo-magnetic field B_3 is defined at leading order in eq. (E.4.4). The $\mathcal{U}_{\rm SI_1}$ potential is the one that was obtained in Ref. [154]. The second spin-independent contribution $\mathcal{U}_{\rm SI_2}$ is temperature suppressed. It derives from the exchange of longitudinal ultrasoft gluons along the same quark line. The leading contribution to the spin-dependent potential reads

$$\begin{aligned}\mathcal{U}_{\mathcal{O}}(\mathbf{r}_1,\mathbf{r}_2;x_3) &= -\frac{g_{\rm E}^2 s_{\mathcal{O}}}{(2\pi T)^2N_c}\times \\ &\qquad \int_0^{x_3}\mathrm{d}z_3\Big\langle \mathrm{Tr}\Big\{B_3(\mathbf{r}_1,x_3)B_3\Big(\frac{z_3}{x_3}\mathbf{r}_2,z_3\Big)+B_3(\mathbf{r}_2,x_3)B_3\Big(\frac{z_3}{x_3}\mathbf{r}_1,z_3\Big)\Big\}\Big\rangle\,.\end{aligned} \tag{4.2.27}$$

It is temperature suppressed, and it is due to the exchange of ultrasoft gluons between two quark lines. Since to extract the screening masses we are interested in the large x_3 behaviour of the Wick contractions in eq. (4.2.19), we take the limit $x_3\to\infty$ in eq. (4.2.23) which reads

$$\left[2M+\partial_3-\sum_{i=1,2}\frac{\nabla^2_{\mathbf{r}_i}}{2\pi T}+U(\mathbf{r}_1-\mathbf{r}_2)\right]\Big\langle W_{\mathcal{O}}(\mathbf{r}_1,\mathbf{r}_2;x_3)\Big\rangle = 0+O(g_{\rm E}^3)\,, \tag{4.2.28}$$

where

$$U(\mathbf{r}_1-\mathbf{r}_2)=\lim_{x_3\to\infty}\Big[\mathcal{U}_{\rm SI_1}(\mathbf{r}_1,\mathbf{r}_2;x_3)+\mathcal{U}_{\rm SI_2}(\mathbf{r}_1,\mathbf{r}_2;x_3)+\mathcal{U}_{\mathcal{O}}(\mathbf{r}_1,\mathbf{r}_2;x_3)\Big]\,, \tag{4.2.29}$$

and, at the order we work, we could replace $W^{(0)}_{\mathcal{O}}\to\langle W_{\mathcal{O}}\rangle$.

Spin-independent contribution

The spin-independent contribution $\mathcal{U}_{\mathrm{SI}_2}$ in eq. (4.2.26) is temperature-suppressed with respect to the one in eq. (4.2.25), and it can be neglected when keeping terms up to $O(g_{\mathrm{E}}^2/T)$ only. By taking into account the discussion in Section 4.2.4, this potential would produce subleading contributions in the wave-functions of the screening mass states, and therefore in the hyperfine splitting. Similarly, since we are interested in the leading contribution to eq. (4.2.2) only, we can safely take the expression of the low energy constant M in equation (3.3.7). By taking the large separation limit of the potential in eq. (4.2.25), see Appendix E.6 for the intermediate steps, we obtain for the next-to-leading spin-independent contribution

$$U_{\mathrm{SI}_1}(\mathbf{r}) = \lim_{x_3\to\infty} \mathcal{U}_{\mathrm{SI}_1}(\mathbf{r}_1,\mathbf{r}_2;x_3) = \frac{g_{\mathrm{E}}^2 C_F}{2\pi}\left[\ln\left(\frac{m_{\mathrm{E}} r}{2}\right) + \gamma_{\mathrm{E}} - K_0\left(m_{\mathrm{E}} r\right)\right] \tag{4.2.30}$$

where $\mathbf{r} = \mathbf{r}_1 - \mathbf{r}_2$ and $r = |\mathbf{r}|$, γ_{E} is the Euler-Mascheroni constant and K_0 is a modified Bessel function. Note that the leading logarithmic behaviour on the r.h.s. of eq. (4.2.30) is a confining Coulomb interaction in $2+1$ dimensions. By combining the power counting reported in table 3.1 and standard dimensional analysis arguments, it is possible to see that a string term, i.e. a non-perturbative confining term, arises in the potential at $O(g^3)$. This limits, de facto, the applicability of the perturbative approach for computing the spin-independent potential to the $O(g^2)$.

Spin-dependent contribution

The explicit expression for the spin-dependent static potential $U_{\mathcal{O}}$ in eq. (4.2.27) is carried out analogously, see Appendix E.6 for the intermediate steps and the detailed calculations. By taking the large separation limit in the longitudinal direction, it yields to

$$U_{\mathcal{O}}(\mathbf{r}) = \lim_{x_3\to\infty} \mathcal{U}_{\mathcal{O}}(\mathbf{r}_1,\mathbf{r}_2;x_3) = -g_{\mathrm{E}}^2 \frac{s_{\mathcal{O}} C_F}{(2\pi T)^2}\delta^{(2)}(\mathbf{r})\,. \tag{4.2.31}$$

Notice that, while it provides an interaction which is of the same order in the effective coupling constant g_{E} with respect to the spin-independent potential in eq. (4.2.30), it is however temperature-suppressed.

4.2.4 Hyperfine splitting

As we have seen in the previous section, the equation of motion for the two-point mesonic screening correlator in the three-dimensional effective theory implies the Schrödinger equation in eq. (4.2.28), and the screening mass corresponds to its ground-state energy. Since the spin-dependent potential in eq. (4.2.31) provides a

temperature-suppressed contribution with respect to the leading spin-independent potential in eq. (4.2.30), $U_{\mathcal{O}}(\mathbf{r})$ can be treated as a perturbative correction. We then start by solving the unperturbed Schrödinger equation, which, in the large x_3 limit, reads

$$\left[-\frac{\nabla^2_{\mathbf{r}_1}+\nabla^2_{\mathbf{r}_2}}{2\pi T}+2M+U_{\mathrm{SI}_1}(\mathbf{r}_1-\mathbf{r}_2)\right]\Psi_0(\mathbf{r}_1,\mathbf{r}_2)=E_0\Psi_0(\mathbf{r}_1,\mathbf{r}_2)\,, \tag{4.2.32}$$

where, with Ψ_0 and E_0, we refer to the ground-state energy and wave-function at leading order in perturbation theory[4]. By going to the center-of-mass frame, we define

$$\mathbf{R}=\frac{\mathbf{r}_1+\mathbf{r}_2}{2}\,,\qquad \mathbf{r}=\mathbf{r}_1-\mathbf{r}_2\,, \tag{4.2.33}$$

and the Laplace operator can accordingly be written as

$$\nabla^2_{\mathbf{r}_1}+\nabla^2_{\mathbf{r}_2}=\frac{1}{2}\nabla^2_{\mathbf{R}}+2\nabla^2_{\mathbf{r}}\,, \tag{4.2.34}$$

where the first term on the r.h.s. describes the motion of the center-of-mass, while the second one is the kinetic term related to the relative motion. By restricting to the relative motion only, and by making explicit the functional form of the potential, see eq. (4.2.30), the spin-independent Schrödinger equation reads

$$\left\{-\frac{\nabla^2_{\mathbf{r}}}{\pi T}+2M+g^2_{\mathrm{E}}\frac{C_F}{2\pi}\left[\ln\left(\frac{m_{\mathrm{E}}r}{2}\right)+\gamma_{\mathrm{E}}-K_0(m_{\mathrm{E}}r)\right]-E_0\right\}\psi_0(\mathbf{r})=0\,, \tag{4.2.35}$$

This is exactly the Schrödinger equation obtained in Ref. [154] which leads the next-to-leading order value of the mesonic screening mass in eq. (4.2.5). Once E_0 and the normalized ψ_0 have been determined for the unperturbed Schrödinger equation, the mesonic screening masses at the first order in the spin-dependent perturbative expansion reads

$$E_{\mathcal{O}}=E_0+\int_{\mathbf{r}}U_{\mathcal{O}}(\mathbf{r})\big|\psi_0(\mathbf{r})\big|^2=E_0-g^2_{\mathrm{E}}\frac{s_{\mathcal{O}}C_F}{(2\pi T)^2}\big|\psi_0(\mathbf{0})\big|^2\,. \tag{4.2.36}$$

It is important to notice that, even though the spin-dependent potential is localized in $\mathbf{r}=0$, the hyperfine correction to the screening masses receives contributions from large distances through the normalization of the wave-function, see discussion below.

[4]In this section we omit any label referring to the eigenstates of the Hamiltonian since we are only interested in the ground state of the system.

Leading contribution

The solution of the spin-independent eigenvalue problem for the ground state is found by going to polar coordinates, and by considering the case of vanishing angular momentum. By defining $\hat{\psi}_0(\hat{r}) = \psi_0(\mathbf{r})\sqrt{2\pi}/m_{\rm E}$, where we introduced the dimensionless variable $\hat{r} = m_{\rm E} r$, Eq. (4.2.32) can then be rewritten as

$$\left\{-\left(\frac{\mathrm{d}^2}{\mathrm{d}\hat{r}^2}+\frac{1}{\hat{r}}\frac{\mathrm{d}}{\mathrm{d}\hat{r}}\right)+\rho\left[\ln\left(\frac{\hat{r}}{2}\right)+\gamma_{\rm E}-K_0(\hat{r})-\hat{E}_0\right]\right\}\hat{\psi}_0(\hat{r})=0\,. \tag{4.2.37}$$

Accordingly to Ref. [154], we introduced the parameterization of the effective coupling

$$\rho=\frac{g_{\rm E}^2 C_F T}{2m_{\rm E}^2}=\frac{4}{9}\,, \tag{4.2.38}$$

where in the last step we used $N_f = 3$, $N_c = 3$ and the expressions at leading order for $m_{\rm E}$ and $g_{\rm E}^2$ reported in equations (3.3.6) and (3.3.7). Furthermore we introduced the dimensionless energy eigenvalue [154]

$$\hat{E}_0=\frac{2\pi}{g_{\rm E}^2 C_F}\left(E_0-2M\right)\,. \tag{4.2.39}$$

By doing the same change of variable in the matrix element of the spin-dependent potential and in the normalization of the wave-function, the spin-dependent eigenvalue in eq. (4.2.36) can be written as

$$E_{\mathcal{O}}=E_0-\frac{g_{\rm E}^2 m_{\rm E}^2}{2\pi}\frac{s_{\mathcal{O}} C_F}{(2\pi T)^2}|\hat{\psi}_0(0)|^2\,, \tag{4.2.40}$$

where

$$\int_0^\infty d\hat{r}\,\hat{r}\,|\hat{\psi}_0(\hat{r})|^2=1\,. \tag{4.2.41}$$

By recalling that $s_{\mathcal{O}} = (+1,-1)$ for the pseudoscalar and the vector correlators respectively, and by inserting the expression at leading order for $m_{\rm E}^2$ and $g_{\rm E}^2$, see equations (3.3.6) and (3.3.7), it follows that the hyperfine-splitting in the pseudoscalar and vector energy levels due to spin-dependent interactions at leading order in perturbation theory, cf. eq. (4.2.2), is

$$\frac{\Delta m_{\rm VP}^{\rm lo}}{2\pi T}=g^4\left(\frac{N_c}{3}+\frac{N_f}{6}\right)\frac{C_F}{8\pi^4}|\hat{\psi}_0(0)|^2\,, \tag{4.2.42}$$

where we substituted $E_{\rm P} = m_{\rm P}$ and $E_{\rm V} = m_{\rm V}$ in eq. (4.2.40). The numerical solution for $\hat{\psi}_0$ of the unperturbed Schrödinger equation (4.2.37) gives

$$\frac{\Delta m_{\rm VP}^{\rm lo}}{2\pi T}=0.002376\cdot g^4\,. \tag{4.2.43}$$

This result justifies a posteriori the choice of neglecting $O(g_{\rm E}^2/T^2)$ terms in the spin-independent potential in Section 4.2.3, since it is clear that the inclusion of the potential obtained from eq. (4.2.26) into eq. (4.2.32) would have produced higher order effects in the spin-splitting between the pseudoscalar and the vector screening masses. A similar discussion holds for the higher order contributions deriving from the perturbative matching between the three-dimensional non-relativistic theory in eq. (4.1.6) and QCD. From the discussion in Section 4.2.3, a string term of non-perturbative origin $\sigma r \simeq g_{\rm E}^2 r \simeq g^3 T \hat{r}$ starts at $O(g^3)$ in the static potential, and, as a consequence, non-perturbative effects are expected to start contributing to the hyperfine splitting at $O(g^5)$. Therefore, to go beyond the result in eq. (4.2.42), a non-perturbative approach is required.

Analysis of the wave-function

The perturbative result for the hyperfine-splitting in eq. (4.2.42) probes the normalized wave function of the quark-antiquark bound system at the origin. In particular its normalization takes contributions from all distances, and therefore from both the scales present in EQCD, i.e. $r \sim m_{\rm E}^{-1}$ and $(g^2 T)^{-1}$. To scrutinize this issue, it is interesting to define the probability

$$P(\hat{r}_{\rm np}) = \int_0^{\hat{r}_{\rm np}} d\hat{r}\, \hat{r} \left|\hat{\psi}_0(\hat{r})\right|^2 , \tag{4.2.44}$$

for the quark-antiquark pair to be at a distance $\hat{r} \leq \hat{r}_{\rm np}$, where

$$\hat{r}_{\rm np} = m_{\rm E} r_{\rm np} = \frac{m_{\rm E}}{g_{\rm E}^2} = \left(\frac{N_c}{3} + \frac{N_f}{6}\right)^{1/2} \frac{1}{g} = \sqrt{\frac{3}{2}} \frac{1}{g} , \tag{4.2.45}$$

and on the r.h.s. we substituted $N_f = 3$ and $N_c = 3$ which is the relevant case to this study. In Figure 4.3 we show the probability density as a function of $\hat{r}$ together with the ratio $\hat{r}_{\rm np}$ of the two relevant scales (dashed line). As expected, at asymptotically high temperatures (left panel) the probability for the quark and the antiquark to be at distances $\hat{r} \leq \hat{r}_{\rm np}$ is close to 1 (blue band), and the perturbative determination in eq. (4.2.42) becomes more and more reliable as the temperature increases. In the central and right panels of Figure 4.3 the cases for $T \sim 4 \times 10^8$ GeV ($P(\hat{r}_{\rm np}) \sim 70\%$) and for $T \sim \times 10^2$ GeV ($P(\hat{r}_{\rm np}) \sim 40\%$) are shown, respectively. It is rather clear that, at temperatures of the order of the electro-weak scale, the probability for the quark and the antiquark to be at distances larger than $\hat{r}_{\rm np}$ approaches 50%. As a consequence, long-distance (ultra-soft) contributions are relevant, and non-perturbative effects must be taken into account. As discussed previously, they start contributing already at $O(g^5)$ for the hyperfine splitting.

This analysis, albeit rather crude, is consistent with the fact that the hierarchy

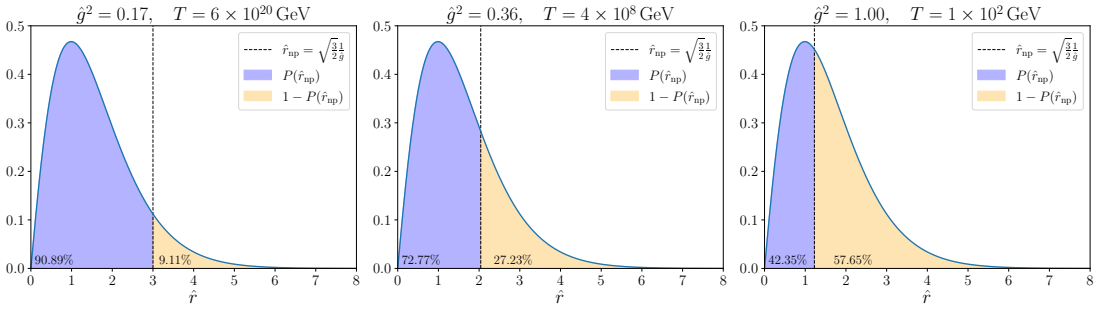

FIGURE 4.3: Probability density for the quark-antiquark pair as a function of the distance $\hat{r}$. The probability for the quark and the antiquark to be at distances $\hat{r} \leq \hat{r}_{\rm np}$, see eq. (4.2.44), is indicated by the blue area for different values of the coupling constant (temperature), with the latter increasing from left to right. As the temperature decreases, the blue area becomes larger and larger.

of scales of equation (3.3.8) sets in only at much higher temperatures with respect to the electro-weak scale, where $g \sim 1$. The result in eq. (4.2.42), however, remains extremely useful to discriminate, among the possible interpolating fit functions of the non-perturbative data, those which have the correct asymptotic behaviour at asymptotically large temperatures.

4.2.5 Comparison with lattice data

About one year prior to the beginning of the work collected in this thesis, the flavour non-singlet pseudoscalar and vector screening masses had been computed in thermal QCD with $N_f = 3$ massless quarks in the range of temperatures from $T \sim 1$ GeV up to ~ 165 GeV with a statistical precision of a few parts per mille on the single channels, and of about 10% on the spin-splitting [54]. In [1] we have compared the lattice data of [54] with the leading-order perturbative prediction computed in the previous section, and here we report the most salient points of such comparison; we anticipate however that in section 5.2 of the next chapter we will present, among other things, results from recent high-precision simulations that allowed us to gain roughly an order of magnitude in the accuracy of the hyperfine splitting, which is now determined at the level of 1%. Therefore, we leave a more in-depth analysis for section 5.3 of the next chapter.

As anticipated in section 3.5.3, we study the non-perturbative data as a function of $\hat{g}(T)$, defined in equation (3.5.11), which is the renormalized coupling in the $\overline{\rm MS}$ scheme at two-loop order evaluated at the renormalization scale $\mu = 2\pi T$. We stress once again that, for our purposes, $\hat{g}$ is just a function of the temperature T, suggested by the effective theory analysis, that we use to analyze the

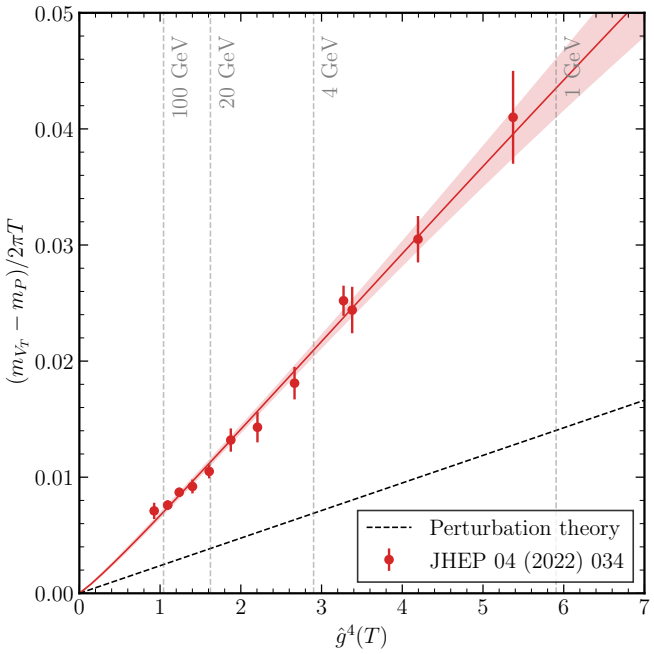

FIGURE 4.4: Difference of the vector and pseudoscalar screening masses normalized to $2\pi T$ versus $\hat{g}^4$. The perturbative result in eq. (4.2.43) is the dashed black line, while the red points are determined by a previous lattice computation in [54]. The red curve and band is the fit in equation (4.2.46). An updated version of this plot, with lattice data about one order of magnitude more precise, is given in section 5.3, see figure 5.14.

non-perturbative data. The crucial point is its leading logarithmic dependence on T. The non-perturbative results for the hyperfine splitting as determined in [54] are reported in Figure 4.4 as a function of $\hat{g}^4$. Within statistical errors, data show an effective quartic dependence on $\hat{g}$ in the entire range of temperature explored. However, the effective slope, 0.00704(14), turns out to be approximatively 3 times the coefficient on the r.h.s. of eq. (4.2.43). Thanks to the perturbative result in eq. (4.2.43), however, we can constrain the asymptotic behaviour of the mass difference between the vector and the pseudoscalar screening masses at asymptotically large temperatures. We then parameterize the non-perturbative data in Ref. [54] as

$$\frac{m_{\rm V} - m_{\rm P}}{2\pi T} = 0.002376\,\hat{g}^4 + s_5\,\hat{g}^5 + s_6\,\hat{g}^6\,, \tag{4.2.46}$$

where a fit to the data gives $s_5 = 0.0063(9)$, $s_6 = -0.0020(7)$, $\mathrm{cov}(s_5, s_6)/\left[\sigma(s_5)\sigma(s_6)\right] = -0.99$, and an excellent $\chi^2/\text{d.o.f.} = 0.75$. The eq. (4.2.46) represents our best parameterization of the non-perturbative data. Being s_5 about 3 times in magnitude with respect to s_4, it follows that the leading $O(\hat{g}^4)$ term accounts only for a

small fraction of the total contribution in the entire range of temperatures studied in Ref. [54]. The bulk of the hyperfine splitting originates from higher order terms which can be present both in the spin-dependent potential and in the unperturbed, spin-independent wave-function. Recalling the discussion in section 4.2.4, this means that contributions of non-perturbative origin have to be taken into account to explain the observed magnitude of the hyperfine splitting up to the electro-weak scale. This does not come as a surprise given the analysis of the wave function reported in the previous sectionin section.

As anticipated, thanks to the improved precision determination that will be described in section 5.2, we will be able to perform an even more precise comparison between the non-perturbative data and the known perturbative terms. We will see that within the now much smaller errors the non-perturbative that can not be described by a single effective g^4 term anymore, and higher order contributions must be taken into account from the start.

Chapter 5

Screening masses from the lattice

This chapter contains the other original results of this thesis, namely the determination of screening masses with non-zero Matsubara frequency from simulations of lattice QCD at high temperatures. The simulations exploit the strategy outlined in section 3.5 to non-perturbatively define QCD with $N_f = 3$ flavors of $\mathcal{O}(a)$–improved Wilson fermions in the chiral limit at 12 temperatures ranging from ~ 1 GeV up to ~ 165 GeV. Section 5.1 details the results published in [2] concerning the first lattice determination of continuum-extrapolated screening masses of baryon states with nucleon quantum numbers, the study of their dependence on the temperature and the comparison with the NLO perturbative result described in section 4.1. Section 5.2 presents first results on screening masses of flavor non-singlet meson states with non-zero Matsubara frequency – namely in the first sector with $\omega_1 = 2\pi T$ – in the pseudoscalar and vector channels. To overcome the severe signal-to-noise problem that affects the correlators from which these screening masses are extracted, noise-reduction techniques based on the use of random sources have been implemented. As a by-product, the static mesonic screening masses which were determined in [54] have been re-computed with significantly improved statistical precision. Preliminary versions of these results have been presented as posters and talks at international conferences, see page i, and they will be the subject of a publication currently in preparation, to be submitted for publication after the completion of this thesis.

5.1 Baryonic screening masses

As in the continuum case, the central object for the determination of screening masses is the two-point correlation function measured on the lattice. Since we adopt the shifted boundary conditions described in section 3.5.1, the projection of the baryonic correlation function in equation (4.1.2) on the first Matsubara

frequency has to be modified according to equation (3.5.7); for a shift vector of the form $\boldsymbol{\xi} = (\xi, 0, 0)$ it reads

$$C_{N^\pm}(x_3) = \int dx_0 dx_1 dx_2 e^{-i\frac{x_0+\xi x_1}{L_0}\gamma^2\pi} \left\langle \mathrm{Tr}\left[P_\pm N(x)\overline{N}(0)\right]\right\rangle , \tag{5.1.1}$$

where at variance with Eq. (4.2.3), the expectation value is computed in the presence of shifted boundary conditions[1].

5.1.1 Lattice strategy and correlation functions

We compute the screening masses in QCD with $N_f = 3$ massless quarks[2] at the 12 temperatures $T_0, \ldots, T_{11}$ given in Table 3.3, i.e. for T from about 1 GeV up to approximately 165 GeV.

We adopt shifted boundary conditions in the compact direction with $\boldsymbol{\xi} = (1, 0, 0)$ and, in order to extrapolate the results to the continuum limit with confidence, several lattice spacings are simulated at each temperature with the extension of the compact direction being $L_0/a = 4, 6, 8, 10$ while the length of the spatial directions is always $L/a = 288$. For the nine highest temperatures $T_0 - T_8$ the Yang-Mills action is discretized with the Wilson plaquette action (2.1.9), while for the three lowest ones $T_9 - T_{11}$ we employ the tree-level improved Lüscher-Weisz action 2.4.10. In both cases, $N_f = 3$ $\mathcal{O}(a)$–improved Wilson quarks in the chiral limit are included. [3]

The lattice transcription of the continuum nulceon correlation functions in equation (4.1.2) for $\boldsymbol{\xi} = (1, 0, 0)$, which is the relevant case to this study, reads

$$\begin{aligned} C_{N^\pm}(x_3) &= a^3 \sum_{x_0,x_1,x_2} e^{-i\frac{x_0+x_1}{2L_0}\pi} \left\langle \mathrm{Tr}\left[P_\pm N(x)\overline{N}(0)\right]\right\rangle \\ &= a^3 \sum_{x_0,x_1,x_2} e^{-i\frac{x_0+x_1}{2L_0}\pi} \left\langle \left[W^1_\pm - W^2_\pm\right]\right\rangle , \end{aligned} \tag{5.1.2}$$

where the two terms in the second line are the Wick contractions obtained by integrating over the fermion fields. Their expressions read

$$\begin{aligned} W^1_{N^\pm} &= \mathrm{Tr}\left[S^{agT}(x,0)C\gamma_5 S^{bf}(x,0)C\gamma_5\right]\mathrm{Tr}\left[S^{ce}(x,0)P_\pm\right]\epsilon^{abc}\epsilon^{feg} , \\ W^2_{N^\pm} &= \mathrm{Tr}\left[S^{agT}(x,0)C\gamma_5 S^{be}(x,0)P_\pm S^{cf}(x,0)C\gamma_5\right]\epsilon^{abc}\epsilon^{feg}, \end{aligned} \tag{5.1.3}$$

where $S(x, y)$ is the quark propagator of the degenerate quarks.

[1] We use the same notation for correlation functions with or without shifted boundary conditions since the precise meaning is clear from the context.

[2] Technically it is feasible to simulate massless quarks thanks to the large spectral gap πT induced by the temperature in the spectrum of the Dirac operator.

[3] See appendices A and B of Ref. [54] for the bare parameters of the simulations.

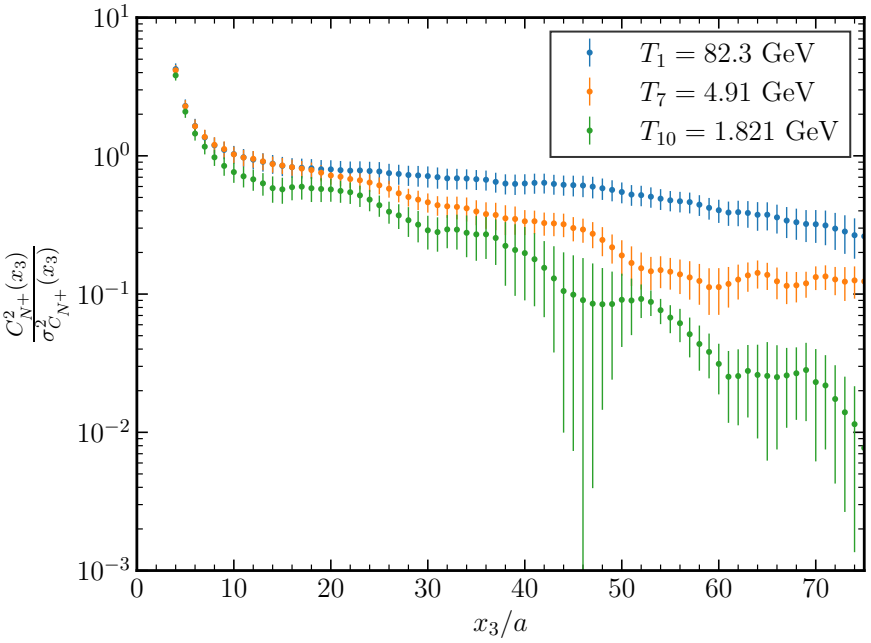

FIGURE 5.1: Ratio of the squared correlator and the variance for the positive parity nucleon two-point function – proportional to the square of the signal-to-noise ratio – as a function of x_3/a for different temperatures on $L_0/a = 6$ lattices.

5.1.2 Signal-to-noise ratio

In section 2.5.2 we highlighted one of the major challenges that are faced when measuring correlation functions at large Euclidean distances from the lattice, namely the exponential depletion of the signal-to-noise (StN) ratio with the distance. In particular, it was shown how the StN for the nucleon two-point function at zero temperature decays with Euclidean time as

$$\frac{C_N(x_0)}{\sigma_{C_N}(x_0)} \underset{x_0 \gg a}{\propto} \sqrt{N} \exp\left\{-\left(m_N - \frac{3}{2} m_\pi\right) x_0\right\}. \tag{5.1.4}$$

It is interesting to notice that, when computing a screening correlator at high temperature such as (5.1.2), the exponential decay of the correlator and the variance is dictated by the screening masses rather than the zero-temperature masses. In the infinite temperature limit, the nucleon and pion screening masses appearing in the exponent of (5.1.4) assume the values $3\pi T$ and $2\pi T$ respectively, and the specific combination that determines the exponential decay with x_3 vanishes. Therefore at asymptotically high temperatures the nucleon correlator measured along a spatial direction does not suffer from an exponential problem; at very high but finite temperature, the correction to the free-theory value of the screening masses is

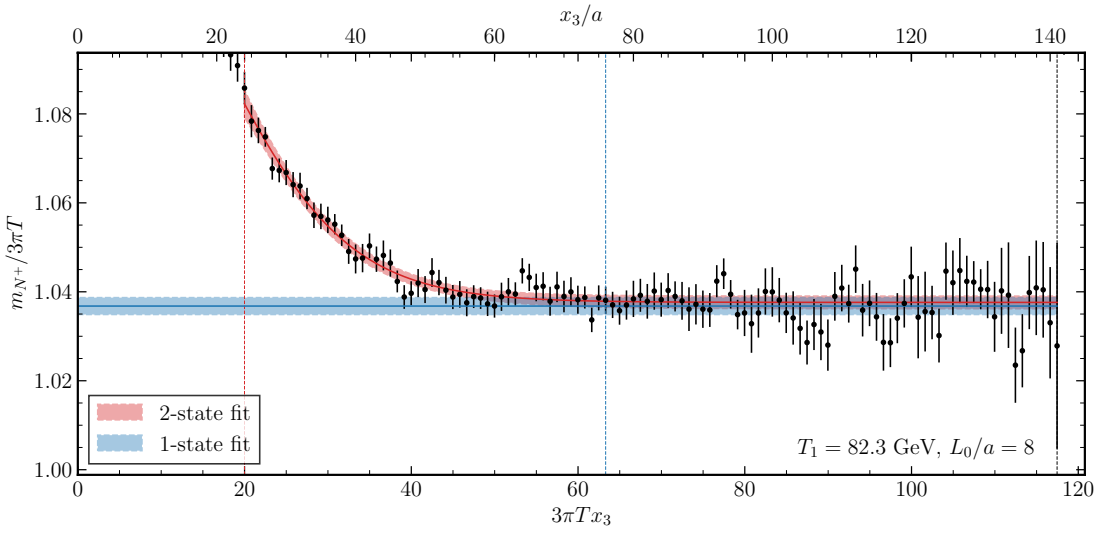

FIGURE 5.2: Plot of the effective mass $m_{N^+}(x_3)$, normalized to $3\pi T$, at the temperature T_1 for $L_0/a = 8$. For the explanation of the various fit curves and bands see the main text.

small, see sections 3.4.2 and 4.1, and therefore the StN problem is expected to be much milder than at zero temperature. This is empirically verified by our data, as depicted in figure 5.1, which shows a very weak dependence of the StN squared on x_3 at the higher temperatures considered, which becomes more pronounced as the temperature is lowered. This feature is one of the factors that allowed us to precisely determine the relevant correlation functions at high temperature, and measure the screening masses at the permille level.

5.1.3 Effective masses

Once the correlators have been computed, the effective screening masses are defined as

$$m_{N^\pm}(x_3) = -\frac{1}{a}\ln\left[\frac{C_{N^\pm}(x_3+a)}{C_{N^\pm}(x_3)}\right]. \tag{5.1.5}$$

As a representative example of the data, the nucleon effective mass is shown in Fig. 5.2 for T_1 and $L_0/a = 8$. In order to determine the value of the screening mass, we start by fitting the effective mass to a constant plus a correction deriving from the contamination of the first excited state (solid red line and band) from a minimum value (red dashed line) up to the last point where we have a good signal (black dashed line). Indeed, assuming that the correlator is given by the contribution of the ground state with screening mass m_0 and one excited state

T	L_0/a	n_{mdu}	n_{nsrc}	$\frac{m_{N^+}}{3\pi T}$	$\frac{m_{N^+}-m_{N^-}}{3\pi T}$
T_0	4	300	4	0.9863(15)	0.0002(3)
	6	390	4	1.0178(17)	0.00041(19)
T_1	4	300	4	0.9892(18)	0.0001(3)
	6	310	4	1.0204(20)	0.0002(4)
	8	500	4	1.0371(18)	-0.00013(23)
	10	500	4	1.0438(28)	0.0003(5)
T_2	4	300	4	0.9909(23)	0.0001(4)
	6	320	4	1.0242(24)	-0.00017(28)
	8	490	4	1.0385(30)	0.00026(29)
	10	500	4	1.048(5)	0.0005(6)
T_3	4	300	4	0.9945(25)	0.0006(4)
	6	340	4	1.027(3)	0.0002(4)
	8	490	4	1.0406(23)	0.0005(3)
	10	500	4	1.048(6)	0.0003(7)
T_4	4	440	4	1.0040(16)	0.0007(5)
	6	310	4	1.0317(26)	-0.0007(4)
	8	490	4	1.0430(29)	-0.0001(4)
	10	500	4	1.054(5)	-0.0013(6)
T_5	4	310	4	1.004(3)	-0.0007(6)
	6	310	4	1.038(3)	0.0005(8)
	8	500	4	1.0466(26)	-0.0001(3)
	10	500	4	1.059(4)	-0.0001(5)

TABLE 5.1: Results for the nucleon screening mass, m_{N^+} , and the mass difference with its parity partner, $(m_{N^+} - m_{N^-})$, normalized to $3\pi T$ at finite lattice spacing for the temperatures $T_0, \ldots, T_5$. The number of molecular dynamic units (MDUs) generated, n_{mdu}, and the number of local sources per configuration on which the two-point correlation functions have been computed, n_{nsrc}, are also reported. The latter are always calculated by skipping $n_{\mathrm{skip}} = 10$ MDUs between two consecutive measurements.

with screening mass m_1

$$C^{2\mathrm{s}}(x_3) = A\exp\{-m_0 x_3\} + B\exp\{-m_1 x_3\} \tag{5.1.6}$$

the effective mass in equation (5.1.5) takes the form

$$am^{2\mathrm{s}}_{N^\pm} = am_0 - \ln\left[\frac{1 + B/A\exp\{-(m_1 - m_0)(x_3 + a)\}}{1 + B/A\exp\{-(m_1 - m_0)x_3\}}\right]. \tag{5.1.7}$$

As long as we are only interested in the determination of the screening mass and not on the ground state matrix element, fitting the effective mass data with the functional form (5.1.7) is as valid as fitting the correlator data directly with the function (5.1.6), but we have observed that fitting the effective mass is numerically more stable than fitting the correlator. The starting point of the effective mass fit is chosen to have a good quality of the fit and to have, at the same time, a non vanishing contribution from the first excited state. On one hand, for the ensembles where the signal is good enough at a large distance, from this fit we estimate the minimum value $x_3^{\min}/a$ (blue dashed line) from which the excited state contamination is below the target statistical precision. The screening mass is then obtained by averaging the plateau (blue band) from $x_3^{\min}/a$ up to the last point where we have a good signal. On the other hand, for the lowest temperatures and for the ensembles corresponding to $L_0/a = 10$, where the loss of signal is more relevant at a large distance, the screening mass is directly estimated from the results of the effective mass fit (red band). All fits we perform are uncorrelated. Our best estimates of the screening masses are reported in Tables 5.1 and 5.2 for all the lattices simulated. In particular, we report the number of MDUs considered and the number of local sources per configuration on which the two-point correlation functions have been computed. For each configuration, the best estimates of $C_{N^\pm}(x_3)$ in Eq. (5.1.2) have been obtained by properly averaging their values from all local sources.

To explicitly check that finite volume effects are negligible within our statistical errors, we have generated three more lattices at T_0 ($L_0/a = 6$), T_1 ($L_0/a = 10$) and T_{11} ($L_0/a = 8$) at three smaller spatial volumes, namely $6 \times 144^2 \times 288$, $10 \times 120^2 \times 288$, and $8 \times 144^2 \times 288$ (direction 3 the longest) respectively, on which we have computed the baryonic screening masses as above. They turn out to be in very good agreement with the analogous ones reported in Tables 5.1 and 5.2, and therefore they confirm the theoretical expectations that finite volume effects are negligible within the statistical precision as expected by the theoretical analysis in Ref. [54].

The statistical error varies from a few permille to at most 5 permille for the smallest temperature. In order to profit from the correlations in our data for reducing the statistical errors, we also compute $(m_{N^+} - m_{N^-})/(3\pi T)$ and report its values in Tables 5.1 and 5.2 as well. This combination is particularly interesting because it is a measure of the chiral symmetry restoration which can be computed very precisely. The data shows that at all temperatures and lattice spacings considered the difference between the positive and negative parity nucleon state's screening masses is compatible with 0 within the statistical uncertainty, confirming the restoration of chiral symmetry in QCD at the temperatures considered. For this reason, from now on we focus on the positive parity screening mass only.

T	L_0/a	n_{mdu}	n_{nsrc}	$\frac{m_{N^+}}{3\pi T}$	$\frac{m_{N^+}-m_{N^-}}{3\pi T}$
T_6	4	300	4	1.0089(25)	-0.0006(9)
	6	320	4	1.034(3)	-0.0002(7)
	8	500	4	1.054(4)	-0.0002(5)
	10	500	4	1.061(6)	0.0004(10)
T_7	4	320	4	1.012(4)	0.0005(12)
	6	310	4	1.043(4)	0.0006(7)
	8	500	4	1.059(3)	-0.0001(8)
	10	500	4	1.062(6)	0.0026(17)
T_8	4	320	8	1.016(4)	0.0023(14)
	6	300	8	1.046(4)	-0.0001(11)
	8	500	4	1.066(4)	-0.0007(8)
	10	500	5	1.061(4)	0.0013(13)
T_9	4	400	4	1.0180(26)	-0.0008(12)
	6	390	4	1.0526(28)	0.0005(10)
	8	390	4	1.052(5)	0.0002(10)
T_{10}	4	410	4	1.029(4)	-0.0019(21)
	6	400	4	1.056(3)	-0.0021(14)
	8	390	4	1.074(3)	0.0013(17)
T_{11}	4	400	4	1.029(4)	0.0001(21)
	6	390	4	1.055(6)	-0.0015(17)
	8	390	4	1.063(5)	0.0016(11)

TABLE 5.2: As in Table 5.1 but for $T_6, \ldots, T_{11}$.

5.1.4 Continuum limit

Once the screening masses are determined for several lattice spacings at each temperature, we can obtain the continuum value of the screening mass by extrapolating the results at fixed lattice spacing to $a \to 0$. Since we employed an $\mathcal{O}(a)-$ improved action, we expect discretization effects to start at order a^2; for this reason, we fit the following function to the data for the positive parity screening mass in tables 5.1 and 5.2:

$$\frac{m_{N^+}(a/L_0, T)}{3\pi T} = \frac{m_{N^+}(T)}{3\pi T} + B\left(\frac{a}{L_0}\right)^2 . \tag{5.1.8}$$

With the aim of reducing the magnitude of lattice artifacts, we performed a tree-level improvement of our data by computing the value of the baryonic screening mass at tree-level on the lattice $m_N^{\mathrm{free}}(a/L_0)$ – the details of the computation are

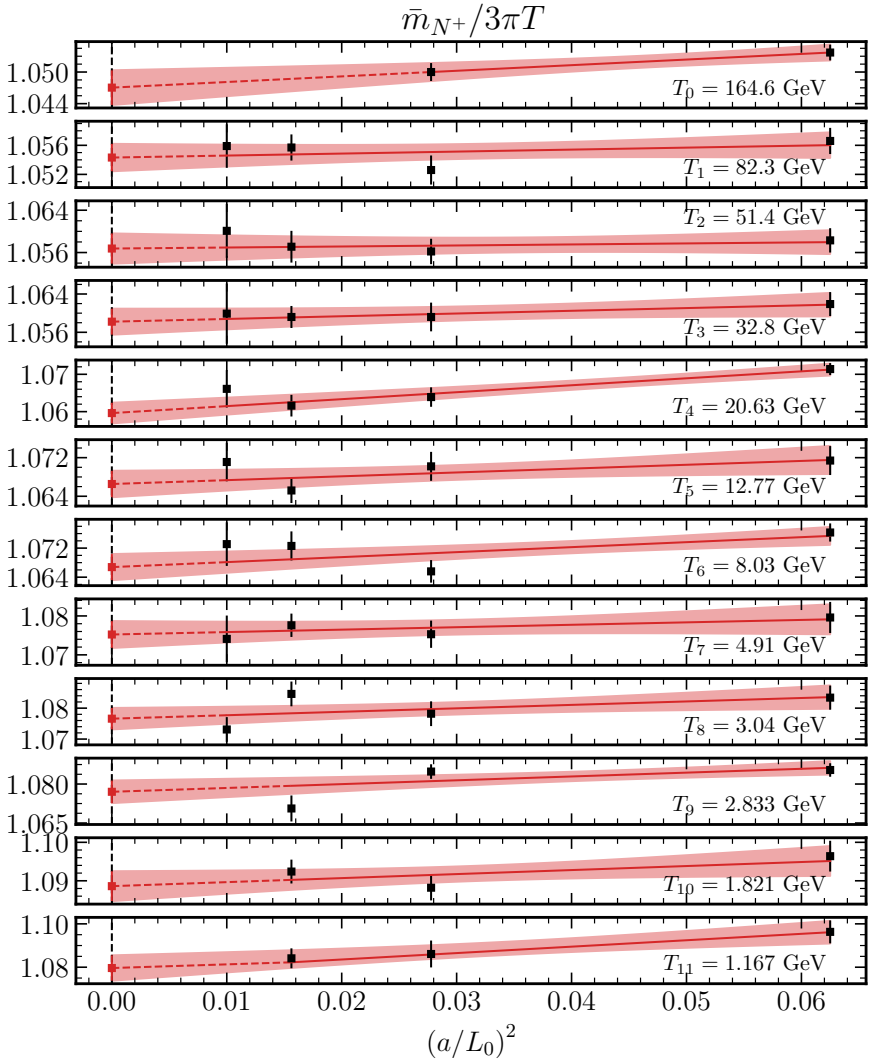

FIGURE 5.3: Numerical results for the tree-level improved positive parity nucleon screening mass at finite lattice spacing (black squares). The red lines and bands lines in the panel represent the linear extrapolations in $(a/L_0)^2$ to the continuum limit, and the red squares are the final continuum values of the screening mass. Each temperature is analyzed independently from the others.

reported in appendix G.2 – and define the tree-level improved mass as

$$\frac{\bar{m}_{N^+}(a/L_0, T)}{3\pi T} = \left(\frac{m_{N^+}(a/L_0, T)}{3\pi T} - \frac{m_N^{\text{free}}}{3\pi T} \right) + 1. \tag{5.1.9}$$

The continuum extrapolations are performed independently for each temperature, and in all cases the tree-level improved data is very well described by the linear

T	T(GeV)	$\frac{m_{N^+}}{3\pi T}$	$\frac{m_{N^+}-m_{N^-}}{3\pi T}$
T_0	165(6)	1.047(3)	0.0006(4)
T_1	82.3(2.8)	1.0544(19)	-0.0001(3)
T_2	51.4(1.7)	1.0569(28)	0.0002(3)
T_3	32.8(1.0)	1.0583(27)	0.0003(4)
T_4	20.6(6)	1.0596(28)	-0.0011(4)
T_5	12.8(4)	1.0662(28)	0.0001(4)
T_6	8.03(22)	1.068(3)	0.0001(6)
T_7	4.91(13)	1.075(4)	0.0004(9)
T_8	3.04(8)	1.077(4)	0.0003(9)
T_9	2.83(7)	1.076(4)	0.0009(12)
T_{10}	1.82(4)	1.089(4)	0.0007(20)
T_{11}	1.167(23)	1.078(6)	0.0016(15)

TABLE 5.3: Temperatures considered in this letter together with the best results for the nucleon mass, m_{N^+}, and the mass difference with its parity partner, $m_{N^+} - m_{N^-}$, in the continuum limit.

ansatz in $(a/L_0)^2$ with very mild discretization effects. Given the high quality of the fits and of the data, it is not necessary to model the temperature dependence of the discretization effects so as to perform a global fit of the data. The continuum limits are displayed in figure 5.3; in a similar way, we extrapolate the difference between positive and negative parity states, which as anticipated turn out to be compatible with zero in the whole temperature range. Our final, continuum-extrapolated measurements of the positive parity nucleon screening mass $(m_{N^+})/3\pi T$ and the splitting $(m_{N^+} - m_{N^-})/3\pi T$ are summarized in table 5.3.

5.1.5 Temperature dependence

The first observation is that, as anticipated in section 5.1.1, within our rather small statistical errors we find an excellent agreement between m_{N^+} and m_{N^-}. This is a clear manifestation of the restoration of chiral symmetry occurring at high temperature in line with the analogous results for mesonic screening masses in Ref. [54]. For this reason in the following we discuss the nucleon mass m_{N^+} only.

A second observation is that the bulk of the nucleon screening mass is given by the free-theory value, $3\pi T$, plus $4-8\%$ positive contribution over the entire range of temperatures explored.

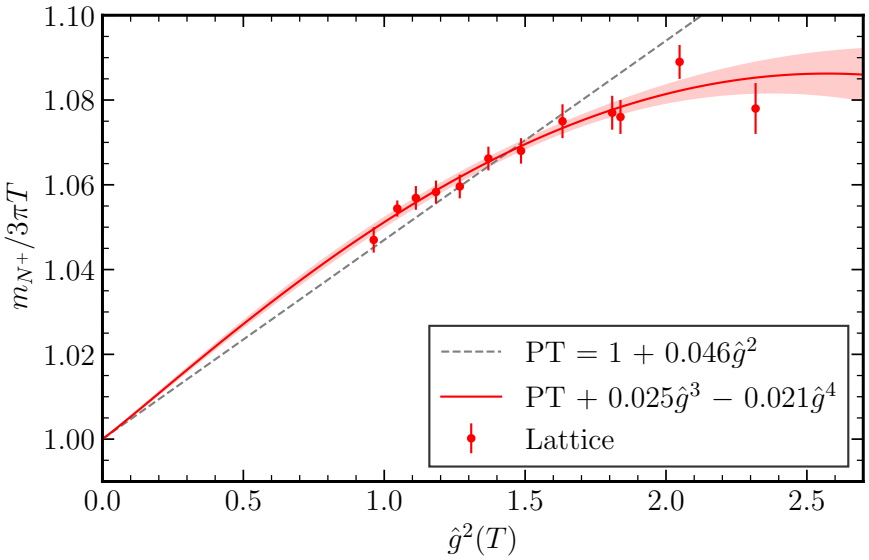

FIGURE 5.4: Nucleon screening mass versus $\hat{g}^2$. The band represent the best fit to Eq. (5.1.11), while the dashed line is the analytically known contribution in Eq. 4.1.44.

To scrutinize in detail the temperature dependence induced by the non-trivial dynamics, we introduce the function $\hat{g}^2(T)$ defined as

$$\frac{1}{\hat{g}^2(T)} \equiv \frac{9}{8\pi^2} \ln \frac{2\pi T}{\Lambda_{\overline{\rm MS}}} + \frac{4}{9\pi^2} \ln \left(2 \ln \frac{2\pi T}{\Lambda_{\overline{\rm MS}}} \right) , \tag{5.1.10}$$

where $\Lambda_{\overline{\rm MS}} = 341$ MeV is taken from Ref. [14]. It corresponds to the 2-loop definition of the strong coupling constant in the $\overline{\rm MS}$ scheme at the renormalization scale $\mu = 2\pi T$. For our purposes, however, this is just a function of the temperature T, suggested by the effective theory, that we use to analyze our results, see Ref. [54] for more details. The screening masses versus $\hat{g}^2(T)$ are plotted in Fig. 5.4. The dashed line in this plot is the next-to-leading contribution to the nucleon screening mass computed in the effective theory as described in section 4.1. It is rather clear that from $T = T_0 \sim 160$ GeV down to $T = T_7 \sim 5$ GeV the perturbative expression is within half a percent or so with respect to the non-perturbative data. If a quick convergence of the perturbative series is assumed, this result would suggest that the bulk of the contribution due to the interactions is given by the $O(g^2)$ term. The full set of data, however, shows a distinct negative curvature which requires higher orders in $\hat{g}^2$ to be parameterized. We thus fit the values of m_{N^+} reported in the third column of Table 5.3 to a quartic polynomial in $\hat{g}$ of the form

$$\frac{m_{N^+}}{3\pi T} = b_0 + b_2\, \hat{g}^2 + b_3\, \hat{g}^3 + b_4\, \hat{g}^4 \, . \tag{5.1.11}$$

The intercept b_0 turns out to be compatible with 1, as predicted by the free theory, within a large error. We thus enforce it to be the free-theory value, $b_0 = 1$, and we fit the data again. The coefficient of the $\hat{g}^2$ term turns out to be compatible with the theoretical expectation in Eq. 4.1.44 within again a large uncertainty. We have thus fixed also this coefficient to its analytical value, $b_2 = 0.046$, and we have performed again the quartic fit of the form in Eq. 5.1.11. As a result, we obtain $b_3 = 0.026(4)$, $b_4 = -0.021(3)$ and $\mathrm{cov}(b_3, b_4)/[\sigma(b_3)\sigma(b_4)] = -0.99$ with $\chi^2/\mathrm{dof} = 0.64$. This is indeed the best parameterization of our results over the entire range of temperatures explored.

For completeness, we notice that if the cubic coefficient is enforced to vanish, i.e. $b_3 = 0$, the fit returns $b_2 = 0.062(3)$, $b_4 = -0.011(2)$ and $\mathrm{cov}(b_2, b_4)/[\sigma(b_2)\sigma(b_4)] = -0.97$ with again an excellent value of $\chi^2/\mathrm{dof} = 0.68$. The coefficient b_2 , however, turns out to be in disagreement with the analytic determination. Data can also be fit to the function in Eq. 5.1.11 with $b_0 = 1$ and $b_4 = 0$ but again the coefficient b_2 would be in disagreement with the perturbative result.

The work collected in this section represents the first computation of continuum-extrapolated QCD baryonic screening masses in the literature, and one of the first studies of thermal QCD at $T \sim 1$ GeV up to the electroweak scale $T \sim 165$ GeV applying the strategy outlined in [54] to define QCD with $N_f = 3$ massless quarks at very high temperatures. The screening masses of the positive and negative parity nucleon states have been determined over the whole temperature range with a precision of a few permille; it has been possible to study the baryonic sector with high precision also thanks to the fact that, as we verfied, baryonic screening correlators suffer for a very mild signal-to-noise ratio problem at high temperature, and in the infinite temperature limit the exponential problem is absent. At all temperatures considered the opposite parity states have degenerate screening mass which, by the discussion in section 3.4.1, signals the restoration of chiral symmetry in the temperature range considered. The bulk of the baryon screening mass is given by the free-theory value $3\pi T$, and interactions generate a correction ranging from $\sim 4\%$ at $T \sim 165$ GeV up to $\sim 8\%$ at $T \sim 1$ GeV. Comparison of the non-perturbative data with the perturbative calculation at NLO described in section 4.1 reveals an overall qualitative agreement down to temperatures of about $T \sim 7$ GeV; to describe the lattice data over the whole temperature range, specifically the distinct negative curvature towards lower temperatures, it is necessary to include contributions from higher powers of the QCD coupling g. Nevertheless, it seems that the agreement of NLO perturbation theory with non-perturbative data for this baryonic observable is better than the one observed in [54] for the screening masses of static mesons.

5.2 Non-static mesonic screening masses

In this section we collect results – not yet published at the time of first submission of this document – for screening masses of flavor non-singlet mesonic fields with non-zero Matsubara frequency in the same high-temperature range studied in the previous section $T \in [1\ \text{GeV},\ 165\ \text{GeV}]$. They are particularly interesting quantities since, for instance, the physics of the non-static vector modes can be related to real-time properties of the QGP such as the photon or dilepton emission rates, see [160, 166–168].

5.2.1 Correlation functions

The objects we set to study are correlators of flavour non-singlet mesonic fields. The basic interpolating fields we consider have the structure

$$O^a_\Gamma(x) = \overline{\psi}(x)\Gamma T^a \psi(x) \tag{5.2.1}$$

or, expressing all but color indices,

$$O^a_\Gamma(x) = \sum_{r,s=1}^{N_f} \sum_{\alpha,\beta=1}^{4} \overline{\psi}_{\alpha,r}(x)\Gamma_{\alpha\beta} T^a_{rs} \psi_{\beta,s}(x) \tag{5.2.2}$$

where α, β are spinorial indices, r, s are flavour indices and T^a with a going from 1 to $N_f^2 - 1$ are the generators of $\mathrm{SU}(N_f)$, i.e. a particular basis for its Lie algebra, assumed to be normalized as $\mathrm{Tr}\,(T^a T^b) = \delta^{ab}/2$. The matrix Γ acts on spin indices only and specifies the Lorentz structure of the operator; it can be chosen among $\Gamma = \{\mathbb{1}, \gamma_5, \gamma_\mu, \gamma_\mu\gamma_5\}$, corresponding, respectively, to a Scalar (S), Pseudoscalar (P), Vector (V_μ), Axial (A_μ) field. Colour indices for the SU(3) gauge group are suppressed and all operators are assumed to be color singlets. We consider two-point functions these operators measured along the x_3 direction, projected to a generic bosonic Matsubara frequency $\omega_n = 2n\pi T$ in presence of shifted boundary conditions:

$$\begin{aligned} C^{(n)}_{\Gamma\Gamma'}(x_3) &= \int_0^{L_0} \mathrm{d}x_0 \int \mathrm{d}x_1 \mathrm{d}x_2 e^{i2\pi n \frac{x_0'}{L_0'}} \langle O^a_\Gamma(x) O^a_{\Gamma'}(0)\rangle \\ &= \int_0^{L_0} \mathrm{d}x_0 \int \mathrm{d}x_1 \mathrm{d}x_2 e^{i2\pi n \gamma^2 \frac{x_0 + \xi x_1}{L_0}} \langle O^a_\Gamma(x) O^a_{\Gamma'}(0)\rangle, \end{aligned} \tag{5.2.3}$$

where no summation over a is intended and, as in the baryonic case, employing shifted boundary conditions implies the modification of the momentum projection according to equation (3.5.7). After the analytic integration over Grassman fermionic variables through Wick's theorem the above correlator can be expressed as the sum of a connected and disconnected contribution, both intended as an

expectation value over gauge fields only with a modified Boltzmann weight:

$$\langle O^a_\Gamma(x) O^a_{\Gamma'}(0)\rangle = \langle O^a_\Gamma(x) O^a_{\Gamma'}(0)\rangle_{\text{conn}} + \langle O^a_\Gamma(x) O^a_{\Gamma'}(0)\rangle_{\text{disc}}, \tag{5.2.4}$$

The connected part is given by

$$\langle O^a_\Gamma(x) O^a_{\Gamma'}(0)\rangle_{\text{conn}} = -\langle \text{Tr}[\Gamma S(x,0)\Gamma' S(0,x)]\rangle_G \,\text{Tr}\left[(T^a)^2\right] \tag{5.2.5}$$

while the disconnected one is

$$\langle O^a_\Gamma(x) O^a_{\Gamma'}(0)\rangle_{\text{disc}} = \langle \text{Tr}[\Gamma S(x,x)]\,\text{Tr}[\Gamma' S(0,0)]\rangle_G \,\text{Tr}[T^a]^2 = 0. \tag{5.2.6}$$

The disconnected contribution is proportional to the trace of an $\text{SU}(N_f)$ generator, and thus vanishes, while in the connected contribution $\text{Tr}\left[(T^a)^2\right] = 1/2$. For this reason, from now on we will always refer to the connected part of the correlators. In the above expressions and in the following we have denoted the quark propagator as $S(x,y)$. The actual correlators we aim to compute are those obtained conisdering two operators with the same spin structure, i.e. $\Gamma = \Gamma'$ in the above equations, we identify the following channels[4]:

$$C^{(n)}_P(x_3) = \int_0^{L_0} dx_0 \int dx_1 dx_2 \; e^{i\phi_n(x)} \langle P(x)P(0)\rangle \tag{5.2.7}$$

$$C^{(n)}_{V_T}(x_3) = \int_0^{L_0} dx_0 \int dx_1 dx_2 \; e^{i\phi_n(x)} \left[\langle V_1'(x)V_1'(0)\rangle + \langle V_2(x)V_2(0)\rangle\right] \tag{5.2.8}$$

$$C^{(n)}_{V_0}(x_3) = \int_0^{L_0} dx_0 \int dx_1 dx_2 \; e^{i\phi_n(x)} \langle V_0'(x)V_0'(0)\rangle\,, \tag{5.2.9}$$

$$C^{(n)}_{V_3}(x_3) = \int_0^{L_0} dx_0 \int dx_1 dx_2 \; e^{i\phi_n(x)} \langle V_3(x)V_3(0)\rangle\,, \tag{5.2.10}$$

where we define for brevity $\phi_n(x) \equiv 2\pi n\gamma^2(x_0 + \xi x_1)/L_0$. It is important to point out that, in the presence of shifted boundary conditions, the contractions that enter the compact and transverse channel are given by $\langle V_0'(x)V_0'(0)\rangle$ and $\langle V_1'(x)V_1'(0)\rangle$ respectively, which are related to the non-shifted components of the currents by the Euclidean Lorentz transformation (3.5.4):

$$\begin{aligned}\langle V_0'(x)V_0'(0)\rangle = {}& \gamma^2\left(\langle V_0(x)V_0(0)\rangle + \xi^2\langle V_1(x)V_1(0)\rangle\right) + \\ & + \gamma^2\xi(\langle V_0(x)V_1(0)\rangle + \langle V_1(x)V_0(0)\rangle),\end{aligned} \tag{5.2.11}$$

$$\begin{aligned}\langle V_1'(x)V_1'(0)\rangle = {}& \gamma^2\left(\langle V_1(x)V_1(0)\rangle + \xi^2\langle V_0(x)V_0(0)\rangle\right) - \\ & - \gamma^2\xi(\langle V_0(x)V_1(0)\rangle + \langle V_1(x)V_0(0)\rangle).\end{aligned} \tag{5.2.12}$$

[4]Similar definiton apply for the scalar and axial correlators which are related to the ones reported by chiral symmetry as explained in section 3.4.1

We point out at this stage that, due to the fact that in the chiral limit the vector current is conserved, see equation (1.5.29), the V_0 and V_3 correlator are related: starting from (1.5.29) it is straightforward to obtain that for non-zero Matsubara frequency it holds

$$\partial_3^2 C_{V_3}^{(n)}(x_3) = -\omega_n^2 C_{V_0}^{(n)}(x_3), \quad n > 0 \tag{5.2.13}$$

while for the static sector the conservation of V_μ^a implies

$$\partial_3 C_{V_3}^{(0)}(x_3) = 0. \tag{5.2.14}$$

Equation (5.2.14) implies that there is no screening mass in the static V_3 channel, whereas equation (5.2.13) tells us that the non-static screening masses extracted from the V_0 and V_3 correlators are degenerate, see also [160].

5.2.2 Lattice correlators with point sources

The lattice transcription of eq. (5.2.3) reads [5]

$$C_{\Gamma\Gamma'}^{(n)}(x_3) = a^3 \sum_{\boldsymbol{x}} e^{i2\pi n\gamma^2(x_0+\xi x_1)/L_0} \langle \mathrm{Tr}[\Gamma S(x,0)\Gamma' S(0,x)] \rangle, \tag{5.2.15}$$

Since in our setting the third direction plays the role of the temporal direction at zero temperature, we denoted $\boldsymbol{x} = (x_0, x_1, x_2)$. To lighten the notation, for the moment we suppress the dependence on the Matsubara frequency index (n) and on the Γ matrices. In the following it will be useful to define the objects

$$C(x_3; y, z) \equiv a^3 \sum_{\boldsymbol{x}} e^{i\phi_n(x-y)} \left\{ \Gamma S(x,y)\Gamma' S(z,x) \right\}, \tag{5.2.16}$$

$$C(x_3, y) = \langle \mathrm{Tr}\{C(x_3; y, y)\} \rangle, \tag{5.2.17}$$

where the trace is over spin and flavor indices. Equation (5.2.17) corresponds to the computation of the correlation function inverting the Dirac equation on a single point source placed at lattice site y. Its variance is given by

$$\sigma_C^2 = \left\langle \left(\mathrm{Tr}\{C(x_3; y, y)\}\right) \left(\mathrm{Tr}\{C(x_3; y, y)\}^*\right) \right\rangle - C(x_3, y) C^*(x_3, y), \tag{5.2.18}$$

or diagrammatically

$$\sigma_C^2 = \sum_{\boldsymbol{x},\boldsymbol{x}'} \Big\langle \quad \Big\rangle - \Big\langle \sum_{\boldsymbol{x}} \quad \Big\rangle \Big\langle \sum_{\boldsymbol{x}'} \quad \Big\rangle$$

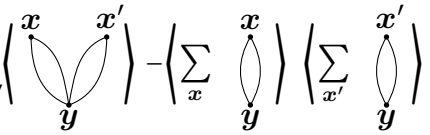

[5] We made use of the cyclic property of the trace, and we dropped the $-\frac{1}{2}$ constant in front of the connected contraction as well as the $_G$ subscript in the expectation value.

In [54] it was possible to precisely measure the static correlators in the P and V_T channels by computing them on a set of local point sources. It is then in principle easy to obtain the non-static correlators from the static ones by applying the desired phase factor when summing over the x_0, x_1 and x_2 coordinates; however, as we will see in the next section, the non-static correlators suffer in general from a severe exponential StN problem, and point sources will reveal insufficient to determine the correlators in the range of interest for the extraction of the screening mass.

5.2.3 Exponential StN problem

A correlator of the form in eq. (5.2.15) suffers from an exponential depletion of the StN with distance. Schematically, this is due to the fact that for large $|x_3 - y_3|$ the correlator itself decays exponentially, with a decay rate given by the screening mass (energy) with given Matsubara frequency (see section 3.4)

$$C_\Gamma^{(n)}(x_3, y) \overset{|x_3-y_3|\gg 1}{\sim} \exp\Big\{-m_\Gamma^{(n)}|x_3 - y_3|\Big\}, \tag{5.2.19}$$

while at large distances the variance of $C_\Gamma^{(n)}(x_3, y)$ is dominated by twice the screening mass of the lightest meson state with zero Matsubara frequency[6], i.e.

$$\sigma^2_{C_\Gamma^{(n)}} \overset{|x_3-y_3|\gg 1}{\sim} \exp\Big\{-2m_P^{(0)}|x_3 - y_3|\Big\}. \tag{5.2.20}$$

The last two equations imply that for large distances the StN decays exponentially:

$$\frac{C_\Gamma^{(n)}(x_3, y)}{\sigma_{C_\Gamma^{(n)}}} \overset{|x_3-y-3|\gg 1}{\sim} \exp\Big\{-\Big(m_\Gamma^{(n)} - m_P^{(0)}\Big)|x_3 - y_3|\Big\}, \tag{5.2.21}$$

and the fundamental reason is that the non-static screening mass $m_\Gamma^{(n)}$ is significantly larger than the static pesudoscalar screening mass $m_P^{(0)}$. The behavior of the StN for static and non static pseudoscalar density correlator, measured on a set of 4 equally spaced point sources, is depicted in figure 5.5, together with and example of the resulting non-static effective mass, from which it is evident that a strategy to reduce the variance of our estimators is necessary if we aim to determine the screening masses. In the following sections, we will detail the use of random sources to stochastically estimate a volume-averaged version of the non-static correlators which have the same central value but reduced variance, which proved to be an extremely effective way to ameliorate the exponential problem enough to determine non-static screening masses at the percent level or better.

[6] The projection of a correlation function to non-zero momentum typically results in an exponential problem [189]. In our setting, non-zero Matsubara frequencies can formally be seen as adding a large momentum in the Euclidean time direction, thus resulting in a rather severe StN problem.

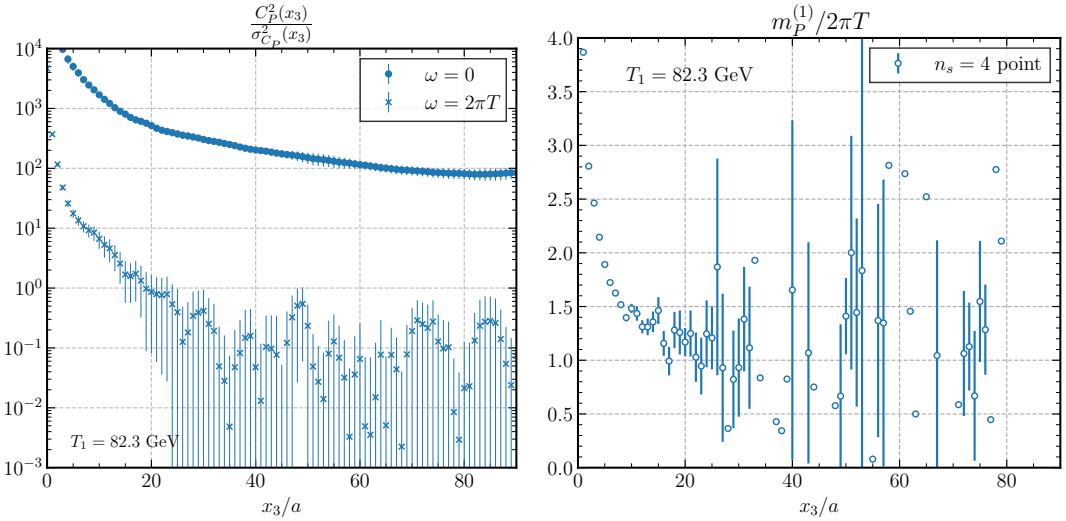

FIGURE 5.5: Left: StN ratio squared for the pseudoscalar correlator (5.2.7) with zero (points) and non-zero (crosses) Matsubara frequency $\omega_1 = 2\pi T$, measured with 4 local point sources. Right: effective screening mass for the pseudoscalar channel with non-zero Matsubara frequency $\omega_1 = 2\pi T$ obtained from the correlator measured with 4 point sources. Both plots refer to the $6 \times (288)^3$ lattice at temperature $T_1 = 82.3$ GeV.

5.2.4 Volume-averaging

Due to the rapid depletion of the signal in the non-zero Matsubara frequency sector, a strategy to reduce the correlator variance without an exponential increase in computational cost is necessary. The first idea that may come to mind is to compute the correlator with different choices of source position and average over them. Specifically, since we always measure along the third direction, we define the volume $V = L_0 L^2$. By translation invariance of eq. (5.2.17), we can average over all possible source positions[7] to obtain an estimator with the same expectation value of (5.2.17)

$$\overline{C}(x_3, y_3) \equiv \frac{a^3}{V} \sum_{\boldsymbol{y}} C(x_3, y) = C(x_3, y). \tag{5.2.22}$$

The variance of the above estimator can be shown to be (using again translation invariance)

$$\sigma^2_{\overline{C}} = \frac{a^3}{V} \sum_{\boldsymbol{y}} \Big\langle \left(\mathrm{Tr}\{C(x_3; y, y)\}\right) \left(\mathrm{Tr}\{C\left(x_3; (\mathbf{0}, y_3), (\mathbf{0}, y_3)\right)\}^*\right) \Big\rangle - \overline{C}(x_3, y_3)\overline{C}^*(x_3, y_3) \tag{5.2.23}$$

[7]The same argument can be applied to the case in which only a subset of the lattice volume is considered

Since the correlator falls off exponentially with a correlation length $1/\xi = m_\Gamma^{(n)} \gtrsim 2\pi T = \gamma 2\pi/L_0$ (for $n = 0, 1$), the sum in equation (5.2.23) will be saturated by the region $|\boldsymbol{y}| \lesssim 1/m_\Gamma^{(n)}$, hence reducing the coefficient entering the variance to an "effective volume" $\sigma^2_{\overline{C}} \propto 1/((m_\Gamma^{(n)})^3 V)$. Given the size of our lattices ($L_0/a = 4, 6, 8, 10$ and $L/a = 288$) as a very rough estimate we can expect a reduction of the variance of the order

$$\sigma^2_{\overline{C}} \propto \frac{L_0^2}{(\gamma 2\pi)^3 (288)^2}. \tag{5.2.24}$$

The square root of the above expression gives an order of magnitude estimate of the expected gain on the statistical error with which we are able to compute the correlator. For $\gamma = 1/\sqrt{2}$, the gain on the error ranges from $\sim 1/674$ ($L_0 = 4$) and $\sim 1/337$ ($L_0 = 10$). However, the cost of this approach scales badly with the lattice volume. Indeed, each inversion of the Dirac equation is an operation whose cost grows with the (4-dimensional) lattice volume V. For a fixed number of point sources n_s, the cost of computing the correlator then grows essentially like $n_s V$. We now see that if one wants to saturate the volume-averaged variance of equation (5.2.23) a number V of point sources are required, thus making this approach scale as $\sim V^2$. Given the fact that the gain in the error (root of the variance) is only of $\sqrt{V}$, we see how this is a prohibitively inefficient way to reduce the variance with volume averaging. We will try to leverage the statistical gain of volume averaging without the $\mathcal{O}(V^2)$ cost by employing random sources [190, 191] to stochastically estimate the correlation functions.

5.2.5 Random wall sources

To this end, we introduce a set of N_s auxiliary fields $\eta_i(y)$ which are decoupled from the dynamical fields of the theory. The label i runs from 1 to N_s. The source fields have support on lattice slices – or walls – with fixed third component, say $\overline{y}_3$:

$$\eta_i(y) = \delta_{y_3 \overline{y}_3} \eta_i(\boldsymbol{y}) \quad \forall a = 0, \dots 11, \tag{5.2.25}$$

and distributed so that the only non-zero cumulant is

$$\langle \eta_i(\boldsymbol{y}) \eta_j^*(\boldsymbol{z}) \rangle = \delta_{ij} \delta_{\boldsymbol{yz}}. \tag{5.2.26}$$

Possible choices include Gaussian, $\mathbb{Z}_2$ or U(1) noise. With the above introductions we can define an estimator which depends on the extra auxiliary fields and has the same expectation value as the correlator in equation (5.2.17), averaged over the

lattice volume:

$$\mathcal{C}(x_3,\overline{y}_3) \equiv \frac{a^3}{V}\frac{1}{N_s}\sum_{i=1}^{N_s}\sum_{\boldsymbol{x},\boldsymbol{y},\boldsymbol{z}} e^{i\phi_n(x-y)}\,\mathrm{Tr}\{\eta_i^*(y)\Gamma S(x,y)\Gamma' S(z,x)\eta_i(z)\}\Big|_{z_3=y_3=\overline{y}_3} \tag{5.2.27}$$

$$= \frac{a^3}{V}\sum_{\boldsymbol{x},\boldsymbol{y}}\langle \mathrm{Tr}\{C(x_3;y,y)\}\rangle\Big|_{y_3=\overline{y}_3}$$

Note that for a given configuration of link fields and source fields, the expression (5.2.27) can be evaluated by solving the Dirac equation for fields $\varphi_i(x)$ and $\tilde{\varphi}_i(x)$ with sources given by

$$\varphi_i(x) = \sum_{\boldsymbol{z}} S(x,z)\Big|_{z_3=\overline{y}_3}\eta_i(\boldsymbol{z}), \tag{5.2.28}$$

$$\tilde{\varphi}_i(x) = e^{-i\phi_n(x)}\sum_{\boldsymbol{y}} S(x,y)\Big|_{y_3=\overline{y}_3}\gamma_5\Gamma^\dagger e^{i\phi_n(y)}\eta_i(\boldsymbol{y}) \tag{5.2.29}$$

through the identity

$$\mathcal{C}(x_3,\overline{y}_3) = \frac{a^6}{L_0L_1L_2}\frac{1}{N_s}\sum_{i=1}^{N_s}\sum_{\boldsymbol{x}}\tilde{\varphi}^\dagger(x)\gamma_5\Gamma'\varphi_i(x) \tag{5.2.30}$$

When computing the variance of the estimator in equation (5.2.27), two contributions appear due to the two possible contractions of four source fields in the square of equation (5.2.27). In addition to the gauge variance of the volume-averaged correlator in equation (5.2.23), an extra "noise" contribution arises:

$$\sigma_{\mathcal{C}}^2 = \sigma_{\overline{C}}^2 + \frac{a^6}{V^2}\frac{1}{N_s}\sum_{\substack{\boldsymbol{x},\boldsymbol{y}\\ \boldsymbol{x}',\boldsymbol{y}'}} e^{i\phi_n(x-x')}\langle \mathrm{Tr}\big[\Gamma S(x,y)\Gamma' S(y',x)\Gamma^\dagger S^\dagger(y',x')\Gamma'^\dagger S^\dagger(x',y)\big]\rangle\Big|_{\substack{y_3=y_3'\\ x_3=x_3'}} \tag{5.2.31}$$

The noise contribution can be depicted diagrammatically as:

$$\sigma_{\mathcal{C}}^2 - \sigma_{\overline{C}}^2 = \sum_{\substack{\boldsymbol{x},\boldsymbol{x}'\\ \boldsymbol{y},\boldsymbol{y}'}}$$

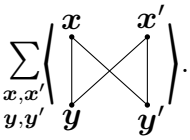

We comment on a few important aspects at this ponit. First of all, equations (5.2.28) and (5.2.29) tell us that to estimate the correlator with Matsubara frequency labeled by n, two inversions of the Dirac equation are required: one on

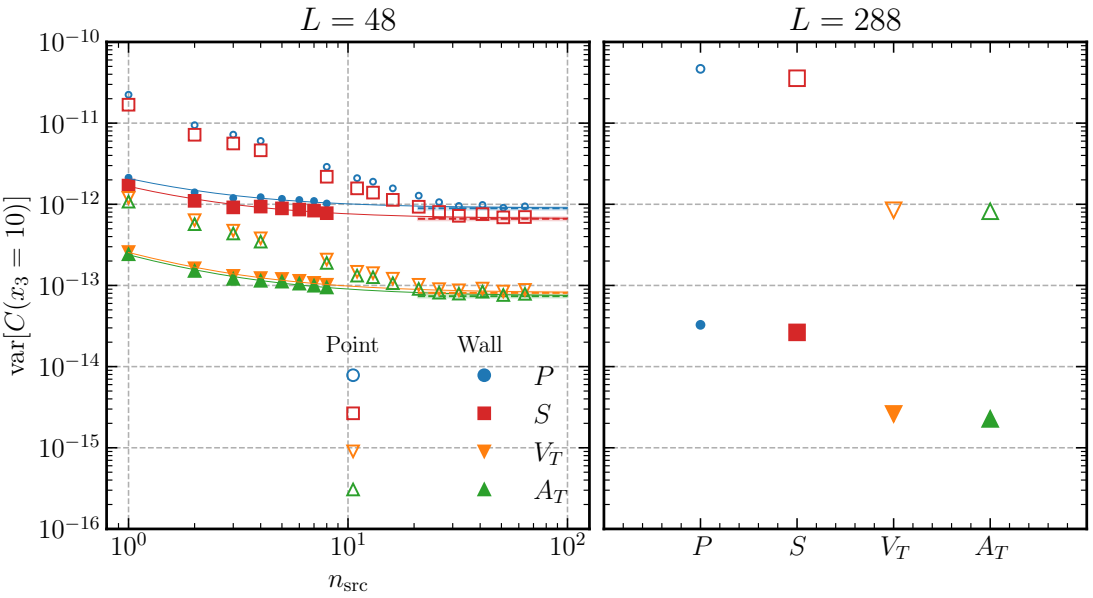

FIGURE 5.6: Left: variance of mesonic correlators in different channels at $x_3/a = 10$ as a function of the number of sources used, for both point sources (empty symbols) and random wall sources (full symbols) on a $6{\times}48^3$ lattice. Colored lines are fits of the random source variance to a function reproducing the expected behaviour given by (5.2.31), i.e. a constant (the gauge variance, represented by the dashed line around which the point source vairance saturates) plus a term suppressed with $1/n_{\mathrm{src}}$ (the noise variance). Right: variance of the correlator at $x_3/a = 10$ in different meson channels obtained on a single point source (empty symbols) and a single random source (full symbols) on a 6×288^3 lattice.

the extracted random source and one random source multiplied by the suitable phase factor that projects to the desired Matsubara sector. This means that, by construction, one always computes the necessary elements to estimate the static correlators with $n = 0$, which can be reconstructed from the φ fields alone. For this reason, the computational cost to determine the non-static correlators already includes the possibility to compute the volume-averaged static ones, at the sole cost (by far subdominant with respect to the inversion of the Dirac operator) of performing the relevant contractions. In our application we have used random sources to compute volume-averaged correlators in the $n = 1$ and $n = 2$ non-static sectors, and as a by-product re-computed the static correlators determined with point sources in [54] with increased precision.

The benefit of using random sources to reduce the variance is essentially due to the fact that the extra contribution to the volume-averaged gauge variance due

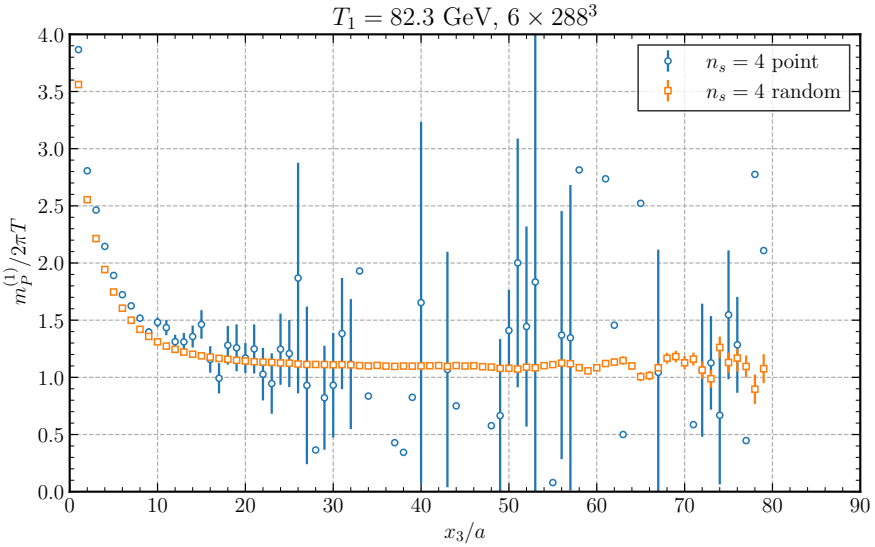

FIGURE 5.7: Effective pseudoscalar screening mass with Matsubara frequency $\omega_1 = 2\pi T$ extracted from a correlator computed with 4 point sources (blue points, same as figure 5.5) and with 4 random sources (orange squares), at temperature T_1 on a 6×288^3 lattice.

to the presence of the random sources scales as $1/N_s$: it may thus be possible that with a moderate number of random sources the noise contribution becomes smaller than the gauge one. If this were the case, one could reach the volume-averaged variance (5.2.23) – which would require a number V/a^3 of inversions on point sources as argued in section 5.2.4 – with a much smaller number of random sources, thus saving computational resources.

We have implemented random U(1) sources, which amount to setting $\eta(\boldsymbol{x}) = \exp\{2\pi i r(\boldsymbol{x})\}$ where r is an $\boldsymbol{x}$-dependent random number uniformly distributed in the interval $[0, 1]$, in our measurement programs and extensively tested how the error on the correlator scales with the number of random sources utilized and the lattice volume, and compared it with the error on the correlator obtained with point sources as depicted in figure 5.6. This analysis fully confirms the expected scaling of the variance with the number of sources in our setup, and shows that a significant gain in precision can be achieved even with a single random source with respect to a single point source. Moreover, it also confirms that the variance reduction is more effective with larger volumes. In this regard it is also intersting to notice that in our high temperature ensembles random sources provide an effective way to reduce the variance across all mesonic channels considered, while at zero temperature the variance in the pseudoscalar and vector channels show quite

different behaviour, see for instance [192]. The fact that, for the high temperatures considered, the bulk of all meson screening masses in the $n = 0, 1$ sectors is given by $2\pi T$ and the very large spatial volumes employed in our simulations make the use of random sources extremely effective in significantly improving the StN of mesonic correlators, and allows the extraction of screening masses in channels which would be inaccessible with point sources, see figure 5.7.

5.2.6 Effective mass analysis

In this section we describe the strategy employed to determine the mesonic screening masses in the P, V_T and V_0 channels for both $n = 0$ and $n = 1$ Matsubara sectors. While in principle very similar to the approach employed for the baryonic screening mass described in section 5.1.3, we adopt a more automated and systematic approach to the determination of the two-state and one-state fit windows given the larger number of channels with different singal quality. The end point of both fits $x_3^{\max}$ was chosen as the last available point for which the relative error on the correlator is below 12.5%.

Two-state fit

To identify a range $[x_3^{\min}, x_3^{\max}]$ where the lowest energy state dominates we model the contribution to the effective mass of an excited state in a range $[x_3^{\text{start}}, x_3^{\max}]$, and determine when it becomes negligible with respect to the ground state. To do this, we begin by fitting the effective mass values with a functional form given by the contribution of two states to the correlator. Since bosonic fields are periodic in the x_3 direction, the contribution of the ground state to the correlator assumes the form

$$C_{\text{gs}}(x_3) = A\cosh(m_0(x_3 - L/2)), \tag{5.2.32}$$

where m_0 is the ground state screening mass, L is the spatial extent of the lattice and A is proportional to the matrix element of the relevant operator between the vacuum and the ground state. A better definition of the effective mass in this case is given by

$$am_{\text{eff}}(x_3) = \cosh^{-1}\left[\frac{C(x_3 + a) + C(x_3 - a)}{2C(x_3)}\right] \tag{5.2.33}$$

assuming that the correlator is given by the 4-parameter ansatz

$$C^{2s}(x_3; A, m_0, B, m_1) = A\cosh(m_0(x_3 - L/2)) + B\exp(-m_1 x_3) \tag{5.2.34}$$

where m_0 models the screening mass and m_1 the first excited state, the function we fit to the effective mass data is

$$am^{2s}(x_3; B/A, m_0, m_1) = \cosh^{-1}\left(\frac{C^{2s}(x_3 + a) + C^{2s}(x_3 - a)}{2C^{2s}(x_3)}\right), \tag{5.2.35}$$

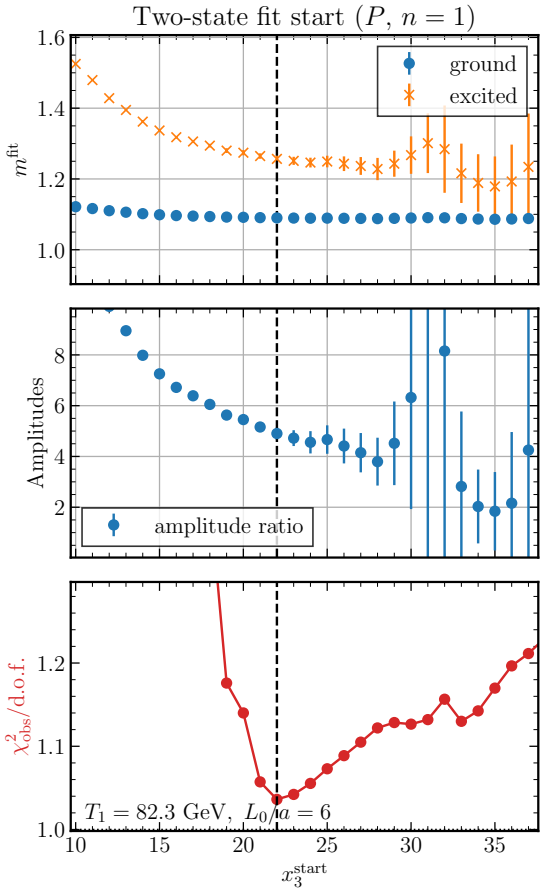

FIGURE 5.8: Selection of the starting point for the two-state fit to the function (5.2.35) for the pseudoscalar screening mass in the $n = 1$ Matsubara sector for T_1 on a 6×288^3. Panels show the ground state –blue points– and first excited state mass -orange crosses– (top), the ratio of the amplitudes of the first excited and ground state (middle, B/A in equation (5.2.35)) and the reduced uncorrelated χ^2 of the fit as a function of the starting point for the two-state fit. The dashed vertical line is the chosen starting point for the two-state fit as described in the main text ($x_3^{\text{start}} = 23$ in this case).

which depends only on 3 parameters (the two screening masses and the ratio of amplitudes B/A). We systematically vary the starting point of the fit x_3^{start} and monitor the quality of the fit (uncorrelated χ^2/d.o.f.), the stability and relative error of the fit parameters. We select the starting point by looking for a local minimum of the χ^2 where all the parameters are different from 0 within their uncertainties and relatively stable under variation of the starting point. An example of this procedure is shown in figure 5.8.

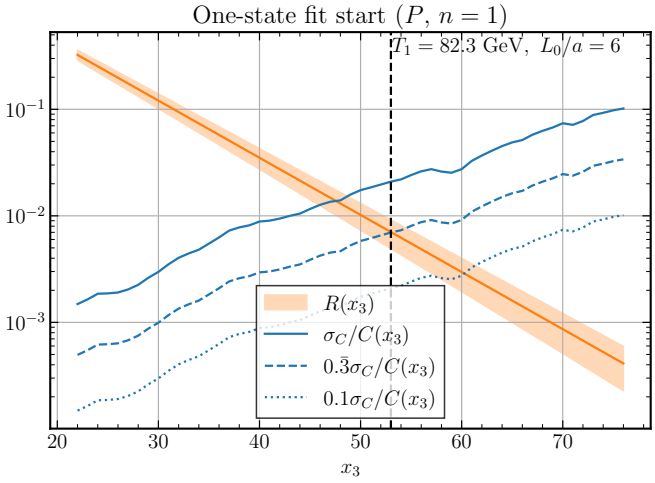

FIGURE 5.9: Selection of the starting point for the one-state fit (plateau). The contribution of the first excited state relative to the ground state defined in equation (5.2.36) (orange band) is compared to fractions of the relative error on the correlator (blue lines) to determine when it becomes negligible. The starting point is depicted by a dashed vertical line ($x_3^{\min} = 53$ in this case)

One-state fit

Once we have a credible description of the data in terms of ground and first excited state contribution, we can quantitatively decide when the correlator is dominated by a single state. Indeed, with the results of the fit to eq (5.2.35) we can build the following dimensionless ratio:

$$R(x_3) = \frac{C^{2s}(x_3) - C^{1s}(x_3)}{C^{1s}(x_3)} \tag{5.2.36}$$

which only depends on m_0, m_1 and B/A and quantifies the contribution of the excited state relative to the ground state. This can be compared with the relative error on the measured correlator, and we can define the start of the plateau as the value of $x_3^{\min}$ for which $R(x_3)$ becomes smaller than a chosen fraction of the relative error. As anticipated, the precision with which we can determine correlators varies significantly across channels and sectors. The P and V_T channels in the static sector do not suffer from a StN problem and are now determined with an impressive precision below the permille (see figure 5.11 for an example of the gain in statistical precision obtained in the static sector with respect to [54]). In practice we adopt

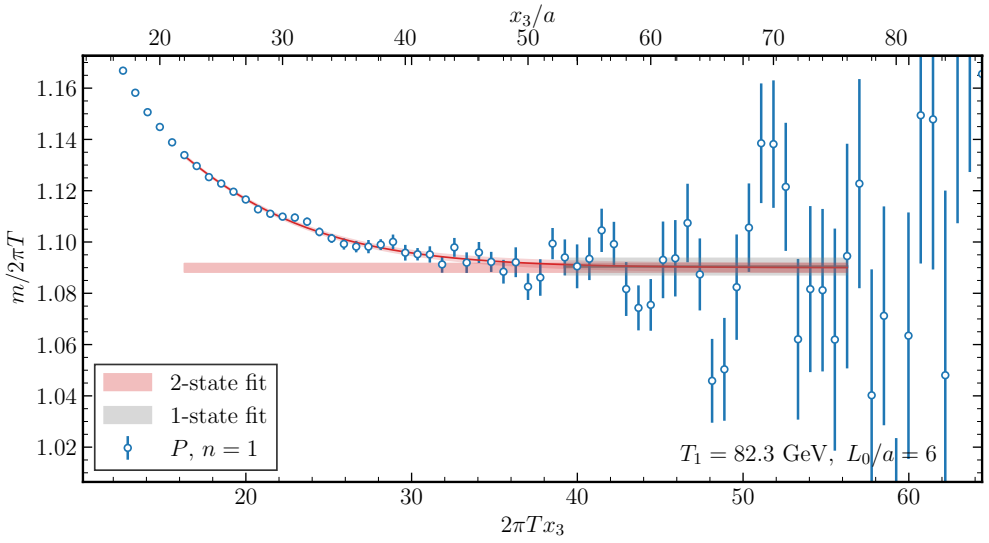

FIGURE 5.10: Effective pseudoscalar screening mass in the $n = 1$ Matsubara sector. The red curve is the two-state fit of equation (5.2.35) to the data, and the red horizontal band corresponds to the estimate of the ground state screening mass with this fit. The gray band is the result of the fit to a constant in a range where the contribution from the excited state is negligible, and serves as our final estimate of the screening mass. The results of the fits are drawn in the ranges where they have been applied, determined as described in the main text.

the following thresholds:

$$x_3^{\min} = \min\left\{ x_3 \quad \text{s.t.} \quad R(x_3) \leq \frac{\sigma_C(x_3)}{C(x_3)} \times \begin{cases} \dfrac{1}{10} & \text{for } P,\ V_T \text{ at } n = 0 \\ \dfrac{1}{3} & \text{otherwise} \end{cases} \right\} \tag{5.2.37}$$

An example of this operation is displayed in figure 5.9 Once the starting point for the one-state fit has been determined, our final estimate for the screening mass is given by a fit of a constant to the effective mass in the range $[x_3^{\min}, x_3^{\max}]$. An example of both the two-state and one-state fits for the the pseudoscalar effective mass is displayed in figure 5.10 for the $n = 1$ sector and figure 5.11 for the $n = 0$ sector. Our best estimates of mesonic screening masses at all temperatures and lattice spacings are reported in appendix F in tables F.1 and F.2 for the static sector, and in tables F.3 and F.4 for the non-static $n = 1$ sector.

Before discussing the continuum limit extrapolation of our data and studying its dependence on the temperature, we highlight a few important aspects of the non-perturbative data contained in the aforementioned tables. As anticipated, the

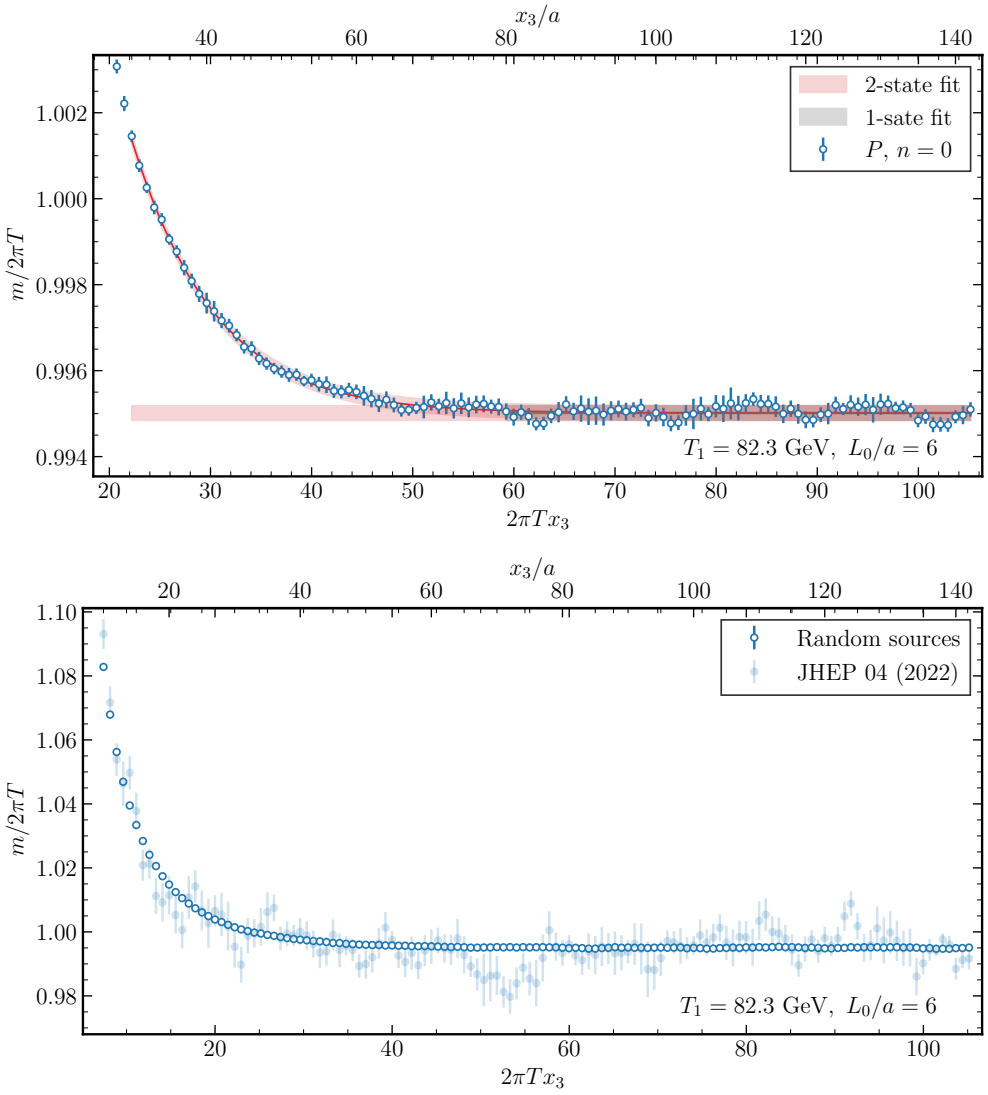

FIGURE 5.11: Top: as in figure 5.10, but for the static $n = 0$ Matsubara sector. Bottom: comparison of the effective pseudoscalar static screening mass as obtained with point sources in [54] (shaded points) and in this work with random wall sources (full points).

static P and V_T channels are now determined with very high precision below the permille, and also their splitting shows an increased precision with respect to the original determination of [54]. The screening masses in the other channels and sector are determined at the percent level or better. We remark on the fact that the V_0 and V_3 channels in the $n = 1$ sector are degenerate within their rather small errors, which is expected in the continuum since the two correlators are related by the Ward Identity associated to the conservation of the vector current

(5.2.13). Similarly, it is interesting to notice that also the P and V_T screening masses in the $n = 1$ sector are compatible within uncertainties, at variance with what happens in the static sector where a spin splitting is clearly observable. Although the screening masses in this sector are determined with less precision than their static counterparts, it could mean that the spin-dependent potential in the $n = 1$ sector, analogous to the one computed in section 4.2 for the $n = 0$ sector, is more suppressed. Prelimary investigations suggest that the hyperfine splitting in the $n = 1$ sector assumes a similar for as the one found for the static sector; however, the ground state wavefunction of the non-static potential is a p-state in this case, which vanishes at the origin and would therefore be consistent with the much smaller spin-splitting observed in the lattice data. It will be interesting to investigate this further in the future. With these remarks in mind, for the $n = 1$ sector we will focus only on the P and V_0 channels in the following discussion.

5.2.7 Continuum limit and temperature dependence

Once the screening mass of different channels has been obtained for all temperatures and lattice spacings a controlled continuum limit can be taken. Like for the baryonic case, we have computed the mesonic screening masses at tree level in the lattice theory as reported in appendix G.1. We find that the screening mass at tree level is the same not only across all mesonic channels considered, but also between the $n = 0$ and $n = \pm 1$ Matsubara sectors, and we thus denote it with m^{free}. We define tree-level improved mesonic screening masses in the $n = 0, 1$ sectors as

$$\frac{m_\Gamma^{(n),\text{tli}}}{2\pi T} = \left(\frac{m_\Gamma^{(n)}}{2\pi T} - \frac{m^{\text{free}}}{2\pi T} \right) + 1, \tag{5.2.38}$$

where Γ labels the channels we consider $\Gamma \in \{P, V_0, V_T\}$, and extrapolate the tree-level improved data to the continuum. As reported in tables F.1–F.4, the precision with which we have determined the screening mass varies significantly across sectors and channels, essentially due to different severity of the exponential problem. The P and V_T channels in the static sectors are determined with a precision well below the permille; the V_0 channel in the $n = 1$ sector – which is actually lighter than in the static sector, see also [160] – is determined at the permille level, while the P and V_T channels in the $n = 1$ sector and the static V_0 channel are determined with a precision of about 1%. In the static P and V_T channels particularly the continuum extraction must be performed with care[8]. Indeed, not only does data

[8]We have also chekced that the systematic error on the screening masses induced by the uncertainty in the determination of the lines of constant physics is negligible with respect to the statistical error.

at fixed temperature show relevant discretization effects that require higher powers than $(a/L_0)^2$ to be described, but attempting to perform separate continuum limits for each temperature as done for the baryonic case reveals unacceptably χ^2/d.o.f. For this reason, we decide to leverage the large number of data points and perform a global fit of the data at different temperatures and lattice spacing, modeling the temperature dependence of discretization effects and of the continuum data directly. As a matter of fact, the strategy described below turned out to be preferable also in the other channels and sectors, and therefore in this thesis we present results obtained applying it in all cases.

Similarly to what we did when investigating the temperature dependence of baryonic screening masses, we study the lattice data as a function of $\hat{g}(T)$, where we now opt for the 5-loop $\overline{\text{MS}}$ coupling renormalized at a scale $\mu = 2\pi T$, obtained by numerically integrating the 5-loop beta function [16, 17]. We stress once again that for our purposes this is just a convenient choice to parameterize the dependence of the non-perturbative data on the temperature, and which also allows to exploit the information coming from perturbation theory to guide the interpretation of the lattice data.
As a first step, for each channel and sector we fit the data in tables F.1–F.4 with the following *ansatz*, which we label as FULL

$$\begin{aligned}\frac{m}{2\pi T}(a/L_0, T) = &\left(1 + b_2\ \hat{g}^2(T) + b_3\ \hat{g}^3(T) + b_4\ \hat{g}^4(T)\right) \\ &+ \left(\frac{a}{L_0}\right)^2 \left(d^X_{2,2}\ \hat{g}^2(T) + d^X_{2,3}\ \hat{g}^3(T)\right) \\ &+ d^X_{3,2}\ \left(\frac{a}{L_0}\right)^3\ \hat{g}^2(T).\end{aligned} \tag{5.2.39}$$

The first line represents the parameterization of the screening mass in the continuum as a funciton of $\hat{g}(T)$. Both the tree-level contribution and the $\mathcal{O}(g^2)$ one are set to the analytically known parts of the weak coupling expansion summarized in table 3.2, while b_3 and b_4 are free parameters in the fit. Having a large number of precise points, lattice artifacts are modeled with the aim to capture both the deviation from the leading $\mathcal{O}((a/L_0)^2)$ discretization effects (represented by the cubic term proportional to the coefficients $d^X_{3,2}$) and also subleading temperature-dependent effects in the leading lattice artifact, given by the $d^X_{2,3}$ term. We stress that since the high temperatures $T_0 - T_8$ are discretized with the Wilson plaquette action and the low ones $T_9 - T_{11}$ with the Lüscher-Weisz action, they are affected by different discretization effects. For this reason we employ two different coefficients for each term $d^X_{i,j}$ in equation (5.2.39), one referring to lattice artifacts for the nine highest temperatures and labeled by $d^{\text{H}}_{i,j}$ and one referring to the three

	$P,\ n=0$		$V_T,\ n=0$	
	FULL	MOD	FULL	MOD
b_3	0.00962(49)	0.0128(10)	0.00389(67)	0.0057(15)
b_4	-0.02181(36)	-0.02421(77)	-0.01006(49)	-0.0114(11)
$\frac{\mathrm{cov}(b_3 b_4)}{\sigma_{b_3}\sigma_{b_4}}$	-0.9760	-0.9823	-0.9806	-0.9853
$d^{\mathrm{H}}_{2,2}$	0.282(16)	-0.04(12)	0.325(22)	0.20(14)
$d^{\mathrm{L}}_{2,2}$	0.343(19)	0.281(30)	0.280(40)	0.235(52)
$d^{\mathrm{H}}_{2,3}$	-0.0063(67)	0.212(98)	-0.0440(82)	0.01(12)
$d^{\mathrm{L}}_{2,3}$	-0.016(12)	0.048(22)	-0.024(28)	0.016(42)
$d^{\mathrm{H}}_{3,2}$	-0.304(43)	-	-0.308(58)	-
$d^{\mathrm{L}}_{3,2}$	-0.437(51)	-0.532(85)	-0.273(67)	-0.31(12)
χ^2/d.o.f.	5.11	1.29	5.31	1.08

TABLE 5.4: Results of the combined continuum limit and temperature fit for the P and V_T channels in the static Matsubara sector. The labels FULL and MOD refer to the fit strategies described in the main text.

lowest temperatures denoted as $d^{\mathrm{L}}_{i,j}$. This fit therefore has $2 + 2 \times 3 = 8$ free parameters and 43 data points, resulting in 35 degrees of freedom. While it is able to capture the dependence of the data on the lattice spacing and temperature, this fit yields in general – particularly so for the static P and V_T channels – rather high values of χ^2/d.o.f.. We find that most of the discrepancy can be traced back to the data at $L_0/a = 4$, which is affected by large discretization effects and displays very small errors which highly influence the fit. We have tried changing the functional form of equation (5.2.39) by adding or removing terms to both the continuum parameterization or the modeling of lattice artifacts, without noticeable gains in the fit quality. We have also tried excluding the $L_0/a = 4$ data for all temperatures or subsets of the temperatures considered and repeat the fit, without finding an improvement in quality. Especially for the lower temperatures, where only three lattice spacings are available, it is crucial to extract as much information also from the coarsest ensemble.

For this reason, we treat the data at high temperatures ($T_0 - T_8$) and at low temperatures ($T_9 - T_{11}$) in a slightly different way. We discard the $L_0/a = 4$ data for the 9 highest temperatures only while retaining it for the lowest 3; in addition to that, we use the results of the previous fit to estimate the magnitude of subleading discretization effects in the finer ensembles at high temperatures, and inflate the errors on the $L_0/a = 6, 8, 10$ points accordingly. Specifically, we compute the contribution due to the $\mathcal{O}((a/L_0)^3)$ term arising from the fit of equation (5.2.39)

	$P,\ n=1$		$V_0,\ n=1$	
	FULL	MOD	FULL	MOD
b_3	0.088(15)	0.087(28)	0.0213(15)	0.0245(23)
b_4	-0.047(11)	-0.039(23)	-0.0131(11)	-0.0156(19)
$\frac{\mathrm{cov}(b_3 b_4)}{\sigma_{b_3}\sigma_{b_4}}$	-0.9670	-0.9865	-0.9762	-0.9911
$d^{\mathrm{H}}_{2,2}$	0.47(56)	0.76(2.28)	0.200(52)	0.03(16)
$d^{\mathrm{L}}_{2,2}$	0.13(1.01)	-0.35(1.20)	0.053(80)	0.000(78)
$d^{\mathrm{H}}_{2,3}$	0.24(31)	-0.98(1.94)	-0.115(23)	-0.01(14)
$d^{\mathrm{L}}_{2,3}$	0.55(74)	0.07(1.09)	-0.016(51)	0.055(69)
$d^{\mathrm{H}}_{3,2}$	-4(1)	-	-0.18(14)	-
$d^{\mathrm{L}}_{3,2}$	-4(2)	-0.26(2.75)	-0.24(17)	-0.40(24)
χ^2/d.o.f.	1.65	0.72	2.28	1.37

TABLE 5.5: Same as in table 5.4 but for the P and V_0 channels in the $n=1$ Matsubara sector. We have observed that at all lattice spacings and temperatures considered, the V_T channel is compatible with the P channel, and the V_3 with the V_0 (see tables F.3 and F.4), and we therefore omit them from this analysis for the time being.

in the high-temperature data, namely

$$\Delta\left(a/L_0, \hat{g}(T)\right) = d^{\mathrm{H}}_{3,2}\hat{g}^2(T)\left(\frac{a}{L_0}\right)^3, \quad T \in [T_0,\ T_8], \tag{5.2.40}$$

and treat it as a systematic error for the data points at $L_0/a = 6, 8, 10$ by adding it in quadrature to the statistical error

$$\sigma^2_{\mathrm{mod}}(a/L_0, \hat{g}(T)) = \sigma^2_{\mathrm{stat}}(a/L_0, \hat{g}(T)) + \Delta^2(a/L_0, \hat{g}(T)), \quad T \in [T_0,\ T_8]. \tag{5.2.41}$$

We then perform a global fit of all data at T_0–T_8 excluding the $L_0/a = 4$ points with the modified weights given by equation (5.2.41) and all data at $T_9 - T_{11}$, including the $L_0/a = 4$ points with unaltered errors, with a functional form given by equation (5.2.39) excluding the term proportional to $(a/L_0)^3$ for the high temperature ensembles:

$$\begin{aligned}\frac{m}{2\pi T}(a/L_0, T) = &\left(1 + b_2\ \hat{g}^2(T) + b_3\ \hat{g}^3(T) + b_4\ \hat{g}^4(T)\right) \\ &+ \left(\frac{a}{L_0}\right)^2 \left(d^X_{2,2}\ \hat{g}^2(T) + d^X_{2,3}\ \hat{g}^3(T)\right) \\ &+ d^{\mathrm{L}}_{3,2}\ \left(\frac{a}{L_0}\right)^3\ \hat{g}^2(T).\end{aligned} \tag{5.2.42}$$

The resulting fit, which we label MOD, has 7 free parameters for 34 points corre-

	$V_0,\ n=0$	
	FULL	MOD
b_3	0.052(12)	0.059(34)
b_4	-0.0283(90)	-0.031(25)
$\frac{\mathrm{cov}(b_3 b_4)}{\sigma_{b_3}\sigma_{b_4}}$	-0.9772	-0.9826
$d^{\mathrm{H}}_{2,2}$	1.89(43)	-0.68(3.82)
$d^{\mathrm{L}}_{2,2}$	3.07(85)	3(1)
$d^{\mathrm{H}}_{2,3}$	-0.16(25)	0.72(3.17)
$d^{\mathrm{L}}_{2,3}$	-0.59(58)	-0.56(91)
$d^{\mathrm{H}}_{3,2}$	-10(1)	-
$d^{\mathrm{L}}_{3,2}$	-12(2)	-11(3)
χ^2/d.o.f.	1.88	0.17

TABLE 5.6: Same as in tables 5.4 and 5.5 but for the V_0 channels in the $n = 0$ Matsubara sector.

sponding to 27 degrees of freedom, provides a very good description of the lattice data and furnishes a precise parameterization of temperature dependence of the screening masses in the continuum, encoded in the b_3 and b_4 parameters. The results of both fits are reported in tables 5.4, 5.5 and 5.6, see figure 5.12 for an example of the combined fit.

Following the same combined fit strategy as above, we are also able to compute the hyperfine splitting with increased precision with respect to [54]. The fit functions have to be adapted to account for the fact that the hyperfine splitting starts at $\mathcal{O}(g^4)$; for instance, equation (5.2.39) is modified according to

$$\begin{aligned}\frac{m_{V_T}-m_P}{2\pi T}(a/L_0,T) = &\left(s_4\ \hat{g}^4(T) + s_5\ \hat{g}^5(T) + s_6\ \hat{g}^6(T)\right)\\ &+\left(\frac{a}{L_0}\right)^2\ \left(d^X_{2,4}\ \hat{g}^4(T) + d^X_{2,5}\ \hat{g}^5(T)\right)\\ &+ d^X_{3,4}\ \left(\frac{a}{L_0}\right)^3\ \hat{g}^4(T).\end{aligned} \tag{5.2.43}$$

where the coefficient $s_4 = 0.002376\ldots$ is the one we computed in perturbation theory in section 4.2. With these modification, the fit proceeds exactly as described above, and the results are summarized in table 5.7. We remark on the fact that within the current level of precision including a single $\mathcal{O}(g^4)$ term as a free parameter in the interpolation of the continuum data does not yield a satisfactory fit quality, and higher powers of g must be included from the start.

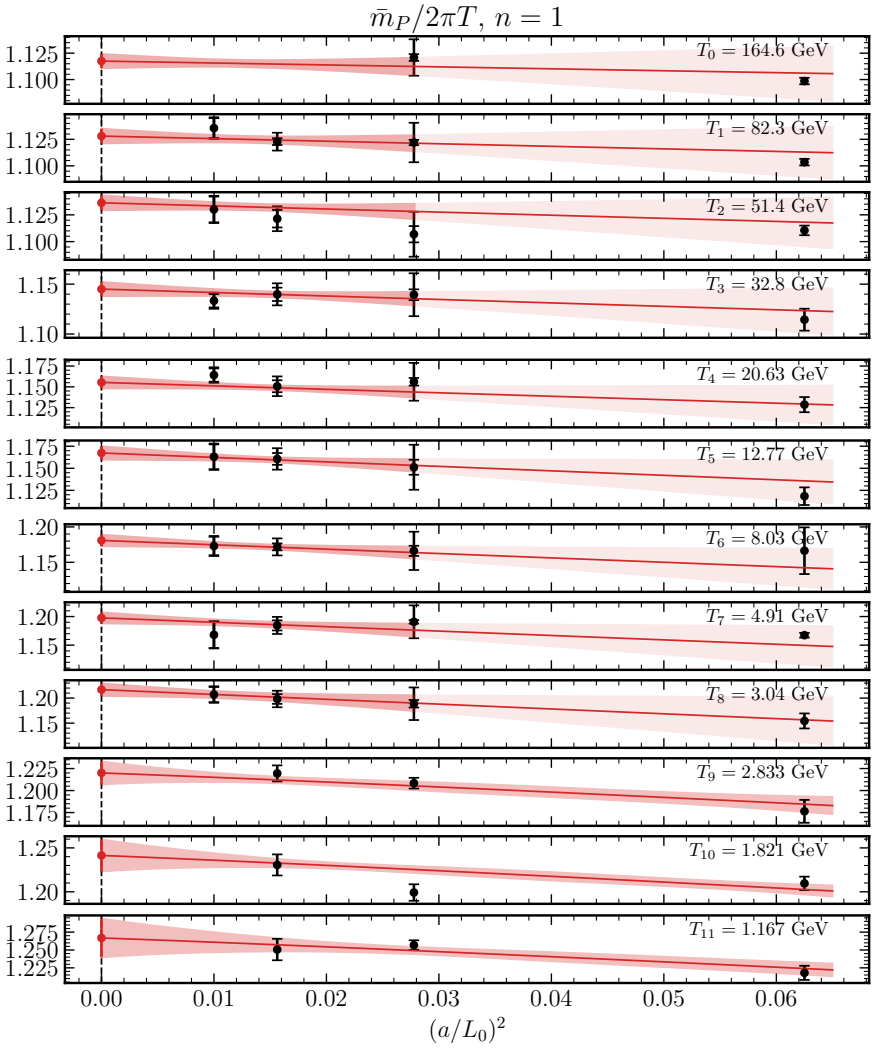

FIGURE 5.12: Tree-level improved pseudoscalar screening mass in the $n = 1$ Matsubara sector (black points) and the result of the combined continuum extrapolation and interpolation in $\hat{g}(T)$ (red lines and bands) performed as described in the main text (fit MOD). Data for $L_0/a = 4$ at the 9 highest temperatures is excluded from the fit, and the errors for the $L_0/a = 6, 8, 10$ points at these temperatures are rescaled as described in the main text (outer errorbars).

5.3 Comparison with perturbation theory

Our final results for the continuum screening masses parameterized as a function of $\hat{g}(T)$ as described above are reported in figure 5.13. The NLO perturbative expressions reported in table 3.2 are instrumental to guide the parameterization of the

	Hyperfine splitting	
	FULL	MOD
s_5	0.00507(20)	0.00468(28)
s_6	-0.00096(15)	-0.00065(23)
$\frac{\mathrm{cov}(s_5 s_6)}{\sigma_{s_5}\sigma_{s_6}}$	-0.9766	-0.9883
$d^{\mathrm{H}}_{2,4}$	-0.0114(74)	0.040(22)
$d^{\mathrm{L}}_{2,4}$	-0.072(13)	-0.064(14)
$d^{\mathrm{H}}_{2,5}$	-0.0000(32)	-0.040(19)
$d^{\mathrm{L}}_{2,5}$	0.029(20)	0.017(11)
$d^{\mathrm{H}}_{3,4}$	0.0279(92)	-
$d^{\mathrm{L}}_{3,4}$	0.069(25)	0.097(30)
χ^2/d.o.f.	3.85	1.65

TABLE 5.7: Results of the combined fits for the hyperfine splitting in the static sector.

lattice data, ensuring that the correct behaviour is reproduced at asymptotically high temperatures. Although we observe that the hierarchy of screening masses predicted by the perturbative analysis holds also in the lattice data, significant deviations from $\mathcal{O}(g^2)$ perturbation theory persist over the whole temperature range explored. This is particularly striking, for instance, in the non-static pseudoscalar or in the static temporal vector channels: not only does the non-perturbative data show deviations from the free-theory value ranging from 10% up to 25%, but also discrepancies of about 10% with respect to the NLO perturbative value persist at all temperatures considered. It is also interesting to notice that in these channels the fit parameters b_3 and b_4, which effectively encapsulate contributions from all powers higher than g^2 to the screening mass, have similar magnitude and opposite sign, amounting to an effective compensation similar to the one observed in the hyperfine splitting and pointed out in section 4.2.

As anticipated in the previous sections, the high-precision determination of the hyperfine splitting allows us to study in more detail the comparison with perturbation theory. Figure 5.14 displays the result of the combined continuum limit and interpolation in $\hat{g^4}(T)$, compared to the pertubative result discussed above and the lattice data of [54], from which it is possible to appreciate the increased precision, of about a factor 10, with which we have determined the spin-splitting in the continuum. As mentioned before, with this level of precision it is not possible anymore to describe the non-perturbative data with a single g^4 effective term, and higher orders are necessary from the start. Having computed the leading perturbative coefficient is instrumental to parameterize the lattice data

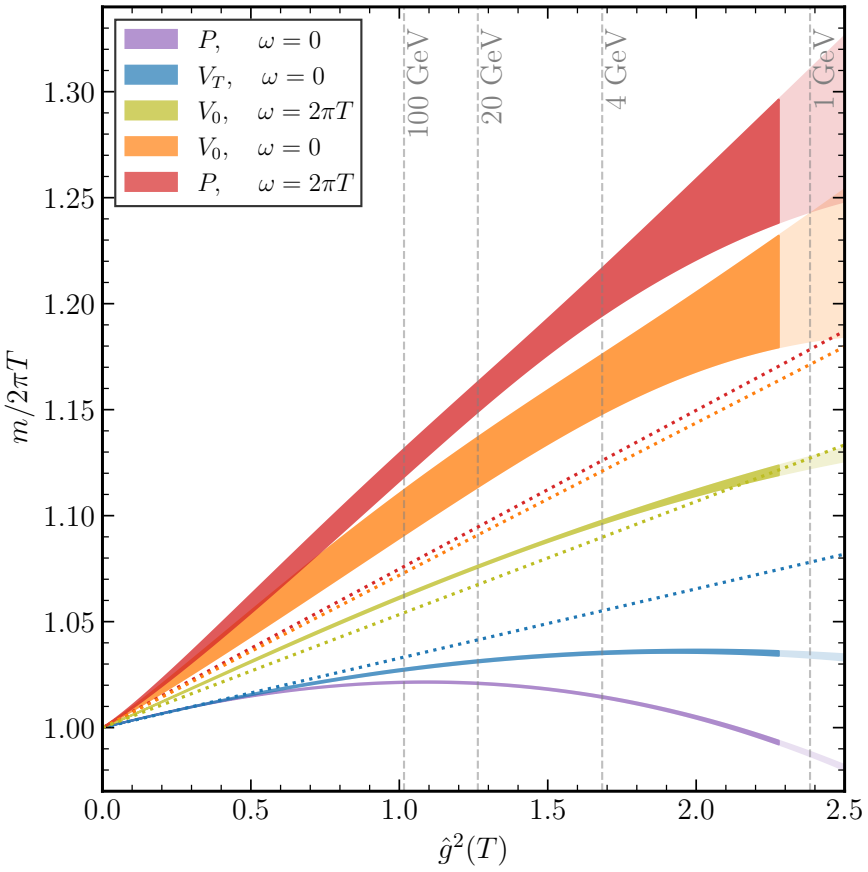

FIGURE 5.13: Temperature dependence of the continuum extrapolated mesonic screening masses in the various channels and sectors investigated in this thesis. The screening masses are normalized to the free-theory value i.e. $2\pi T$. Bands represent 1σ intervals of the continuum parameterization of screening masses as a function of the temperature-dependent coupling $\hat{g}(T)$. Straight lines represent the value of the screening masses at $\mathcal{O}(g^2)$ in perturbation theory, showing significant qualitative and quantitative discrepancies with the non-perturbative data over the whole temperature range. The grey vertical lines show some indicative temperature values.

and ensure that the correct asymptotics are reproduced. We stress once again that the higher powers than g^4 in the hyperfine splitting receive contributions of non-perturbative orgin, for example from a string term in the spin-independent potential, limiting the applicability of perturbation theory to the leading order[9]. Our non-perturbative data clearly show that these non-perturbative contributions remain relevant, and in this case dominant, up to electroweak-scale temperatures.

[9]See [193] for a qualitative study on the non-perturbative effects in static mesonic screening masses

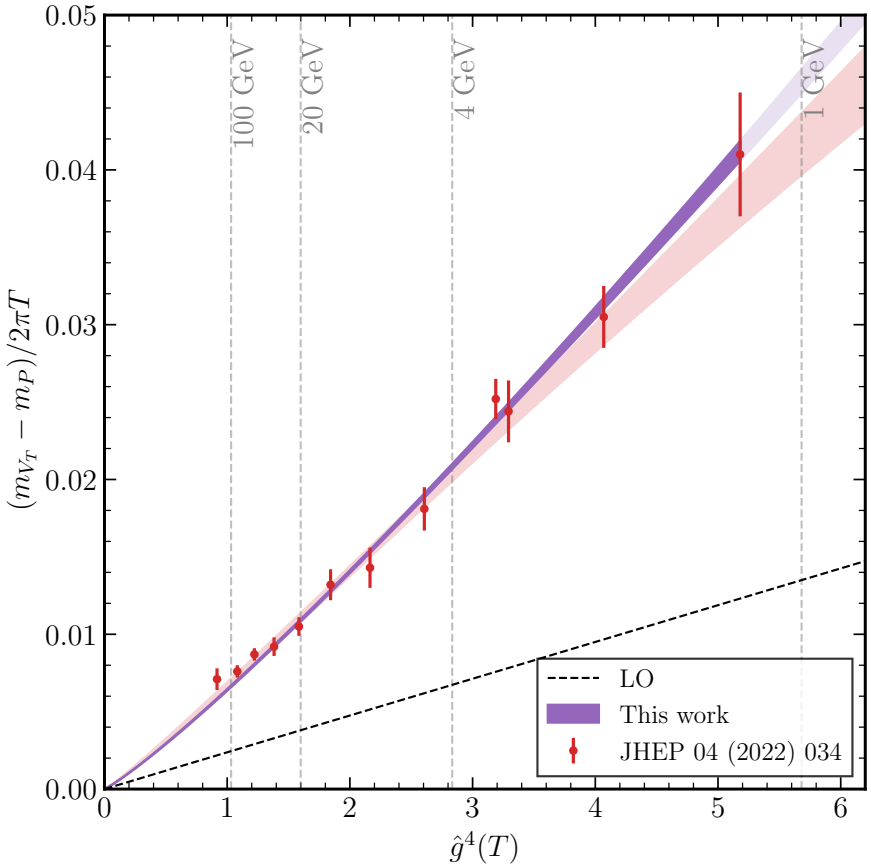

FIGURE 5.14: Comparison of the temperature dependence of the hyperfine splitting in the continuuum determined with point and random wall sources. The red points and bands are the same as in figure 4.4, while the purple band is the result of the combined continuum extrapolation of the random source data described in the main text.

Conclusions and perspectives

In this thesis we have presented an in-depth study of screening masses in thermal QCD over a wide temperature range going from $T \sim 1$ GeV up to the electroweak scale $T \sim 165$ GeV. We have determined the screening masses of states with quantum numbers corresponding to the nucleon and flavor non-singlet mesons, the latter with both spin 0 and 1, both in the static and non-static Matsubara sectors. Our results have been obtained with non-perturbative simulations of lattice QCD with $N_f = 3$ flavors of massless $\mathcal{O}(a)$-improved Wilson fermions, exploiting a recently proposed strategy that allows to efficiently simulate the theory at very high temperatures. They represent the first results for nucleon screening masses in the literature [2], and the first determination of non-static mesonic screening masses for temperatures up to $T \sim 165$ GeV. It was possible to investigate the non-static mesonic sector, which is affected by a severe signal-to-noise ratio problem, thanks to an algorithmic strategy we developed to efficiently perform averages over the lattice volume of the relevant correlators to reduce the error on our estimators. As a by-product, this also allowed us to measure the static screening masses, which were previously determined at the permille level [54], with up to an order of magnitude smaller errors. With the aim of aiding the interpretation of the non-perturbative data, we have also performed perturbative computations of screening masses in the three-dimensional effective theory that describes QCD at asymptotically high temperatures. Specifically, we have determined the $\mathcal{O}(g^2)$ next-to-leading order correction to the nucleon screening mass [3], and the $\mathcal{O}(g^4)$ leading order value of the hyperfine splitting in static mesonic masses [1], which were not previously known. We find that the available terms in the weak coupling expansion are not able to explain the screening masses at the obtained level of precision, with sizeable deviations persisting over the whole temperature range. In particular the hyperfine splitting, now determined at the percent level, is dominated by terms beyond the leading order which can be shown to receive contributions of non-perturbative origin. Moreover, owing to the increased precision, it is not possible anymore to describe the non-perturbative data with a single effective $\mathcal{O}(g^4)$ term, as was previously found in [54]. Our results across all channels and sectors considered are summarized in figure 5.15.

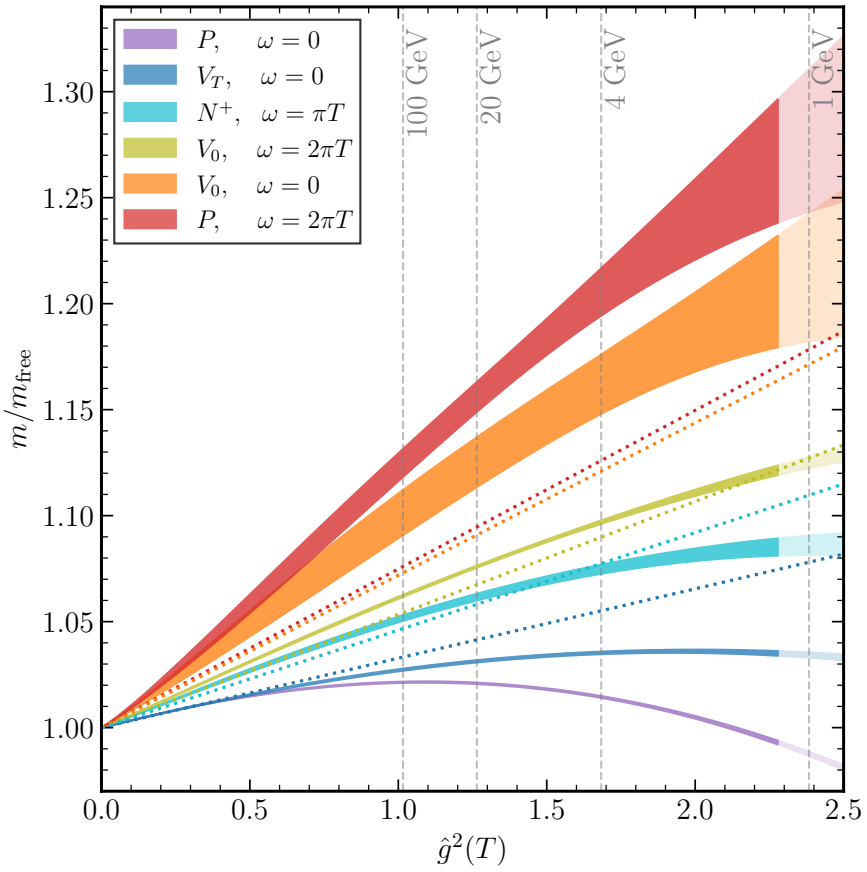

FIGURE 5.15: Screening masses of all the channels considered in this thesis as a function of $\hat{g}^2(T)$, normalized to their value in the free theory ($3\pi T$ for the N^+ channel, $2\pi T$ for the mesonic channels). Colored bands are 1σ intervals of the non-perturbative determinations, while the dotted lines of the corresponding color are the screening masses in $\mathcal{O}(g^2)$ perturbation theory.

Our findings consolidate the numerical strategy employed as a solid way to obtain high-precision non-perturbative predicitions of thermal QCD up to the electroweak scale. They furthermore indicate that the accuracy of the perturbative expansion of the effective theory is limited to temperatures even higher than those explored, and crucially that non-perturbative contributions remain relevant in thermal QCD up to the highest temperatures explored $T \sim 165$ GeV, meaning that a non-perturbative treatment of thermal QCD is necessary up to the electroweak scale. These conclusions are consistent with what was recently observed for the Equation of State, determined non-perturbatively up to the electroweak scale employing the same strategy adopted in this thesis [176, 177].

Looking forward, to complete the investigation of the hadronic screening spectrum it will be interesting to compute the screening masses of spin 3/2 baryons which, of the spin-splitting also in the baryonic sector. Our analysis of the mesonic hyperfine splitting shows that non-perturbative effects in the EFT are relevant in the whole temperature range. On the theoretical side, these results call for the non-perturbative matching of the three dimensional effective theory to full QCD. Once the non-perturbative relation between the matching coefficients of the EFT and the parameters of QCD will be determined, it will allow us to properly identify the presence and magnitude of non-perturbative contributions in the observables of the theory.

Appendix A

Notation and conventions

Throughout this thesis we adopt natural units, i.e. we set

$$c = \hbar = k_B = 1, \tag{A.0.1}$$

where c is the speed of light in the vacuum, $\hbar$ is the reduced Planck constant and k_B is the Boltzmann constant. Unless otherwise specified we adopt Einstein notation, meaning that repeated indices are summed over.

A.1 $\mathrm{SU}(N)$ conventions

The special unitary group $\mathrm{SU}(N)$ is defined as the set

$$\mathrm{SU}(N) \equiv \left\{ U \in \mathrm{GL}(N,\mathbb{C}) \mid UU^\dagger = U^\dagger U = \mathbb{1},\ \det U = 1 \right\}, \tag{A.1.1}$$

with respect to the matrix product, and where the general linear group $\mathrm{GL}(N,\mathbb{C})$ is the set of all invertible $N \times N$ matrices with entries in $\mathbb{C}$. It is generated via exponentiation by its Lie algebra, the set of Hermitean traceless $N \times N$ matrices

$$\mathfrak{su}(N) \equiv \left\{ H \in \mathrm{GL}(N,\mathbb{C}) \mid H = H^\dagger,\ \mathrm{Tr}\, H = 0 \right\}, \tag{A.1.2}$$

and since $\mathrm{SU}(N)$ is a compact and simply connected Lie group, a generic elements U can be written as

$$U = \exp\{i\theta^a T^a\}, \tag{A.1.3}$$

where $a = 1, \ldots, N^2 - 1$, $\theta^a \in \mathbb{R}$ and $T^a \in \mathfrak{su}(N)$ are the generators of the group. They satisfy the following defining commutation and anticommutation relations

$$\left[T^a, T^b\right] = i f^{abc} T^c, \quad \left\{T^a, T^b\right\} = \frac{\delta^{ab}}{N}\mathbb{1} + d^{abc} T^c. \tag{A.1.4}$$

The structure constants f are totally antisymmetric in all indices, while the constants d are symmetric. It is customary to choose a basis of generators which satisfy the following normalization condition

$$\mathrm{Tr}\left(T^a T^b\right) = \frac{\delta^{ab}}{2}\mathbb{1}. \tag{A.1.5}$$

Two relevants examples are given by the case of SU(2) and SU(3). For SU(2) the three generators are taken to be $T^a = \frac{1}{2}\sigma_a$, where σ_a are the Pauli matrices:

$$\sigma_1 = \begin{pmatrix} 0 & 1 \\ 1 & 0 \end{pmatrix} \quad \sigma_2 = \begin{pmatrix} 0 & -i \\ i & 0 \end{pmatrix} \quad \sigma_3 = \begin{pmatrix} 1 & 0 \\ 0 & -1 \end{pmatrix}. \tag{A.1.6}$$

For SU(3), we consider the generators $T^a = \frac{1}{2}\lambda^a$, where λ^a are the Gell-Mann matrices:

$$\begin{aligned}
\lambda^1 &= \begin{pmatrix} 0 & 1 & 0 \\ 1 & 0 & 0 \\ 0 & 0 & 0 \end{pmatrix} \quad \lambda^2 = \begin{pmatrix} 0 & -i & 0 \\ i & 0 & 0 \\ 0 & 0 & 0 \end{pmatrix} \quad \lambda^3 = \begin{pmatrix} 1 & 0 & 0 \\ 0 & -1 & 0 \\ 0 & 0 & 0 \end{pmatrix} \\
\lambda^4 &= \begin{pmatrix} 0 & 0 & 1 \\ 0 & 0 & 0 \\ 1 & 0 & 0 \end{pmatrix} \quad \lambda^5 = \begin{pmatrix} 0 & 0 & -i \\ 0 & 0 & 0 \\ i & 0 & 0 \end{pmatrix} \\
\lambda^6 &= \begin{pmatrix} 0 & 0 & 0 \\ 0 & 0 & 1 \\ 0 & 1 & 0 \end{pmatrix} \quad \lambda^7 = \begin{pmatrix} 0 & 0 & 0 \\ 0 & 0 & -i \\ 0 & i & 0 \end{pmatrix} \quad \lambda^8 = \frac{1}{\sqrt{3}}\begin{pmatrix} 1 & 0 & 0 \\ 0 & 1 & 0 \\ 0 & 0 & -2 \end{pmatrix}.
\end{aligned} \tag{A.1.7}$$

A.2 Dirac matrices

The Dirac action for the quark spinor fields involves the 4×4 matrices denoted by γ_μ. Their defininig property is the following anticommutator relation, known as the Clifford algebra:

$$\{\gamma_\mu, \gamma_\nu\} = 2\eta_{\mu\nu}\mathbb{1}_4, \tag{A.2.1}$$

where $\eta_{\mu\nu}$ is the metric tensor, which in this thesis is taken to be the 4-dimensional Euclidean metric, i.e. $\eta_{\mu\nu} = \delta_{\mu\nu}$. Different explicit representation for the Dirac matrices γ_μ exhist. In the *chiral representation* they are chosen as

$$\gamma_0 = \begin{pmatrix} 0 & -\mathbb{1}_2 \\ -\mathbb{1}_2 & 0 \end{pmatrix}, \quad \gamma_j = \begin{pmatrix} 0 & -i\sigma_j \\ i\sigma_j & 0 \end{pmatrix}, \quad j = 1, 2, 3. \tag{A.2.2}$$

The matrix $\gamma_5 \equiv \gamma_0\gamma_1\gamma_2\gamma_3$ plays a central role when discussing chiral properties of the QCD action, see section 1.5. In the chosen representation it is given by

$$\gamma_5 = \begin{pmatrix} \mathbb{1}_2 & 0 \\ 0 & -\mathbb{1}_2 \end{pmatrix}, \tag{A.2.3}$$

and it satisfies

$$\{\gamma_5, \gamma_\mu\} = 0 \quad \forall \mu, \quad \gamma_5^\dagger = \gamma_5, \quad \gamma_5^2 = \mathbb{1}_4. \tag{A.2.4}$$

The charge conjugation operator is defined from the Dirac matrices as $C = i\gamma_0\gamma_2$, and in this basis reads

$$C = i\gamma_0\gamma_2 = \begin{pmatrix} \sigma_2 & 0 \\ 0 & -\sigma_2 \end{pmatrix}. \tag{A.2.5}$$

It is an antisymmetric matrix that furthermore satisfies

$$C\gamma_\mu C = -\gamma_\mu^T, \quad [C, \gamma_5] = 0. \tag{A.2.6}$$

When constructing the three-dimensional effective field theory that describres QCD at high temperature (see section 3.3.3), it is convenient to adopt a non-relativistic representation of the Dirac matrices to select the third direction as the screening direction in which we will study the propagation. In this representation they read

$$\gamma_0 = \begin{pmatrix} 0 & \mathbb{1}_2 \\ \mathbb{1}_2 & 0 \end{pmatrix}, \quad \gamma_1 = \begin{pmatrix} \sigma_2 & 0 \\ 0 & -\sigma_2 \end{pmatrix}, \quad \gamma_2 = \begin{pmatrix} -\sigma_1 & 0 \\ 0 & \sigma_1 \end{pmatrix}, \quad \gamma_3 = \begin{pmatrix} 0 & -i\mathbb{1}_2 \\ i\mathbb{1}_2 & 0 \end{pmatrix}, \tag{A.2.7}$$

and the γ_5 and charge conjugation matrix are

$$\gamma_5 = \begin{pmatrix} -\sigma_3 & 0 \\ 0 & \sigma_3 \end{pmatrix}, \quad C = \begin{pmatrix} 0 & i\sigma_1 \\ -i\sigma_1 & 0 \end{pmatrix} \tag{A.2.8}$$

A.3 QCD field content

Quarks and antiquarks are described by spinor fields $\psi(x)$ and $\bar{\psi}(x)$ which transform in the fundamental and antifundamental representation of the gauge group SU(3) respectively, i.e. under a transformation $\Omega(x) \in \mathrm{SU}(3)$ they are sent into

$$\psi(x) \xrightarrow{\Omega(x)} \Omega(x)\psi(x), \quad \bar{\psi}(x) \xrightarrow{\Omega(x)} \bar{\psi}(x)\Omega^\dagger(x). \tag{A.3.1}$$

Gluons are represented by Lie algebra-values fields $A_\mu(x) = A_\mu^a(x)T^a$. Their interaction with quarks is represented by the gauge-invariant term

$$\bar{\psi}(x)\gamma_\mu D_\mu \psi(x) = \bar{\psi}(x)\gamma_\mu \left(\partial_\mu - iA_\mu(x)\right)\psi(x), \tag{A.3.2}$$

where D_μ is the gauge-covariant derivative. This determines how the gluon fields transform under gauge transformations:

$$A_\mu(x) \xrightarrow{\Omega(x)} \Omega(x)A_\mu(x)\Omega^\dagger(x) + i\Omega(x)\partial_\mu\Omega^\dagger(x) \tag{A.3.3}$$

Their dynamics of described by the kinetic term in equation (1.1.1), which is written in terms of the field-strength tensor, itself taking values in the Lie-algebra $F_{\mu\nu}(x) = F^a_{\mu\nu}(x)T^a$, and transforming in the adjoint representation of SU(3)

$$F_{\mu\nu}(x) = i\left[D_\mu, D_\nu\right], \quad F_{\mu\nu} \xrightarrow{\Omega(x)} \Omega(x)F_{\mu\nu}(x)\Omega^\dagger(x). \tag{A.3.4}$$

Appendix B

Faddeev-Popov procedure

The Faddeev-Popov (FP) procedure allows to define the path integral for Yang-Mills theories in the continuum; for non-abelian theories such as the SU(3) gauge sector of QCD the definition is valid order-by-order in perturbation theory. Intuitively, the issue that the FP construction addresses is an "overcounting" of physically equivalent field configurations. Indeed, a field configuration A_μ and its value A_μ^Ω after a gauge transformation Ω could assume very different values, but they contain the same physical information, which is reflected in the fact that the action is gauge-invariant. To overcome this problem a gauge fixing procedure is required, which means imposing that the gauge fields satify a certain condition that partially or completely lifts the gauge invariance. While gauge invariance will be eventually lost at the level of the action, it will continue to hold for physical quantities. One thus imposes a condition on the field A_μ expressed as

$$f(A) = 0 \tag{B.0.1}$$

for a given function f. It is convenient to employ a covariant gauge of the form

$$f(A) = \partial_\mu A_\mu(x) - \Lambda(x) \tag{B.0.2}$$

for a matrix-valued function $\Lambda(x)$. The idea is to only consider one representative configuration A in the path integral from the equivalence class of all configurations A^Ω obtained by gauge transformations and that satisfy the condition above. This can be done with the introduction of the Faddeev-Popov factor $\Delta_{\mathrm{FP}}(A)$ defined by the following equation

$$\Delta_{\mathrm{FP}}(A) \int D\Omega \; \delta\left(f(A^\Omega)\right) \equiv 1; \tag{B.0.3}$$

the aforementioned overcounting is bypassed for each configuration A by integrating over all possible gauge transformations, and the FP factor exactly compensates

this integration. Inserting the above equation in the partition function and exploiting the gauge invariance of the measure, action and $\Delta_{\mathrm{FP}}(A)$ allows to re-write it, up to an irrelevant constant, as

$$\mathcal{Z} = \int DA_\mu D\bar{\psi} D\psi \Delta_{\mathrm{FP}}(A)\, \delta(f(A))\, e^{-\mathcal{S}_{\mathrm{QCD}}}. \tag{B.0.4}$$

For conditions of the form (B.0.2) the Faddeev-Popov factor can be evaluated to be

$$\Delta_{\mathrm{FP}}(A) = \det(\partial_\mu D_\mu) \tag{B.0.5}$$

which depends on the gauge field through the covariant derivative. The determinant can be seen as the result of a functional integral over auxiliary fields $c, \bar{c}$ described by anticommuting Grassman variables, specifically

$$\det(\partial_\mu D_\mu) = \int D\bar{c} Dc \ \exp\{-\mathcal{S}_{\mathrm{FP}}[c, \bar{c}]\}, \tag{B.0.6}$$

$$\mathcal{S}_{\mathrm{FP}}[c, \bar{c}] = \frac{2}{g_0^2} \int d^4x \ \mathrm{Tr}\{\partial_\mu \bar{c} D_\mu c\}. \tag{B.0.7}$$

While the action of the auxiliary ghost field is that of a complex scalar field in the adjoint representation, which describes spin 0 bosonic excitations, they are reperesented by anticommuting variables which characterize fermions. This means that ghost fields violate the spin-statistics theorem, and although they need to be taken into account in perturbative computations to obtain the correct results, their quanta are not physical states of the theory. This implies, for instance, that they can only appear as internal propagators in Feynman diagrams and never as external legs. The resulting partition function now depends on the constant Λ appearing in the gauge fixing condition

$$\mathcal{Z}_\Lambda = \int DA_\mu D\bar{\psi} D\psi D\bar{c} Dc \ \delta(\partial_\mu A_\mu - \Lambda) \exp\{-S_{\mathrm{QCD}} - S_{\mathrm{FP}}\}, \tag{B.0.8}$$

and integrating over Λ with a Gaussian weight $\propto \exp\left\{-\frac{1}{g_0^2 \alpha} \mathrm{Tr}\{\Lambda\}^2\right\}$ yields the complete continuum definition of the partition function

$$\mathcal{Z}_{\mathrm{QCD}} = \int DA_\mu D\bar{\psi} D\psi D\bar{c} Dc \ \exp\{-\mathcal{S}_{\mathrm{QCD}} - \mathcal{S}_{\mathrm{FP}} - \mathcal{S}_{\mathrm{GF}}\}, \tag{B.0.9}$$

with the gauge-fixing term defined as

$$\mathcal{S}_{\mathrm{GF}}[A_\mu] = \frac{1}{2\alpha} \int d^4x \ \mathrm{Tr}\left[(\partial_\mu A_\mu(x))^2\right]. \tag{B.0.10}$$

Appendix C

More on lattice field theory

C.1 Haar measure

Because SU(N) is a compact group, the notions of volume and measure can be extended to it. The central properties of the Haar measure can all be derived by requiring gauge invariance; in particular, since the action (2.1.9) is gauge invariant and the partition function must not change after gauge transforming the link variables as in (2.1.3), the Haar measure for a single link variable must satify

$$dU_\mu(x) = dU'_\mu(x) = d\big(\Omega(x)U_\mu(x)\Omega(x+a\hat{\mu})\big), \tag{C.1.1}$$

and since the transformations at different points can be choosen independently, the measure must more generally be invariant under left and right multiplication by any group element:

$$dU = d\big(VU\big) = d\big(UW\big), \ \forall \ U, \ V, \ W \in \mathrm{SU}(N_c). \tag{C.1.2}$$

Specifying the normalization

$$\int dU \ 1 = 1 \tag{C.1.3}$$

completes the definition of the Haar measure. The centrality of gauge invariance is manifest in the fact that the integral over any product of SU(N_c) elements that does not contain a singlet in its irreducible representations, i.e. that is not gauge invariant, vanishes identically. To list a few examples for the relevant case of SU(3)

$$\int dU \ U_{ab} = 0 \tag{C.1.4}$$

$$\int dU \ U_{ab}U_{cd} = 0 \tag{C.1.5}$$

$$\int dU \ U_{ab}U^\dagger_{cd} = \frac{1}{3}\delta_{ad}\delta_{bc} \tag{C.1.6}$$

$$\int dU \ U_{ab}U_{cd}U_{ef} = \frac{1}{6}\varepsilon_{ace}\varepsilon_{bdf}; \tag{C.1.7}$$

the only possibly non-zero integrals (C.1.6) and (C.1.7) are those that correspond to a $q\bar{q}$ and qqq state respectively, which contain a gauge invariant combination, see equations (1.4.1) and (1.4.2).

C.2 Grassmann variables

Because of their statistics, fermionic fields are represented by anticommuting Grassmann variables. We consider a Grassmann algebra generated by $2N$ elements $\eta_1, \ldots, \eta_N$ and $\bar{\eta}_1, \ldots, \bar{\eta}_N$ defined by the fact that they anticommute among themeselves:

$$\{\eta_i, \eta_j\} = \{\bar{\eta}_i, \bar{\eta}_j\} = \{\eta_i, \bar{\eta}_j\} = 0 \quad \forall i, j = 1, \ldots, N, \tag{C.2.1}$$

and in particular the square of any Grassmann number is 0. Functions of Grassmann numbers are defined as a power series in the variables, which due to the previous statement only have a finite number of terms, since any power higher or equal to 2 of any variable vanishes. A relevant case for our application to the path integral of fermionic fields is given by the Gaussian function of Grassmann variables

$$g(\eta, \bar{\eta}) = \exp\left\{-\sum_{i,j} \bar{\eta}_i D_{ij} \eta_j\right\} \tag{C.2.2}$$

with some matrix D (in practice, this will be the Dirac operator). Because only terms of order 1 in η and $\bar{\eta}$ contribute to the power series of the exponential, the Gaussian function can be written as

$$g(\eta, \bar{\eta}) = \prod_{i,j=1}^{N} \left(1 - \bar{\eta}_i D_{ij} \eta_j\right). \tag{C.2.3}$$

Next, we need the notion of integration over Grassmann variables. We are interested in evaluating an integral of the form

$$\int D\bar{\eta} D\eta \; f(\eta, \bar{\eta}) \tag{C.2.4}$$

for a given function f of the Grassmann variables, and where we introduce the shorthand notation for the measure as

$$D\bar{\eta} \equiv \prod_{i=1}^{N} \mathrm{d}\bar{\eta}_i, \qquad D\eta \equiv \prod_{i=1}^{N} \mathrm{d}\eta_i. \tag{C.2.5}$$

Due to the fact that the integration measure over each variables anticommutes with all other integration measures, and because of the finite number of term present in any funcion of Grassmann variables, integration looks quite different

from the usual. Indeed, one can calculate any arbitrary integral once the following elemetary rules are specified:

$$\begin{aligned} \int \mathrm{d}\eta_i \ &= 0, \\ \int \mathrm{d}\eta_i \ \eta_i &= 1. \end{aligned} \tag{C.2.6}$$

In particular, it can be shown that the integral over Grassmann variables of the Gaussian function (C.2.2) can be evaluated analytically and yields

$$\int D\bar{\eta} D\eta \ \exp\left\{ -\sum_{i,j} \bar{\eta}_i D_{ij} \eta_j \right\} = \det D, \tag{C.2.7}$$

which explains the appearance of the fermion determinant in equation (2.2.26). A central class of integrals are those that involve pairs of η and $\bar{\eta}$ variables in presence of a Gaussian weight. The elementary integral has the form

$$\int D\bar{\eta} D\eta \ \eta_i \bar{\eta}_j \exp\{-\bar{\eta} D \eta\} = \det D \times \left(D^{-1}\right)_{ij}, \tag{C.2.8}$$

where we suppress the sum in the exponent for brevity. Adopting the notation that is relevant for the QCD path integral, we derive the elementary fermionic expectation value:

$$\overbrace{\eta_i \bar{\eta}_j} \equiv \langle \eta_i \bar{\eta}_j \rangle = \frac{\int D\bar{\eta} D\eta \ \eta_i \bar{\eta}_j \exp\{-\bar{\eta} D \eta\}}{\int D\bar{\eta} D\eta \ \exp\{-\bar{\eta} D \eta\}} = \left(D^{-1}\right)_{ij}, \tag{C.2.9}$$

which, in the case of QCD, is nothing but the quark propagator between lattice sites i and j. The above formula and notation denotes a so-called Wick contraction; when multiple pairs of Grassmann variables are present, like when the two-point function of an hadronic interpolating field is computed, Wick's theorem tells us that the expectation value is given by the sum of all possible Wick contractions that can be obtained from the fermionic fields. Because the order in which Grassmann variables appear is important for the validity of equation (C.2.9), each contraction will come with a sign factor from the necessary permutations of fermionic variables.

C.3 Finite volume renormalization

In this section, the strategy developed in [47, 52, 53, 194] to determine the non-perturbative running of the renormalized QCD coupling $\bar{g}^2(\mu)$ up to energies of ~ 100 GeV is reviewed. One starts by considering the theory in a box with finite volume L^4 and employing a definition of the renormalized coupling at an energy scale μ given by the inverse spatial extent of the box:

$$\bar{g}^2_{\mathrm{FV}}(\mu = 1/L). \tag{C.3.1}$$

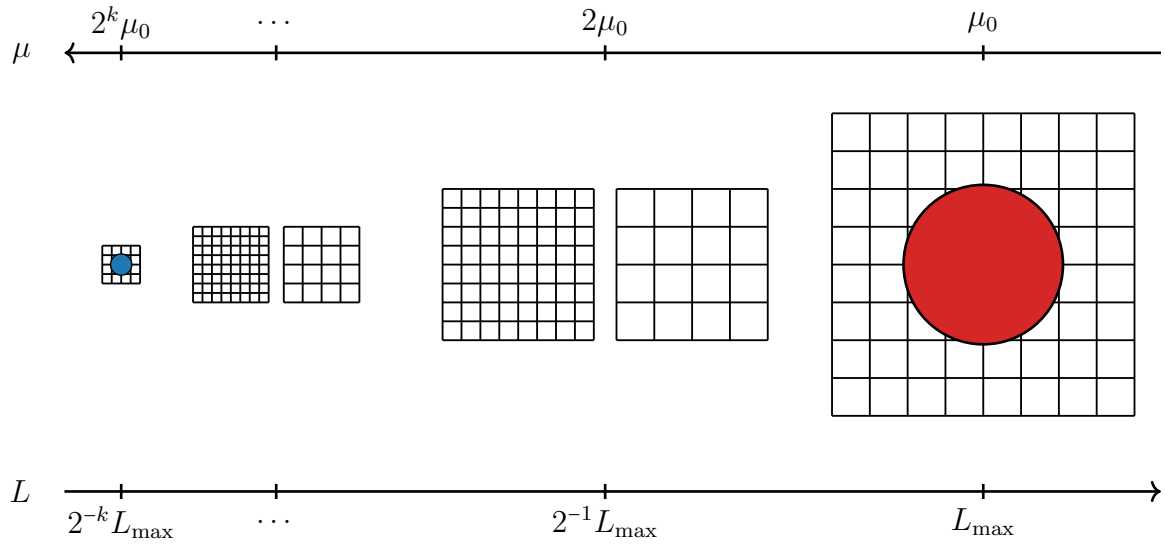

FIGURE C.1: Sketch of the step scaling approach to study broadly different energy scales. The low energy scale (red circle) requires large volumes, while the high energy scale (blue circle) requires fine spacing. The two are connected by recursively scaling down the lattice volume - which corresponds to the (inverse) renormalization scale μ - and the lattice spacing, so that each intermediate energy scale can be simulated with reasonable resources.

A concrete example could be the coupling defined in the Schrödinger Functional scheme [180]. To track its non-perturbative running, one defines the step-scaling function σ at a given value of the coupling $\bar{g}^2_{\mathrm{FV}}(1/L)$ and for a given scale factor s as the value of the coupling computed in a box with extent $L' = sL$:

$$\sigma(\bar{g}^2_{\mathrm{FV}}(1/L), s) \equiv \bar{g}^2_{\mathrm{FV}}(1/sL). \tag{C.3.2}$$

While the beta function describes how the coupling changes under infinitesimal variation of the scale μ, the step scaling function encodes the same information for finite rescalings of μ. The relation bewteen the two functions is

$$\ln(s) = -\int_u^{\sigma(s,u)} dv\ \frac{1}{\beta(v)}. \tag{C.3.3}$$

To renormalize the regulated theory, one fixes g_0^2 such that the finite volume coupling $\bar{g}^2_{\mathrm{FV}}(g_0^2, a/L)$ (now computed on the lattice) assumes a prescribed value $\tilde{g}^2$

$$\bar{g}^2_{\mathrm{FV}}(g_0^2, a\mu) = \tilde{g}^2; \tag{C.3.4}$$

rescaling L/a by a factor s at the value of g_0 (and thus a) determined from the above condition and measuring again the renormalized coupling $\bar{g}^2_{\mathrm{FV}}(g_0^2, a\mu/s) = (\tilde{g}^2)'$ probes the energy scale μ/s. One can now decrease the lattice spacing at the new energy scale by increasing the number of points in each direction and tuning g_0^2 until the renormalized coupling assumes the same value $(\tilde{g}^2)'$. In this way, the scales μ and μ/s can be simulated with good control over cutoff effects, and even though the imposed renormalization condition changes with the different energy scale, one still describes the same continuum theory because the different values of the coupling are connected by the renormalization group. At sufficiently low energy an hadronic scheme can independently be employed to set the physical scale [14], so that one can determine a low-enegy renormalization scale μ_0 in physical units, corresponding to a lattice extent L_{max}. A visual representation of the strategy is depicted in figure C.1. With just 7 steps of the described procedure for a scale factor $s = 1/2$ one can span two orders of magnitude in the renormalization scale; for the case of QCD, this means being able to connect the non-perturbative low-energy regime to high-energy conditions in a single unified approach, also allowing to make contact with the perturbative regime, see figure C.2.

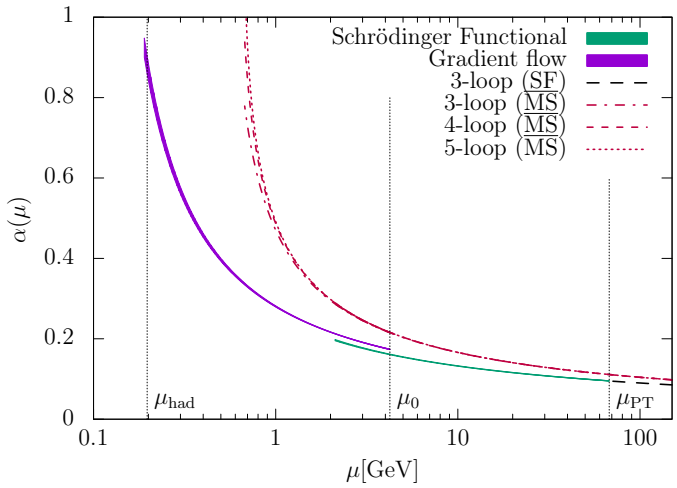

FIGURE C.2: From [194]: running of α in QCD determined non-perturbatively through the step-scaling procedure described in the main text. The results refer to the Schrödinger Functional and Gradient flow definitions of the coupling, which are matched at a suitably chosen scale. The non-perturbative running is compared to perturbation theory to several loops both in the $\overline{\mathrm{MS}}$ and in the Schrödinger Functional schemes.

Appendix D

Ensemble generation

The extraction of random numbers distributed according to a generic target distribution is not a trivial effort, particularly so given the complicated functional form (2.5.5) of the distribution we are interested in. At present, the most efficient way to generate an ensemble $\{U_1, U_2, \ldots, U_N\}$ of field configurations distributed according to a target probability distribution is based on *Markov chains*, which are stochastic processes that generate a new field configuration U' based solely on the previous configuration U, according to a transition probability $T[U'|U]$. The sequence of configurations can be thought of as an evolution in a "Markov time" starting from an initial state U_0. Since the goal is to estimate a path integral which receives contributions from all possible field configurations, it is crucial to ensure that the Markov chain is able, at least in principle and given enough time, to explore the whole state space. Chains that respect this properties are called *ergodic*: any state in the system is reached in a finite number of steps (on average) by any other state. A central theorem guarantees that at large enough Markov time, after a *thermalization phase* the states extracted by an ergodic chain are distributed according to a well defined *equilibrium distribution*. Finally, to ensure that the equilibrium distribution is the desired one $P[U]$, it is sufficient to propose states with a transition probability that satisfies the *detailed balance* condition:

$$P[U]\,T[U|U'] = P[U']\,T[U'|U]\,. \tag{D.0.1}$$

D.1 Metropolis-Hastings algorithm

A straightforward way to build an ergodic Markov chain whose transition matrix satisfies detailed balance with respect to a target distribution $P[U]$ is provided by the renowned Metropolis-Hastings algorithm [195, 196]. Starting from a configuration U, a new configuration U' is proposed. The procedure to propose U' starting from U should respect *microreversibility*, i.e. it must be equally likely to propose

U' starting from U and to propose U starting from U'. The new configuration is *accepted*, meaning it will be taken as the next state in the Markov chain, with the following probability

$$P_{\text{acc}}[U, U'] = \min\left\{1, \frac{P[U']}{P[U]}\right\}; \tag{D.1.1}$$

otherwise, the proposed configuration is *rejected*, and the next state of the chain is given by U. This means that if the proposed configuration has a higher target probability than the current one, it will always be accepted, whereas if it has lower probability it is accepted with probability $P[U']/P[U]$. With these conditions met, it is easy to prove that the algorithm satisfies detailed balance with respect to $P[U]$. Another convenient feature is that there is no need to know the normalization factor of $P[U]$ since all the steps involve ratios of the distribution evaluated on different configurations. The details of how new configurations are proposed are usually tuned such that the acceptance rate of the algorithm is sufficiently high.
In the particular case of a Boltzmann-type distribution, the acceptance probability is related to the variation of the action between the starting and proposed configuration

$$\frac{P[U']}{P[U]} = \exp\{-\Delta S\}, \quad \Delta S \equiv S[U'] - S[U] \tag{D.1.2}$$

meaning that if the proposed configuration has a lower action than the starting one it will be accepted, otherwise it will be accepted with probability given by the above equation.
This expression also highlights the role played by the locality of the action in the efficiency of simulation algorithms: if the action is local in the link variables, like in the pure gauge theory, an update of a single link variable causes a variation of the action which is itself local, meaning that it only depends on the value of links nearby the updated one, making it efficient to compute the acceptance probability (D.1.2) and to update configurations. More specifically, the cost of updating all link variables scales like the lattice volume V. On the other hand for actions that are not ultra-local, which is the case of lattice QCD after integrating over the fermionic variables, the variation of the action due to the change of a single link depends on all links in the lattice, which makes the update cycle prohibitively inefficient: extracting pseudofermion fields involves the inversion of the Dirac operator, which is an operation whose cost scales like V, making a local update of the whole lattice an $\mathcal{O}(V^2)$ operation. The currently most efficient algorithm to sample gauge field configurations in QCD, the Hybrid Monte Carlo [197], compensates this issue by proposing global updates of all link variables in the lattice, and its main features will be described in the next section.

D.2 Hybrid Monte Carlo

The Hybrid Monte Carlo (HMC) is a realization of the Metropolis-Hastings aglorithm that achieves $\mathcal{O}(V)$ cost also in the presence of dynamical fermions by proposing global updates of all link variables in the lattice, which are evolved in an additional fictitious time τ mimicking the Hamiltonian flow of classical systems. In this picture, a set of Lie-algebra valued normally distributed momenta $\pi_\mu^a(x) \in \mathfrak{su}(3)$ are introduced, with associated partition function

$$\mathcal{Z}_\pi = \int D\pi \ \exp\left\{-\frac{1}{2}\sum_{x,\mu,a} \pi_\mu^a(x)^2\right\}, \tag{D.2.1}$$

and which are conjugate to the link variables. By multiplying and dividing an expectation value like (2.5.1) by the above equation the conjugate momenta can be formally included in the path integral, leading to

$$\langle O\rangle = \frac{1}{\mathcal{Z}_H}\int D\pi DU D\phi^\dagger D\phi \ O \ \exp\left\{-H\left[U,\phi,\phi^\dagger,\pi\right]\right\}, \quad \mathcal{Z}_H = \mathcal{Z}\mathcal{Z}_\pi, \tag{D.2.2}$$

where the system's Hamiltonian has been introduced

$$H\left[U,\pi,\phi,\phi^\dagger\right] \equiv \frac{1}{2}\sum_{x,\mu,a}\pi_\mu^a(x)^2 + S_G\left[U\right] + S_{\text{pf}}\left[U,\phi,\phi^\dagger\right]. \tag{D.2.3}$$

As anticipated, this can be interpreted as the generator of translation in an additional dimension τ. The link variables and the conjugate momenta are thus allowed to depend on this extra coordinate, and their evultion is governed by Hamilton's equations

$$\frac{\mathrm{d}U_\mu(x,\tau)}{\mathrm{d}\tau} = \frac{\delta H\left[U,\pi,\phi,\phi^\dagger\right]}{\delta\pi_\mu(x,\tau)} = \pi_\mu(x,\tau)U_\mu(x,\tau), \tag{D.2.4}$$

$$\frac{\mathrm{d}\pi_\mu(x,\tau)}{\mathrm{d}\tau} = -\frac{\delta H\left[U,\pi,\phi,\phi^\dagger\right]}{\delta U_\mu(x,\tau)} = -F_G(x,\tau) - F_{\text{pf}}(x,\tau), \tag{D.2.5}$$

where the gauge and fermion forces are defined as

$$F_G(x,\tau) \equiv \frac{\delta S_G\left[U\right]}{\delta U_\mu(x,\tau)}, \tag{D.2.6}$$

$$F_{\text{pf}}(x,\tau) \equiv \frac{\delta S_{\text{pf}}\left[U,\phi,\phi^\dagger\right]}{\delta U_\mu(x,\tau)}. \tag{D.2.7}$$

Notice that the pseudofermion fields are not evolved in τ, but their effect is encoded in the fermionic force. If equations (D.2.4) and (D.2.5) could be solved exactly,

the Hamiltonian would be a constant of motion along the time evolution, and it would be possible to define a procedure to propose field configurations that satisfy all the properties described in the previous section and would always be accepted since $\Delta H = 0$. This procedure is composed of the following steps:

I starting with a gauge field configuration $U_\mu(x, \tau = 0)$, conjugate momenta $\pi_\mu(x, \tau = 0)$ are extracted according to (D.2.1), as well as an ensemble of pseudofermions $\phi(x), \phi^\dagger(x)$ according to (2.5.6);

II the equations of motion (D.2.4), (D.2.5) are solved up to a maximum time $\bar{\tau}$;

III the resulting link fields $U_\mu(x, \bar{\tau})$ are taken as the new configuration of the system.

The evolution of the field according to the Hamiltonian equations is referred to as the "molecular dynamics" step. Microreversibility of the proposal is guaranteed since Hamiltonian dynamics is time-invertible. Given the non-linear nature of the equations of motion, the molecular dynamics evolution needs to be solved numerically by discretizing the time interval in N_{md} steps of length $\delta\tau = \bar{\tau}/N_{\text{md}}$. The use of high-order symplectic numerical integrators such as the leapfrog, Verlet or the more refined Omelyan-Mrygold-Folk [198, 199] is essential to guarantee microreversibility and accuracy of the approximate solution. Nevertheless, due to the numerical integration, the Hamiltonian will cease to be exactly conserved, and at the end of the trajectory one will have in general $\Delta H \neq 0$. For this reason, step III of the above procedure is replaced by an accept-reject step:

III' configuration $U_\mu(x, \bar{\tau})$ is accepted with probability given by $\min\{1, \exp\{-\Delta H\}\}$.

Notice how the effect of the fermion determinant is encoded in the computation of the fermionic force derived from the pseudofermion action. The computation of the force on a given link configuration involves the inversions of the Dirac operator, making this step the computationally dominant part of the global proposal and thus of ensemble generation.
To mitigate the fluctuations of the fermionic force along the molecular dynamics trajectory it is often convenient to separate the contributions to the determinant coming from different scales. The idea behind the frequency splitting of the quark determinant [200–202] is to factor the fluctuations in the spectrum due to energies below and above a scale μ through the identity

$$\det\left\{DD^\dagger\right\} = \det\left\{DD^\dagger + \mu^2\right\} \det\left\{DD^\dagger \left(DD^\dagger + \mu^2\right)^{-1}\right\}; \tag{D.2.8}$$

each determinant can now be represented by an independent set of pseudofermion fields, resulting in an action given by

$$S_{\mathrm{pf}}\left[U,\phi_1,\phi_2\right] = a^8 \sum_{x,y} \phi_1^\dagger(x)\left[DD^\dagger + \mu^2\right]^{-1}(x,y)\phi_1(y) + \phi_2^\dagger(x)\left[\mathbb{1} + \mu^2\left(DD^\dagger\right)^{-1}\right](x,y)\phi_2(y). \tag{D.2.9}$$

The fermionic force (D.2.7) therefore also splits in two contributions $F_{\mathrm{pf}}^{(1)}$ and $F_{\mathrm{pf}}^{(2)}$ related to eigenvalues of the Dirac operator larger and smaller than μ respectively. These two components exhibit smaller fluctuations along the molecular dynamics trajectory compared to the full force, allowing integrations with coarser step size. The parameter μ can furthermore be tuned to make the force $F_{\mathrm{pf}}^{(2)}$ smaller in magnitude than $F_{\mathrm{pf}}^{(1)}$, since the former is computationally more expensive to determine than the latter. The spectral range can be - and usually is - split in more than two intervals introducing multilple scales $\mu_1, \mu_2, \ldots, \mu_N$ and corresponding pseudofermion fields $\phi_1, \phi_2, \phi_3, \ldots, \phi_{N+1}$ to ensure stringent control over the efficiency of the force computation.

D.3 Rational HMC

As anticipated at the end of section 2.5, for an odd number of quark flavors it is not guaranteed that the product of the fermion determinats is positive, even in the case of degenerate masses, potentially spoiling the interpretation of (2.5.2) as a probability density distribution. The underlying reason is that eigenvalues of the Dirac operator are of the form

$$m_i + \lambda\left[U\right], \tag{D.3.1}$$

with m_i the mass of the i^{th} quark flavor and where $\lambda\left[U\right]$ are the eigenvalues of the massless operator. Discretizations that break chiral symmetry such as Wilson fermions are not protected from negative eigenvalues, and it is possible that on some configurations the fluctuating values of $\lambda\left[U\right]$ result in very small or even negative eigenvalues of the massive operator. The presence of such "exceptional" configurations has made it historically hard, among other things, to reach the physical point of light quark masses with Wilson fermions. For the concrete case of 2+1 simulations, i.e. 2 degenerate light quarks with a heavier strange quark, the fact that the additional single quark flavor has a comparatively larger mass makes the appearance of exceptional configurations less frequent, and their contribution to the path integral is expected to be negligible. A similar situation occurs when simulating the theory at high temperature, where thermal modes provide *de facto*

an infraried cutoff to the spectrum. These considerations justify the substitution of the operator Q defined in equation (2.5.7) with its positive definite absolute value

$$Q \to |Q| \equiv \left(Q^2\right)^{1/2}. \tag{D.3.2}$$

Since it involves the square root of a matrix, the actual evaluation of the above operator is not trivial. For this reason, one looks for an operator R that approximates the non-integer matrix power $(Q^2)^{-1/2}$ which enters the pseudofermion action. The determinant can thus be split in

$$\det\{|Q|\} = \det\left\{|Q|RR^{-1}\right\} = \det\{|Q|R\}\det\left\{R^{-1}\right\}, \tag{D.3.3}$$

where the determinant of R^{-1} can be represented by pseudofermion fields and serves as a computable proxy of the positive definite quark determinant. If R were exact equal to $|Q|^{-1}$ the factor $\det\{|Q|R\}$ would be identically 1, while in practical situations, it will fluctuate around unity: the better R approximates $|Q|^{-1}$, the milder the fluctuations will be. In practice, this factor is included in the definition of the observable and is treated as a reweighting factor, meaning that expectation values are expressed as

$$\langle O\rangle = \frac{\langle \det\{|Q|R\}O\rangle_R}{\langle \det\{|Q|R\}\rangle_R}, \tag{D.3.4}$$

with the expectation value with respect to R defined as

$$\langle\cdot\rangle_R \equiv \frac{1}{\mathcal{Z}_R}\int DU\ \det\left\{R^{-1}\right\}\exp\{-S_G[U]\}, \quad \mathcal{Z}_R \equiv \int DU\ \det\left\{R^{-1}\right\}; \tag{D.3.5}$$

at this point the reweighting factor can be estimated stochastically for each gauge field configuration.

The Rational Hybrid Monte Carlo algorithm (RHMC) [203–205] employs an accurate rational approximation of the square root function, specifically constructed from the Zolotarev approximant $R_{n,\epsilon}$ of order (n,n) in the interval $[\epsilon,1]$:

$$x^{-1/2} \simeq R_{n,\epsilon}(x) = A\frac{(x+r_1)(x+r_3)\dots(x+r_{2n-1})}{(x+r_2)(x+r_4)\dots(x+r_{2n})} \tag{D.3.6}$$

with $A, r_1, \dots, r_{2n}$ known constants. If one is able to measure, typically on a dedicated simulation, the spectral range of $|Q|$, i.e. the interval $[\lambda_{\min}, \lambda_{\max}]$ containing all its eigenvalues, an approximation of the Dirac operator is given by

$$R \equiv \lambda_{\max} R_{n,\epsilon}\left(\lambda_{\max}^{-2}Q^2\right), \quad \epsilon = \left(\lambda_{\max}/\lambda_{\min}\right)^2. \tag{D.3.7}$$

The degree n can be adjusted to reach a desired precision on the approximation; moreover, the rational approximation is by construction amenable to the application of frequency splitting techniques given the presence of poles in the function that suggest a factorization of the spectral range.

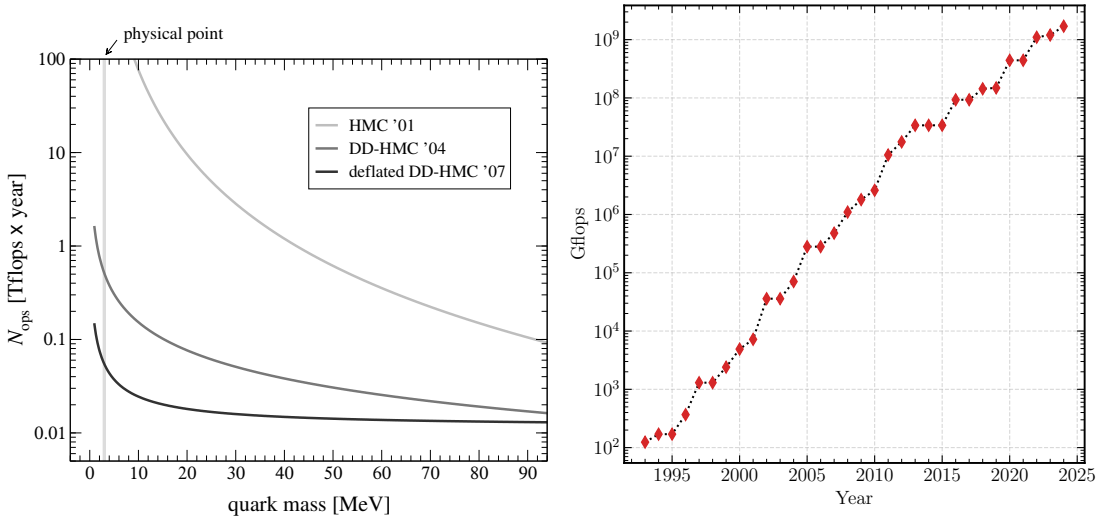

FIGURE D.1: (Left) From [206]: Number of floating point operations required for the generation of 100 independent gauge field configurations configurations as a function of the quark mass, for different variants of the HMC algorithm (see main text). Data refers to $N_f = 2$ $\mathcal{O}(a)$–improved Wilson fermions on a 64×32^3 lattice with spacing $a = 0.08$ fm. (Right) Evolution of the number of floating point operations per second achieved by the top 1 supercomputer over time [207].

D.4 Algorithmic advancements

Whatever algorithm is employed for its numerical solution, the generation of gauge field configurations and the evaluation of the path integral are formidably expensive tasks from the computational point of view, and for this reason lattice QCD applications run for several months on the world's most powerful supercomputers. Different portions of the lattice are assigned to different computing units of the machines and simulations can efficiently be run in parallel; several codes for ensemble generation and measurement of correlation functions are currently publicly available [208–213]. Since its early days in the 1980s, the field of lattice QCD has seen tremendous progress in the complexity of the systems that can be feasibly simulated, and it is now possible to simulate QCD with dynamical u, d, s, c quarks at physical masses, for fine values of the lattice spacing and at large physical volumes. What enabled this progress is the sinergy between two equally important factors: on one hand, steady technological developements have consolidated an exponential growth in time of computational power over the last decades, as is summarized on the right side of figure D.1. On the other hand, the left side of the same figure highlights how many of the breakthroughs in the field have in great part occurred due to the discovery and design of better-performing

simulation algorithms, which not only require orders-of-magnitude less resources and time to achieve the same results as their predecessors, but which also have better scaling properties with the relevant parameters of the system, allowing to approach the continuum, infinte volume and phyiscal quark mass limits in an efficient way. As a matter of fact, detailed studies of the HMC algorithm revealed that its computational cost had rather bad scaling behavior close to the physical point, suggesting that simulations would become prohibitively more expensive in the regime of physical interest [214]. Some of the algorithmic developements that lead to overcome this *impasse*[1] - arguably more so than the increase in computational power - have been represented for instance by the Domain Decomposed Hybrid Monte Carlo (DD-HMC) [215, 216] and its deflated variant [217], which inspired algorithms that are now routinely employed in simulations.

[1]The alarming, seemingly insurmountable estimate of the computational cost of the HMC algorithm, first presented at the Berlin Lattice conference in 2001, came to be humorously known as the *Berlin wall* in the lattice community.

Appendix E

EFT and perturbation theory

In this appendix we provide some additional information about the construction of the three-dimensional effective field theory, specifically the non-relativistic fermionic part, described in section 3.3, and the perturbative computations described in chapter 4.

E.1 Non-relativistic fermionic action

Here we provide some more details on the construction of the non-relativistic quark action in equation (3.3.10). Because at high temperature quarks behave as heavy fields with mass $m \sim \pi T$ and since we will study screening in the third spatial direction, we employ the non-realativistic representation of Dirac matrices in equation (A.2.7). With this choice, the Dirac operator reads

$$\gamma_0\gamma_\mu D_\mu = \begin{pmatrix} D_0 + iD_3 & -\epsilon_{jk}D_j\sigma_k \\ \epsilon_{jk}D_j\sigma_k & D_0 - iD_3 \end{pmatrix}, \tag{E.1.1}$$

where ϵ_{jk} is the two-dimensional Levi-Civita symbol with $\epsilon_{12} = -\epsilon_{21} = 1$. We consider the Matsubara modes of the quark fields in equation (3.2.8) and decompose them in their two-dimensional Weyl components

$$\psi_n(\boldsymbol{x}) = \begin{pmatrix} \psi_n^{\uparrow}(\boldsymbol{x}) \\ \psi_n^{\downarrow}(\boldsymbol{x}) \end{pmatrix} \tag{E.1.2}$$

and the fermionic action for the $n = 0$ Matsubara mode thus reads

$$\begin{aligned} S_F = \int \mathrm{d}^3\boldsymbol{x} \big\{ & i\psi_0^{\uparrow,\dagger}\left[\omega_0 - gA_0 + D_3\right]\psi_0^{\uparrow} + \psi_0^{\downarrow,\dagger}\left[\omega_0 - gA_0 - D_3\right]\psi_0^{\downarrow} \\ & + \psi_0^{\downarrow,\dagger}\epsilon_{jk}D_j\sigma_k\psi_0^{\uparrow} - \psi_0^{\uparrow,\dagger}\epsilon_{jk}D_j\sigma_k\psi_0^{\downarrow}\big\} \end{aligned} \tag{E.1.3}$$

Notice that at high temperature, and for small transverse momenta, one spinor behaves as a light field and one spinor as a heavy field. For instance, close to the

pole at $p_3 \sim i\omega_0$, $\psi_0^{\uparrow}$ is the light field while $\psi_0^{\downarrow}$ is heavy. At this point, one can integrate out the heavy fields by solving its equations of motion and substituting them into the action. For the $\psi_0^{\downarrow,\dagger}$ field we find

$$\psi_0^{\downarrow} = \frac{i\epsilon_{jk} D_j \sigma_k}{\omega_0 - gA_0 - D_3} \psi_0^{\uparrow}, \tag{E.1.4}$$

with similar considerations for $\psi_0^{\uparrow,\dagger}$. We can now insert these terms in the action (E.1.3), and expand in powers of $1/\omega_0$, to obtain

$$\begin{aligned} S_F = i \int \mathrm{d}\boldsymbol{x} \; \psi_0^{\uparrow,\dagger} \Bigg[\omega_0 - gA_0 + D_3 - \frac{1}{2\omega_0} \left(D_\perp^2 + \frac{g}{4i} \left[\sigma_j, \sigma_k\right] F_{jk} \right) \Bigg] \psi_0^{\uparrow} \\ \psi_0^{\downarrow,\dagger} \Bigg[\omega_0 - gA_0 - D_3 - \frac{1}{2\omega_0} \left(D_\perp^2 + \frac{g}{4i} \left[\sigma_j, \sigma_k\right] F_{jk} \right) \Bigg] \psi_0^{\downarrow} \; + \mathcal{O}\left(\frac{1}{\omega_0^2}\right), \end{aligned} \tag{E.1.5}$$

with an anologous expression for the $n = -1$ sector. This expression identifies the relevant fermionic degrees of freedom in the high-temperature regime and determines the structure of their interactions. The NRQCD action (3.3.10) is then obtained by identifying the three-dimensional Matsubara modes in the $n = 0, -1$ sector as the dynamical degrees of freedom and inserting the appropriate matching coefficients M and g_{E}, see the main text.

E.2 Fermionic propagators in the effective theory

In coordinate space, by making explicit the source and the sink locations, the propagator from eq. (4.1.12) becomes

$$S_\chi^{(0)}(\boldsymbol{x}, x_3; \boldsymbol{y}, y_3) = \frac{-i\theta(x_3 - y_3) T \mathbb{1}}{2(x_3 - y_3)} \exp\left[-M(x_3 - y_3) - \frac{\pi T \left(\boldsymbol{x} - \boldsymbol{y}\right)^2}{2\left(x_3 - y_3\right)} \right], \tag{E.2.1}$$

and similarly but with opposite sign for ϕ. At the next order, from eq. (4.1.10), the propagator for χ reads

$$S_\chi^{(1)}(\boldsymbol{x}, x_3; \boldsymbol{y}, y_3) \; = \; i \int \mathrm{d}z_3 \int \mathrm{d}^2\boldsymbol{z} \, S_\chi^{(0)}(\boldsymbol{x}, x_3; \boldsymbol{z}, z_3) \left[iA_3 + A_0 \right](\boldsymbol{z}, z_3) S_\chi^{(0)}(\boldsymbol{z}, z_3; \boldsymbol{y}, y_3) \,, \tag{E.2.2}$$

implying that χ propagates freely from the source to the position $(\boldsymbol{z}, z_3)$, where it emits a gluon, and then again freely propagates up to the sink position. 1 By

inserting eq. (E.2.1) into eq. (E.2.2) and taking $(\boldsymbol{y}, y_3) = (\boldsymbol{0}, 0)$, the result can be rewritten as

$$\begin{aligned} S_\chi^{(1)}(\boldsymbol{x}, x_3; \boldsymbol{0}, 0) \;=\; S_\chi^{(0)}(\boldsymbol{x}, x_3; \boldsymbol{0}, 0) \int_0^{x_3} \mathrm{d}z_3 \int \mathrm{d}^2\boldsymbol{z}\, \frac{x_3 T}{2(x_3 - z_3) z_3} \\ \times \exp\left[-\frac{1}{2} \frac{\pi T}{(x_3 - z_3)} \frac{x_3}{z_3} \left(\boldsymbol{z} - \frac{z_3}{x_3} \boldsymbol{x} \right)^2 \right] [iA_3 + A_0]\,(\boldsymbol{z}, z_3)\,. \end{aligned} \tag{E.2.3}$$

From table 3.1 we see that the prefactor of the quadratic dependence is parametrically of order $\pi T x_3/[(x_3 - z_3)z_3] \sim \pi T g_{\mathrm{E}}^2$, implying that fermions probe the variation of gauge fields at distances $|\boldsymbol{z} - z_3\boldsymbol{x}/x_3| \sim 1/(gT) \sim 1/m_{\mathrm{E}}$. For the static potential, we need the $x_3 \to \infty$ limit, and then only the position of the gauge field at $z_3 \sim x_3$ matters. Then the prefactor is large, and we may evaluate the integral in the saddle point approximation, yielding

$$S_\chi^{(1)}(\boldsymbol{x}, x_3; \boldsymbol{0}, 0) \;\simeq\; S_\chi^{(0)}(\boldsymbol{x}, x_3; \boldsymbol{0}, 0) \int_0^{x_3} \mathrm{d}z_3\, [iA_3 + A_0] \left(\frac{z_3}{x_3} \boldsymbol{x}, z_3 \right), \tag{E.2.4}$$

justifying eq. (4.1.15).

E.3 Evaluation of the baryonic potential

We show here details for the manipulation of eq. (4.1.24). The free-theory gauge field propagator reads

$$\left\langle A_\mu^a(x) A_\nu^b(0) \right\rangle_0 = \delta^{ab} \Delta_{\mu\nu}(x)\,, \tag{E.3.1}$$

where $\mu, \nu = 0, \ldots, 3$, $a, b = 1, \ldots, 8$ and, in Feynman gauge,

$$\Delta_{\mu\nu}(x) \;=\; \int \frac{\mathrm{d}^3 p}{(2\pi)^3}\, e^{ip\cdot x} \left[\frac{\delta_{\mu 0}\delta_{\nu 0}}{p^2 + m_{\mathrm{E}}^2} + \frac{\delta_{\mu i}\delta_{\nu i}}{p^2 + \lambda^2} \right], \quad p = (\boldsymbol{p}, p_3)\,. \tag{E.3.2}$$

The Debye mass m_{E} is given in eq. (3.3.7), and λ is an auxiliary mass parameter, used as an IR regulator. The Wick contractions following from eq. (4.1.24) lead to the colour algebra

$$\epsilon^{abc}\epsilon^{gfe} (T^d T^d)^{ag} \delta^{bf} \delta^{ce} = 8\,, \quad \epsilon^{abc}\epsilon^{gfe} (T^d)^{ag} (T^d)^{bf} \delta^{ce} = -4\,, \tag{E.3.3}$$

where T^d are Hermitean generators of SU(3), normalized as $\mathrm{tr}(T^c T^d) = \delta^{cd}/2$. Subsequently, we are left over with the time-integrals

$$\mathcal{V}^{\pm}(\boldsymbol{r}_1, \boldsymbol{r}_2, x_3) \equiv -\int_0^{x_3} \mathrm{d}z_3 \left[\Delta_{33}\Big(\boldsymbol{r}_1 - \boldsymbol{r}_2 + \frac{z_3}{x_3}\boldsymbol{r}_2, z_3 \Big) \mp \Delta_{00}\Big(\boldsymbol{r}_1 - \boldsymbol{r}_2 + \frac{z_3}{x_3}\boldsymbol{r}_2, z_3 \Big) \right]. \tag{E.3.4}$$

The propagators are written in a Fourier representation, like in eq. (E.3.2). In the limit $x_3 \to \infty$, noting that

$$\lim_{\delta\to 0^+}\lim_{x_3\to\infty}\int_0^{x_3}\mathrm{d}z_3\, e^{\left[i\left(\frac{\boldsymbol{p}\cdot\boldsymbol{r}}{x_3}+p_3\right)-\delta\right]z_3} = \lim_{\delta\to 0^+}\lim_{x_3\to\infty}\frac{i}{\frac{\boldsymbol{p}\cdot\boldsymbol{r}}{x_3}+p_3+i\delta} = \mathbb{P}\left(\frac{i}{p_3}\right)+\pi\delta(p_3)\,, \tag{E.3.5}$$

where $\mathbb{P}$ denotes a principal value, and pulling the time integral inside the Fourier representation, the Fourier transform becomes

$$\int_{\boldsymbol{p}}\int_{-\infty}^{\infty}\frac{\mathrm{d}p_3}{2\pi}\int_0^{x_3}\mathrm{d}z_3\,\frac{e^{i\boldsymbol{p}\cdot\left(\boldsymbol{r}_1-\boldsymbol{r}_2+\frac{z_3}{x_3}\boldsymbol{r}_2\right)+ip_3z_3}}{f(\boldsymbol{p}^2,p_3^2)} \xrightarrow{x_3\to\infty} \frac{1}{2}\int_{\boldsymbol{p}}\frac{e^{i\boldsymbol{p}\cdot(\boldsymbol{r}_1-\boldsymbol{r}_2)}}{f(\boldsymbol{p}^2,0)}\,. \tag{E.3.6}$$

Carrying out the two-dimensional momentum integral, the potential reads

$$\lim_{x_3\to\infty}\mathcal{V}^{\pm}(\boldsymbol{r}_1,\boldsymbol{r}_2,x_3) = \frac{1}{4\pi}\left[\ln\left(\frac{\lambda\, r_{12}}{2}\right)+\gamma_{\mathrm{E}}\pm K_0(m_{\mathrm{E}}r_{12})\right], \tag{E.3.7}$$

where $r_{12}\equiv|\boldsymbol{r}_1-\boldsymbol{r}_2|$, γ_{E} is the Euler-Mascheroni constant, and K_0 a modified Bessel function. The combinations that appear in eq. (4.1.26) are defined as

$$V^{\pm}(r_{12}) \equiv \frac{4g_{\mathrm{E}}^2}{3}\lim_{\lambda\to 0}\lim_{x_3\to\infty}\left[\mathcal{V}^{\pm}(\boldsymbol{r}_1,\boldsymbol{r}_2,x_3)+\mathcal{V}^{\pm}(\boldsymbol{r}_2,\boldsymbol{r}_1,x_3)-\mathcal{V}^{+}(\boldsymbol{r}_1,\boldsymbol{r}_1,x_3)-\mathcal{V}^{+}(\boldsymbol{r}_2,\boldsymbol{r}_2,x_3)\right]. \tag{E.3.8}$$

By using the expansion of $K_0(x)$ for small x, it is straightforward to show that

$$\lim_{x_3\to\infty}\mathcal{V}^{+}(\boldsymbol{r}_1,\boldsymbol{r}_1,x_3) = \frac{1}{4\pi}\ln\left(\frac{\lambda}{m_{\mathrm{E}}}\right). \tag{E.3.9}$$

This then leads to the explicit expressions for $V^{\pm}(r)$ reported in eq. (4.1.28).

E.4 Simplification of the fermionic action

For the computation of the leading contribution to the hyperfine splitting in the mesonic screening masses, the action in eq. (4.1.6) can be further simplified and written in a more compact way. In particular, we can safely neglect the interacting terms appearing in the transverse covariant derivative $D_\perp$ because they would produce either spin-independent or sub-leading spin-dependent contributions. For each flavour, the action in eq. (4.1.6) can then be written as

$$\begin{aligned} S_{\mathrm{NRQCD}} = i\int d^3x\Bigg\{&\bar{\chi}\left[M+\partial_3-g_{\mathrm{E}}\mathcal{A}^{+}-\frac{1}{2\pi T}\left(\nabla_\perp^2+\frac{g_{\mathrm{E}}}{4i}[\sigma_j,\sigma_k]F_{jk}\right)\right]\chi \\ &+\quad\bar{\phi}\left[M-\partial_3-g_{\mathrm{E}}\mathcal{A}^{-}-\frac{1}{2\pi T}\left(\nabla_\perp^2+\frac{g_{\mathrm{E}}}{4i}[\sigma_j,\sigma_k]F_{jk}\right)\right]\phi\Bigg\}+\ldots\,, \end{aligned} \tag{E.4.1}$$

where we introduced the spin-independent vertex operator $\mathcal{A}^{\pm}$ defined as

$$\mathcal{A}^{\pm} = \mathcal{A}^{\pm,\lambda} T^{\lambda} = \left(A_0^{\lambda} \pm i A_3^{\lambda}\right) T^{\lambda}\,, \qquad \lambda = 1, \ldots, N_c^2 - 1\,. \tag{E.4.2}$$

Furthermore, by recalling that $[\sigma_j, \sigma_k] = 2i\epsilon_{jkl}\sigma_l$ and since we are only interested in $j, k = 1, 2$ and therefore $l = 3$, the spin-dependent term in the action can be readily written as

$$[\sigma_j, \sigma_k] F_{jk} = -4i\sigma_3 B_3\,, \tag{E.4.3}$$

where the chromo-magnetic field is defined as

$$B_3 = -\Big[\partial_1 A_2 - \partial_2 A_1\Big] + O(g_{\mathrm{E}})\,, \tag{E.4.4}$$

and we can safely neglect $O(g_{\mathrm{E}})$ terms since we are only interested in the leading spin-dependent corrections. By introducing the differential operators

$$\mathcal{D}^{\pm} = M \pm \partial_3 - \frac{\nabla_{\perp}^2}{2\pi T}\,, \tag{E.4.5}$$

and the interaction vertices

$$\mathcal{K}^{\pm}(x) = \mathcal{K}^{\pm,\lambda}(x) T^{\lambda} = \left(\mathcal{A}^{\pm,\lambda}(x)\mathbb{1} - \frac{1}{2\pi T}\sigma_3 B_3^{\lambda}(x)\right) T^{\lambda}\,, \tag{E.4.6}$$

with $\mathbb{1}$ being the identity matrix in the spin indices, the NRQCD action can be written in the compact way given in eq. (4.2.8).

E.5 Equations of motion at NLO

In this appendix we report the intermediate steps to obtain eq. (4.2.23) from eq. (4.2.22). By inserting eq. (4.2.14) into the r.h.s. of eq. (4.2.22), we obtain

$$\left[2M + \partial_3 - \sum_{i=1,2} \frac{\nabla_{\boldsymbol{r}_i}^2}{2\pi T}\right] \langle W_{\mathcal{O}}(\boldsymbol{r}_1, \boldsymbol{r}_2; x_3)\rangle = g_{\mathrm{E}}^2 \Bigg\langle \mathrm{Tr}\left\{\Big[\mathcal{A}^{+}(\boldsymbol{r}_1, x_3) + \mathcal{A}^{-}(\boldsymbol{r}_2, x_3)\Big]\right. \tag{E.5.1}$$

$$\left.\Big[\Sigma_{\mathcal{O}}\,\mathcal{S}_{+}^{(0)}(\boldsymbol{r}_1, x_3)\,\Sigma_{\mathcal{O}}\,\mathcal{S}_{-}^{(1)}(\boldsymbol{r}_2, x_3) + \Sigma_{\mathcal{O}}\,\mathcal{S}_{+}^{(1)}(\boldsymbol{r}_1, x_3)\,\Sigma_{\mathcal{O}}\,\mathcal{S}_{-}^{(0)}(\boldsymbol{r}_2, x_3)\Big]\right\} - \frac{1}{2\pi T}\mathrm{Tr}\Bigg\{\Big[s_{\mathcal{O}} B_3(\boldsymbol{r}_1, x_3)$$

$$+B_3(\boldsymbol{r}_2, x_3)\Big]\sigma_3\Big[\Sigma_{\mathcal{O}}\mathcal{S}_{+}^{(0)}(\boldsymbol{r}_1, x_3)\Sigma_{\mathcal{O}}\mathcal{S}_{-}^{(1)}(\boldsymbol{r}_2, x_3) + \Sigma_{\mathcal{O}}\mathcal{S}_{+}^{(1)}(\boldsymbol{r}_1, x_3)\Sigma_{\mathcal{O}}\mathcal{S}_{-}^{(0)}(\boldsymbol{r}_2, x_3)\Big]\Bigg\}\Bigg\rangle + O(g_{\mathrm{E}}^3)\,.$$

By inserting the expression for the quark propagators at next-to-leading order in eq. (4.2.15) and by recalling that, given the expression for $\mathcal{K}^{\pm}$ in eq. (4.1.28),

$\mathcal{A}^{\pm}$ only contracts with $\mathcal{A}^{\pm}$ and B_3 only with B_3, the equation of motion can be written as

$$\left[2M+\partial_3-\sum_{i=1,2}\frac{\nabla^2_{\boldsymbol{r}_i}}{2\pi T}\right]\langle W_{\mathcal{O}}(\boldsymbol{r}_1,\boldsymbol{r}_2;x_3)\rangle=\frac{g_{\mathrm{E}}^2}{N_c}W^{(0)}_{\mathcal{O}}(\boldsymbol{r}_1,\boldsymbol{r}_2;x_3)\times$$
$$\left\{\left\langle \mathrm{Tr}\left\{\left[\mathcal{A}^+(\boldsymbol{r}_1,x_3)+\mathcal{A}^-(\boldsymbol{r}_2,x_3)\right]\int_0^{x_3}\mathrm{d}z_3\left[\mathcal{A}^+(\frac{z_3}{x_3}\boldsymbol{r}_1,z_3)+\mathcal{A}^-(\frac{z_3}{x_3}\boldsymbol{r}_2,z_3)\right]\right\}\right\rangle+\right.$$
$$\frac{1}{(2\pi T)^2}\int_0^{x_3}\mathrm{d}z_3\left\langle \mathrm{Tr}\left\{B_3(\boldsymbol{r}_1,x_3)B_3(\frac{z_3}{x_3}\boldsymbol{r}_1,z_3)+B_3(\boldsymbol{r}_2,x_3)B_3(\frac{z_3}{x_3}\boldsymbol{r}_2,z_3)\right\}\right\rangle+$$
$$\left.\frac{s_{\mathcal{O}}}{(2\pi T)^2}\int_0^{x_3}\mathrm{d}z_3\left\langle \mathrm{Tr}\left\{B_3(\boldsymbol{r}_1,x_3)B_3(\frac{z_3}{x_3}\boldsymbol{r}_2,z_3)+B_3(\boldsymbol{r}_2,x_3)B_3(\frac{z_3}{x_3}\boldsymbol{r}_1,z_3)\right\}\right\rangle\right\}+O(g_{\mathrm{E}}^3)\,, \tag{E.5.2}$$

where the tree-level value $W^{(0)}_{\mathcal{O}}(\boldsymbol{r}_1,\boldsymbol{r}_2;x_3)$ is defined in eq. (4.2.20), and we have introduced $s_{\mathcal{O}}=(+1,-1)$ for the pseudoscalar and the vector fields respectively. Moreover we have exploited the fact that, when contracting the gauge fields $\langle\mathcal{A}^{\pm,\rho}\mathcal{A}^{\pm,\lambda}\rangle\propto\delta^{\rho\lambda}$ and $\langle B_3^{\rho}B_3^{\lambda}\rangle\propto\delta^{\rho\lambda}$.

E.6 Evaluation of the mesonic potential

In this appendix we explicitly show the intermediate steps which lead to the final expression of the static potentials in eq. (4.2.30) and (4.2.31).

E.6.1 Spin-independent contribution

Starting from eq. (4.2.25), the leading spin-independent static potential can be written as

$$\mathcal{U}_{\mathrm{SI}_1}(\boldsymbol{r}_1,\boldsymbol{r}_2;x_3)=-\frac{g_{\mathrm{E}}^2}{N_c}\Big\langle \mathrm{Tr}\left\{\left[\mathcal{A}^+(\boldsymbol{r}_1,x_3)+\mathcal{A}^-(\boldsymbol{r}_2,x_3)\right]\times\right. \tag{E.6.1}$$
$$\left.\int_0^{x_3}\mathrm{d}z_3\left[\mathcal{A}^+(\frac{z_3}{x_3}\boldsymbol{r}_1,z_3)+\mathcal{A}^-(\frac{z_3}{x_3}\boldsymbol{r}_2,z_3)\right]\right\}\Big\rangle=2g_{\mathrm{E}}^2C_F\left[\mathcal{V}^-(\boldsymbol{r}_1,\boldsymbol{r}_2,x_3)-\mathcal{V}^+(\boldsymbol{r}_1,\boldsymbol{r}_1,x_3)\right].$$

where, we contracted the gauge fields and, similarly to the procedure used in the previous section, we introduced the integrals

$$\mathcal{V}^{\pm}(\boldsymbol{r}_1,\boldsymbol{r}_2,x_3)=-\int_0^{x_3}\mathrm{d}z_3\left[\Delta_{33}\left(\boldsymbol{r}_1-\boldsymbol{r}_2+\frac{z_3}{x_3}\boldsymbol{r}_2,z_3\right)\mp\Delta_{00}\left(\boldsymbol{r}_1-\boldsymbol{r}_2\frac{z_3}{x_3}\boldsymbol{r}_2,z_3\right)\right], \tag{E.6.2}$$

where $\Delta_{\mu\nu}$ is the gauge field propagator defined in eq. (E.3.2), in which we made explicit the dependence on the transverse and longitudinal coordinates. Notice that it holds $\mathcal{V}^{\pm}(\boldsymbol{r}_1, \boldsymbol{r}_2, x_3) = \mathcal{V}^{\pm}(\boldsymbol{r}_2, \boldsymbol{r}_1, x_3)$ under the exchanges $\boldsymbol{r}_1 \leftrightarrow \boldsymbol{r}_2$. By taking the large separation limit in the third spatial direction we arrive at

$$U_{\mathrm{SI}_1}(\boldsymbol{r}_1 - \boldsymbol{r}_2) = \lim_{x_3\to\infty} \mathcal{U}_{\mathrm{SI}_1}(\boldsymbol{r}_1, \boldsymbol{r}_2, x_3) = \frac{g_{\mathrm{E}}^2 C_F}{2\pi}\left[\ln\left(\frac{m_{\mathrm{E}} r}{2}\right) + \gamma_{\mathrm{E}} - K_0(m_{\mathrm{E}} r)\right], \quad \text{(E.6.3)}$$

where we introduced $r = |\boldsymbol{r}_1 - \boldsymbol{r}_2|$, γ_{E} is the Euler-Mascheroni constant, K_0 is a modified Bessel function, and m_{E} is the Debye mass introduced in eq. (3.3.7). The potential above is exactly the expression reported in (4.2.30), and which was found in Ref. [154].

E.6.2 Spin-dependent contribution

Analogously, the temperature-suppressed, spin-dependent potential in eq. (4.2.27) can be written as

$$\mathcal{U}_{\mathcal{O}}(\boldsymbol{r}_1, \boldsymbol{r}_2, x_3) = -g_{\mathrm{E}}^2 \frac{2 s_{\mathcal{O}} C_F}{(2\pi T)^2} \mathcal{B}(\boldsymbol{r}_1, \boldsymbol{r}_2, x_3)\,, \quad \text{(E.6.4)}$$

where we introduced the definition

$$\mathcal{B}(\boldsymbol{r}_1, \boldsymbol{r}_2, x_3) = \frac{1}{N_c^2 - 1}\int_0^{x_3} \mathrm{d}z_3 \Big\langle \mathrm{Tr}\left\{ B_3(\boldsymbol{r}_1, x_3) B_3\Big(\frac{z_3}{x_3}\boldsymbol{r}_2, z_3\Big) + B_3(\boldsymbol{r}_2, x_3) B_3\Big(\frac{z_3}{x_3}\boldsymbol{r}_1, z_3\Big)\right\}\Big\rangle. \quad \text{(E.6.5)}$$

By taking the contractions of the gauge fields in the above equation, and by expressing the chromo-magnetic field as in eq. (E.4.4), the integral can be written as[1]

$$\begin{aligned} B(\boldsymbol{r}_1 - \boldsymbol{r}_2) &= \lim_{x_3\to\infty} \mathcal{B}(\boldsymbol{r}_1, \boldsymbol{r}_2, x_3) \quad \text{(E.6.6)} \\ &= \lim_{x_3\to\infty} \int_0^{x_3} \mathrm{d}z_3 \Big[\partial_1^{\boldsymbol{r}_2}\partial_1^{\boldsymbol{r}_1}\Delta_{22}(\boldsymbol{r}_1 - \boldsymbol{r}_2, x_3 - z_3) + \partial_2^{\boldsymbol{r}_2}\partial_2^{\boldsymbol{r}_1}\Delta_{11}(\boldsymbol{r}_1 - \boldsymbol{r}_2, x_3 - z_3)\Big]. \end{aligned}$$

By recalling the expression of the spatial components of the gluon propagators, see eq. (E.3.2), the derivative terms in the expression above read

$$\partial_j^{\boldsymbol{r}_2}\partial_j^{\boldsymbol{r}_1}\Delta_{ii}(\boldsymbol{r}_1 - \boldsymbol{r}_2, x_3 - z_3) = \int \frac{\mathrm{d}^3 p}{(2\pi)^3} e^{i\boldsymbol{p}(\boldsymbol{r}_1 - \boldsymbol{r}_2)} e^{ip_3(x_3 - z_3)} \frac{p_j^2}{p^2}\,. \quad \text{(E.6.7)}$$

[1] Here the superscript in the partial derivative refers to which $\boldsymbol{r}_i$ (either $\boldsymbol{r}_1$ or $\boldsymbol{r}_2$) the derivative is taken with respect to. Therefore $\partial_i^{\boldsymbol{r}_j}$ indicates the partial derivative with respect to the ith component of the $\boldsymbol{r}_j$ coordinate.

By inserting this expression in eq. (E.6.6), the integral can be written as

$$B\left(\boldsymbol{r}_1-\boldsymbol{r}_2\right)=\lim_{x_3\to\infty}\int_0^{x_3}\mathrm{d}z_3\int\frac{\mathrm{d}^3p}{(2\pi)^3}e^{i\boldsymbol{p}(\boldsymbol{r}_1-\boldsymbol{r}_2)}e^{ip_3(x_3-z_3)}\left[1-\frac{p_3^2}{p^2}\right], \tag{E.6.8}$$

where we used the fact that $p^2-p_3^2=p_1^2+p_2^2=\boldsymbol{p}^2$. Therefore the integral above can be split into two different contributions as

$$\begin{aligned}B\left(\boldsymbol{r}_1-\boldsymbol{r}_2\right) &= \lim_{x_3\to\infty}\left[\delta^{(2)}(\boldsymbol{r}_1-\boldsymbol{r}_2)\int_0^{x_3}\mathrm{d}z_3\,\delta(x_3-z_3)-\mathcal{R}\left(\boldsymbol{r}_1-\boldsymbol{r}_2,x_3\right)\right] \\ &= \frac{1}{2}\delta^{(2)}(\boldsymbol{r}_1-\boldsymbol{r}_2)-\lim_{x_3\to\infty}\mathcal{R}\left(\boldsymbol{r}_1-\boldsymbol{r}_2,x_3\right),\end{aligned} \tag{E.6.9}$$

where we have introduced the remainder time-integral

$$\mathcal{R}\left(\boldsymbol{r}_1-\boldsymbol{r}_2,x_3\right)=\int\frac{\mathrm{d}p_3}{2\pi}\,p_3^2\int_0^{x_3}\mathrm{d}z_3\,e^{ip_3(x_3-z_3)}\int\frac{\mathrm{d}^2\boldsymbol{p}}{(2\pi)^2}\,\frac{e^{i\boldsymbol{p}(\boldsymbol{r}_1-\boldsymbol{r}_2)}}{\boldsymbol{p}^2+p_3^2}\,. \tag{E.6.10}$$

The integration over the transverse components of the momentum can be carried out by recalling that it holds

$$\int\frac{\mathrm{d}^2\boldsymbol{p}}{(2\pi)^2}\,\frac{e^{i\boldsymbol{p}(\boldsymbol{r}_1-\boldsymbol{r}_2)}}{\boldsymbol{p}^2+p_3^2}=\frac{1}{2\pi}K_0\big(|p_3|\,r\big)\,, \tag{E.6.11}$$

where K_0 is a modified Bessel function. Analogously by performing the integration over the longitudinal spatial coordinate, the integral in eq. (E.6.10) is reduced to a one-dimensional integral over the p_3 variable that reads

$$\mathcal{R}\left(\boldsymbol{r}_1-\boldsymbol{r}_2,x_3\right)=\frac{i}{2\pi}\int\frac{\mathrm{d}p_3}{2\pi}\,p_3\left(1-e^{ip_3x_3}\right)K_0\big(|p_3|\,r\big). \tag{E.6.12}$$

Finally the integral over the longitudinal momentum can be carried out by taking into account the symmetry properties of the integrand under the change $p_3\to-p_3$, yielding to

$$\mathcal{R}\left(\boldsymbol{r}_1-\boldsymbol{r}_2,x_3\right)=\frac{1}{2\pi^2}\int_0^\infty\mathrm{d}p_3\,p_3\sin\left(p_3x_3\right)K_0\left(p_3\,r\right)=\frac{x_3}{4\pi\left(x_3^2+r^2\right)^{3/2}}\,. \tag{E.6.13}$$

Therefore by taking the large separation limit in the third spatial direction in eq. (E.6.6), and by recalling that, according to eq. (E.6.13), $\lim_{x_3\to\infty}\mathcal{R}\left(\boldsymbol{r}_1-\boldsymbol{r}_2,x_3\right)=0$, we obtain

$$B\left(\boldsymbol{r}_1-\boldsymbol{r}_2\right)=\frac{1}{2}\delta^{(2)}(\boldsymbol{r}_1-\boldsymbol{r}_2)\,. \tag{E.6.14}$$

Finally, by inserting this expression into eq. (E.6.4) we obtain the final expression for the spin-dependent static potential

$$U_{\mathcal{O}}(\boldsymbol{r}_1-\boldsymbol{r}_2)=\lim_{x_3\to\infty}\mathcal{U}_{\mathcal{O}}\left(\boldsymbol{r}_1,\boldsymbol{r}_2,x_3\right)=-g_{\mathrm{E}}^2\frac{s_{\mathcal{O}}C_F}{(2\pi T)^2}\delta^{(2)}(\boldsymbol{r}_1-\boldsymbol{r}_2) \tag{E.6.15}$$

reported in eq. (4.2.31).

E.7 Discretized Hamiltonian

In this appendix we describe the method we employed to numerically solve the eigenvalue problem. The central idea is to discretize the spatial coordinates of the system and then explicitly construct the Hamiltonian operator as matrix in position basis. This matrix can then be diagonalized to obtain part of the eigenvalue and eigenvector spectrum.

E.7.1 Coordinate label

Consider a system parametrized by a total number of space coordinates D. They could refer to different components of position vectors as well as to the coordinates of different bodies in the problem. In particular, if we consider N_{bod} bodies moving in N_{dim} - dimensional space, the total number of space coordinates is[2] $D = N_{\text{dim}} N_{\text{bod}}$. Assigning an ordering rule for the coordinates, we will denote them as X^α, with Greek letters at the beginning of the alphabet $\alpha \in \{1, ..., D\}$. The particular ordering one uses is arbitrary, but for definiteness we choose to cycle through the N_{dim} coordinates of each body in order. Therefore denoting with $x^\mu_{(a)}$ the μ-th component of the a-th's body position, the D dimensional collective coordinate vector X will be

$$X^{\boldsymbol{T}} = \left(x^1_{(1)}, \dots, x^{N_{\text{dim}}}_{(1)}, x^1_{(2)}, \dots, x^{N_{\text{dim}}}_{(2)}, \dots, x^{N_{\text{dim}}}_{(N_{\text{bod}})}\right) \tag{E.7.1}$$

One easily convinces themselves that the μ-th component of the a-th body is labeled by the collective index α if the following relation holds between the three:

$$\alpha = \mu + (N_{\text{bod}} - 1)a \tag{E.7.2}$$

To lighten the notation, in the following we lose contact with indexes μ and a and only refer to α.

E.7.2 Lexicographic order

We now discretize each component X^α to take N evenly spaced values in the interval $[-L/2, L/2]$. We label the discrete values of each component α with a latin index $X^\alpha_{j_\alpha}$, $j_\alpha \in \{1, \dots, N\}$. This defines a $\underbrace{N \times N \times \dots \times N}_{D}$ grid of position values, corresponding to N^D possible system configurations. A point in this grid can be uniquely characterized by a D-tuple of indexes $\{j_\alpha\}_{\alpha=1,\dots,D}$ each one going from 1 to N. Similarly to what we did earlier, we can equivalently associate to

[2] To our purposes, the baryon case involves two relative positions living in 2 dimensional space, therefore requiring $D = 4$ coordinates

each point of the grid a single *lexicographic* index $I \in \{1, \dots, N^D\}$ if the relation among I and the D indexes j_α is:

$$I = j_1 + N(j_2 - 1) + N^2(j_3 - 1) + \cdots + N^{D-1}(j_D - 1) \tag{E.7.3}$$

Essentially, the first N values of I correspond to cycling the N possible value of the first index j_1 while all other indexes remain fixed to their first value. The next N values of I cycle through the N values of j_1, but with the second index set to its second value, and so on. The inverse map, which associates to the value of the lexicographic index I the corresponding values of the D indexes j_α, is given by

$$j_\alpha = \mod \{I, N^\alpha\}. \tag{E.7.4}$$

E.7.3 Matrix representation of operators

When sampled over the discretized position space, a function of the D variables $f\left(x^1_{j_1}, x^2_{j_2}, \dots, x^D_{j_D}\right)$ can be represented by a N^D dimensional vector f whose components $f_I, I \in \{1, \dots, N^D\}$ contain the value of the function at the I-th point of the discrete grid. In the context of Non Relativistic Quantum Mechanics, we can think of $f\left(x^1, \dots, x^D\right)$ as a wave function of the system representing the state $|f\rangle$ in position basis: $f\left(x^1_{j_1}, \dots, x^D_{j_D}\right) = \left\langle x^1_{j_1}, \dots, x^D_{j_D} \middle| f \right\rangle$. Any linear operator $\hat{O}$ acting on $|f\rangle$ can thus be represented by a $N^D \times N^D$ matrix. We will be interested in Hamiltonians of the form

$$\hat{H} = \hat{T} + \hat{V} \tag{E.7.5}$$

where we assume that the potential term $\hat{V}$ is a local function of the space coordinates, while the kinetic term $\hat{T}$ contains derivatives with respect to such coordinates. We now describe the form these two terms assume for our choice of lexicographic ordering and how to explicitly "build" them with code.

Potential term

As stated above, we assume the potential to be a local function of the D coordinates $V\left(x^1_{j_1}, \dots, x^D_{j_D}\right)$. To determine how the potential is represented as a $N^D \times N^D$ matrix in the discretized coordinate space, it is useful to first derive the action of the single coordinates $\hat{x}^\alpha$ (intended as operators) on a state $|f\rangle$. Consider for instance the action of the first coordinate $\hat{x}^1$ on a state $|f\rangle$, and take its component on $\left\langle x^1_{j_1}, \dots, x^D_{j_D} \right|$:

$$\left\langle x^1_{j_1}, \dots, x^D_{j_D} \middle| \hat{x}^1 \middle| f \right\rangle = x^1_{j_1} f(x^1_{j_1}, \dots, x^D_{j_D}) \tag{E.7.6}$$

or in explicit matrix form:

$$\hat{x}^1 \begin{pmatrix} f\left(x_1^1, x_1^2, \ldots, x_1^D\right) \\ f\left(x_2^1, x_1^2, \ldots, x_1^D\right) \\ \vdots \\ f\left(x_N^1, x_1^2, \ldots, x_1^D\right) \\ f\left(x_1^1, x_2^2, \ldots, x_1^D\right) \\ f\left(x_2^1, x_2^2, \ldots, x_1^D\right) \\ \vdots \\ f\left(x_N^1, x_2^2, \ldots, x_1^D\right) \\ \vdots \\ f\left(x_N^1, x_N^2, \ldots, x_N^D\right) \end{pmatrix} = \begin{pmatrix} x_1^1 f\left(x_1^1, x_1^2, \ldots, x_1^D\right) \\ x_2^1 f\left(x_2^1, x_1^2, \ldots, x_1^D\right) \\ \vdots \\ x_N^1 f\left(x_N^1, x_1^2, \ldots, x_1^D\right) \\ x_1^1 f\left(x_1^1, x_2^2, \ldots, x_1^D\right) \\ x_2^1 f\left(x_2^1, x_2^2, \ldots, x_1^D\right) \\ \vdots \\ x_N^1 f\left(x_N^1, x_2^2, \ldots, x_1^D\right) \\ \vdots \\ x_N^1 f\left(x_N^1, x_N^2, \ldots, x_N^D\right) \end{pmatrix} \tag{E.7.7}$$

Form this depiction it should be clear that the matrix representation of $\hat{x}^1$ has the following form:

$$\hat{x}^1 = \left.\begin{pmatrix} \mathcal{X}^1 & & \\ & \ddots & \\ & & \mathcal{X}^1 \end{pmatrix}\right\} N^{D-1} \tag{E.7.8}$$

Where the matrix $\mathcal{X}^1$ repeated N^{D-1} times on the diagonal is an $N \times N$ diagonal matrix given by

$$\mathcal{X}^1 = \begin{pmatrix} x_1^1 & & & & \\ & x_2^1 & & & \\ & & x_3^1 & & \\ & & & \ddots & \\ & & & & x_N^1 \end{pmatrix} \tag{E.7.9}$$

We now point out that one can write both $\mathcal{X}^1$ and $\hat{x}^1$ in a neat way using the Kronecker tensor product $\otimes$. Denoting with $\mathrm{d}\{x^1\}$ the $N \times N$ diagonal matrix whose components are the N components of x^1 ($\mathrm{d}\{x^1\}_{ij} = x_j^1 \delta_{ij}$) and with $\mathbb{1}_N$ the $N \times N$ identity matrix (with $\mathbb{1}_1 = 1$), we have

$$\mathcal{X}^1 = \mathrm{d}\{x^1\} \otimes \mathbb{1}_1 \tag{E.7.10}$$

$$\hat{x}^1 = \mathbb{1}_{N^{D-1}} \otimes \mathcal{X}^1 \tag{E.7.11}$$

In this case equation (E.7.10) is trivial and we have $\mathcal{X}^1 = \mathrm{d}\{x^1\}$, but it was expressed in this form to more easily generalize to the other coordinates. Indeed, following a line of reasoning completely analogous to the one for x^1, one can convince themselves that the matrix representation for the m^{th} coordinate $\hat{x}^m$ has the following form:

$$\hat{x}^m = \left.\begin{pmatrix} \mathcal{X}^m & & \\ & \ddots & \\ & & \mathcal{X}^m \end{pmatrix}\right\} N^{D-m} \tag{E.7.12}$$

Where now $\mathcal{X}^m$ is an $N^m \times N^m$ diagonal matrix repeated N^{D-m} times; both $\mathcal{X}^m$ and $\hat{x}^m$ can be constructed through the Kronecker product similarly to (E.7.10) and (E.7.11):

$$\mathcal{X}^m = \mathrm{d}\{x^m\} \otimes \mathbb{1}_{N^{m-1}} \tag{E.7.13}$$

$$\hat{x}^m = \mathbb{1}_{N^{D-m}} \otimes \mathcal{X}^m \tag{E.7.14}$$

This outlines a simple procedure to represent all coordinates as matrices (operators) in the discretized position space. Once we have such representations, we can determine the matrix form of any function of the coordinates, in particular of the potential, by simply applying said function to the main diagonal of the coordinate matrices. As a matter of fact, the potential term of the Hamiltonian is exactly diagonal in the position basis we choose.

Kinetic term

For the kinetic term $\hat{T}$ we assume that it is given by some combination of the Laplacian for the various coordinates. The question is then how to represent (minus) the second derivative with respect to a given coordinate x^m with our choice of basis, which we denote

$$\mathcal{L}^m \equiv -\frac{d^2}{d(x^m)^2} \tag{E.7.15}$$

To this end it is useful to first consider the one-dimensional case, which will be easily generalized to arbitrary dimension D. There are many different ways to discretize the second derivative; here we will focus on two alternatives: so called finite difference methods and a representation of the second derivative based on the discrete Fourier transform.

Finite differences Consider a function of one variable $f(x)$. Suppose we only have access to the value of f at N equispaced values of the variable x: $x_j = x_0 + (j-1)\cdot a$, with $j = 1 \dots N$. Denoting $f_j = f(x_j)$, we would like to determine a linear combination of the f_j that approximates the value of (minus) the second derivative of f at a certain site x_i. The Taylor expansion in a of terms like $f_{i+n} + f_{i-n}$ contains only even derivatives and powers of a, including the 0^{th} term. It is then clear that one can look for $p+1$ coefficients α_j, $j = 0 \dots p$ such that the following combination yields the value of $-f^{(2)}(x_i)$ up to a correction which scales as a^{2p}:

$$2\alpha_0 f(x_i) + \sum_{j=1}^{p} \alpha_j \left[f(x_i + j\cdot a) + f(x_i - j\cdot a) \right] = -a^2 \left(f^{(2)}(x_i) + O\left(a^{2p}\right) \right) \tag{E.7.16}$$

Taylor expanding the left hand side of (E.7.16) and requiring that only the term $-a^2 f^{(2)}(x_i)$ survives (up to order $2p$) results in $p+1$ equations for the α_j that can be summarized in the following linear system:

$$\begin{pmatrix} 2 & 2 & 2 & 2 & \dots & 2 \\ 0 & 1 & 2^2 & 3^2 & \dots & p^2 \\ 0 & 1 & 2^4 & 3^4 & \dots & p^4 \\ \vdots & \vdots & \vdots & \vdots & \ddots & \vdots \\ 0 & 1 & 2^{2p} & 3^{2p} & \dots & p^{2p} \end{pmatrix} \begin{pmatrix} \alpha_0 \\ \alpha_1 \\ \alpha_2 \\ \vdots \\ \alpha_p \end{pmatrix} = \begin{pmatrix} 0 \\ -1 \\ 0 \\ \vdots \\ 0 \end{pmatrix} \tag{E.7.17}$$

Thus for a chosen order p the coefficients that grant an approximation of the one dimensional Laplacian of order $2p$ can be obtained by inverting the system (E.7.17). Finally, converting equation (E.7.16) in matrix form, the matrix representation of the one dimensional Laplace operator at order $2p$ is given by the multidiagonal matrix

$$\left(-a^2 \frac{d^2}{dx^2}\right)_p \equiv a^2 \boldsymbol{L}_p = \begin{pmatrix} 2\alpha_0 & \alpha_1 & \alpha_2 & \dots & \alpha_p & 0 & \dots & \dots & \dots & \\ \alpha_1 & 2\alpha_0 & \alpha_1 & \alpha_2 & \dots & \alpha_p & 0 & \dots & \dots & \\ \alpha_2 & \alpha_1 & 2\alpha_0 & \alpha_1 & \alpha_2 & \dots & \alpha_p & 0 & \dots & \\ \vdots & \alpha_2 & \alpha_1 & 2\alpha_0 & \alpha_1 & \alpha_2 & \dots & \alpha_p & 0 & \vdots \\ \alpha_p & & \ddots & \ddots & \ddots & \ddots & \ddots & & \ddots & 0 \\ 0 & \ddots & & & & & & & & \alpha_p \\ \vdots & & \ddots & & \ddots & \ddots & \ddots & \ddots & \ddots & \vdots \\ & \dots & 0 & \alpha_p & \dots & \alpha_2 & \alpha_1 & 2\alpha_0 & \alpha_1 & \alpha_2 \\ & \dots & \dots & 0 & \alpha_p & \dots & \alpha_2 & \alpha_1 & 2\alpha_0 & \alpha_1 \\ & \dots & \dots & \dots & 0 & \alpha_p & \dots & \alpha_2 & \alpha_1 & 2\alpha_0 \end{pmatrix} \tag{E.7.18}$$

The entries at the bottom and top of the first and last column respectively define the boundary conditions imposed on the function f. In particular, with Dirichlet boundary conditions these terms are all zero, while with periodic boundary conditions the coefficients "wrap around" the first and last column.

D dimensions

Now that we know how to represent the one dimensional Laplace operator as matrix, we can build a matrix representation of the Laplace operator acting on any of the D discretized coordinates. In a line of reasoning identical to that of section E.7.3, one can convince themselves that the second derivative with respect to the m^{th} coordinate, which we earlier dubbed $\mathcal{L}^m$ can be obtained as

$$\mathbb{L}^m = \boldsymbol{L}^m \otimes \mathbb{1}_{N^{m-1}} \tag{E.7.19}$$

$$\mathcal{L}^m = \mathbb{1}_{N^{D-m}} \otimes \mathbb{L}^m \tag{E.7.20}$$

Where $\boldsymbol{L}^m$ is the discretized one dimensional Laplace operator with respect to the m^{th} coordinate, as obtained by any of the methods described earlier. With these building blocks one is able to build a matrix representation of any local "standard" Hamiltonian, which can then be diagonalized with a suitable algorithm to determine part of the eigenvalue and eigenvector spectrum of the system.
The main drawback of this method is that the dimension of H, and thus the memory required by the computer to store it / the computation time scales exponentially with the number of coordinates D. H is however in general very sparse (if the Laplacian is represented with finite differences), and thus only a fraction of the components need to be stored. The `python` code used to implement this procedure handles the Hamiltonian as a sparse matrix, and is able to obtain the ground state in around 1 minute for $N = 40$ ($2.56\text{E}6 \times 2.56\text{E}6$ Hamiltonian) and 20 minutes for $N = 60$ ($\sim 1.3\text{E}7 \times 1.3\text{E}7$). The largest number of points we were able to accomodate before running into memory issues (on a laptop) was $N = 64$, for which the partial diagonalization took around 1 hour.

Appendix F

Lattice results for mesonic screening masses

In this appendix we collect the full set of data for static and non-static mesonic screening masses obtained from the lattice as described in chapter 5. Tables F.1, F.2, F.3 and F.4 collect the screening masses of mesonic fields in the static ($n = 0$) and non-static ($n = 1$) Matsubara sectors at all temperatures and lattice spacings, as obtained from the effective mass analysis explained in section 5.2.6. The number of gauge field configurations, and thus the number of MDUs generated and skipped between consecutive measuremnents, are the same reported in tables 5.1 and 5.2. Mesonic correlation functions have been computed on 1 random source per configuration in all cases except for the ensemble with $L_0/a = 6$ at T_1, which was used to study the properties of random sources in detail as described in section 5.2.5, and for which we used 16 random sources per configuration.

Static sector ($n = 0$)

T	L_0/a	$\frac{m_P}{2\pi T}$	$\frac{m_{V_T}}{2\pi T}$	$\frac{m_{V_0}}{2\pi T}$	$\frac{m_{V_T} - m_P}{2\pi T}$
T_0	4	0.964906(46)	0.970649(60)	0.9675(51)	0.005743(29)
	6	0.99376(19)	0.99959(20)	1.0594(46)	0.00582(14)
T_1	4	0.966332(84)	0.97311(12)	0.9762(37)	0.006780(63)
	6	0.99502(17)	1.00195(18)	1.0656(46)	0.006936(43)
	8	1.00641(50)	1.01361(54)	1.0934(70)	0.007199(66)
	10	1.01149(34)	1.01851(41)	1.0908(49)	0.00702(12)
T_2	4	0.967019(62)	0.974798(86)	0.9772(24)	0.007779(42)
	6	0.99457(20)	1.00217(28)	1.0672(35)	0.007601(96)
	8	1.00556(39)	1.01342(41)	1.0923(29)	0.00786(10)
	10	1.01108(35)	1.01879(47)	1.0956(47)	0.00771(15)
T_3	4	0.967708(73)	0.976602(99)	0.9793(23)	0.008895(48)
	6	0.99540(19)	1.00427(23)	1.0630(57)	0.008878(73)
	8	1.00641(25)	1.01571(28)	1.0949(56)	0.009316(80)
	10	1.01137(34)	1.02075(43)	1.1136(72)	0.009380(93)
T_4	4	0.968641(61)	0.979049(75)	0.9783(22)	0.010408(44)
	6	0.99579(15)	1.00632(26)	1.0950(25)	0.01053(13)
	8	1.00590(25)	1.01651(21)	1.1066(33)	0.010606(96)
	10	1.01042(27)	1.02089(39)	1.1194(43)	0.01046(14)
T_5	4	0.968867(78)	0.98100(11)	0.9851(28)	0.012131(59)
	6	0.99604(11)	1.00859(15)	1.0999(68)	0.012543(96)
	8	1.00661(17)	1.01942(22)	1.1126(54)	0.01282(12)
	10	1.01119(32)	1.02410(36)	1.1313(48)	0.01291(12)

TABLE F.1: Mesonic screening masses in the static $n = 0$ sector for all lattice spacings at temperatures $T_0 - T_5$. We report data for the pseudoscalar (P), transverse (V_T) and compact (V_0) vector channels and the splitting $(m_{V_T} - m_P)/2\pi T$. The values are determined from the effective mass analysis detailed in section 5.2.6.

Static sector ($n = 0$)

T	L_0/a	$\frac{m_P}{2\pi T}$	$\frac{m_{V_T}}{2\pi T}$	$\frac{m_{V_0}}{2\pi T}$	$\frac{m_{V_T} - m_P}{2\pi T}$
T_6	4	0.968859(59)	0.983501(87)	0.9867(49)	0.014642(65)
	6	0.99533(13)	1.01036(17)	1.1173(39)	0.01503(11)
	8	1.00479(15)	1.01971(20)	1.1338(51)	0.01492(12)
	10	1.00898(29)	1.02397(35)	1.1319(63)	0.01500(16)
T_7	4	0.968470(69)	0.986833(93)	0.9901(38)	0.018364(76)
	6	0.99328(13)	1.01185(17)	1.106(26)	0.01857(12)
	8	1.00358(22)	1.02249(22)	1.1351(64)	0.01891(33)
	10	1.00621(34)	1.02445(39)	1.1494(64)	0.01824(24)
T_8	4	0.966273(95)	0.98955(13)	0.9893(67)	0.02328(12)
	6	0.99087(20)	1.01424(60)	1.136(13)	0.02337(42)
	8	0.99980(20)	1.02259(26)	1.169(12)	0.02279(17)
	10	1.00556(36)	1.02897(31)	1.1618(64)	0.02341(19)
T_9	4	0.96747(13)	0.98867(23)	1.0051(44)	0.02119(11)
	6	0.99150(20)	1.01377(29)	1.1427(80)	0.02226(18)
	8	1.00052(26)	1.02365(46)	1.1551(99)	0.02313(27)
T_{10}	4	0.96416(11)	0.99114(32)	0.994(10)	0.02698(23)
	6	0.98689(20)	1.01539(30)	1.161(16)	0.02850(32)
	8	0.99446(29)	1.02392(63)	1.1855(71)	0.02946(57)
T_{11}	4	0.95687(10)	0.99348(54)	1.000(12)	0.03661(46)
	6	0.97691(30)	1.01544(84)	1.1730(93)	0.03853(61)
	8	0.98477(44)	1.02410(65)	1.198(11)	0.03932(26)

TABLE F.2: Same as table F.1, but for temperatures $T_6 - T_{11}$.

Non-static sector ($n = 1$)

T	L_0/a	$\frac{m_P}{2\pi T}$	$\frac{m_{V_0}}{2\pi T}$	$\frac{m_{V_T} - m_P}{2\pi T}$	$\frac{m_{V_0} - m_{V_3}}{2\pi T}$
T_0	4	1.0312(31)	0.99479(23)	0.0001(30)	-0.00013(16)
	6	1.0887(32)	1.02712(75)	0.0038(38)	-0.00018(56)
T_1	4	1.0361(31)	0.99911(22)	-0.0014(43)	-0.00001(18)
	6	1.0898(25)	1.03328(22)	0.0025(27)	0.00023(23)
	8	1.1042(32)	1.04717(55)	0.0010(29)	0.00071(47)
	10	1.1235(94)	1.05376(78)	-0.009(15)	-0.0007(17)
T_2	4	1.0431(45)	1.00262(23)	-0.0026(48)	-0.00009(26)
	6	1.108(22)	1.03501(60)	-0.0005(80)	-0.00028(54)
	8	1.1028(82)	1.04952(64)	0.0037(88)	0.00031(50)
	10	1.118(12)	1.05702(47)	-0.009(21)	-0.0011(16)
T_3	4	1.0440(54)	1.00602(37)	-0.0088(58)	0.00004(36)
	6	1.1072(54)	1.04068(37)	0.0007(61)	-0.00008(32)
	8	1.1212(67)	1.05483(49)	0.0001(54)	0.00012(48)
	10	1.1213(67)	1.06059(86)	0.014(11)	0.0024(27)
T_4	4	1.0612(91)	1.01040(42)	-0.0072(98)	0.00052(54)
	6	1.1239(46)	1.04659(49)	-0.0054(93)	0.00043(50)
	8	1.1321(72)	1.05782(79)	0.0035(99)	0.00094(84)
	10	1.1521(80)	1.06492(79)	0.014(11)	0.0025(27)
T_5	4	1.051(10)	1.01708(49)	-0.008(15)	0.00098(43)
	6	1.1190(85)	1.05168(57)	0.0040(77)	0.00027(53)
	8	1.1420(67)	1.06373(63)	0.0022(88)	0.00037(62)
	10	1.151(14)	1.07221(67)	0.003(15)	0.0022(24)

TABLE F.3: Mesonic screening masses in the non-static $n = 1$ sector for all lattice spacings at temperatures T_0–T_5. We report data for the pseudoscalar (P) and compact (V_0) vector channels and the mass differences $(m_{V_T} - m_P)/2\pi T$ and $(m_{V_0} - m_{V_3})/2\pi T$. Notice that while the latter channels are expected to be degenerate (in the continuum) due to the Ward Identity (5.2.13), the degeneracy of non-static pseudoscalar and transverse vector channel is not expected *a priori*.

Non-static sector ($n = 1$)

T	L_0/a	$\frac{m_P}{2\pi T}$	$\frac{m_{V_0}}{2\pi T}$	$\frac{m_{V_T} - m_P}{2\pi T}$	$\frac{m_{V_0} - m_{V_3}}{2\pi T}$
T_6	4	1.099(33)	1.02079(66)	-0.0007(86)	-0.00035(69)
	6	1.1340(72)	1.05762(66)	-0.0020(86)	0.00010(72)
	8	1.1532(49)	1.0696(12)	-0.0010(89)	-0.0017(12)
	10	1.161(13)	1.0776(12)	0.028(18)	-0.0025(47)
T_7	4	1.1000(41)	1.02918(57)	-0.0033(42)	-0.00034(48)
	6	1.1586(31)	1.06568(62)	0.0102(41)	-0.00024(73)
	8	1.1659(88)	1.07828(78)	0.0103(84)	-0.00047(94)
	10	1.156(23)	1.0822(11)	0.028(31)	0.0005(41)
T_8	4	1.087(15)	1.03750(32)	-0.006(19)	0.00032(51)
	6	1.1565(75)	1.07379(95)	-0.005(11)	0.00097(75)
	8	1.1796(97)	1.08570(75)	-0.007(15)	-0.00097(82)
	10	1.195(15)	1.09118(83)	0.002(18)	0.0021(49)
T_9	4	1.109(13)	1.03541(30)	-0.006(17)	0.00003(40)
	6	1.1762(61)	1.0716(10)	0.0053(68)	-0.0004(12)
	8	1.2009(91)	1.0863(10)	0.021(13)	0.0003(21)
T_{10}	4	1.1422(77)	1.04506(77)	-0.0029(65)	0.00141(93)
	6	1.187(22)	1.0822(11)	0.011(16)	-0.0019(17)
	8	1.212(12)	1.0970(15)	0.019(10)	-0.0004(16)
T_{11}	4	1.1506(99)	1.05392(97)	-0.004(12)	-0.0004(10)
	6	1.2247(67)	1.09511(67)	0.0194(77)	0.0008(13)
	8	1.232(15)	1.1084(14)	0.000(19)	-0.0024(22)

TABLE F.4: Same as table F.3 but for temperatures $T_6 - T_{11}$.

Appendix G

Tree-level screening masses on the lattice

In order to accelerate the extrapolation to the continuum limit, we have computed the screening masses in the free theory on the lattice, both for the baryonic and mesonic sectors. In this appendix we report some salient details of the computations.

G.1 Mesonic screening mass

We set to evaluate the lattice correlator in equation (5.2.15) in the free theory. By going to momentum space and denoting $\boldsymbol{p} = (p_0, p_1, p_2)$, we can carry out the sums in the x_0, x_1, x_2 direction to obtain delta functions, yielding:

$$C_\Gamma^{(n)}(x_3) = \sum_{p_3,q_3} \sum_{\boldsymbol{p},\boldsymbol{q}} \mathrm{Tr}\{S(p)\Gamma S(q)\Gamma\} e^{ix_3(p_3-q_3)} \delta(p_0-q_0+\omega_n\gamma^2)\delta(p_1-q_1+\omega_n\gamma^2\xi)\delta(p_2-q_2) \tag{G.1.1}$$

where p, q are the two valence quarks' momenta. The propagator for non-interacting Wilson fermions $S(p)$ can be cast in the form

$$S(p) = \frac{-i\gamma_\mu s_\mu(p) + M(p)}{D(p)} \tag{G.1.2}$$

with the following defintions:

$$M(p) \equiv m_0 + 4 - \sum_\mu c_\mu(p) \equiv \tilde{M}(p) - c_3(p), \qquad D(p) = \sum_\mu s_\mu^2(p) + M^2(p) \tag{G.1.3}$$

with $s_\mu(p) \equiv \sin(p_\mu), c_\mu(p) \equiv \cos(p_\mu)$ (the definition of $\tilde{M}(p)$ will be useful later). We recall that in the presence of shifted boundary conditions with shift vectors of

the form $\boldsymbol{\xi} = (\xi, 0, 0)$ the 0-component of quark momenta is given by

$$p_0 = (2n_0 + 1)\frac{\pi}{L_0} - p_1\xi\,, \qquad n_0 = 0, \dots, L_0/a - 1\,, \tag{G.1.4}$$

and the spatial momenta are $p_k \in [-\pi/a, \pi/a)$. The trace over spinor indices in equation (G.1.1) is given by the following expressions in the P, S, V, A channels:

$$P/S: \qquad \mathrm{Tr}\{S(p)\Gamma S(q)\Gamma\} = 4\frac{\pm s_\mu(p)s_\mu(q) + M(p)M(q)}{D(p)D(q)} \tag{G.1.5}$$

$$V/A: \qquad \mathrm{Tr}\{S(p)\Gamma S(q)\Gamma\} = 8\frac{s_\mu(p)s_\mu(q) \pm 2M(p)M(q)}{D(p)D(q)}. \tag{G.1.6}$$

Plugging the above equations into (G.1.1), the sums in p_3 and q_3 can be carried out explicitly using the result

$$\mathrm{S}_{\boldsymbol{p}}(x_3) \equiv \sum_{p_3} \frac{e^{ip_3x_3}}{D(p)} = \frac{1}{2\tilde{M}(p)} \frac{\cosh\left(\hat{\omega}_p(L - 2x_3)\right)}{\sinh 2\hat{\omega}_p \sinh L\hat{\omega}_p}, \tag{G.1.7}$$

where L is the extent of the spatial directions, and we introduced

$$\hat{\omega}_p \equiv \log\left(\omega_p + \sqrt{1 + \omega_p^2}\right), \qquad \omega_p \equiv \frac{\left(1 - \tilde{M}(p)\right)^2 + \sum_{j=0}^{2} s_j(p)^2}{4\tilde{M}(p)}. \tag{G.1.8}$$

It is useful to notice that in the thermodynamic limit $L \to \infty$ eq (G.1.7) tends to

$$\mathrm{S}_{\boldsymbol{p}}(x_3) \underset{L\to\infty}{\to} \frac{1}{4\tilde{M}(p)} \frac{e^{-2\hat{\omega}_p x_3}}{\omega_p\sqrt{1 + \omega_p^2}}. \tag{G.1.9}$$

Once the sums in p_3, q_3 have been carried out and the thermodynamic limit has been taken, the correlator for channel $X \in \{P, S, V, A\}$ can be cast in the form

$$C_X^{(n)}(x_3) = \sum\!\!\!\!\!\!\int_{\boldsymbol{p},\boldsymbol{q}} \mathcal{M}_X(\boldsymbol{p}, \boldsymbol{q}) e^{-2(\hat{\omega}_p + \hat{\omega}_q)x_3} \delta(p_0 - q_0 + \omega_n\gamma^2)\delta(p_1 - q_1 + \omega_n\gamma^2\xi)\delta(p_2 - q_2). \tag{G.1.10}$$

The above equation can be interpreted as a spectral decomposition for the screening correlator. The channel-dependent function $\mathcal{M}_X(\boldsymbol{p}, \boldsymbol{q})$ plays the role of a weight for each momentum configuration. The exponential factor is instead the same for all channels: the screening mass will hence be the same for all channels and it will be given by the minimum of the function that multiplies x_3 in the exponential, subject to the constraint imposed by the delta's:

$$m^{(n)} = 2\min_{\boldsymbol{p},\boldsymbol{q}}\{\hat{\omega}_p + \hat{\omega}_q\}, \quad \boldsymbol{p}, \boldsymbol{q} \text{ subject to } \begin{cases} q_0 = p_0 + \omega_n\gamma^2 \\ q_1 = p_1 + \omega_n\gamma^2\xi \\ q_2 = p_2 \end{cases} \tag{G.1.11}$$

It can be shown that the function $\hat{\omega}_p$ has a minimum for $\boldsymbol{p} = (\pi\gamma^2/L_0, \pi\gamma^2\xi/L_0, 0)$. In the static case $n = 0$ it is clear that setting both $\boldsymbol{p}$ and $\boldsymbol{q}$ to the minimal point satisfies the constraint in eq. (G.1.11), therefore the screening mass assumes the smallest possible value $m^{(0)} = 4\min\{\hat{\omega}_p\}$. For $n = 1$ it would seem that it is no longer the case, however exploiting the fact that $\hat{\omega}_p$ is an even function of all its components we can see that the choice

$$\begin{pmatrix} p_0 \\ p_1 \\ p_2 \end{pmatrix} = \begin{pmatrix} -\pi\gamma^2/L_0 \\ -\pi\gamma^2\xi/L_0 \\ 0 \end{pmatrix}, \qquad \begin{pmatrix} q_0 \\ q_1 \\ q_2 \end{pmatrix} = \begin{pmatrix} \pi\gamma^2/L_0 \\ \pi\gamma^2\xi/L_0 \\ 0 \end{pmatrix} \tag{G.1.12}$$

does satisfy the constraint, with both momenta still corresponding to a minimum of $\hat{\omega}_p$. Hence, the tree level meson screening mass on the lattice is the same for the $n = 0$ and $n = 1$ Matsubara sectors. One could wonder whether this continues to be the case for all Matsubara sectors, i.e. whether it is always possible for all values of n to find values of $\boldsymbol{p}$ and $\boldsymbol{q}$ that are equivalent to the minimum of $\hat{\omega}_p$ and satisfy the constraint. We can start by requiring that $p_1 = \pm\pi\gamma^2\xi/L_0$ and using the constraint to obtain the value of q_1:

$$q_1 = \frac{\pi}{L_0}\gamma^2\xi(2n \pm 1). \tag{G.1.13}$$

If also the second momentum is to be equivalent to the minimal point, we should require that $q_1 = \pm\pi\gamma^2\xi/L_0$. Then at least one of the four following relations must hold:

$$\begin{aligned} 2n + 1 &= 1, \quad & 2n - 1 &= 1, \\ 2n + 1 &= -1, \quad & 2n - 1 &= -1, \end{aligned} \tag{G.1.14}$$

which can be only statisfied if $n = 0$ or $n = \pm 1$. We conclude that for $n \geq 2$ the tree level screening mass will cease to be the absolute minimum. To find the minimal value in this case, we can resolve the constraint and numerically minimize the exponent as a function of $\boldsymbol{p}$ alone. This analysis suggests that for $n = 2$ the minimum is attained, for instance, for the choice

$$\begin{pmatrix} p_0 \\ p_1 \\ p_2 \end{pmatrix} = \begin{pmatrix} -\pi\gamma^2/L_0 \\ -\pi\gamma^2\xi/L_0 \\ 0 \end{pmatrix}, \qquad \begin{pmatrix} q_0 \\ q_1 \\ q_2 \end{pmatrix} = \begin{pmatrix} 3\pi\gamma^2/L_0 \\ 3\pi\gamma^2\xi/L_0 \\ 0 \end{pmatrix}. \tag{G.1.15}$$

A non-trivial consistency check consists in verifying that in the limit $L_0 \to \infty$ the tree level screening mass approaches the continuum value $4\pi T$ ($2n\pi T$ for generic $n \geq 2$), which was found to be the case. Table G.1 summarizes the tree level screening mass on the lattice normalized to the continuum value for the $n = 0, \pm 1$ and $n = 2$ sectors, which seem to suggest that higher Matsubara sectors suffer from larger discretization effects.

L_0/a	$\frac{m^{(0,1)}}{2\pi T}$	$\frac{m^{(2)}}{4\pi T}$
4	0.932614077...	0.746250105...
6	0.967811412...	0.843315708...
8	0.981401809...	0.896717157...
10	0.987944825...	0.927961230...
12	0.991569612...	0.947352961...

TABLE G.1: Tree level mesonic screening mass on the lattice for the static, $n = 1$ and $n = 2$ Matsubara sectors, normalized by the respective continuum values, for shift vector $\boldsymbol{\xi} = (1, 0, 0)$.

G.2 Baryonic screening mass

Following completely analogous steps, the baryonic correlators (5.1.2) in the free lattice theory can be written as

$$C_{N^\pm}(x_3) = \pm \sum_{p_0,q_0} \int dp_1 dp_2 dq_1 dq_2 \mathcal{M}(p,q) e^{-2\,\Omega(p,q,k)x_3}\,, \tag{G.2.1}$$

The function $\Omega(p,q,k)$ is given by

$$\Omega(p,q,k) \;=\; \hat{\omega}(p) + \hat{\omega}(q) + \hat{\omega}(k)\,, \tag{G.2.2}$$

with p, q and k denoting the momenta of the three quarks, while the weight matrix $\mathcal{M}(p,q)$ once again does not influence the value of the baryonic screening mass. Like in the mesonic case, the sum over spatial momenta and frequencies is subject to energy-momentum conservation, which reads

$$\begin{cases} p_0 + q_0 + k_0 \;=\; \frac{\pi}{L_0}\gamma^2 \\ p_1 + q_1 + k_1 \;=\; \frac{\pi}{L_0}\xi\gamma^2 \\ p_2 + q_2 + k_2 \;=\; 0 \end{cases}\,, \tag{G.2.3}$$

and once again the screening mass is obtained by minimizing $\Omega(p,q,k)$ satisfying the above constraint. Recalling the fact that the function $\hat{\omega}(p)$ is even and the position of its minimum, we can see that setting the quarks' momenta to

$$p = q = \frac{\pi}{2L_0}(1,1,0)\,, \qquad k = \frac{\pi}{2L_0}(-1,-1,0)\,. \tag{G.2.4}$$

satisfies momentum conservation with each quark's momentum corresponding to a minimum of $\hat{\omega}(p)$, which guarantees that the value of Ω is the minimal one. Table G.2 summarizes the value of the screening mass normalized to $3\pi T$ for the temporal extents relevant to this work.

L_0/a	$m_{N^\pm}^{\mathrm{free}}/3\pi T$
4	0.932614077...
6	0.967811412...
8	0.981401809...
10	0.987944825...

TABLE G.2: Tree-level values of the baryonic screening mass on lattices with temporal extent L_0/a, infinite spatial volume and shift vector $\boldsymbol{\xi} = (1, 0, 0)$

Bibliography

[1] Marco Cè et al. "The hyperfine splitting in QCD mesonic screening masses at asymptotically large temperatures". In: *JHEP* 06 (2025), p. 44. DOI: https://doi.org/10.1007/JHEP05(2025)044. arXiv: 2502.07674 [hep-lat].

[2] Leonardo Giusti et al. "Baryonic screening masses in QCD at high temperature". In: *Physics Letters B* 855 (2024), p. 138799. ISSN: 0370-2693. DOI: https://doi.org/10.1016/j.physletb.2024.138799. URL: https://www.sciencedirect.com/science/article/pii/S0370269324003575.

[3] Leonardo Giusti et al. "Baryonic thermal screening mass at NLO". In: *JHEP* 06 (2024), p. 205. DOI: 10.1007/JHEP06(2024)205. arXiv: 2405.03975 [hep-ph].

[4] Pietro Rescigno et al. "Baryonic screening masses in high temperature QCD". In: *PoS* LATTICE2023 (2024), p. 196. DOI: 10.22323/1.453.0196. arXiv: 2311.17761 [hep-lat].

[5] Davide Laudicina et al. "Non-perturbative thermal QCD at very high temperatures: computational strategy and hadronic screening masses". In: *PoS* LATTICE2024 (2025), p. 181. DOI: 10.22323/1.466.0181. arXiv: 2411.14127 [hep-lat].

[6] Leonardo Giusti et al. "Non-perturbative thermal QCD at very high temperatures". In: *PoS* ICHEP2024 (2025), p. 503. DOI: 10.22323/1.476.0503. arXiv: 2410.12626 [hep-lat].

[7] Franz Gross et al. "50 Years of Quantum Chromodynamics". In: *Eur. Phys. J. C* 83 (2023), p. 1125. DOI: 10.1140/epjc/s10052-023-11949-2. arXiv: 2212.11107 [hep-ph].

[8] Konrad Osterwalder and Robert Schrader. "AXIOMS FOR EUCLIDEAN GREEN'S FUNCTIONS". In: *Commun. Math. Phys.* 31 (1973), pp. 83–112. DOI: 10.1007/BF01645738.

[9] Konrad Osterwalder and Robert Schrader. "Axioms for Euclidean Green's Functions. 2." In: *Commun. Math. Phys.* 42 (1975), p. 281. DOI: 10.1007/BF01608978.

[10] G. Martinelli et al. "A general method for non-perturbative renormalization of lattice operators". In: *Nucl. Phys. B* 445 (1995), pp. 81–108. DOI: 10.1016/0550-3213(95)00126-D. arXiv: hep-lat/9411010.

[11] David J. Gross and Frank Wilczek. "Ultraviolet Behavior of Nonabelian Gauge Theories". In: *Phys. Rev. Lett.* 30 (1973). Ed. by J. C. Taylor, pp. 1343–1346. DOI: 10.1103/PhysRevLett.30.1343.

[12] H. David Politzer. "Reliable Perturbative Results for Strong Interactions?" In: *Phys. Rev. Lett.* 30 (26 June 1973), pp. 1346–1349. DOI: 10.1103/PhysRevLett.30.1346. URL: https://link.aps.org/doi/10.1103/PhysRevLett.30.1346.

[13] O. Nachtmann and W. Wetzel. "The Beta Function for Effective Quark Masses to Two Loops in QCD". In: *Nucl. Phys. B* 187 (1981), pp. 333–342. DOI: 10.1016/0550-3213(81)90278-9.

[14] Mattia Bruno et al. "QCD Coupling from a Nonperturbative Determination of the Three-Flavor Λ Parameter". In: *Phys. Rev. Lett.* 119.10 (2017), p. 102001. DOI: 10.1103/PhysRevLett.119.102001. arXiv: 1706.03821 [hep-lat].

[15] D. d'Enterria et al. "The strong coupling constant: state of the art and the decade ahead". In: *J. Phys. G* 51.9 (2024), p. 090501. DOI: 10.1088/1361-6471/ad1a78. arXiv: 2203.08271 [hep-ph].

[16] F. Herzog et al. "The five-loop beta function of Yang-Mills theory with fermions". In: *JHEP* 02 (2017), p. 090. DOI: 10.1007/JHEP02(2017)090. arXiv: 1701.01404 [hep-ph].

[17] P. A. Baikov, K. G. Chetyrkin, and J. H. Kühn. "Five-Loop Running of the QCD Coupling Constant". In: *Phys. Rev. Lett.* 118.8 (2017), p. 082002. DOI: 10.1103/PhysRevLett.118.082002. arXiv: 1606.08659 [hep-ph].

[18] Mattia Dalla Brida et al. "The strength of the interaction between quarks and gluons". In: (Jan. 2025). arXiv: 2501.06633 [hep-ph].

[19] Gerard 't Hooft. "Renormalization of Massless Yang-Mills Fields". In: *Nucl. Phys. B* 33 (1971), pp. 173–199. DOI: 10.1016/0550-3213(71)90395-6.

[20] Gerard 't Hooft. "Renormalizable Lagrangians for Massive Yang-Mills Fields". In: *Nucl. Phys. B* 35 (1971). Ed. by J. C. Taylor, pp. 167–188. DOI: 10.1016/0550-3213(71)90139-8.

[21] Gerard 't Hooft and M. J. G. Veltman. "Regularization and Renormalization of Gauge Fields". In: *Nucl. Phys. B* 44 (1972), pp. 189–213. DOI: 10.1016/0550-3213(72)90279-9.

[22] S. Navas et al. "Review of Particle Physics". In: *Phys. Rev. D* 110 (3 Aug. 2024), p. 030001. DOI: 10.1103/PhysRevD.110.030001. URL: https://link.aps.org/doi/10.1103/PhysRevD.110.030001.

[23] Murray Gell-Mann. "A Schematic Model of Baryons and Mesons". In: *Phys. Lett.* 8 (1964), pp. 214–215. DOI: 10.1016/S0031-9163(64)92001-3.

[24] G. Zweig. "An SU(3) model for strong interaction symmetry and its breaking. Version 1". In: (Jan. 1964). DOI: 10.17181/CERN-TH-401.

[25] Yan-Rui Liu et al. "Pentaquark and Tetraquark states". In: *Prog. Part. Nucl. Phys.* 107 (2019), pp. 237–320. DOI: 10.1016/j.ppnp.2019.04.003. arXiv: 1903.11976 [hep-ph].

[26] Eberhard Klempt and Alexander Zaitsev. "Glueballs, Hybrids, Multiquarks. Experimental facts versus QCD inspired concepts". In: *Phys. Rept.* 454 (2007), pp. 1–202. DOI: 10.1016/j.physrep.2007.07.006. arXiv: 0708.4016 [hep-ph].

[27] V. Crede and C. A. Meyer. "The Experimental Status of Glueballs". In: *Prog. Part. Nucl. Phys.* 63 (2009), pp. 74–116. DOI: 10.1016/j.ppnp.2009.03.001. arXiv: 0812.0600 [hep-ex].

[28] Hua-Xing Chen et al. "An updated review of the new hadron states". In: *Rept. Prog. Phys.* 86.2 (2023), p. 026201. DOI: 10.1088/1361-6633/aca3b6. arXiv: 2204.02649 [hep-ph].

[29] Davide Vadacchino. "A review on Glueball hunting". In: *39th International Symposium on Lattice Field Theory*. May 2023. arXiv: 2305.04869 [hep-lat].

[30] Jeffrey Goldstone, Abdus Salam, and Steven Weinberg. "Broken Symmetries". In: *Phys. Rev.* 127 (3 Aug. 1962), pp. 965–970. DOI: 10.1103/PhysRev.127.965. URL: https://link.aps.org/doi/10.1103/PhysRev.127.965.

[31] Murray Gell-Mann, R. J. Oakes, and B. Renner. "Behavior of Current Divergences under $SU_3 \times SU_3$". In: *Phys. Rev.* 175 (5 Nov. 1968), pp. 2195–2199. DOI: 10.1103/PhysRev.175.2195. URL: https://link.aps.org/doi/10.1103/PhysRev.175.2195.

[32] Georg P. Engel et al. "Chiral Symmetry Breaking in QCD with Two Light Flavors". In: *Phys. Rev. Lett.* 114 (11 Mar. 2015), p. 112001. DOI: 10.1103/PhysRevLett.114.112001. URL: https://link.aps.org/doi/10.1103/PhysRevLett.114.112001.

[33] Tom Banks and A. Casher. "Chiral Symmetry Breaking in Confining Theories". In: *Nucl. Phys. B* 169 (1980), pp. 103–125. DOI: 10.1016/0550-3213(80)90255-2.

[34] Edward Witten. "Current Algebra Theorems for the U(1) Goldstone Boson". In: *Nucl. Phys. B* 156 (1979), pp. 269–283. DOI: 10.1016/0550-3213(79)90031-2.

[35] G. Veneziano. "U(1) Without Instantons". In: *Nucl. Phys. B* 159 (1979), pp. 213–224. DOI: 10.1016/0550-3213(79)90332-8.

[36] Marco Cè et al. "The topological susceptibility in the large-N limit of SU(N) Yang–Mills theory". In: *Phys. Lett. B* 762 (2016), pp. 232–236. DOI: 10.1016/j.physletb.2016.09.029. arXiv: 1607.05939 [hep-lat].

[37] Claudio Bonati et al. "θ dependence of 4D $SU(N)$ gauge theories in the large-N limit". In: *Phys. Rev. D* 94.8 (2016), p. 085017. DOI: 10.1103/PhysRevD.94.085017. arXiv: 1607.06360 [hep-lat].

[38] Claudio Bonanno, Claudio Bonati, and Massimo D'Elia. "Large-N $SU(N)$ Yang-Mills theories with milder topological freezing". In: *JHEP* 03 (2021), p. 111. DOI: 10.1007/JHEP03(2021)111. arXiv: 2012.14000 [hep-lat].

[39] Andreas Athenodorou and Michael Teper. "SU(N) gauge theories in 3+1 dimensions: glueball spectrum, string tensions and topology". In: *JHEP* 12 (2021), p. 082. DOI: 10.1007/JHEP12(2021)082. arXiv: 2106.00364 [hep-lat].

[40] Claudio Bonanno. "The large-N limit of the topological susceptibility of SU(N) Yang-Mills theories via Parallel Tempering on Boundary Conditions". In: (Oct. 2025). arXiv: 2510.08006 [hep-lat].

[41] Christof Gattringer and Christian B. Lang. *Quantum chromodynamics on the lattice*. Vol. 788. Berlin: Springer, 2010. ISBN: 978-3-642-01849-7, 978-3-642-01850-3. DOI: 10.1007/978-3-642-01850-3.

[42] Heinz J. Rothe. *Lattice Gauge Theories : An Introduction (Fourth Edition)*. Vol. 43. World Scientific Publishing Company, 2012. ISBN: 978-981-4365-87-1, 978-981-4365-85-7. DOI: 10.1142/8229.

[43] Kenneth G. Wilson. "Confinement of Quarks". In: *Phys. Rev. D* 10 (1974). Ed. by J. C. Taylor, pp. 2445–2459. DOI: 10.1103/PhysRevD.10.2445.

[44] Holger Bech Nielsen and M. Ninomiya. "Absence of Neutrinos on a Lattice. 1. Proof by Homotopy Theory". In: *Nucl. Phys. B* 185 (1981). Ed. by J. Julve and M. Ramón-Medrano. [Erratum: Nucl.Phys.B 195, 541 (1982)], p. 20. DOI: 10.1016/0550-3213(82)90011-6.

[45] Holger Bech Nielsen and M. Ninomiya. "Absence of Neutrinos on a Lattice. 2. Intuitive Topological Proof". In: *Nucl. Phys. B* 193 (1981), pp. 173–194. DOI: 10.1016/0550-3213(81)90524-1.

[46] Holger Bech Nielsen and M. Ninomiya. "No Go Theorem for Regularizing Chiral Fermions". In: *Phys. Lett. B* 105 (1981), pp. 219–223. DOI: 10.1016/0370-2693(81)91026-1.

[47] Martin Lüscher et al. "A Precise determination of the running coupling in the SU(3) Yang-Mills theory". In: *Nucl. Phys. B* 413 (1994), pp. 481–502. DOI: 10.1016/0550-3213(94)90629-7. arXiv: hep-lat/9309005.

[48] Stefano Capitani et al. "Non-perturbative quark mass renormalization in quenched lattice QCD". In: *Nucl. Phys. B* 544 (1999). [Erratum: Nucl.Phys.B 582, 762–762 (2000)], pp. 669–698. DOI: 10.1016/S0550-3213(98)00857-8. arXiv: hep-lat/9810063.

[49] Michele Della Morte et al. "Computation of the strong coupling in QCD with two dynamical flavors". In: *Nucl. Phys. B* 713 (2005), pp. 378–406. DOI: 10.1016/j.nuclphysb.2005.02.013. arXiv: hep-lat/0411025.

[50] S. Aoki et al. "Precise determination of the strong coupling constant in N_f = 2+1 lattice QCD with the Schrodinger functional scheme". In: *JHEP* 10 (2009), p. 053. DOI: 10.1088/1126-6708/2009/10/053. arXiv: 0906.3906 [hep-lat].

[51] Fatih Tekin, Rainer Sommer, and Ulli Wolff. "The Running coupling of QCD with four flavors". In: *Nucl. Phys. B* 840 (2010), pp. 114–128. DOI: 10.1016/j.nuclphysb.2010.07.002. arXiv: 1006.0672 [hep-lat].

[52] Mattia Dalla Brida et al. "Determination of the QCD Λ-parameter and the accuracy of perturbation theory at high energies". In: *Phys. Rev. Lett.* 117.18 (2016), p. 182001. DOI: 10.1103/PhysRevLett.117.182001. arXiv: 1604.06193 [hep-ph].

[53] Mattia Dalla Brida et al. "A non-perturbative exploration of the high energy regime in N_{f} = 3 QCD". In: *Eur. Phys. J. C* 78.5 (2018), p. 372. DOI: 10.1140/epjc/s10052-018-5838-5. arXiv: 1803.10230 [hep-lat].

[54] Mattia Dalla Brida et al. "Non-perturbative thermal QCD at all temperatures: the case of mesonic screening masses". In: *JHEP* 04 (2022), p. 034. DOI: 10.1007/JHEP04(2022)034. arXiv: 2112.05427 [hep-lat].

[55] K. Symanzik. "Continuum Limit and Improved Action in Lattice Theories. 1. Principles and φ^4 Theory". In: *Nucl. Phys. B* 226 (1983), pp. 187–204. DOI: 10.1016/0550-3213(83)90468-6.

[56] K. Symanzik. "Continuum Limit and Improved Action in Lattice Theories. 2. O(N) Nonlinear Sigma Model in Perturbation Theory". In: *Nucl. Phys. B* 226 (1983), pp. 205–227. DOI: 10.1016/0550-3213(83)90469-8.

[57] M. Lüscher and P. Weisz. "On-shell improved lattice gauge theories". In: *Commun. Math. Phys.* 98.3 (1985). [Erratum: Commun.Math.Phys. 98, 433 (1985)], p. 433. DOI: 10.1007/BF01205792.

[58] B. Sheikholeslami and R. Wohlert. "Improved Continuum Limit Lattice Action for QCD with Wilson Fermions". In: *Nucl. Phys. B* 259 (1985), p. 572. DOI: 10.1016/0550-3213(85)90002-1.

[59] Martin Lüscher et al. "Chiral symmetry and O(a) improvement in lattice QCD". In: *Nucl. Phys. B* 478 (1996), pp. 365–400. DOI: 10.1016/0550-3213(96)00378-1. arXiv: hep-lat/9605038.

[60] Martin Lüscher et al. "Nonperturbative O(a) improvement of lattice QCD". In: *Nucl. Phys. B* 491 (1997), pp. 323–343. DOI: 10.1016/S0550-3213(97)00080-1. arXiv: hep-lat/9609035.

[61] N. Yamada et al. "Non-perturbative O(a)-improvement of Wilson quark action in three-flavor QCD with plaquette gauge action". In: *Phys. Rev. D* 71 (2005), p. 054505. DOI: 10.1103/PhysRevD.71.054505. arXiv: hep-lat/0406028.

[62] John Bulava and Stefan Schaefer. "Improvement of $N_f = 3$ lattice QCD with Wilson fermions and tree-level improved gauge action". In: *Nucl. Phys. B* 874 (2013), pp. 188–197. DOI: 10.1016/j.nuclphysb.2013.05.019. arXiv: 1304.7093 [hep-lat].

[63] G. Parisi. "The Strategy for Computing the Hadronic Mass Spectrum". In: *Phys. Rept.* 103 (1984). Ed. by C. Itzykson, Y. Pomeau, and N. Sourlas, pp. 203–211. DOI: 10.1016/0370-1573(84)90081-4.

[64] G. Peter Lepage. "The Analysis of Algorithms for Lattice Field Theory". In: *Theoretical Advanced Study Institute in Elementary Particle Physics*. June 1989.

[65] M. Albanese et al. "Glueball Masses and String Tension in Lattice QCD". In: *Phys. Lett. B* 192 (1987), pp. 163–169. DOI: 10.1016/0370-2693(87)91160-9.

[66] Anna Hasenfratz and Francesco Knechtli. "Flavor symmetry and the static potential with hypercubic blocking". In: *Physical Review D* 64.3 (July 2001). ISSN: 1089-4918. DOI: 10.1103/physrevd.64.034504. URL: http://dx.doi.org/10.1103/PhysRevD.64.034504.

[67] Colin Morningstar and Mike J. Peardon. "Analytic smearing of SU(3) link variables in lattice QCD". In: *Phys. Rev. D* 69 (2004), p. 054501. DOI: 10.1103/PhysRevD.69.054501. arXiv: hep-lat/0311018.

[68] Benoit Blossier et al. "On the generalized eigenvalue method for energies and matrix elements in lattice field theory". In: *JHEP* 04 (2009), p. 094. DOI: 10.1088/1126-6708/2009/04/094. arXiv: 0902.1265 [hep-lat].

[69] Martin Luscher and Peter Weisz. "Locality and exponential error reduction in numerical lattice gauge theory". In: *JHEP* 09 (2001), p. 010. DOI: 10.1088/1126-6708/2001/09/010. arXiv: hep-lat/0108014.

[70] Marco Cè, Leonardo Giusti, and Stefan Schaefer. "Domain decomposition, multi-level integration and exponential noise reduction in lattice QCD". In: *Phys. Rev. D* 93.9 (2016), p. 094507. DOI: 10.1103/PhysRevD.93.094507. arXiv: 1601.04587 [hep-lat].

[71] Marco Cè, Leonardo Giusti, and Stefan Schaefer. "A local factorization of the fermion determinant in lattice QCD". In: *Phys. Rev. D* 95.3 (2017), p. 034503. DOI: 10.1103/PhysRevD.95.034503. arXiv: 1609.02419 [hep-lat].

[72] Leonardo Giusti, Marco Cè, and Stefan Schaefer. "Multi-boson block factorization of fermions". In: *EPJ Web Conf.* 175 (2018). Ed. by M. Della Morte et al., p. 01003. DOI: 10.1051/epjconf/201817501003. arXiv: 1710.09212 [hep-lat].

[73] Leonardo Giusti and Matteo Saccardi. "Four-dimensional factorization of the fermion determinant in lattice QCD". In: *Phys. Lett. B* 829 (2022), p. 137103. DOI: 10.1016/j.physletb.2022.137103. arXiv: 2203.02247 [hep-lat].

[74] Mattia Dalla Brida et al. "Multi-level Monte Carlo computation of the hadronic vacuum polarization contribution to $(g_\mu - 2)$". In: *Phys. Lett. B* 816 (2021), p. 136191. DOI: 10.1016/j.physletb.2021.136191. arXiv: 2007.02973 [hep-lat].

[75] Kai Schmitz. "Modern Cosmology, an Amuse-Gueule". In: (2022). Ed. by Marilena Streit-Bianchi et al., pp. 37–70. DOI: 10.1007/978-3-031-05625-3_3. arXiv: 2203.04757 [physics.pop-ph].

[76] R. Hagedorn. "Statistical thermodynamics of strong interactions at high-energies". In: *Nuovo Cim. Suppl.* 3 (1965), pp. 147–186.

[77] R. Hagedorn and J. Ranft. "Statistical thermodynamics of strong interactions at high-energies. 2. Momentum spectra of particles produced in pp-collisions". In: *Nuovo Cim. Suppl.* 6 (1968), pp. 169–354.

[78] N. Cabibbo and G. Parisi. "Exponential Hadronic Spectrum and Quark Liberation". In: *Phys. Lett. B* 59 (1975), pp. 67–69. DOI: 10.1016/0370-2693(75)90158-6.

[79] Edward V. Shuryak. "Theory of Hadronic Plasma". In: *Sov. Phys. JETP* 47 (1978), pp. 212–219.

[80] José Correia et al. "Gravitational waves from strong first order phase transitions". In: (May 2025). arXiv: 2505.17824 [astro-ph.CO].

[81] Djuna Croon and David J. Weir. "Gravitational Waves from Phase Transitions". In: *Contemp. Phys.* 65 (2024), p. 75. DOI: 10.1080/00107514.2024.2423496. arXiv: 2410.21509 [hep-ph].

[82] Mark Hindmarsh et al. "Gravitational waves from the sound of a first order phase transition". In: *Phys. Rev. Lett.* 112 (2014), p. 041301. DOI: 10.1103/PhysRevLett.112.041301. arXiv: 1304.2433 [hep-ph].

[83] Eric Thrane and Joseph D. Romano. "Sensitivity curves for searches for gravitational-wave backgrounds". In: *Phys. Rev. D* 88.12 (2013), p. 124032. DOI: 10.1103/PhysRevD.88.124032. arXiv: 1310.5300 [astro-ph.IM].

[84] Chiara Caprini et al. "Detecting gravitational waves from cosmological phase transitions with LISA: an update". In: *JCAP* 03 (2020), p. 024. DOI: 10.1088/1475-7516/2020/03/024. arXiv: 1910.13125 [astro-ph.CO].

[85] Stanislav Babak, Antoine Petiteau, and Martin Hewitson. "LISA Sensitivity and SNR Calculations". In: (Aug. 2021). arXiv: 2108.01167 [astro-ph.IM].

[86] Gabriella Agazie et al. "The NANOGrav 15 yr Data Set: Detector Characterization and Noise Budget". In: *The Astrophysical Journal Letters* 951.1 (June 2023), p. L10. ISSN: 2041-8213. DOI: 10.3847/2041-8213/acda88. URL: http://dx.doi.org/10.3847/2041-8213/acda88.

[87] Larry D. McLerran and Benjamin Svetitsky. "Quark Liberation at High Temperature: A Monte Carlo Study of SU(2) Gauge Theory". In: *Phys. Rev. D* 24 (1981), p. 450. DOI: 10.1103/PhysRevD.24.450.

[88] Leonard Susskind. "Lattice Models of Quark Confinement at High Temperature". In: *Phys. Rev. D* 20 (1979), pp. 2610–2618. DOI: 10.1103/PhysRevD.20.2610.

[89] Benjamin Svetitsky and Laurence G. Yaffe. "Critical Behavior at Finite Temperature Confinement Transitions". In: *Nucl. Phys. B* 210 (1982), pp. 423–447. DOI: 10.1016/0550-3213(82)90172-9.

[90] Leonardo Giusti et al. "A precise study of the thermodynamic properties of the SU(3) Yang-Mills theory across the deconfinement transition". In: *Phys. Lett. B* 868 (2025), p. 139775. DOI: 10.1016/j.physletb.2025.139775. arXiv: 2501.10284 [hep-lat].

[91] Martin Lüscher. "Properties and uses of the Wilson flow in lattice QCD". In: *JHEP* 08 (2010). [Erratum: JHEP 03, 092 (2014)], p. 071. DOI: 10.1007/JHEP08(2010)071. arXiv: 1006.4518 [hep-lat].

[92] Y. Aoki et al. "The QCD transition temperature: Results with physical masses in the continuum limit". In: *Phys. Lett. B* 643 (2006), pp. 46–54. DOI: 10.1016/j.physletb.2006.10.021. arXiv: hep-lat/0609068.

[93] Y. Aoki et al. "The Order of the quantum chromodynamics transition predicted by the standard model of particle physics". In: *Nature* 443 (2006), pp. 675–678. DOI: 10.1038/nature05120. arXiv: hep-lat/0611014.

[94] Y. Aoki et al. "The QCD transition temperature: results with physical masses in the continuum limit II." In: *JHEP* 06 (2009), p. 088. DOI: 10.1088/1126-6708/2009/06/088. arXiv: 0903.4155 [hep-lat].

[95] Szabolcs Borsanyi et al. "Is there still any T_c mystery in lattice QCD? Results with physical masses in the continuum limit III". In: *JHEP* 09 (2010), p. 073. DOI: 10.1007/JHEP09(2010)073. arXiv: 1005.3508 [hep-lat].

[96] A. Bazavov et al. "Equation of state and QCD transition at finite temperature". In: *Phys. Rev. D* 80 (2009), p. 014504. DOI: 10.1103/PhysRevD.80.014504. arXiv: 0903.4379 [hep-lat].

[97] A. Bazavov et al. "The chiral and deconfinement aspects of the QCD transition". In: *Phys. Rev. D* 85 (2012), p. 054503. DOI: 10.1103/PhysRevD.85.054503. arXiv: 1111.1710 [hep-lat].

[98] Zaven Arzoumanian et al. "The NANOGrav 12.5 yr Data Set: Search for an Isotropic Stochastic Gravitational-wave Background". In: *The Astrophysical Journal Letters* 905.2 (Dec. 2020), p. L34. DOI: 10.3847/2041-8213/abd401. URL: https://doi.org/10.3847/2041-8213/abd401.

[99] Boris Goncharov et al. "On the Evidence for a Common-spectrum Process in the Search for the Nanohertz Gravitational-wave Background with the Parkes Pulsar Timing Array". In: *The Astrophysical Journal Letters* 917.2 (Aug. 2021), p. L19. ISSN: 2041-8213. DOI: 10.3847/2041-8213/ac17f4. URL: http://dx.doi.org/10.3847/2041-8213/ac17f4.

[100] S. Chen et al. "Common-red-signal analysis with 24-yr high-precision timing of the European Pulsar Timing Array: inferences in the stochastic gravitational-wave background search". In: *Mon. Not. Roy. Astron. Soc.* 508.4 (2021), pp. 4970–4993. DOI: 10.1093/mnras/stab2833. arXiv: 2110.13184 [astro-ph.HE].

[101] J. Antoniadis et al. "The second data release from the European Pulsar Timing Array - IV. Implications for massive black holes, dark matter, and the early Universe". In: *Astron. Astrophys.* 685 (2024), A94. DOI: 10.1051/0004-6361/202347433. arXiv: 2306.16227 [astro-ph.CO].

[102] K. Kajantie et al. "The Electroweak phase transition: A Nonperturbative analysis". In: *Nucl. Phys. B* 466 (1996), pp. 189–258. DOI: 10.1016/0550-3213(96)00052-1. arXiv: hep-lat/9510020.

[103] K. Kajantie et al. "Is there a hot electroweak phase transition at $m_H \gtrsim m_W$?" In: *Phys. Rev. Lett.* 77 (1996), pp. 2887–2890. DOI: 10.1103/PhysRevLett.77.2887. arXiv: hep-ph/9605288.

[104] Michela D'Onofrio and Kari Rummukainen. "Standard model cross-over on the lattice". In: *Phys. Rev. D* 93 (2 Jan. 2016), p. 025003. DOI: 10.1103/PhysRevD.93.025003. URL: https://link.aps.org/doi/10.1103/PhysRevD.93.025003.

[105] Oliver Gould, Sinan Güyer, and Kari Rummukainen. "First-order electroweak phase transitions: A nonperturbative update". In: *Phys. Rev. D* 106.11 (2022). [Erratum: Phys.Rev.D 110, 119903 (2024)], p. 114507. DOI: 10.1103/PhysRevD.106.114507. arXiv: 2205.07238 [hep-lat].

[106] Robert D. Pisarski and Frank Wilczek. "Remarks on the Chiral Phase Transition in Chromodynamics". In: *Phys. Rev. D* 29 (1984), pp. 338–341. DOI: 10.1103/PhysRevD.29.338.

[107] Owe Philipsen. "Lattice Constraints on the QCD Chiral Phase Transition at Finite Temperature and Baryon Density". In: *Symmetry* 13.11 (2021), p. 2079. DOI: 10.3390/sym13112079. arXiv: 2111.03590 [hep-lat].

[108] Francesca Cuteri, Owe Philipsen, and Alessandro Sciarra. "On the order of the QCD chiral phase transition for different numbers of quark flavours". In: *JHEP* 11 (2021), p. 141. DOI: 10.1007/JHEP11(2021)141. arXiv: 2107.12739 [hep-lat].

[109] Yu Zhang et al. "Three flavor QCD phase transition with Mobius domain wall fermions". In: *PoS* LATTICE2024 (2025), p. 193. DOI: 10.22323/1.466.0193. arXiv: 2501.15494 [hep-lat].

[110] Frank R. Brown et al. "On the existence of a phase transition for QCD with three light quarks". In: *Phys. Rev. Lett.* 65 (1990), pp. 2491–2494. DOI: 10.1103/PhysRevLett.65.2491.

[111] Dániel Kincses, Márton Nagy, and Máté Csanád. "Lévy walk of pions in heavy-ion collisions". In: *Commun. Phys.* 8.1 (2025), p. 55. DOI: 10.1038/s42005-025-01973-x. arXiv: 2409.10373 [nucl-th].

[112] Paul Sorensen. "Elliptic Flow: A Study of Space-Momentum Correlations In Relativistic Nuclear Collisions". In: *Quark-gluon plasma 4*. Ed. by Rudolph C. Hwa and Xin-Nian Wang. 2010, pp. 323–374. DOI: 10.1142/9789814293297_0006. arXiv: 0905.0174 [nucl-ex].

[113] Jonah E. Bernhard, J. Scott Moreland, and Steffen A. Bass. "Bayesian estimation of the specific shear and bulk viscosity of quark–gluon plasma". In: *Nature Phys.* 15.11 (2019), pp. 1113–1117. DOI: 10.1038/s41567-019-0611-8.

[114] Ulrich Heinz and Maurice Jacob. *Evidence for a New State of Matter: An Assessment of the Results from the CERN Lead Beam Programme*. 2000. arXiv: nucl-th/0002042 [nucl-th]. URL: https://arxiv.org/abs/nucl-th/0002042.

[115] Hans J. Specht and NA60 Collaboration. "Thermal Dileptons from Hot and Dense Strongly Interacting Matter". In: *AIP Conference Proceedings* 1322.1 (Dec. 2010), pp. 1–10. ISSN: 0094-243X. DOI: 10.1063/1.3541982. eprint: https://pubs.aip.org/aip/acp/article-pdf/1322/1/1/12167347/1_1_online.pdf. URL: https://doi.org/10.1063/1.3541982.

[116] A. D. Panagiotou et al. "Experimental Evidence for a Liquid-Gas Phase Transition in Nuclear Systems". In: *Phys. Rev. Lett.* 52 (7 Feb. 1984), pp. 496–499. DOI: 10.1103/PhysRevLett.52.496. URL: https://link.aps.org/doi/10.1103/PhysRevLett.52.496.

[117] Bertrand C. Barrois. "Superconducting Quark Matter". In: *Nucl. Phys. B* 129 (1977), pp. 390–396. DOI: 10.1016/0550-3213(77)90123-7.

[118] Francois Gelis et al. "The Color Glass Condensate". In: *Annual Review of Nuclear and Particle Science* 60.1 (Nov. 2010), pp. 463–489. ISSN: 1545-4134. DOI: 10.1146/annurev.nucl.010909.083629. URL: http://dx.doi.org/10.1146/annurev.nucl.010909.083629.

[119] N. Dupuis et al. "The nonperturbative functional renormalization group and its applications". In: *Physics Reports* 910 (May 2021), pp. 1–114. ISSN: 0370-1573. DOI: 10.1016/j.physrep.2021.01.001. URL: http://dx.doi.org/10.1016/j.physrep.2021.01.001.

[120] Christof Wetterich. "Exact evolution equation for the effective potential". In: *Phys. Lett. B* 301 (1993), pp. 90–94. DOI: 10.1016/0370-2693(93)90726-X. arXiv: 1710.05815 [hep-th].

[121] Wei-jie Fu, Jan M. Pawlowski, and Fabian Rennecke. "Strangeness neutrality and QCD thermodynamics". In: *SciPost Physics Core* 2.1 (Feb. 2020). DOI: 10.21468/scipostphyscore.2.1.002. URL: http://dx.doi.org/10.21468/SciPostPhysCore.2.1.002.

[122] M. Leonhardt et al. "Symmetric Nuclear Matter from the Strong Interaction". In: *Phys. Rev. Lett.* 125 (14 Sept. 2020), p. 142502. DOI: 10.1103/PhysRevLett.125.142502. URL: https://link.aps.org/doi/10.1103/PhysRevLett.125.142502.

[123] Jens Braun, Marc Leonhardt, and Martin Pospiech. "Fierz-complete NJL model study. III. Emergence from quark-gluon dynamics". In: *Phys. Rev. D* 101 (3 Feb. 2020), p. 036004. DOI: 10.1103/PhysRevD.101.036004. URL: https://link.aps.org/doi/10.1103/PhysRevD.101.036004.

[124] Jens Braun et al. "Chiral susceptibility in (2+1)-flavor QCD". In: *Phys. Rev. D* 102 (5 Sept. 2020), p. 056010. DOI: 10.1103/PhysRevD.102.056010. URL: https://link.aps.org/doi/10.1103/PhysRevD.102.056010.

[125] Fei Gao and Jan M. Pawlowski. "Chiral phase structure and critical end point in QCD". In: *Phys. Lett. B* 820 (2021), p. 136584. DOI: 10.1016/j.physletb.2021.136584. arXiv: 2010.13705 [hep-ph].

[126] Fei Gao and Jan M. Pawlowski. "QCD phase structure from functional methods". In: *Phys. Rev. D* 102 (3 Aug. 2020), p. 034027. DOI: 10.1103/PhysRevD.102.034027. URL: https://link.aps.org/doi/10.1103/PhysRevD.102.034027.

[127] Christian S. Fischer. "QCD at finite temperature and chemical potential from Dyson–Schwinger equations". In: *Progress in Particle and Nuclear Physics* 105 (Mar. 2019), pp. 1–60. ISSN: 0146-6410. DOI: 10.1016/j.ppnp.2019.01.002. URL: http://dx.doi.org/10.1016/j.ppnp.2019.01.002.

[128] Philipp Isserstedt et al. "Baryon number fluctuations in the QCD phase diagram from Dyson-Schwinger equations". In: *Physical Review D* 100.7 (Oct. 2019). ISSN: 2470-0029. DOI: 10.1103/physrevd.100.074011. URL: http://dx.doi.org/10.1103/PhysRevD.100.074011.

[129] Wei-jie Fu, Jan M. Pawlowski, and Fabian Rennecke. "QCD phase structure at finite temperature and density". In: *Phys. Rev. D* 101.5 (2020), p. 054032. DOI: 10.1103/PhysRevD.101.054032. arXiv: 1909.02991 [hep-ph].

[130] Philippe de Forcrand. "Simulating QCD at finite density". In: *PoS* LAT2009 (2009). Ed. by Chuan Liu and Yu Zhu, p. 010. DOI: 10.22323/1.091.0010. arXiv: 1005.0539 [hep-lat].

[131] Gert Aarts. "Complex Langevin dynamics and other approaches at finite chemical potential". In: *PoS* LATTICE2012 (2012). Ed. by Derek Leinweber et al., p. 017. arXiv: 1302.3028 [hep-lat].

[132] G. Parisi. "ON COMPLEX PROBABILITIES". In: *Phys. Lett. B* 131 (1983), pp. 393–395. DOI: 10.1016/0370-2693(83)90525-7.

[133] Marco Cristoforetti, Francesco Di Renzo, and Luigi Scorzato. "New approach to the sign problem in quantum field theories: High density QCD on a Lefschetz thimble". In: *Phys. Rev. D* 86 (7 Oct. 2012), p. 074506. DOI: 10.1103/PhysRevD.86.074506. URL: https://link.aps.org/doi/10.1103/PhysRevD.86.074506.

[134] A. Bazavov et al. "The QCD Equation of State to $\mathcal{O}(\mu_B^6)$ from Lattice QCD". In: *Phys. Rev. D* 95.5 (2017), p. 054504. DOI: 10.1103/PhysRevD.95.054504. arXiv: 1701.04325 [hep-lat].

[135] A. Bazavov et al. "Skewness and kurtosis of net baryon-number distributions at small values of the baryon chemical potential". In: *Phys. Rev. D* 96.7 (2017), p. 074510. DOI: 10.1103/PhysRevD.96.074510. arXiv: 1708.04897 [hep-lat].

[136] Claudio Bonati et al. "Curvature of the pseudocritical line in QCD: Taylor expansion matches analytic continuation". In: *Phys. Rev. D* 98.5 (2018), p. 054510. DOI: 10.1103/PhysRevD.98.054510. arXiv: 1805.02960 [hep-lat].

[137] Szabolcs Borsanyi et al. "Higher order fluctuations and correlations of conserved charges from lattice QCD". In: *JHEP* 10 (2018), p. 205. DOI: 10.1007/JHEP10(2018)205. arXiv: 1805.04445 [hep-lat].

[138] A. Bazavov et al. "Chiral crossover in QCD at zero and non-zero chemical potentials". In: *Phys. Lett. B* 795 (2019), pp. 15–21. DOI: 10.1016/j.physletb.2019.05.013. arXiv: 1812.08235 [hep-lat].

[139] Jana N. Guenther et al. "Lattice thermodynamics at finite chemical potential from analytical Continuation". In: vol. 1070. 1. Cited by: 10; All Open Access, Gold Open Access. 2018. DOI: 10.1088/1742-6596/1070/1/012002. URL: https://www.scopus.com/inward/record.uri?eid=2-s2.0-85054538462&doi=10.1088%2f1742-6596%2f1070%2f1%2f012002&partnerID=40&md5=ffe9021d4ee4a4e09a3362cd78f631f5.

[140] Heng-Tong Ding et al. "Chiral phase transition in (2 + 1)-flavor QCD". In: *PoS* LATTICE2018 (2019), p. 171. DOI: 10.22323/1.334.0171. arXiv: 1905.11610 [hep-lat].

[141] A. Bazavov et al. "Skewness, kurtosis, and the fifth and sixth order cumulants of net baryon-number distributions from lattice QCD confront high-statistics STAR data". In: *Phys. Rev. D* 101.7 (2020), p. 074502. DOI: 10.1103/PhysRevD.101.074502. arXiv: 2001.08530 [hep-lat].

[142] Takeo Matsubara. "A New approach to quantum statistical mechanics". In: *Prog. Theor. Phys.* 14 (1955), pp. 351–378. DOI: 10.1143/PTP.14.351.

[143] Eric Braaten. "Solution to the perturbative infrared catastrophe of hot gauge theories". In: *Phys. Rev. Lett.* 74 (1995), pp. 2164–2167. DOI: 10.1103/PhysRevLett.74.2164. arXiv: hep-ph/9409434.

[144] Eric Braaten and Agustin Nieto. "Effective field theory approach to high temperature thermodynamics". In: *Phys. Rev. D* 51 (1995), pp. 6990–7006. DOI: 10.1103/PhysRevD.51.6990. arXiv: hep-ph/9501375.

[145] K. Kajantie et al. "Generic rules for high temperature dimensional reduction and their application to the standard model". In: *Nucl. Phys. B* 458 (1996), pp. 90–136. DOI: 10.1016/0550-3213(95)00549-8. arXiv: hep-ph/9508379.

[146] M. Laine and Y. Schroder. "Two-loop QCD gauge coupling at high temperatures". In: *JHEP* 03 (2005), p. 067. DOI: 10.1088/1126-6708/2005/03/067. arXiv: hep-ph/0503061.

[147] Ioan Ghisoiu, Jan Moller, and York Schroder. "Debye screening mass of hot Yang-Mills theory to three-loop order". In: *JHEP* 11 (2015), p. 121. DOI: 10.1007/JHEP11(2015)121. arXiv: 1509.08727 [hep-ph].

[148] Andrei D. Linde. "Infrared Problem in Thermodynamics of the Yang-Mills Gas". In: *Phys. Lett. B* 96 (1980), pp. 289–292. DOI: 10.1016/0370-2693(80)90769-8.

[149] K. Kajantie et al. "The Pressure of hot QCD up to g6 ln(1/g)". In: *Phys. Rev. D* 67 (2003), p. 105008. DOI: 10.1103/PhysRevD.67.105008. arXiv: hep-ph/0211321.

[150] O. Philipsen. "Debye screening in the QCD plasma". In: *4th International Conference on Strong and Electroweak Matter*. June 2000, pp. 95–106. DOI: 10.1142/9789812799913_0008. arXiv: hep-ph/0010327.

[151] Su-zhou Huang and Marcello Lissia. "The Dimensionally reduced effective theory for quarks in high temperature QCD". In: *Nucl. Phys. B* 480 (1996), pp. 623–654. DOI: 10.1016/S0550-3213(96)00463-4. arXiv: hep-ph/9511383.

[152] W. E. Caswell and G. P. Lepage. "Effective Lagrangians for Bound State Problems in QED, QCD, and Other Field Theories". In: *Phys. Lett. B* 167 (1986), pp. 437–442. DOI: 10.1016/0370-2693(86)91297-9.

[153] Nora Brambilla et al. "Potential NRQCD: An Effective theory for heavy quarkonium". In: *Nucl. Phys. B* 566 (2000), p. 275. DOI: 10.1016/S0550-3213(99)00693-8. arXiv: hep-ph/9907240.

[154] M. Laine and M. Vepsalainen. "Mesonic correlation lengths in high temperature QCD". In: *JHEP* 02 (2004), p. 004. DOI: 10.1088/1126-6708/2004/02/004. arXiv: hep-ph/0311268.

[155] Leonardo Giusti and Martin Lüscher. "Topological susceptibility at $T > T_c$ from master-field simulations of the SU(3) gauge theory". In: *Eur. Phys. J. C* 79.3 (2019), p. 207. DOI: 10.1140/epjc/s10052-019-6706-7. arXiv: 1812.02062 [hep-lat].

[156] Sz. Borsanyi et al. "Calculation of the axion mass based on high-temperature lattice quantum chromodynamics". In: *Nature* 539.7627 (2016), pp. 69–71. DOI: 10.1038/nature20115. arXiv: 1606.07494 [hep-lat].

[157] Claudio Bonati et al. "Axion phenomenology and θ-dependence from N_f = 2+1 lattice QCD". In: *JHEP* 03 (2016), p. 155. DOI: 10.1007/JHEP03(2016)155. arXiv: 1512.06746 [hep-lat].

[158] Chen Chen, Fei Gao, and Si-xue Qin. "Screening masses of positive- and negative-parity hadron ground states, including those with strangeness". In: *Phys. Rev. D* 112.1 (2025), p. 014022. DOI: 10.1103/527r-mtxb. arXiv: 2412.15045 [hep-ph].

[159] M. A. Ramírez-Garrido et al. "Screening masses for scalar and pseudoscalar mesons and their diquark partners: Insights from the contact interaction model". In: *Phys. Rev. D* 112.3 (2025), p. 034024. DOI: 10.1103/jfzy-2nt4. arXiv: 2508.01099 [hep-ph].

[160] B. B. Brandt et al. "A relation between screening masses and real-time rates". In: *JHEP* 05 (2014), p. 117. DOI: 10.1007/JHEP05(2014)117. arXiv: 1404.2404 [hep-ph].

[161] T. H. Hansson, M. Sporre, and I. Zahed. "Baryonic and gluonic correlators in hot QCD". In: *Nucl. Phys. B* 427 (1994), pp. 545–560. DOI: 10.1016/0550-3213(94)90639-4. arXiv: hep-ph/9401281.

[162] Alexei Bazavov et al. "Meson screening masses in (2+1)-flavor QCD". In: *Phys. Rev. D* 100.9 (2019), p. 094510. DOI: 10.1103/PhysRevD.100.094510. arXiv: 1908.09552 [hep-lat].

[163] Carleton E. Detar and John B. Kogut. "The Hadronic Spectrum of the Quark Plasma". In: *Phys. Rev. Lett.* 59 (1987), p. 399. DOI: 10.1103/PhysRevLett.59.399.

[164] M. Cheng et al. "Meson screening masses from lattice QCD with two light and the strange quark". In: *Eur. Phys. J. C* 71 (2011), p. 1564. DOI: 10.1140/epjc/s10052-011-1564-y. arXiv: 1010.1216 [hep-lat].

[165] Bastian B. Brandt et al. "On the strength of the $U_A(1)$ anomaly at the chiral phase transition in $N_f = 2$ QCD". In: *JHEP* 12 (2016), p. 158. DOI: 10.1007/JHEP12(2016)158. arXiv: 1608.06882 [hep-lat].

[166] Marco Cè et al. "Probing the photon emissivity of the quark-gluon plasma without an inverse problem in lattice QCD". In: *Phys. Rev. D* 109.1 (2024), p. 014507. DOI: 10.1103/PhysRevD.109.014507. arXiv: 2309.09884 [hep-lat].

[167] Ardit Krasniqi et al. "Hot QCD matter around the chiral crossover: A lattice study with O(a)-improved Wilson fermions". In: *Phys. Rev. D* 110.11 (2024), p. 114506. DOI: 10.1103/PhysRevD.110.114506. arXiv: 2407.01657 [hep-lat].

[168] Ardit Krasniqi et al. "Probing how bright the quark-gluon plasma glows in lattice QCD". In: *Phys. Rev. D* 112.7 (2025), p. 074503. DOI: 10.1103/8dq9-q62p. arXiv: 2505.10295 [hep-lat].

[169] Carleton E. Detar and John B. Kogut. "Measuring the Hadronic Spectrum of the Quark Plasma". In: *Phys. Rev. D* 36 (1987), p. 2828. DOI: 10.1103/PhysRevD.36.2828.

[170] Andreas Gocksch, Pietro Rossi, and Urs M. Heller. "QUENCHED HADRONIC SCREENING LENGTHS AT HIGH TEMPERATURE". In: *Phys. Lett. B* 205 (1988), pp. 334–338. DOI: 10.1016/0370-2693(88)91674-7.

[171] Steven A. Gottlieb et al. "Hadronic Screening Lengths in the High Temperature Plasma". In: *Phys. Rev. Lett.* 59 (1987), p. 1881. DOI: 10.1103/PhysRevLett.59.1881.

[172] Leonardo Giusti and Harvey B. Meyer. "Thermodynamic potentials from shifted boundary conditions: the scalar-field theory case". In: *JHEP* 11 (2011), p. 087. DOI: 10.1007/JHEP11(2011)087. arXiv: 1110.3136 [hep-lat].

[173] Leonardo Giusti and Harvey B. Meyer. "Thermal momentum distribution from path integrals with shifted boundary conditions". In: *Phys. Rev. Lett.* 106 (2011), p. 131601. DOI: 10.1103/PhysRevLett.106.131601. arXiv: 1011.2727 [hep-lat].

[174] Leonardo Giusti and Harvey B. Meyer. "Implications of Poincare symmetry for thermal field theories in finite-volume". In: *JHEP* 01 (2013), p. 140. DOI: 10.1007/JHEP01(2013)140. arXiv: 1211.6669 [hep-lat].

[175] Leonardo Giusti and Michele Pepe. "Equation of state of the SU(3) Yang–Mills theory: A precise determination from a moving frame". In: *Phys. Lett. B* 769 (2017), pp. 385–390. DOI: 10.1016/j.physletb.2017.04.001. arXiv: 1612.00265 [hep-lat].

[176] Matteo Bresciani et al. "QCD Equation of State with Nf=3 Flavors up to the Electroweak Scale". In: *Phys. Rev. Lett.* 134.20 (2025), p. 201904. DOI: 10.1103/PhysRevLett.134.201904. arXiv: 2501.11603 [hep-lat].

[177] Matteo Bresciani et al. "QCD Equation of State at very high temperature: computational strategy, simulations and data analysis". In: (Nov. 2025). arXiv: 2511.09160 [hep-lat].

[178] Matteo Bresciani et al. "Non-perturbative renormalization of the QCD flavour-singlet local vector current". In: *Phys. Lett. B* 835 (2022), p. 137579. DOI: 10.1016/j.physletb.2022.137579. arXiv: 2203.14754 [hep-lat].

[179] Matteo Bresciani et al. "Progresses on high-temperature QCD: Equation of State and energy-momentum tensor". In: *PoS* LATTICE2023 (2024), p. 192. DOI: 10.22323/1.453.0192. arXiv: 2312.11009 [hep-lat].

[180] Martin Lüscher et al. "The Schrödinger functional: A Renormalizable probe for nonAbelian gauge theories". In: *Nucl. Phys. B* 384 (1992), pp. 168–228. DOI: 10.1016/0550-3213(92)90466-O. arXiv: hep-lat/9207009.

[181] Patrick Fritzsch and Alberto Ramos. "The gradient flow coupling in the Schrödinger functional". In: *JHEP* 10 (2013), p. 008. DOI: 10.1007/JHEP10(2013)008. arXiv: 1301.4388 [hep-lat].

[182] Mattia Dalla Brida et al. "Slow running of the gradient flow coupling from 200 MeV to 4 GeV in N_{f} = 3 QCD". In: *Phys. Rev. D* 95 (1 Jan. 2017), p. 014507. DOI: 10.1103/PhysRevD.95.014507. URL: https://link.aps.org/doi/10.1103/PhysRevD.95.014507.

[183] Isabel Campos et al. "Non-perturbative quark mass renormalisation and running in N_f = 3 QCD". In: *Eur. Phys. J. C* 78.5 (2018), p. 387. DOI: 10.1140/epjc/s10052-018-5870-5. arXiv: 1802.05243 [hep-lat].

[184] Marco Cè et al. "Non-static mesonic screening masses in high temperature QCD". In: (2025). In preparation.

[185] Saumen Datta et al. "Nucleons near the QCD deconfinement transition". In: *JHEP* 02 (2013), p. 145. DOI: 10.1007/JHEP02(2013)145. arXiv: 1212.2927 [hep-lat].

[186] C. Rohrhofer et al. "Symmetries of the Light Hadron Spectrum in High Temperature QCD". In: *PoS* LATTICE2019 (2020), p. 227. DOI: 10.22323/1.363.0227. arXiv: 1912.00678 [hep-lat].

[187] Tapan Kumar Das. *Hyperspherical Harmonics Expansion Techniques: Application to Problems in Physics*. Vol. 170. Springer / Theoretical and Mathematical Physics, 2016. DOI: 10.1007/978-81-322-2361-0.

[188] T. H. Hansson and I. Zahed. "Hadronic correlators in hot QCD". In: *Nucl. Phys. B* 374 (1992), pp. 277–287. DOI: 10.1016/0550-3213(92)90353-D.

[189] Michele Della Morte et al. "Improved interpolating fields for hadrons at non-zero momentum". In: *Eur. Phys. J. A* 48 (2012), p. 139. DOI: 10.1140/epja/i2012-12139-9. arXiv: 1208.0189 [hep-lat].

[190] Shao-Jing Dong and Keh-Fei Liu. "Stochastic estimation with Z(2) noise". In: *Phys. Lett. B* 328 (1994), pp. 130–136. DOI: 10.1016/0370-2693(94)90440-5. arXiv: hep-lat/9308015.

[191] Christopher Michael and J. Peisa. "Maximal variance reduction for stochastic propagators with applications to the static quark spectrum". In: *Phys. Rev. D* 58 (1998), p. 034506. DOI: 10.1103/PhysRevD.58.034506. arXiv: hep-lat/9802015.

[192] Leonardo Giusti et al. "Frequency-splitting estimators of single-propagator traces". In: *Eur. Phys. J. C* 79.7 (2019), p. 586. DOI: 10.1140/epjc/s10052-019-7049-0. arXiv: 1903.10447 [hep-lat].

[193] Dibyendu Bala et al. "Spatial String Tension and Its Effects on Screening Correlators in a Thermal QCD Plasma". In: *Phys. Rev. Lett.* 135.1 (2025), p. 012301. DOI: 10.1103/3tmf-s94w. arXiv: 2501.17943 [hep-lat].

[194] Mattia Dalla Brida. "Past, present, and future of precision determinations of the QCD parameters from lattice QCD". In: *Eur. Phys. J. A* 57.2 (2021), p. 66. DOI: 10.1140/epja/s10050-021-00381-3. arXiv: 2012.01232 [hep-lat].

[195] Nicholas Metropolis et al. "Equation of State Calculations by Fast Computing Machines". In: *The Journal of Chemical Physics* 21.6 (June 1953), pp. 1087–1092. ISSN: 0021-9606. DOI: 10.1063/1.1699114. eprint: https://pubs.aip.org/aip/jcp/article-pdf/21/6/1087/18802390/1087_1_online.pdf. URL: https://doi.org/10.1063/1.1699114.

[196] W. K. Hastings. "Monte Carlo sampling methods using Markov chains and their applications". In: *Biometrika* 57.1 (Apr. 1970), pp. 97–109. ISSN: 0006-3444. DOI: 10.1093/biomet/57.1.97. eprint: https://academic.oup.com/biomet/article-pdf/57/1/97/23940249/57-1-97.pdf. URL: https://doi.org/10.1093/biomet/57.1.97.

[197] S. Duane et al. "Hybrid Monte Carlo". In: *Phys. Lett. B* 195 (1987), pp. 216–222. DOI: 10.1016/0370-2693(87)91197-X.

[198] I. P. Omelyan, I. M. Mryglod, and R. Folk. "Optimized Verlet-like algorithms for molecular dynamics simulations". In: *Phys. Rev. E* 65.5 (2002), p. 056706. DOI: 10.1103/PhysRevE.65.056706.

[199] I. P. Omelyan, I. M. Mryglod, and R. Folk. "Symplectic analytically integrable decomposition algorithms: classification, derivation, and application to molecular dynamics, quantum and celestial mechanics simulations". In: *Comput. Phys. Commun.* 151.3 (2003), pp. 272–314. DOI: 10.1016/S0010-4655(02)00754-3.

[200] Martin Hasenbusch. "Speeding up the hybrid Monte Carlo algorithm for dynamical fermions". In: *Phys. Lett. B* 519 (2001), pp. 177–182. DOI: 10.1016/S0370-2693(01)01102-9. arXiv: hep-lat/0107019.

[201] M. Hasenbusch and K. Jansen. "Speeding up lattice QCD simulations with clover improved Wilson fermions". In: *Nucl. Phys. B* 659 (2003), pp. 299–320. DOI: 10.1016/S0550-3213(03)00227-X. arXiv: hep-lat/0211042.

[202] C. Urbach et al. "HMC algorithm with multiple time scale integration and mass preconditioning". In: *Comput. Phys. Commun.* 174 (2006), pp. 87–98. DOI: 10.1016/j.cpc.2005.08.006. arXiv: hep-lat/0506011.

[203] A. D. Kennedy, Ivan Horvath, and Stefan Sint. "A New exact method for dynamical fermion computations with nonlocal actions". In: *Nucl. Phys. B Proc. Suppl.* 73 (1999). Ed. by Thomas A. DeGrand et al., pp. 834–836. DOI: 10.1016/S0920-5632(99)85217-7. arXiv: hep-lat/9809092.

[204] M. A. Clark and A. D. Kennedy. "The RHMC algorithm for two flavors of dynamical staggered fermions". In: *Nucl. Phys. B Proc. Suppl.* 129 (2004). Ed. by S. Aoki et al., pp. 850–852. DOI: 10.1016/S0920-5632(03)02732-4. arXiv: hep-lat/0309084.

[205] M. A. Clark, A. D. Kennedy, and Z. Sroczynski. "Exact 2+1 flavour RHMC simulations". In: *Nucl. Phys. B Proc. Suppl.* 140 (2005). Ed. by Geoffrey T. Bodwin et al., pp. 835–837. DOI: 10.1016/j.nuclphysbps.2004.11.192. arXiv: hep-lat/0409133.

[206] Martin Lüscher. "Computational Strategies in Lattice QCD". In: *Les Houches Summer School: Session 93: Modern perspectives in lattice QCD: Quantum field theory and high performance computing*. Feb. 2010, pp. 331–399. arXiv: 1002.4232 [hep-lat].

[207] Dongarra et al. - with minor processing by Our World in Data. *Computational capacity of the fastest supercomputers*. 2024. URL: https://archive.ourworldindata.org/20250909-093708/grapher/supercomputer-power-flops.html.

[208] M. Lüscher and S. Schaefer. *openQCD - Simulation programs for lattice QCD*. URL: https://luscher.web.cern.ch/luscher/openQCD/.

[209] Yutaro Akahoshi et al. "General purpose lattice QCD code set Bridge++ 2.0 for high performance computing". In: *Journal of Physics: Conference Series* 2207.1 (Mar. 2022), p. 012053. ISSN: 1742-6596. DOI: 10.1088/1742-6596/2207/1/012053. URL: http://dx.doi.org/10.1088/1742-6596/2207/1/012053.

[210] Robert G. Edwards and Bálint Joó. "The Chroma Software System for Lattice QCD". In: *Nuclear Physics B - Proceedings Supplements* 140 (Mar. 2005), pp. 832–834. ISSN: 0920-5632. DOI: 10.1016/j.nuclphysbps.2004.11.254. URL: http://dx.doi.org/10.1016/j.nuclphysbps.2004.11.254.

[211] Peter Boyle et al. *Grid: A next generation data parallel C++ QCD library*. 2015. arXiv: 1512.03487 [hep-lat]. URL: https://arxiv.org/abs/1512.03487.

[212] MILC Collaboration. *MILC code*. URL: https://web.physics.utah.edu/~detar/milc/milc_qcd.html.

[213] M.A. Clark et al. "Solving lattice QCD systems of equations using mixed precision solvers on GPUs". In: *Computer Physics Communications* 181.9 (Sept. 2010), pp. 1517–1528. ISSN: 0010-4655. DOI: 10.1016/j.cpc.2010.05.002. URL: http://dx.doi.org/10.1016/j.cpc.2010.05.002.

[214] A. Ukawa. "Computational cost of full QCD simulations experienced by CP-PACS and JLQCD Collaborations". In: *Nucl. Phys. B Proc. Suppl.* 106 (2002). Ed. by M. Muller-Preussker et al., pp. 195–196. DOI: 10.1016/S0920-5632(01)01662-0.

[215] Martin Lüscher. "Solution of the Dirac equation in lattice QCD using a domain decomposition method". In: *Comput. Phys. Commun.* 156 (2004), pp. 209–220. DOI: 10.1016/S0010-4655(03)00486-7. arXiv: hep-lat/0310048.

[216] L. Del Debbio et al. "QCD with light Wilson quarks on fine lattices. II. DD-HMC simulations and data analysis". In: *JHEP* 02 (2007), p. 082. DOI: 10.1088/1126-6708/2007/02/082. arXiv: hep-lat/0701009.

[217] Martin Lüscher. "Deflation acceleration of lattice QCD simulations". In: *JHEP* 12 (2007), p. 011. DOI: 10.1088/1126-6708/2007/12/011. arXiv: 0710.5417 [hep-lat].